MODELLING AND ANALYSIS OF HYBRID MICROGRID SYSTEM

Thesis Submitted to

Electrical Engineering Department

DELHI TECHNOLOGICAL UNIVERSITY, DELHI

in fulfillment of the requirement of the degree of

DOCTOR OF PHILOSOPHY

by

SHIKHA GUPTA

(2K12/Ph.D./EE/04)

Under the supervision of

Prof. Rachana Garg and Prof. Alka Singh

DECLARATION

This is to certify that the thesis titled "**Modelling and Control of Hybrid Microgrid System**" was carried out by me under the supervision of Prof. Rachana Garg and Prof. Alka Singh, Delhi Technological University, Delhi, India.

The interpretations put forth are based on my reading and understanding of the original texts and they are not published anywhere in the form of books, monographs or articles. The other books, articles and websites, which I have made use of are acknowledged at the respective place in the text.

For the present thesis, which I am submitting to the University, no degree or diploma or distinction has been conferred on me before, either in this or in any other University.

Place: Delhi *Shikha Gupta*

Date:28.08.2020 *2K12/PhDEE/04*

CERTIFICATE

This is to certify that the thesis titled "**Modelling and Control of Hybrid Microgrid System**" submitted for the award of the Doctor of Philosophy is original to the best of our knowledge. The work was carried out by **Ms. Shikha Gupta** under our guidance and has not been submitted in parts or full to this or any other University for the award of any degree or diploma. All the assistance and help received during the course of study have been duly acknowledged.

Shikha Gupta

Supervisors

Prof. Rachana Garg
Department of Electrical Engg.
D.T.U., Delhi

Prof. Alka Singh
Department of Electrical Engg.
D.T.U., Delhi

Acknowledgement

Writing this thesis has been fascinating and extremely rewarding. First of all, I am thankful to God, who has blessed me strength and support throughout my life and always provides me with a path to acquire knowledge and learning.

It gives me immense pleasure to express sincere gratitude towards my supervisors Prof. Rachana Garg and Prof. Alka Singh, for all their help, guidance, valuable suggestions, explanation, advices and above all, their support for carrying out this thesis work. Throughout my thesis-writing period, they were highly supportive and encouraging.

I would also like to thank Dr. Bhim Singh, IITD for his valuable suggestions and comments which motivated me to look into areas that we never thought of venturing into.

Sincere thanks to Delhi Technological University, Delhi, IIT, Delhi and Bhagwan Parshuram Institue of Technology (BPIT, Delhi) authorities for providing me the necessary facilities for the smooth completion of my work. I would like to give special thanks to Dr. Devanjali Relan and Dr. Snekha for their help and moral support during my study. I am indebted to my husband Mr. Yogesh Gupta, daughter Aadya and son Avyaan for their tremendous support, unfailing faith and patience throughout my study period. I would like to express my deepest regards and gratitude to my parents for their unmitigated love. Finally, I especially extend appreciation to Miss Seema Kewat and Mr. Anjeet for their encouragement, understanding and support.

Shikha Gupta

Abstract

Electrical practices for the power industry are enormously changing and those advancements will mark an evolution of new principles and techniques in the future, predominantly related to the planning and operation of the electricity generation and distribution. The proliferation of electricity requirements escalates the use of renewable energy sources (RESs) in the present and future energy technology. Therefore, the emphasis on the networks, which comprises a combination of RESs and their integration into the main grid has tremulously increased. RESs such as wind, photovoltaic, fuel cell have made a significant contribution to the world. Due to their eco-friendly nature, flexibility and worldwide availability, RESs have proved to be an attractive solution for designing modern grids. The proposed research work entitled "Modelling and Analysis of Hybrid Microgrid System" focuses on microgrid (MG) control to enhance its power quality performance. Microgrids are a crucial component of a modern power system and are capable of supplying growing energy needs as well as providing flexibility. Microgrids offer a platform to interface the RES and energy storage elements. The conceptualization of microgrid is based on the integration of several energy sources using power electronics equipment. Thus, the power electronic interface is a key feature in realizing the revolutionary concept of the microgrid. At the same time, the interfacing of RES with the grid through power electronic equipment also raise the concern about the reliable and stable operation.

Various configurations of the power electronics converters such as rectifiers, inverters, bidirectional converters are integral elements of microgrid (MG). Power conditioning devices add reliability and functionality to the MG system. Reliability allows large penetration of RESs while functionality ensures the optimal usage of RES in an MG. However, power electronic converters also increase the system cost due to

complex technical control and increased losses in the system.

Increased interconnection of RES may lead to severe voltage distortions and voltage fluctuations. Furthermore, the contribution of nonlinear load in the power system is high and leads to power quality (PQ) problems such as harmonic injection in voltages and currents in the system. The continued presence of PQ problems deteriorates the quality of power at the user end which is highly undesirable, hence solutions to PQ problems are mandatory for a healthy power system. A promising solution for the mitigation of PQ problems is Shunt Active Power Filter (SAPF). SAPF is a shunt connected voltage source converter with a DC-link capacitor. It is capable of mitigating PQ issues such as voltage unbalancing, current harmonics and poor power factor. It also gives superior functional characteristics such as faster response, low cost, reduced size and it is also able to deliver reactive power efficiently and improves transient condition response. However, SAPF does not contribute in terms of the active power requirement of the load, so it must be integrated with the RESs as a cost-effective solution to mitigate PQ problems.

With these considerations in the present study, three RESs, PV, wind and fuel cell are considered and modelled to frame an MG that can deliver good quality of supply at the consumer end. Further, MG is studied under the varying RESs generation, as RESs are not a constant source of power and their power generation directly dependent on the environmental conditions. Simulation results have been investigated under nonlinear load, unbalanced nonlinear load, linear load under varying environmental conditions using models developed in MATLAB/SIMULINK platform. Both grid-connected microgrid and standalone microgrid PQ issues are addressed. To develop grid-connected microgrid, different RES viz. photovoltaic, wind and fuel cell have been interfaced at a common DC-link and then with the grid through VSC. In a stand-alone microgrid, PV and wind are primary energy sources, FC and battery are secondary energy sources and electrolyzer as a dump load is used.

Initially, detailed modelling and characteristics of interfaced RESs are discussed. Further, wind-photovoltaic-fuel cell powered grid-connected microgrid has been developed. The developed MG has been tested and analyzed using conventional control techniques of VSC such as synchronous reference frame theory (SRFT),

power balance theory (PBT) with the simulated models of RESs. Further, new control techniques for DC-link voltage control based on adaptive neuro-fuzzy inference system (ANFIS), hybrid-fuzzy-PI controller (H-FLC), Takagi-Sugeno Fuzzy Logic Controller (TSFLC) DC-link voltage controller and fuzzy controller have been developed, analyzed and compared with conventional PI-based DC-link voltage control scheme. New control techniques for VSC to improve the convergence rate and to achieve DC offset rejection have been designed and developed in this research work. These techniques have been implemented in grid-connected microgrid interfaced with wind power generation source, PV power generation system and fuel cell power generation. These techniques include hyperbolic tangent least mean square (H-LMS), adaptive neuro-fuzzy inference system least mean square (ANFIS-LMS), zero attracting quaternion least mean square (ZAQ-LMS) and modified shrinkage widely linear complex-valued LMS (MSWL-CLMS). PQ issues such as load unbalancing, current harmonics, reactive power compensation and power factor correction have been considered. Detailed simulation results have been recorded and analyzed for load changes and environmental variations. Subsequently, the hybrid microgrid integrated with electric vehicle (EV) load at DC-link is developed and analyzed using the self-tuning filter (STF) control technique of VSC. EV is in plug and play role, it can be charged through RESs and on the other hand, it allows the owner to sell EV energy to the grid for revenue generation. In an electrical power system, the presence of unbalanced grid voltage is also a major PQ problem. The grid voltage can be highly distorted due to large grid impedance. Double second-order generalized integrator (DSOGI) filter to extract positive sequence voltage from the grid voltage is proposed and for the reference currents extraction, self-tuning filter (STF) is implemented. The prime characteristic of the MG is its capability of the seamless transition from grid-connected mode to standalone mode and vice-versa. The designed MG is capable of going into standalone operation during the grid outage and exhibits seamless synchronization with the grid after removal of the grid fault. Synchronization operation has been carried out using Low-Pass Notch Filter PLL (LNP-PLL) based grid-synchronization control. Grid synchronization allows the practical implementation of such a system in the real-world on a large scale.

Besides the modelling and analysis of grid-connected microgrid and its control, a standalone microgrid consisting of photovoltaic-wind power-fuel cell, battery and electrolyzer (dump load) has been developed. New power controllers and control strategy has been presented for the standalone system. Developed controllers are simple in design and based on the measurement of DC-link voltage and current. The proposed hybrid system is suitable to achieve power equilibrium through the developed controllers. Power-sharing is based on the regulation of DC-link voltage and state of charge in the battery. FC is capable to deliver power to load when power generation of PV and wind is less than the load requirement. Under all the aforementioned cases PQ issues for the presented microgrid have been mitigated successfully.

Contents

List of Figures

List of Tables

Acronyms

ANFIS	Adaptive Neuro-Fuzzy Inference System
ANN	Artificial Neural Network
APF	Active Power Filter
BES	Battery Energy System
DSOGI	Double Second-Order Generalized Integrator
EMF	Electromotive Field
EV	Electric Vehicle
FCGS	Fuel cell Power Generation Source
FLC	Fuzzy Logic Controller
HCC	Hysteresis Current Control
HMG	Hybrid Micro Grid
H-FLC	Hybrid Fuzzy Logic Controller
H-LMS	Hyperbolic Tangent LMS
IC	Incremental Conductance
IGBT	Insulated Gate Bipolar Transistor
LMS	Least Mean Square
MF	Membership Function
MG	Microgrid
MSWL-CLMS	Modified Shrinkage Widely Linear Complex-Valued LMS
PBT	Power Balance Theory
PCI	Point of Common Integration
PF	Power Factor
PI	Proportional Integral
PLL	Phase Lock Loop
PO	Perturbation and Observation

PQ	Power Quality
PWM	Pulse Width Modulation
PVGS	Photovoltaic Power Generation Source
RES	Renewable Energy Source
SRFT	Synchronous Reference Frame Theory
STF	Self Tuning Filter
THD	Total Harmonic Distortion
TSFLC	Takagi-Sugeno Fuzzy Logic Controller
UPF	Unity Power Factor
VSC	Voltage Source Controller
WPGS	Wind Power Generation Source
ZAQ	Zero-Attracting Quaternion
LNP-PLL	Low-Pass Notch Filter PLL

Notation

δ	Learning Rate
v_{ga}, v_{gb}, v_{gc}	Phase a, b, c grid voltage
i_{ga}, i_{gb}, i_{gc}	Phase a, b, c supply currents
v_a, v_b, v_c	Phase a, b, c supply voltage
i_{La}, i_{Lb}, i_{Lc}	Phase a, b, c load currents
i_{vsc}	Phase a, b, c VSC currents
C_{dc}	DC-link capacitor
V_{dcl}	DC-link voltage
V^*_{dcl}	Reference DC-link voltage
i_{loss}	Loss component due to IGBT switching
I_{Lp}	Effective fundamental active power component
$i^*_{ga}, i^*_{gb}, i^*_{gc}$	Phase a, b, c supply reference currents
V_t	Amplitude of PCI voltage
u_a, u_b, u_c	Phase a, b, c unit templates
W_{avg}	Average fundamental active power component
W_{ta}, W_{tb}, W_{tc}	Phase a, b, c average fundamental active power component
e_{dc}	Error between V_{dcl} and V^*_{dcl}
k_i, k_p	Proportional and integral gain of PI controller

Chapter 1

INTRODUCTION

Exponential growth in the consumption of electrical energy has been witnessed worldwide in the past few decades. Consequently, the conventional power system faces stress in terms of operational efficiency, increased pollution, gradual price increment and fossil fuel exhaustion. These economic and environmental concerns have revolutionized electricity generation. One attractive and sustainable solution is the use of renewable energy sources (RESs) which can help in improving fuel savings, energy efficiency and reliability. The power system, in the future, may contain several RESs such as solar cells, wind turbines, micro-turbines (natural gas), fuel cells (FC) and storage batteries as alternative power sources. Such type of power generation is known as distributed generation and the penetration of distributed generation brought the concept of the microgrid [1].

1.1 State of the Art

Microgrid articulates the idea of integration of RESs to harness their potential as a solution to meet continuously increasing energy needs. It offers a robust platform comprising of RES, control unit, load and energy-storage elements [2,3]. Microgrid can be operated in autonomous and/or grid-connected mode [4]. The microgrid offers several benefits such as energy security, reliability, stability, increased efficiency and reduced transmission losses since generators are in close proximity to the load. They differ from the traditional power systems as they use smaller power generators, distributed generation and are located near the energy users [5].

Fig. 1.1 presents the schematic diagram of microgrid in which power generating sources are integrated the load and grid through power electronic interface.

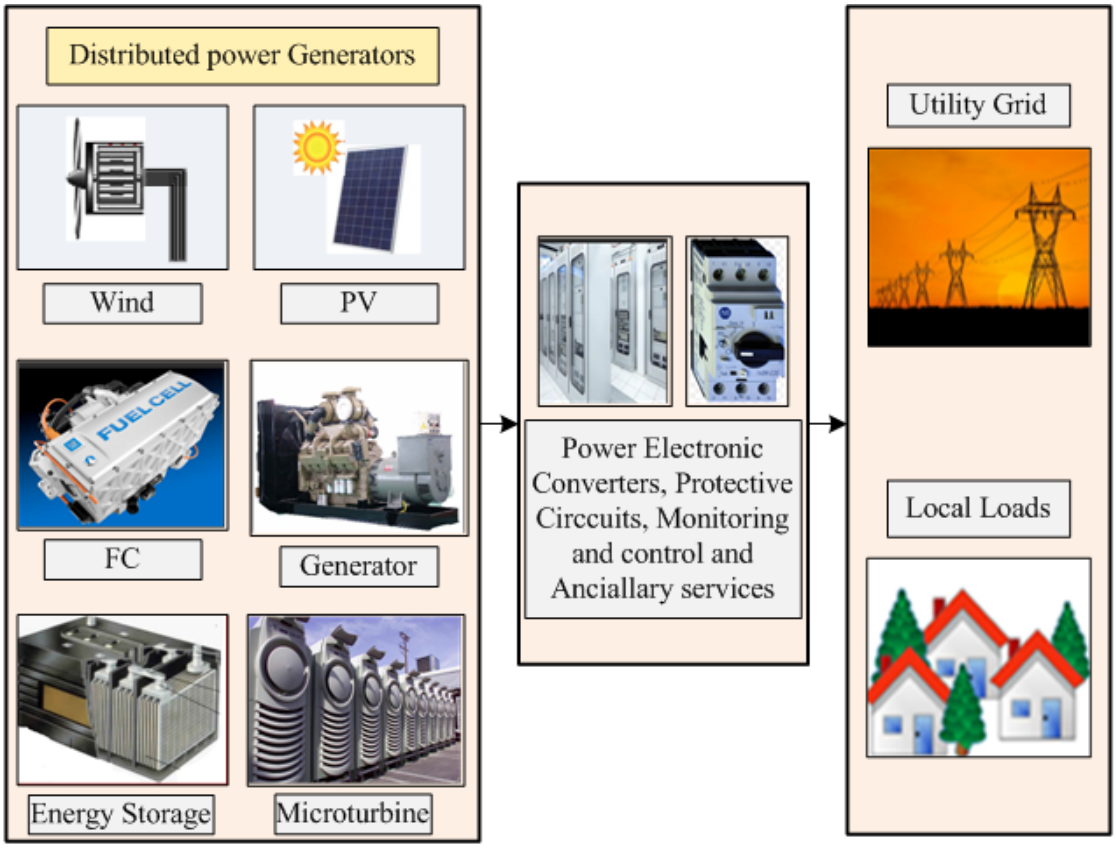

Figure 1.1: Microgrid architecture

Microgrids are designed by interfacing numerous units viz. AC and DC power sources, storage elements, AC and DC loads, AC-DC, DC-DC, or DC-AC converters [6, 7]. The selection of configuration depends upon the geographical, economic and technological aspects.

1.2 Microgrid Energy Sources

The main attribute of the microgrid is that the electricity generation is in close proximity to the end-user load [8, 9]. There are several RESs as distributed generators available today such as Photovoltaic Power Generation System (PVGS), Fuel cell Power Generation System (FCGS) with an electrolyzer and Wind Power Generation System (WPGS), etc. An overview of the generation systems is given in the following subsections.

1.2.1 Photovoltaic Power Generation System (PVGS)

Among the available green energy sources, PVGS are becoming popular due to technological advancement, decreasing prices and satisfactory performance. It is the most promising energy source for future MGs due to the advantages such as abundance in nature, pollution-free and distributed throughout the earth [10]. But it has some drawbacks also viz. intermittency, high cost and low efficiency. Although PVGS is expensive than other resources, government promotions and technological developments in the area of power electronics has made it popular worldwide. Recent surveys exhibit that during the last few years, the retail price of solar modules has gone down drastically. The output power of the PV system ranges from a few watts to megawatt [11]. In the photovoltaic energy production process, solar energy is converted to electricity through the photovoltaic effect. PV cell has two layers of semiconductors, coated with a photosensitive material and working is similar to the p-n junction. The current flowing through the circuit depends on the irradiation level. If radiation is higher, more current is produced by the solar PV cell [12]. Parallel and series connected solar cells form a solar panel, further solar panels connected in series or parallel form solar string [13, 14]. The development of the PV panel from the PV cell is shown in Fig. 1.2. In typical PV characteristics, there is a unique point of maximum power. To operate the system at this point several Maximum Power Point Techniques (MPPT) algorithms have been well established in the literature [15–21]. These algorithms are realized by controlling the switching of the DC-DC boost converter.

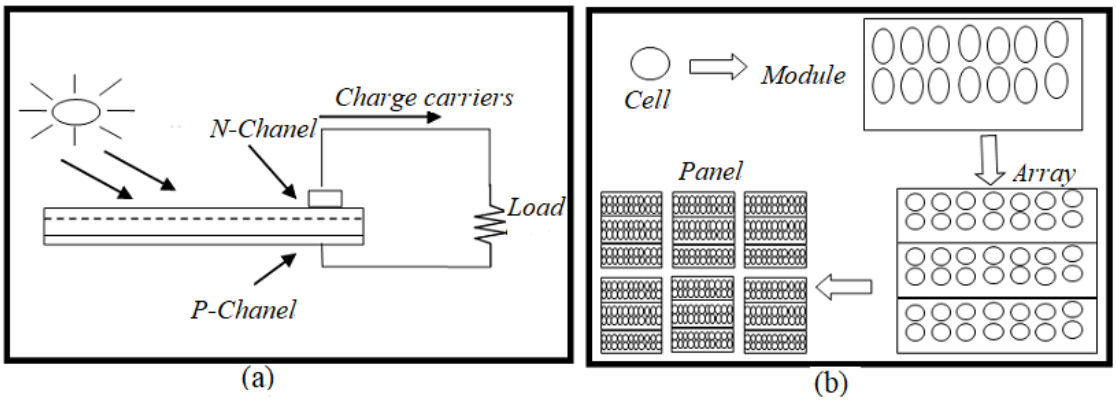

Figure 1.2: PV configuration(a) PV cell (b)Development of PV array

1.2.2 Wind Energy Power Generation System (WPGS)

A WPGS converts the wind energy into electrical energy. The main component of a WPGS is the turbine which is used to convert the kinetic energy of wind into mechanical torque. This torque of the turbine can be calculated from available mechanical power at the turbine [22]. Wind energy provides an attractive solution due to its low cost and rapid technological developments [22, 23]. However, due to the intermittent nature of the wind, generators face rapid deviations in the output voltage and frequency. Therefore, the stochastic nature of wind limits its penetration in the microgrid system. Intermittent energy problems of wind generators can be overcome by interfacing other RESs or battery energy system (BES) as a backup [24–27]. Battery energy system provides short term energy solutions whereas integration of PVGS or FCGS appears to be an effective long term solution. Variable speed wind turbine is becoming popular owing to its capability of extracting optimum power through MPPT with overall improved efficiency. Further, due to its low rotational speed, the gearbox can be excluded [28–30]. Usage of direct drive permanent magnet synchronous generator (PMSG) is technically attractive, particularly for the small wind turbines.

1.2.3 Fuel Cell Power Generation System

Among the sustainable power sources, FCs are picking up conspicuousness and developing at a fast pace [31]. Fuel cells are the electrochemical device which converts chemical-energy of fuel in electrical energy. FCs are broadly classified in Solid Oxide Fuel Cell (SOFC), Molten Carbonate Fuel Cell and Proton Exchange Membrane fuel cell. Solid oxide fuel cells are feasible option for power creation in the range of few kilo Watts to hundreds of kilo Watts. The accessibility of a wide scope of hydrocarbon based fuels, higher operational capability and high efficiency in power-conversion made them alluring. Higher efficiency, low carbon footprints, lesser noise and higher modularity are attractive features of FC [32]. Moreover, they can support the power system as long as the fuel is available. The by-products of fuel cells are only water and heat, thus, they are suitable for indoor operation also [33]. Despite several advantages, the limitation of FC is its higher cost and

limited life span in comparison to other conventional energy sources [34]. Further, FC has a slow dynamic response to cope up with sudden load changes. Nevertheless, using energy storage systems such as ultra-capacitors or Battery Energy System (BES) in combination with FCGS can supply power instantaneously. These energy storage units can fill the gap between fuel cells output power and load demand.

1.2.4 Battery Energy System

In standalone systems, the energy storage system such as the battery energy system plays a crucial role to maintain power balance. It stores the power during surplus generation and at the time of power deficit act as a backup and provides energy to the load [35]. The battery is a source of DC power and thus the use of DC-AC converter is essential for its integration in the microgrid. Also, a bidirectional DC–DC converter is used to integrate the battery to the DC bus. It allows bidirectional power flow between the system and BES. The electrochemical battery can be classified as: lead-acid battery, nickel-cadmium battery, nickel-metal hydride battery etc. Lead-acid battery technology is one of the most developed battery technologies [36] and in spite of its limitation of the short life cycle, they are a common choice for energy storage.

1.3 Power Quality Problems in Microgrid System

Consumer loads consist of electronic devices, lights, electrical motors and other similar devices. The use of electronic loads is increasing rapidly which deteriorates the quality of power. Microgrid system suffers from PQ issues such as voltage fluctuations, harmonic distortions, poor power factor (PF), load balance and DC-offset [37–43]. The interfacing of RESs, particularly due to the intermittent nature of solar and wind power sources, cause voltage fluctuations at PCI (Point of Common Interconnection) and DC-link. This impacts negatively on the quality of power supplied to the end user. Furthermore, different kinds of domestic nonlinear loads also create PQ problems for the microgrid as well as utility grid. The substantial growth of nonlinear industrial and commercial loads inject harmonics which cause poor quality of power supplied to the consumer. PQ problems such as

total harmonic distortion (THD), regulation of voltage at PCI, DC-link voltage control, power flow management, reactive power compensation load unbalancing are needed to be addressed. Stable and reliable AC and DC-link voltages having a good quality of power at the consumer end are critical challenges in the microgrids. PQ problems can also limit the maximum penetration of renewable energy sources into a microgrid. It is mandatory to mitigate these PQ problems and provide a sinusoidal balanced supply to the load connected in the system [42–51]. Various PQ problems are summarized in Fig. 1.3.

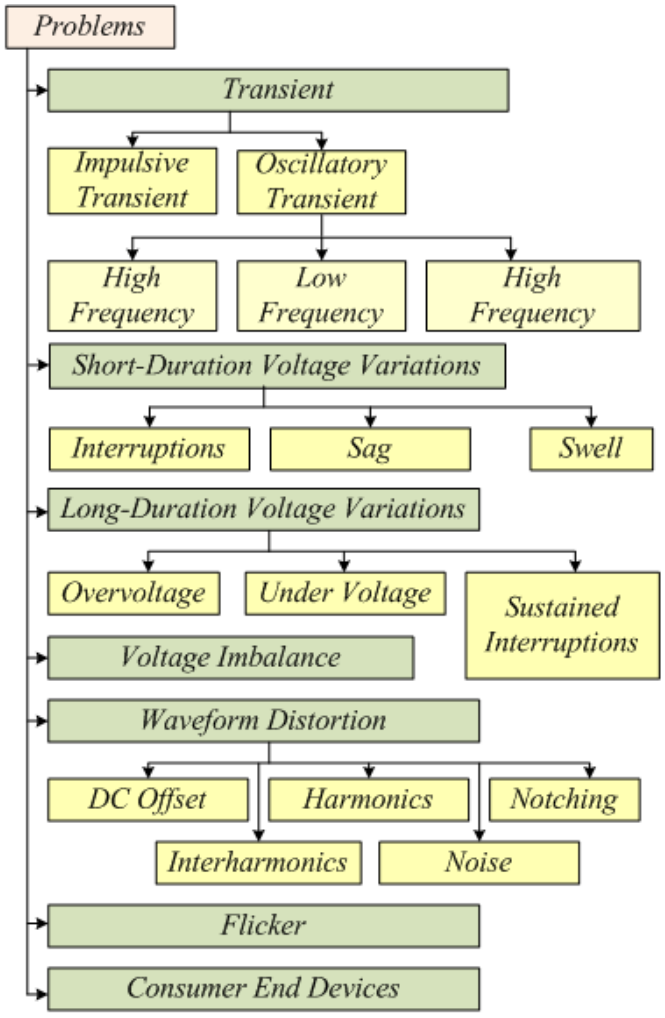

Figure 1.3: General power quality problems

Power quality also impact life span of electrical equipment installed at the consumer end. PQ is a measure of the efficiency of power generation, power transmission loss and accurate power grid monitoring. Various PQ standards such as IEEE-519 and IEC provide guidelines, limits and recommendations to ensure the

quality of power between the power system and end-user equipment [52–69]. To counter the aforementioned issues, microgrid with distributed generating sources is emerging an attractive solution. One acceptable solution for current related PQ problems is to install shunt active power filter (SAPF). Various PQ issues such as harmonic distortion, poor power factor, load unbalancing and reactive power compensation can be addressed through SAPF. It has fast response time, eliminates specific harmonics and has a small size. Its implementation has become cost-effective due to tremendous advancement in the field of power semiconductors. The performance of SAPF mainly depends on the extraction of the fundamental load current component which in turn depends upon the control algorithm of the voltage source controller. The fundamental load current component is utilized to estimate reference supply currents, which are additionally used for the generation of the gating pulses of VSC. This necessitates the development of fast and accurate control algorithms for the VSC. SAPF integration with the RESs is a cost-effective solution to mitigate PQ problems and can be effectively used for the microgrid.

1.4 Configuration of Microgrid System

A microgrid may be classified into two categories i.e. stand-alone or off-grid mode and grid-connected mode. The grid-connected microgrid can be further classified as DC microgrid (central DC bus), AC microgrid (central AC bus), hybrid microgrid (hybrid AC–DC bus).

1.4.1 Grid-Connected Microgrid System

A microgrid is relatively a new concept realized in the modern power system to provide increasing energy demand [70]. The microgrid can generate and supply electrical power to the load in a close vicinity through small distributed generation units. The power circuit components of the microgrid are Voltage Source Converter (VSC), DC-link capacitor, interfacing inductors, ripple filters, DC-DC converters and their control.

The grid-connected microgrid may be classified broadly in three configurations and this is shown in Fig. 1.4. Various configurations viz. DC microgrid, AC microgrid

and hybrid microgrid are reported in the literature [71–75]. In DC microgrid all the DC and AC energy sources are integrated at the DC-link through suitable power electronic interfacing units and the load is integrated at the DC-link directly. In the AC microgrid, all the DC and AC energy sources are integrated at the grid through the AC bus. DC sources such as photovoltaic (PV) system and fuel cell (FC) system are interfaced at the AC bus through DC–AC converter using DC–DC boost converter to step up the low input voltage. In case of the hybrid microgrid, AC and DC energy sources are interfaced at AC and DC bus respectively. Further, AC energy source may also be integrated at DC-link through suitable converters. AC load is connected at the AC-bus and DC load is integrated at the DC-link, proper power electronics interfacing is provided between AC and DC bus and operates as a single controllable unit [9].

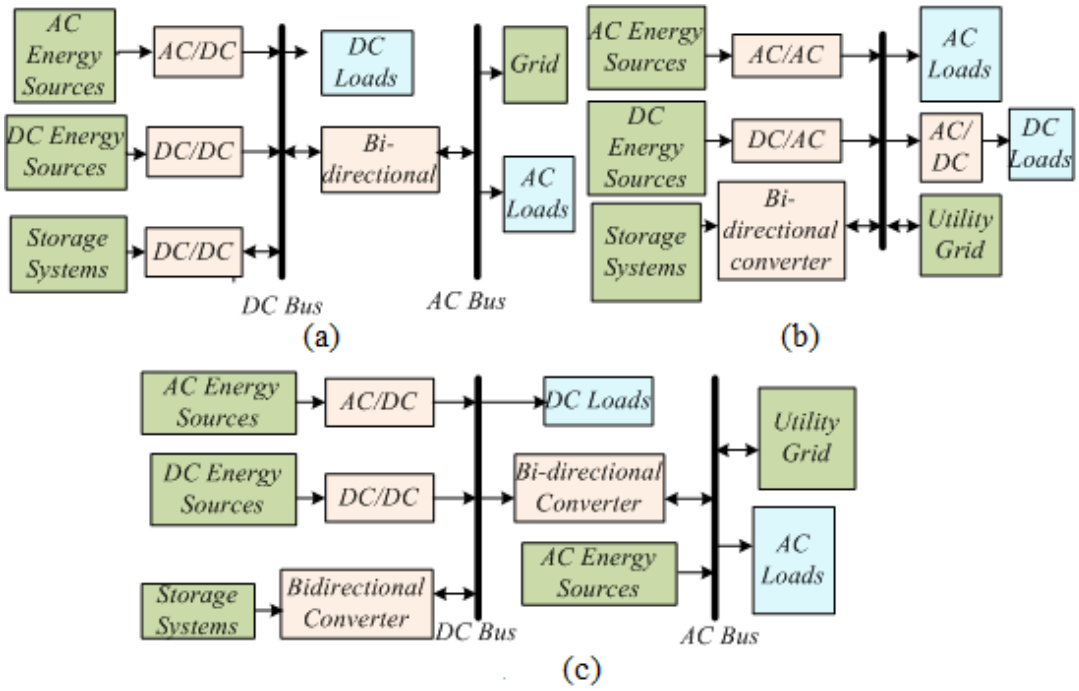

Figure 1.4: Microgrid configurations (a)DC microgrid (b)AC microgrid (c)Hybrid microgrid

The selection and interfacing of energy sources and their rating in microgrid systems depend on the load requirements and reliability. The operation of the microgrid to improve Power Quality (PQ) depends on the required PQ features to be mitigated. Shunt active power filter based microgrid is capable of mitigating the power quality problems in grid-connected microgrid [76–81]. The design of the microgrid system and its analysis for harmonics elimination and load balancing is

carried out through extensive simulation studies in this thesis.

1.4.2 Standalone Microgrid

The remote communities usually thrive on costly and polluting diesel generation as a conventional energy source for their electricity demand. Renewable energy sources in the form of a microgrid system are gradually evolving as a sustainable and economical solution to meet the electricity demand for remote areas. The wind power generation system and photovoltaic power generation system are favorable solutions. The key challenge of PVGS and WPGS is the intermittent nature due to their dependency on environmental factors. To overcome this problem, the system needs a battery energy system for continuous power supply which has another limitation related to the battery life cycle. However, the integration of renewable energy sources such as a fuel cell generation system provides an excellent solution to design a reliable microgrid system as well as enhance the battery life cycle. Further, the addition of electrolyzer as a dump load enhances the cost-effectiveness of the system.

A standalone MG realizes itself as a self-sustained unit that can be operated in off-grid mode as a self-sustained power system. The PQ issues such as voltage distortion, PCI voltage imbalance, harmonics and poor PF are more significant in standalone microgrid systems [82, 83]. The presence of nonlinear load may impose an adverse effect on the other connected load. Another major concern area is to achieve energy equilibrium among the integrated RESs. Standalone hybrid source microgrid ensures reliability and provides a sustainable solution for the remote area [84–98].

1.5 DC-Link Voltage Control Algorithm

In microgrid systems, the connected loads are normally mixed type such as linear and nonlinear loads. Furthermore, numerous RESs are an integral part of the microgrid system. Any deviation in power generation of RESs or deviation in connected load causes the fluctuation in DC-link voltage. These fluctuations have

to be damped out as soon as possible for the stability of the microgrid system. Disturbances in DC-link voltage further lead to unbalancing in PCI voltage. In such scenario with diverse load and variable generation, it is difficult to maintain faster settling of DC-link voltage through the conventional PI controller. To achieve this, it is required to investigate new faster and simpler control techniques for DC-link voltage control [99–106]. Hence, the control of DC-link voltage is an important issue to develop a reliable microgrid. The new control schemes such as FLC, H-FLC, AFIS and TSFLC have been presented in this thesis and their simulation is carried out under MATLAB/SIMULINK platform. In the present work, RESs and electrical vehicle (EV) load are interfaced at DC-link, which is further interfaced with VSC to integrate load and grid for the grid-connected systems. Conventional control technique SRFT is implemented for VSC control to analyze the performance of new DC-link voltage controllers and their effectiveness in microgrid systems.

1.6 Control Algorithm of Grid-interfaced MG

The most crucial feature of the microgrid is its configuration, which accommodates the interfacing of numerous RESs, energy storing devices, grid and various critical AC and DC loads. MG offers integration of RESs with the conventional grid. In order to accomplish the functionalities, grid side converters are the essential part, which provides interfacing of RESs with the grid. At the demand-side, adequate energy and good quality of power are required. Grid side converter (such as VSC) can play several roles in the microgrid operation such as power flow management, harmonics mitigation, reactive power compensation and conversions into AC/DC as per the requirement [107–109]. Deduction of the accurate compensating signals is the most significant phase of VSC control and the effective working of an MG principally relies upon the techcnique used to reference current generation for VSC. Several control techniques, either in frequency domain or in time domain are reported in various works in literature. Time domain VSC control techniques are capable to provide various functionalities in the system such as proper control strategy and power management. Additionally, it also assists

in several vital functions such as reactive power compensation, power factor correction and harmonics mitigation. The development of a new control strategy for VSC control has emerged as an important area of research during the last decade [110–116]. Various control algorithms for VSC controls are reported in the available literature [117–155]. Further, accurate functioning of microgrid under unbalanced microgrid conditions can also be ensured through VSC control techniques. Various literature [156–166] presented the operation of microgrid under a distorted grid environment. In the area of power quality improvement, control under non-ideal grid conditions is one of the prominent fields of research.

The unique feature of the microgrid is its capability to operate in standalone mode during grid failure to feed the critical load. Further, microgrid is recoupled to the grid after removal of a fault. The restoration of the grid required an accurate estimation of the phase and frequency of the grid. Various synchronous control techniques are available in the literature [167–172].

1.7 Motivation

Microgrid offers a promising solution to escalating electricity needs using renewable energy sources for future energy technology. They can provide reliable electricity in urban areas and rural areas at a reasonable price. Mixed source microgrid perfectly aligns with the present energy demand and provides an adequate solution to the various consumer energy need such as household loads, lighting, cooking, water pumping, electric vehicle, telecom industries and issues raised by energy planners. The key challenges for such systems are to maintain power balance, reliable supply with good quality of power and cost-effective implementation, which can be perfectly mitigated by the effective design of microgrid.

The power electronic interfacing in microgrid causes some serious power quality problems. Further, extensive use of nonlinear loads deteriorates the quality of power at the user end. Also, devices at the customer end become more sensitive to the quality of power. Therefore, current research is to cope up with the expanding microgrids and mitigation of PQ issues. Recent trends are geared towards the multifunctional converters that may address various PQ issues, such

as voltage regulation, reactive power compensation, harmonics compensation, etc., concurrently to optimize the performance of microgrid. Shunt active power filters are found to be effective to keep grid free from supplying reactive power to load and to improve the quality of power supply by the grid. Further, RES can be interfaced at the point of SAPF installation in the existing conventional system. With this motivation, SAPF based microgrid is developed in this thesis to address PQ issues and provide a cost-effective solution for energy needs.

1.8 Objectives of the Current Research

The objectives of the presented research work are to develop a microgrid to enhance the power quality of the microgrid system. Based on the extensive literature review related to microgrid design, development and VSC control techniques some major issues are identified which need to be investigated. The presented thesis investigates and develops new control techniques for VSC to mitigate PQ problems in microgrid. New control techniques are designed and developed which are robust and simple in terms of complexity and are capable of DC offset rejection as compared to traditionally available control schemes. The PQ issues considered in this thesis are the effect of unbalanced grid supply, presence of harmonics, linear and nonlinear unbalanced load, DC offset rejection capability and poor power factor. Coordinated power-sharing between the load, microgrid and utility grid is also demonstrated. The objectives of this research can be divided into the following parts:

(i) To investigate grid-connected microgrid system along with detailed modelling of RESs and investigate existing control topologies for VSC that are suited for the RESs interfaced microgrid.

(ii) To investigate novel DC-link voltage control techniques for microgrid and compare their performance with respect to settling time and transients under the dynamics of load change.

(iii) To develop new control techniques for VSC in grid-connected microgrid with fast convergence and high DC-offset rejection capability. Further, these control schemes are tested to ensure the microgrid operation under unity

power factor. Control schemes should ensure the sinusoidal grid current even in highly distorted load and unbalanced grid conditions to improve the quality of power.

(iv) To develop a hybrid microgrid and seamless transition of the microgrid for synchronization and de-synchronization with the grid.

(v) To develop standalone microgrid with suitable energy management strategy.

1.9 Outline of the Thesis

The structure of the thesis is organized as follows:

Chapter 1: This chapter covers the introductory concept of microgrid, RESs and associated power quality problems and their solution in a microgrid. This chapter introduces the structure of the microgrid and objectives of the research work. Mitigation of power quality problems is a crucial issue for the utility side as well as customer end.

Chapter 2: This chapter presents an overview of the related literature and the background topics to support the concepts developed in the thesis. Based on the literature survey, the identified research gaps are presented at the end of the chapter and the same is elaborated in the subject chapter.

Chapter 3: This chapter provides the system configuration of grid-connected microgrid. The detailed modelling and characteristics of interfaced RESs under the MATLAB/SIMULINK platform are exhibited in this chapter. Further, two conventional algorithms SRFT and PBT are tested for the proposed grid-connected microgrid. The selection of various parameters and components such as DC-link voltage, DC-link capacitance, interfacing inductors, ripple filters is also presented in detail.

Chapter 4: In this chapter, various DC-link voltage control techniques have been developed. The comparison of proposed ANFIS, fuzzy, H-FLC and TSFLC are presented for the SRFT control technique of the VSC. The performance of developed controllers on the basis of output settling time, overshoot and undershoot are presented.

Chapter 5: In this chapter, some adaptive control algorithms for hybrid power

source based microgrid are discussed. The controllers which are simulated and developed are based on H-LMS, ANFIS-LMS, ZAQ-LMS and MSWL-CLMS control techniques. A comparison of the developed algorithms has also been presented.

Chapter 6: This chapter presents the hybrid microgrid in which a battery-EV load is integrated at the DC-link. This EV load is interfaced through a bidirectional DC-DC converter. The system is tested for self tuning filter based VSC control technique. The SOGI and D-SOGI control techniques have been demonstrated to extract the positive sequence components under unbalanced grid voltage condition. Furthermore, synchronization and de-synchronization operations of microgrid have been verified. Synchronization operation has been carried out through LPN-PLL control technique.

Chapter 7: This chapter presents standalone microgrid where fuel cell and the battery are acting as backup energy sources and electrolyzer is used as a dump load. The system is developed with new and simplified controllers. Both linear and nonlinear loads are considered to evaluate system performance.

Chapter 8: This chapter provides a summary of the conclusions drawn for the presented microgrid. The scope of future work in this area has been listed at the end of this chapter.

Chapter 2

LITERATURE SURVEY

2.1 Introduction

Ever-growing electricity demand coupled with conventional energy sources raises environmental concerns and sustainability issues. The adoption of renewable energy sources (RESs) offers an attractive solution as an alternative approach. This necessitates the development of the microgrid (MG) concept, which is a cluster of RESs, loads, converters and power conditioning units [1]. The microgrid offers a platform to interface different RESs to the central grid [2, 3].

A power grid consists of power generation, transmission system and load. These loads consist of electronic devices, lights, electric motors and other similar devices. There may be a power dearth because of the rapid rise of electrical and electronic equipment. To overcome this situation, microgrids utilizing distributed power generation are emerging as a solution [4]. Microgrids with distributed generation are economical and useful on grid-connected because it does not require long distance transmission lines. As power systems include distributed generation, there's an increasing need for microgrids to dispersive-ly control each distributed generation [5].

2.1.1 Introduction to Microgrid

A microgrid can be defined as per Lasseter et al.,[2002] "A network consisting of power generation units, energy-storing devices and loads which can fulfill electricity need of a localize area" [6]. The microgrid can be operated in grid-connected mode

and stand-alone mode as a self-sustained power system. Lasseter et al.,[2004] stated in [7] "The heart of the microgrid concept is the notion of a flexible, yet controllable interface between the microgrid and the wider power system". Microgrid acts as a complete entity, which acts as an ideal traditional load for the grid. MG's concept is based on an idea of RESs hence, it is pro environmental. Hatziargyriou et al.,[2007] discussed, through appropriate control of the microgrid components, microgrids are capable of supplying the defined load demand from volatile feeds power generation sources [8]. According to Shahnia et al. [2010], a microgrid is considered as a group of DGs and loads, connected to the utility that provides energy and it should appear as a single controllable unit that responds to the variable load requirement of the system [9]. Microgrid system consists of different generation systems operating in coordination in order to meet the load requirements. The microgrid system with proper control techniques increases system flexibility, reliability and efficiency.

2.2 Development of RES System

Modelling of RES is a crucial factor to analyze MG performance in a realistic environment. The power output of PVGS and WPGS depends on the environmental conditions such as solar irradiation and wind speed respectively. Various literature is available for the modelling of RESs such as PV, FC, WPGS, Battery and electrolyzer.

Photovoltaic generation system includes the model of PV cell, boost converter and MPPT control technique to evacuate maximum available power [10]. Bhuvaneswari et al., [20111] [11] developed a circuit model of a single diode and double diode of a PV cell. Authors concluded that the single diode model can be acceptable for the research purpose due to its simplicity and shows nearly the same response as obtained in the double diode cell model. Saied et al., [1991] [12] presented the design and optimization of the PV cell parameter and the developed optimized model is tested for DC motor load. The output power of solar cell is not sufficient for use. So the solar cell is grouped to make a solar module and then array, Villalva et al., [2009] in [13] reported a circuit-based simulation and modelling of photovoltaic arrays for the common use of circuit designers. Keyhani et al.,

[20111] [14] modelled a PV system for microgrids to bulk power grid analysis. The author presented the detailed modelling procedure for the circuit model with equations using MATLAB/SIMULINK. The proposed model gives better accuracy at low values of solar irradiation and performs solar curve more accurately. MPPT is an extensively addressed issue right from the evolution of PV generating system. Numerous MPPT techniques are available in the literature and vary on the basis of the complexity, convergence speed, parameters, cost and technique to find out maxima/minima. These techniques are based on circuit parameters such as voltage and current. Koutroul et al., [2001] have developed a micro-controller-based MPPT control technique in a PV system [15]. The author reported the technique with faster convergence and minimum error. This is an adaptive solution to reduce ripple oscillations. Leyva et al., [2006] [16] presented a new method for tracking the MPPT in the system consisting of PV generator and a boost converter. The gate pulses of the boost converter are controlled using extremum-seeking control technique. This proposed controller tracked the MPPT under various conditions effectively and efficiently. Ocran et al., [2005] [17] implemented artificial neural network to extract the maximum power in solar electric vehicles. The author of the paper explained the concept, designing and training of ANFIS controller. Kottas et al., [2006] and Adzic et al., [2016] [18]- [19] applied the fuzzy control technique in close cooperation with fuzzy cognitive networks for MPPT. The author discussed the designing and simulation of the Fuzzy controller for tracking MPP with the highly efficient controller. Femia et al., [2009] [20] presented a modified scheme to improve the most commonly used algorithm perturbation observation response in double-stage grid-connected PVGS. In a double stage PV system boost converter is integrated to play the role of MPP controller primarily. Liu et al., [2008] [21] used a variable Step Size incremental conductance MPP technique for the PV System. The author proposed the optimization of step size using small iterations to remove the oscillations around the MPP. This controller has been approximated using the constant voltage method and the system efficiency is improved.

Variable speed wind turbine is becoming popular owing to its capability of extracting optimum power through MPPT with overall improved efficiency. In the class of variable speed wind turbines, two types of generators namely, doubly fed induction

generator and permanent magnet synchronous generator (PMSG) is commonly used. Due to its low rotational speed, the gearbox can be excluded. Further, the PMSG has a growing share in the market due to its cost-effective feature, higher operating efficiency and lesser maintenance requirement in comparison to DFIG. Usage of direct drive PMSG is technically attractive, particularly for the small wind turbines. [22] presented the modelling and analysis of doubly-fed induction generators for a WPGS. Muyeen et al., [2006] [23] presented the comparative study of wind turbine generator system using different drive train models. The authors found that the two-mass model exhibits more accurate performance for transient stability analysis than the one-mass model and provides a realistic environment to test the WPGS. Bhende et al.,[2011] [24] developed a PMSG based WPGS system for the standalone application and exhibit accurate working of PMSG under transient conditions. [25] proposed a sensor-less MPPT strategy for grid-connected WPGS. Koutroulis et al., [2001] [26] designed a maximum power tracking system for wind-energy-conversion systems. Simple and economic control with DC-DC boost converter is used by the authors for MPPT and to extract the maximum generated power. Karbakhsh et al.,[2012] [27] presented a fuzzy control technique for permanent magnet synchronous generator associated wind turbine. A digitally controlled switching of DC-DC boost converters using FLC is introduced to extract maximum power from the wind turbine. FLC scheme is good, however, the execution time depends on design rules which are further based on the complexity of system. Kumar et al., [2016] [28] compared 15 MPPT control techniques in wind energy systems in terms of complexity, convergence speed, wind speed measurement, performance, memory requirement and prior training. In the class of indirect power control based algorithms, The authors found tip speed ratio algorithm is more efficient but expensive because it required an accurate anemometer to measure the speed. Whereas, direct power-based control techniques are simple and required less memory. These techniques do not require prior training and measurement of wind speed to extract the optimum power. However, the authors found unsatisfactory performance under varying wind speed and their application is limited for variable wind operations. The modified hill-climbing overcomes the limitations of traditional hill-climbing methods. This method is simple in implementation since it does

not require mechanical quantities measurements such as rotor speed and wind speed. Direct power based control techniques is sensorless algorithm, therefore economical and more reliable. The other MPPT algorithm viz. adaptive and soft computing algorithms are very efficient in prediction of optimum power and ability to deal with system nonlinearity but needed prior knowledge of the system. The authors found adaptive MPPT technique is more advantageous over other MPPT control schemes because it is adaptive, robust and accurate under unpredicted wind behaviour. Furthermore, Shirazi et al.,[2009] [29] showed the comparative study of maximum power point tracking techniques in PMSG wind turbine system. The authors concluded on the basis of the simulation response that optimal torque control is the best MPPT method among the perturbation observation, tip speed ratio and optimal torque control technique. Kazmi et al., [2010] [30] reported a novel algorithm which is faster, efficient and represents a better trade-off in terms of the power response without using speed-Sensors for WPGS.

Fuel cells are used as distributed power sources in power systems due to their low emission and higher energy conversion. FC also plays an important role as an energy storing device and it is a more reliable source of power because its input fuel is controllable. FCs are capable of supplying power in the long term as long as fuel supply is available. Furthermore, FCs are efficient and eco-friendly [31]. Zhu et al., [2002] [32] developed a dynamic model of solid oxide fuel cell in MATLAB/Simulink. Further, the authors also analyze the load flowing performance of the fuel cell. Ulleberg et al., [2003] and V et al., [2009] presented the fuel cell model integrated with an electrolyzer, which is used as an energy storage device that can supply the fuel to FC [33] and [34]. The authors presented the mathematical modelling and formulation for an advanced alkaline electrolyzer. The developed model is based on the fundamental thermodynamics, heat transfer theory and empirical electrochemical relationship. barsali et al.,[2002] [35] developed the lead-acid battery and presented its mathematical formulation. The authors also discussed the issues encountered in implementation in detail. Song et al.,[2013] in [36] verified the battery system model for environment friendly EVs. The authors established the prototype battery hardware system considering the electrochemical impedance measurement technique and nonlinear electrochemical properties.

2.3 General Power Quality Problems

Wang et al., [2010] discussed, if distributed generators directly interfaced with the traditional power system, the technical challenges arise related to the system control, protection, grid synchronization operational stability, reliability and power quality [37]. Wei et al., [2014] showed that Micro-grid is the technological solution to enhance the PQ of the system in the presence of distributed generation [38]. Power quality denotes the system's capability to generate a pure sinusoidal wave and stable in terms of voltage and frequency. Nevertheless in practice, loads commonly enforce disturbances in the system, which causes deviation from the ideal power supply [39]. Any disruption in the quality of power may result in equipment malfunctioning or reduce the efficiency of the system and lead to power losses. There are commonly five classes of problems such as voltage unbalancing, voltage interruption, voltage sag-swell, flickering, voltage transients and voltage and current harmonics distortion. McGranaghan et al.,[1993] highlights the voltage sag in industrial plants as a major fault concern and explained the adverse effects of short power interruption to the power system [40]. The voltage swell denotes the temporary surge (more than one cycle) in the voltage above the acceptable levels [41]. Flickering refers to the fluctuation of voltage in-between 90% -110% of the nominal power supply voltage. Flickering may damage the load side equipment. To reduce flickering at PCI, Montanari et al., [1994] introduced the installation of a series inductor [42]. Chen et al., [2013] suggested a resolution technique for flicker management and discussed its ill effects [43]. Deviation from ideal sinusoidal wave shape is considered as waveform distortion, which is generally caused by nonlinear loads and can be characterized by DC offset, inter harmonics, notch and noise. Seema et al., [2019] presented a control algorithm for VSC to alleviate DC offset issues and to improve THD [44]. DC offset is an average amplitude displacement from zero. DC offset is a potential source of distortion in an AC power system because the system is not designed to handle. The static VAR compensator is an emerging technology and it is broadly used in transmission applications. Wang et al., [1998] briefly discussed an advanced static VAR compensator and voltage sag effects along with the phase angle jump problem. Furthermore, analyze

the system for static VAR compensator performance to negative sequence and harmonic voltage components in the transmission line [45]. Senjyu et al., [2008] implemented a static VAR compensator, switched capacitor or on-load tap changer for voltage regulation in the distributed power system [46]. Zhao et al., [2012] discussed transient problems in the power system [47]. Transient is a short-lived phenomenon and is commonly triggered due to sudden change, which may arise in the steady-state of voltage, current, or both. Ugale et al., [2008] [48] presented the long-time voltage interruption issue. This problem denotes the total interruption or reduction in the voltage/load current from a few milliseconds to one/two second periods. This may result in malfunctioning in the data processing tool. Fujita et al., [2007] implemented an APF to mitigate harmonics and to overcome distorted voltage and fluctuation problem [49]. The author illustrates that the voltage swell can be alleviated through lagging fundamental current drawn from the supply grid. In literature Lee et al.,[2011] DSTATCOM based microgrid is developed to improve power quality in the microgrid [50]. STATCOM is a regulating device used in AC networks. DSTATCOM is based on the voltage-source converter and can act as a source of reactive power. If it is interfaced with the energy source it can also deliver active power. Hochgraf et al., [1998] [51] proposed the STATCOM implementation to restore positive sequence voltages and to balance the voltage. In [51] Hochgraf et al. also illustrates the DSTATCOM operation with positive-sequence admittance and a negative-sequence conductance.

2.3.1 Power Quality Standards in Microgrid

As the interfacing of RESs continues to increase, hence PQ, stability and power equilibrium becoming critical subjects for microgrid [52], [2011]. International standards have been established to ensure the quality of power in the power system, Institute of Electrical and Electronics Engineers (IEEE) and International Electro-Technical Commission (IEC), has framed and revised the international standards related to PQ on regular basis [53]. Suggested practices and requirement of PQ issues in Power System are elaborated in Table 2.1 below:

Table 2.1: Power quality standards

Power Quality Standards	**Corresponding Guidelines**
IEEE-519	Limit harmonic currents and voltages at the point common control [54], [57], [47]
IEC 61000-3-2 (1995-03)	To limit the harmonic currents for the equipment with input current $<$ 16A [54], [55], [56], [57]
IEC/TS 61000-3-4 (1998-10)	To limit the harmonic currents for the equipment with input current $>$ 16A [58]
IEEE Standard 141-1993	Safety of life, preservation of property, reliability, simplicity, voltage regulation within the tolerance limit, care and maintenance, flexibility [59]
IEEE Standard 1159-1995	Monitoring of power quality (AC systems), definitions of power quality terminology, the impact of poor power quality on utility and customer equipment, and the measurement of electromagnet phenomenon [60], [61], [62].
IEEE Standard 1250-1995	Momentary voltage disturbance in AC systems, their effects on new sensitive, user equipment and mitigation of these effects, to limit harmonic distortion, etc. [64].
IEEE Standard P1564	Characterizing voltage sag performance [65].
IEC Standard 61000-4-15	Characterizing flicker [66].

As per the standards defined by Halpin et al., [2005] in [67], if the voltage level is under 69 kV and $\frac{I_{sc}}{I_L}$ is less than 20, THD of current should have below 5%. Under power quality assessment, the specified THD, for general power system for nonlinear load and recommended, for the specific system supply voltage and current should be below 5% in accordance with the relevant quality standards: the IEEE Standard 519, [68]. Moreover, Zamora et al., [2010] [69] also mentioned

the PQ issue according to IEEE Standard 1547.2-2008, the voltage fluctuation is limited to 5%, 2010].

2.4 Design and Configurations of Microgrid

An MG is a small scale electricity network containing renewable and/or traditional power sources as well as energy-storing elements with suitable energy management techniques. MG provides an opportunity for local power consumers to meet their energy needs through the generation from their power sources. Furthermore, the integration with the grid provides the potential to inject the surplus power into the grid. At the same time, MG can draw power from the grid during the power deficit. The microgrid can also operate independently without integrating it with the grid in standalone mode. Strunz et al., [2013] showed that MG offers onsite power generation and management that can help in addressing the continuously rising energy demands near the end-user [70]. The prospects and benefits of interfacing RESs into a microgrid for both end-users and electricity utilities. In this context configuration of the microgrid is depend on the application. Literature consists of various topologies in MG design and development. Since the conventional power network exists in AC, the research is focused on AC micro-grid initially. In AC micro-grid system, RESs and load are integrated at the AC bus through the appropriate power conditioning devices. Yunwei et al.,[2007] [71] investigated the effects of the shunt filter capacitance variation in an AC microgrid due to the connection of a power factor correction capacitor. Mohd et al., [2009] reported two droop control strategies for the RESs generation in the area of interconnected grids [72]. Significance of the optimum value of droop coefficient in frequency control is also discussed along with the importance of phase. Omari et al., [2007] in [73] investigated simulation model for DC bus based hybrid microgrid configuration. DC/AC converters are used to integrate each power source with the grid and DC/DC converters provide the interface between power sources and DC bus. Xiong et al., [2011] and Sindhu et al., [2013] suggested a hybrid AC/DC microgrid and its synchronized control [74]- [75]. The microgrid is capable of mitigating the power quality problems, [76–80] presented grid-connected hybrid microgrid for voltage

regulation and power quality improvement. The control techniques are key elements in the effective operation of MG. Kamatchi et al., [2012] [76] realize the active power filter as a power compensator for PQ problem mitigation. Reddy et al., [2007] [77] presented a hybrid microgrid structure with reactive power compensation features. Eid et al.,[2013] proposed a current-controlled bidirectional converter to interfaced with the DC-link with the grid and addressed the coordinated energy management system [78]. Ahmed1 et al., [2011] proposed a utility combined microgrid for DC-link voltage regulation [79]. Dash et al., [2016] [81] focused their study on the use of supercapacitor for power quality improvement in a capacitor interfaced VSC.

2.5 Standalone Microgrid System

The remote communities usually have costly and polluting diesel generation to fulfill their electricity demand. The standalone microgrid is a sustainable and economical solution to meet its electricity demand. WPGS, PVGS, BES and FCGS provide an excellent solution to design a reliable microgrid system. The various research work has been conducted in the area of standalone microgrid. Modelling and simulation of grid-independent hybrid microgrid system containing RESs viz. FC, PV, wind, battery is explained in [82] and [83]. The authors [84–87] have presented the hybrid energy system for PV, FC, WPGS and emphasize the energy management technique. Authors Fathabadi et al., [2017] investigated hybrid power source system for the single-phase load [86]. In literature [88], [89], [90] authors have presented the system layout for an autonomous microgrid. In the proposed configuration load resistance is used as a dump load. The framework developed by the authors Mohd et al., [2010] have presented the 'd-q' method for inverter control to get balanced PCI voltage during the unbalance load condition in grid-independent mode and investigated control strategy influence on the efficiency of hybrid system [91]. Sheikh et al., [2016] consider the steady-state conditions of generation, therefore, all the generation sources work under their rated conditions [92]. Psakis et al., [2009] have designed a hybrid DC system with DC load and energy management algorithms [93]. The voltage regulation and active/reactive power-sharing strategy in microgrids are realized by two-layer control approach [94] and modelled predictive

secondary voltage control [95] in a standalone MG system. Malla et al., [2014] present the DC-link voltage regulation and energy management in hybrid source standalone microgrid system [96]. Mostafazadeh et al., [2017] and Uzunoglu et al., [2009] presented a voltage control technique in hybrid PV/Wind/FC/Battery system based standalone microgrid [97] and [98].

2.6 DC-Link Voltage Control Algorithm

In the MG system, voltage regulation of DC-link is necessary for stable and reliable operation. An MG system is a complex system which comprises of various generation systems and loads. Any sudden change in load or change in generating power causes oscillation in DC-link voltage. To maintain the required power quality standards and a constant voltage level under major disturbances, an accurate DC-link controller is required. Conventionally a PI controller is used for this purpose, to improve the dynamic response of the DC-link voltage, a new class of controllers was developed. Myneni et al., [2016] proposed an algorithm which gives the reference DC-link voltage corresponding to load rating and it is computed based on filter burden [99]. The advantage of a proposed algorithm is the reduced switching stresses. The reported controller is a fast-acting DC-link voltage controller and its mathematical formulation is given to calculate the conventional controllers gain. Suryanarayana et al., [2008] [100] implemented a Fuzzy logic controller for DC-link voltage control in the DSTATCOM. It has been observed that soft computing techniques give a promising performance with higher efficiency and good flexibility. Ahmad et al., [2015] implemented a control technique that improves the dynamic performance of DC-link voltage control through values of the error and gives the feedback with its discrete derivative, further the obtained value is multiplied with the constant to sustained the values at the similar scale [101]. Murali et al., [2016] [102] described the ANFIS control technique for DSTATCOM. ANFIS based control techniques showed a better response in terms of the system dynamic speed. The efficiency of ANFIS control is encountered good under different environmental conditions. The ANFIS has to be periodically trained to guarantee accurate control. Ninghot et al., [2017] used particle swarm optimization to keep

DC-link voltage at its desired value with an unbalanced capacitor voltage in the D-STATCOM configuration [103]. Prasad et al., [2018] [104] reported a method for DC-link voltage optimization in DSTATCOM where load compensation is presented through the use of a reduced switch count multilevel converter. Furthermore, the system is interfaced with the PV system. Adaptive DC-link voltage regulation sets down the DC-link voltage at a lower value for off-peak loads this reduces the voltage stress on the VSC switches. The variable DC-link voltage is delivered by using a reduced switch count multilevel converter. Ying [1998] [105] examined analytical assembly of the Takagi–Sugeno (TS) fuzzy controllers. The TS fuzzy controller consists of simplified rules scheme where all rule consequent uses one common function which is proportional to each other, This type of scheme significantly reduced the number of parameters required in rule construction. Farokhnia et al., [2009] [106] presented the use of genetic algorithms to regulate the DC-link voltage which shows the fast and vibrationless tracing of capacitor voltage at the reference value. Genetic algorithms search in parallel hence, it avoids being trapped in the local optimum solution like the conventional control technique of DC-link control voltage that searches from a single point. They apply probabilistic selection rules instead of deterministic ones.

2.7 VSC Control Techniques for Grid-Interfaced Microgrid

Extraction of the accurate compensating signals is the most significant part of VSC control. The performance of the VSC is depended upon the selection of the reference generation scheme. The various control schemes in the time domain and frequency domain are available in the literature. Large response time is the main disadvantage of frequency-controlled techniques. Whereas, time-domain techniques are simple, easy to implement and require less computational time. The control techniques are the key element in the effective operation of the VSC in the microgrid to mitigate PQ problems. This section discusses the various control schemes implemented to improve the operation of VSC.

2.7.1 Conventional Control Algorithms

Various conventional control algorithms are available in the literature viz. SRFT, PBT, IRPT, etc.. The VSC control technique requires immediate extraction of compensating signals from harmonics polluted currents or voltages. Akagi et al., [2007] [107] introduced Instantaneous Reactive Power (IRP) control algorithms. Peng et al., [1996] proposed IRP theory for PQ improvement in three-phase system [108]. Bhattacharya et al., [1995] and Singh et al., [2008] have discussed Synchronous Reference Frame Theory (SRFT) for PQ problem mitigation has been proposed in [109,110]. Brij et al., [2005] [111] introduced the Power Balance Theory (PBT) for PQ mitigation. Karuppanan et al., [2010] [112] proposed the Fryze control approach for nonlinear load, which is based on conductance. Further, many new control algorithms have been applied in [113] such as Instantaneous symmetrical control theory, Adaline [114], LMS [115]. A comparison of the conventional control technique is presented [116–118] for PQ improvement. Montero et al., [2007] [116] presented the comparison of control strategies for VSC in the three-phase four-wire system for balanced and sinusoidal voltages, harmonic cancellation, unbalanced, distorted grid conditions and reactive power compensation. Author compared generalized p-q theory, i_d-i_q theory, perfect harmonic cancellation strategy and unity power factor strategy. Author concluded that the i_d-i_q theory is the most sensitive to distortions, unity power factor strategy is not capable to achieve the goal for three-phase four-wire systems in the presence of zero-sequence components, while perfect harmonic cancellation strategy is found to be accurate under all the conditions and confirmed by the experimental prototype. Zaveri et al., [2012] [117] compared the IRP theory, symmetrical component and instantaneous active and reactive current component theory (ICCT) in terms of RMS value of source current, Total Harmonic Distortion (THD), supply power factor and compensator ratings. The author found that under balanced conditions all three techniques exhibit similar behaviour, whereas, under unbalanced and nonideal grid conditions the ICCT exhibits superior response and capable of taking corrective measures. Solanki et al., [2009] [118] presented the comparison of IRP theory, SRFT and Adaline algorithm for VSC control. The presented Adaline-based scheme used an LMS

scheme to predict the weights. All the computation has been performed online, hence the algorithm is capable of extracting the reference currents in transient condition.

2.7.2 Adaptive Control Algorithms

Adaptive control algorithms has unique advantage of adapting to change in systems parameter in real-time [119]. They are well bandwidth behaving, less complex, automatic grid frequency tracker and robust to system parameters deviation. Step-size is the key factor for the convergence rate. So change in step size allows flexible control for convergence time while retaining the immunity against harmonic-current disturbances. The Adaline based algorithm is an adaptive method for extracting reference currents which results in improved response. LMS algorithms are adaptive control algorithms. Various LMS control algorithms have been reported in the literature such as Winer filter adaptive control technique [120], LMF algorithm [121], Variable LMS [122] and [123], Lorentzian function [124] Affine projection algorithm [125] and [126], Hyperbolic tangent based LMS control technique [127] and [128], etc.

2.7.3 Neural Network Control Based Algorithms

The Artificial Neural Network (ANN) technique uses the set of certain rules to replicate a physical system. These networks are trained off-line hence, they are capable of working effectively on other systems too. Houya et al., [1993] [129] presented the design of adaptive filters using neural networks. Real-time control schemes for training ANN is available in the literature. Stubberud et al., [1998] [130] have implemented an LMS algorithm for the training of recursive neural networks. wal11 et al., [2017] [131] have shown real-time implementation of neural network training to mitigate power quality problems in three-phase, three-wire system. Badoni et al., [2016] [132] used an adaptive neuro-fuzzy system to realize the DSTATCOM, this method is found to be robust in nature and work accurately for PQ problem mitigation. A [133–135] carried out the implementation of the ANN-based predictive controller for active power filters for current harmonics compensation in the distribution network. The ANN is unit vector-based control to

ensure mitigation of power quality problems. Neural network-based load controller estimates the fundamental component of load current which along with the RESs feed-forward loop and improves the dynamic response of the system.

2.7.4 Intelligent Control Algorithms

Power quality improvement is a popular field among the researchers related to the power electronics area. In recent years, various researches have been conducted in this area. Cardoso et al., [2007] [136] suggested an optimum filter theory for the reference current generation in VSC. George et al. [2009] [137] presented a detailed analysis of the system and design of a constant switching frequency controller to mitigate power quality problems. Pigazo et al., [2010] [138] implemented Kalman filtering technique in for VSC, using grid impedance, a control scheme has been developed to control VSC for PQ improvement in the distributed power network. Jin et al., [2006] [139] developed one cycle controlled VSC for the unbalanced load and unbalanced source condition. The author presented a real-time implementation of the control scheme for generation of reference currents under highly distorted current conditions. Haddad et al., [2012] and Rahmani et al., [2011] applied the Lyapunov function for reference current generation and PQ problem mitigation [140] and [141]. The authors also performed stability analysis for the same and found that the system is stable under all considered conditions. [142] have shown implementation of a mixed frame and stationary-frame repetitive control approach to mitigate current harmonics and provide compensation for reactive power. Sabha et al., [2013] [143] proposed application of an enhanced PLL (EPLL) control approach in DSTATCOM. The EPLL scheme is robust and exhibits effective performance fo PQ mitigation the algorithm is also verified for the practical system. Ramos et al., [2012] [144] presented second-order odd-harmonic repetitive control to mitigate PQ problems. Singh et al.,[2012] [145] proposed a linear sinusoidal tracer control algorithm to reduce PQ problems. Singh et al.,[2013] [146] proposed a Back-Propagation control algorithm for power quality improvement. Arya et al., [2014] [147] implemented anti-Hebbian control in DSTATCOM for power quality improvement. Mathuria et al., [2017] and Rodriguez et al., [2006] proposed a double second-order generalized integrator (DSOGI-PLL)

for reference currents generation for the nonlinear load, positive sequence detector and verified the performance [148] and [149]. Adaptive Volterra second-order filter (AVSF) [150], Voltra filter [151], composite observer-based control algorithm [152], notch filter [153], [154], wavelet-based control techniques [155] are the new class of control techniques of VSC which are developed to achieve faster convergence tracking rate, stability and simplicity.

2.7.5 Control Algorithms for Distorted and Unbalanced Grid Supply

For the accurate and reliable operation of the grid-connected microgrid, extraction of the fundamental value of grid supply in highly distorted conditions is necessary. Since harmonic pollution is common problems in the grid, this requires a technique that is able to extract information on the fundamental components from nonsinusoidal and distorted signals [156]. Coluccio et al., [2008] shown the performance improvement of series static compensator under transient conditions using a double vector control algorithm [157]. Salamah et al., [2007] [158] presented a traditional three-phase PLL followed by a Pl-controlled moving average filter along with phase-locking technique. Shayestehfard et al., [2016] have implemented implicit zero-sequence discontinuous pulse width modulation-Based Feed-forward Controller [159]. Feed-forward controllers are accurate in compensating the large numbers of harmonics components from the injected current in grid integrated mode. The controller is fast and directly follows the grid voltage disturbances. The author implemented the feed-forward control on the two-level grid-integrated VSC and it has effectively performed regardless of grid topology. Alepuz et al., [2007] [160] demonstrated a linear quadratic regulator in the current controller in the coordination of a fast sequence separation method to obtain a balanced supply from distorted grid signals. Song et al., [2009] [161] presented the three reference frame control scheme for the MG system at unbalanced grid supply condition to extract fundamental components. Biricik et al., [2014] demonstrated a real-time operation of APF for unbalanced nonlinear load under a distorted grid using a self-tuning filter [162]. Some more literature is available for PQ improvement in distorted supply conditions such as adaptive low-pass filter notch-PLL [163],

third-order sinusoidal signal integrator-based frequency adaptive filters [164], fuzzy logic based FOGI-FLL [165], adaptive digital-control Scheme [166], etc. and it is one of the prominent areas for the research in the PQ improvement field.

2.7.6 Control Algorithms for Grid Synchronization

To provide a reliable supply to the critical load during a grid outage, the transition of microgrid from grid-integrated mode to standalone mode is essential. This transition poses significant technical challenges such as synchronization of MG voltage and frequency with the main grid. The most common synchronization approach is SRF-Phase Locked Loop (SRF-PLL) reported by Ullah et al.,[2019] [167]. Its basic form involves the conversion of the stationary rotating frame. For a non-polluted grid environment, SRF-PLL is fast and precise. However, it is inefficient for grid harmonics and imbalance. To improve the performance of double-SRF-PLL Luna et al.,[2015] presented [168] and Sun et al.,[2011] proposed decoupled double-SRF-PLL [169]. These methods used two SRFs that rotate at the fundamental grid frequency, which makes the control more complicated. Further, Rodríguez et al., [2006] have reported Double-SOGI-PLL [170]. However, this method shows a good response in polluted grid conditions but shows poor dynamic performance due to the presence of the PI controller. Notch filter based grid synchronization is proposed by Lee et al., [2014] [171]. The grid synchronization and desynchronization operations are performed using fast FFT-PLL (Fast Fourier Transform Phase Locked Loop) which is an intelligent synchronization control technique reported in [172] by Singh et al.,[2019].

2.8 Identified Research Gaps

Based on the aforementioned extensive literature survey, following research gaps were identified:

(i) Development of microgrid with the detailed modelling of interfaced RESs to realize the practical microgrid.

(ii) Investigation of new DC-link voltage control strategy for fast damping of

transient in DC-link voltage during dynamics.

(iii) The remedy of power quality issues in grid-connected microgrid through new or modified VSC control algorithms having faster convergence and DC offset rejection capability.

(iv) Investigation of hybrid microgrid and to improve its quality of power through new control algorithms, improving the quality of power under unbalanced grid voltage condition in the grid-connected microgrid, study microgrid operation for synchronization and de-synchronization with the grid through accurate synchronization control technique with power quality improvement.

(v) Development of a standalone microgrid system interfaced with electrolyzer as a dump load in addition to RESs.

2.9 Conclusions

In this chapter, the literature survey has been carried out on the defined problem and associated area. The survey urges the research towards investigating PQ problems improvement and analyze the performance. The challenge of tracking control includes the stochastic behavior of a system that may be due to load transients and generation transients. Extensive literature survey on PQ problems in MG, VSC control techniques, MG operation for unbalanced gird supply, DC-link voltage control and standalone MG have been presented.

Chapter 3

DEVELOPMENT OF GRID CONNECTED MICROGRID

3.1 Introduction

In this chapter, detailed modelling of the grid-connected hybrid source microgrid system integrated with RES for power quality enhancement is discussed. The RES such as Photovoltaic Power Generation System (PVGS), Wind Power Generation System (WPGS) and Fuel cell Power Generation System (FCGS) are integrated at a common DC-link. A three-leg VSC is used to interface the DC-link to the main grid. Two conventional VSC control schemes are discussed in this chapter. Detailed modelling of RES and Maximum Power Point Tracking (MPPT) techniques for PVGS and WPGS are also considered and implemented to design the hybrid source microgrid system. The developed microgrid is also capable of work under DSTATCOM mode when no power generation is available. VSC performs several operations such as PQ mitigation, unity power factor operation, load balancing, reactive power compensation and power balance through control algorithm. The microgrid is tested under balanced and unbalanced nonlinear load with RESs generation and for linear load when RESs generated power is not available. The proposed hybrid source microgrid system is shown in Fig. 3.1.

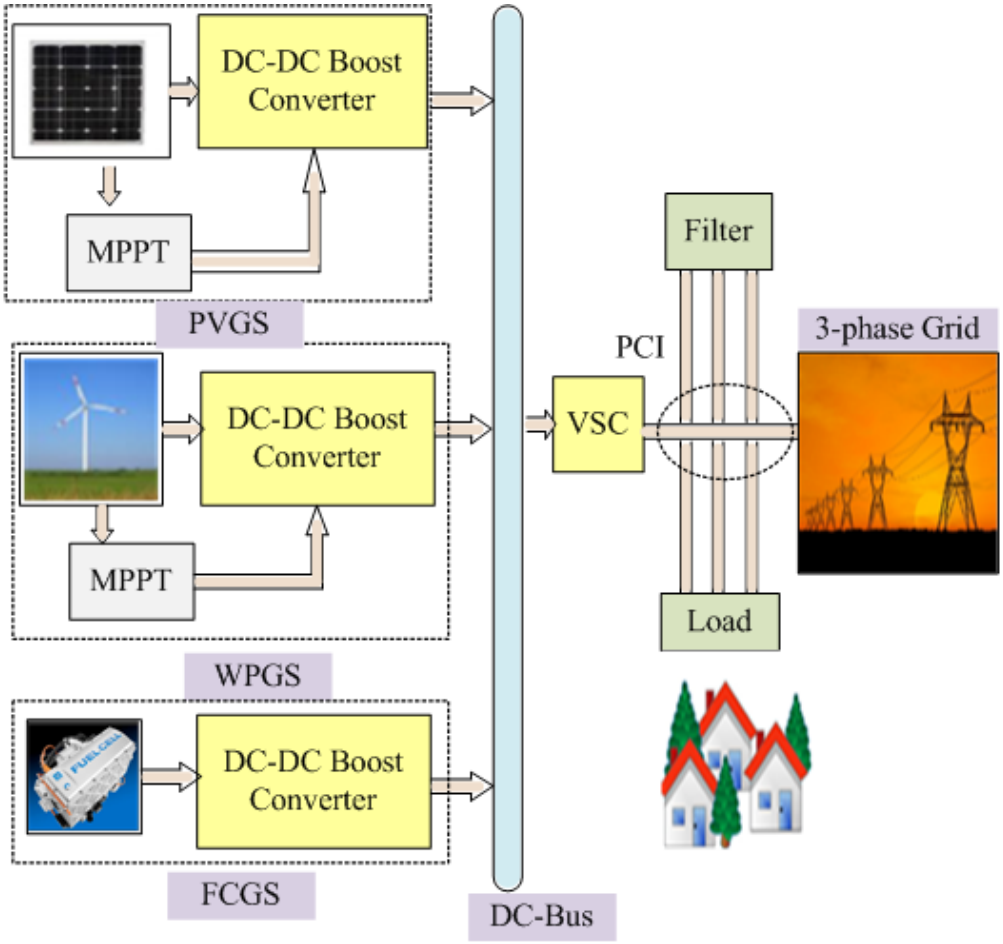

Figure 3.1: Schematic diagram of microgrid

3.2 Photovoltaic Power Generation System

In the photovoltaic power production process, energy from the Sun is converted into electricity through photovoltaic effect. A PV cell has two layers of semiconductors, coated with a photosensitive material and forms a p-n junction. When p-n junction absorbs the energy of the photon, it generates charge carriers that create voltage difference and circulate current through the circuit [13].

3.2.1 Equivalent Circuit of Solar Cell Model

Several research papers are available in the literature [11–14] for modelling of PV panel based on a single-diode model. It is called a general model because it is the commonly used model for the purpose of research. Fig. 3.2 shows the circuit diagram of the single diode PV model.

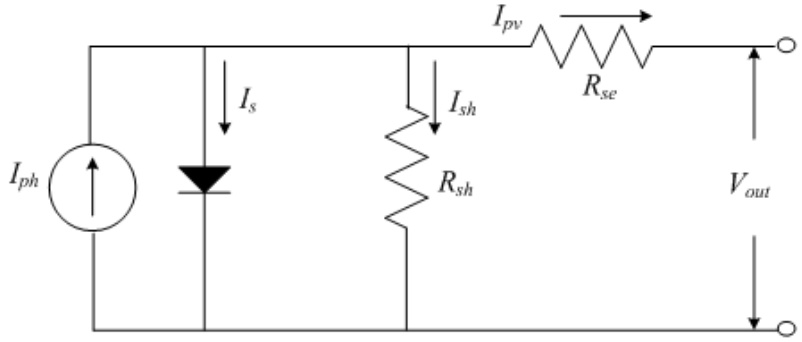

Figure 3.2: Single diode model of solar cell

The defining equations (3.1)-(3.2) of the single diode model are given below [11]:

$$I_{pv} = I_{ph} - I_s[e^{\frac{q(V+IR_{se})}{(AKT)}} - 1] - \frac{V + I_{pv}R_{se}}{R_{sh}} \tag{3.1}$$

$$I_{ph} = I_{sc} * \frac{I_{rr}}{1000} * [1 + (T_{cell} - T_{ref})^* K] \tag{3.2}$$

where I_{pv}, V, I_{ph}, R_{sh}, R_{se} represents solar cell output current(A), PV output voltage, photodiode current(A), shunt resistance(Ω), series resistance(Ω) respectively. k is Boltzmann's constant (1.38 $\times 10^{-38}$ J/K), electron charge (1.6×10^{-19}C), T_{cell} is the working temperature of the cell. To design a PV system of a higher rating, it is required to design PV array with the requisite number of panels connected in series(N_{ser}) and parallel (N_{par}). The photovoltaic array can be simulated with the modified current-voltage (I-V) equation (3.3) given below [13]:

$$I_{pv} = I_{ph}N_{par} - I_s N_{par}[e^{(\frac{V + R_{se}(\frac{N_{ser}}{N_{par}})I_{pv}}{V_t a N_{ser}})} - 1] - \frac{V + R_{se}(\frac{N_{ser}}{N_{par}})I_{pv}}{R_{sh}(\frac{N_{ser}}{N_{par}})} \tag{3.3}$$

3.2.2 Characteristic of PV Array

The P-V and I-V curves of a solar cell are profoundly subject to the solar irradiations. Higher the sun oriented light, higher would be the solar irradiations and henceforth yield higher solar power input to the solar cell and output power would correspondingly increased for the same voltage values. Typical P-V and I-V characteristics for the solar cell at different temperature and irradiation are shown in Figs. 3.3 and 3.4 respectively.

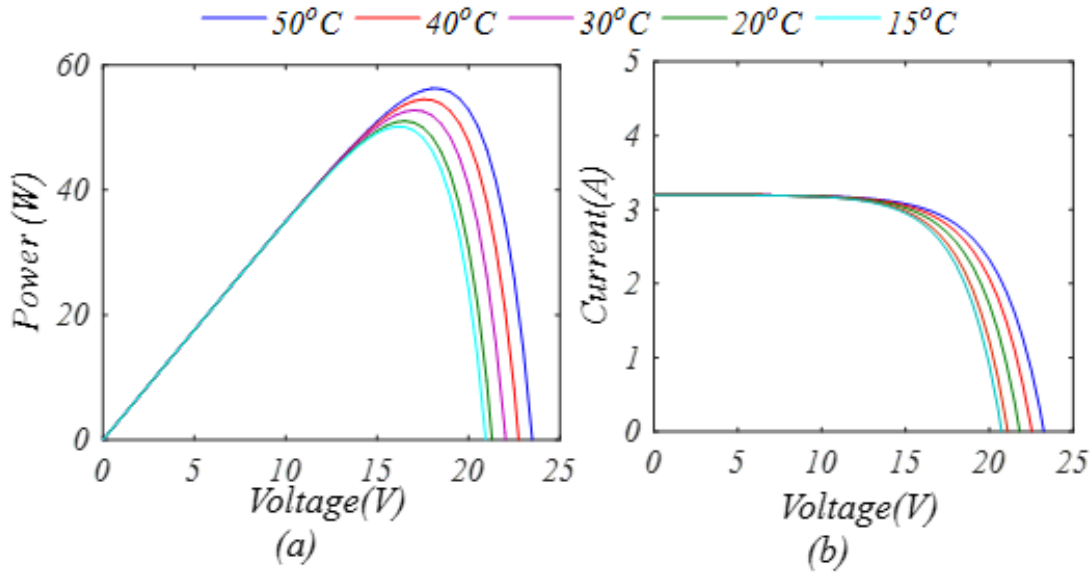

Figure 3.3: Typical P-V and I-V curve of solar panel at different temperatures

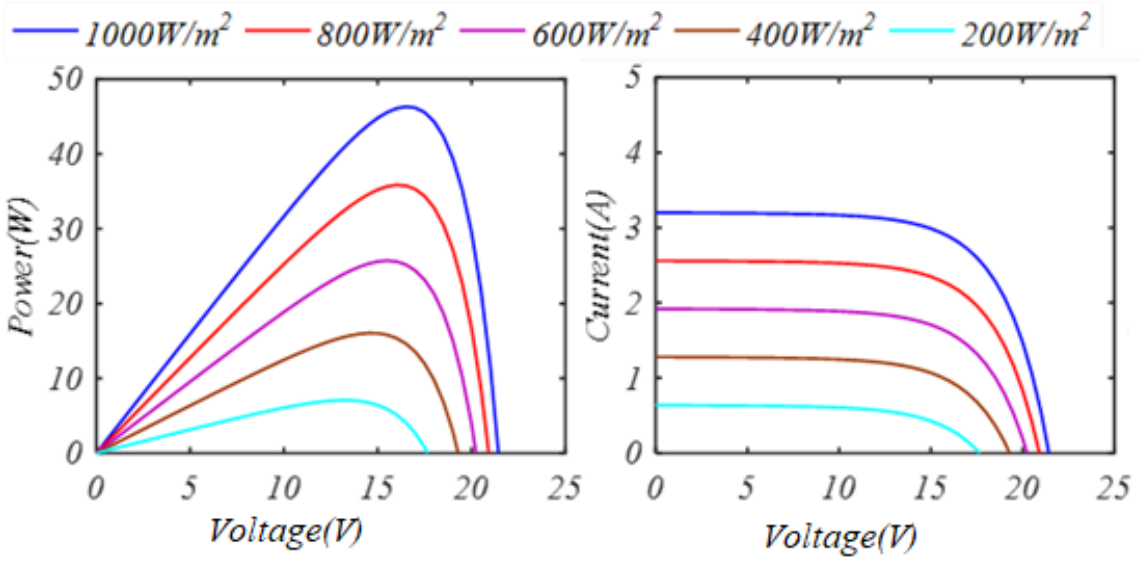

Figure 3.4: Typical I-V and P-V curve of solar panel at variable irradiation

3.2.3 Design of Boost Converter

In the photovoltaic I-V curve, the maximum power is generated at a unique point of the I-V characteristic curve, this point is known as the maximum power point. MPPT algorithms are used to extract this maximum power. A DC/DC boost converter, shown in Fig.3.5, transfer this maximum power to the load. The value of inductor(L) and capacitor (C) of the boost converter is designed and calculated according to desired output power levels. The design of the boost converter [44] is

given by equations (3.4)-(3.5):

$$L_b = \frac{V_{pv} D}{2\Delta i_1 f_s} \tag{3.4}$$

$$C_b = \frac{I_d D}{\Delta V_b f_s} \tag{3.5}$$

where $\triangle i_1$ and $\triangle V$ are input current ripple(10% of the input current) and output voltage ripple (5% of the output voltage) respectively. V_{in} is the input voltage for the converter and it is the same as V_{pv}. Furthermore, I_d, f_s and V_b are output current, switching frequency and output voltage of the converter respectively. The duty cycle (D) of the boost converter is given by equation (3.6):

$$D = 1 - \frac{V_{in}}{V_b} \tag{3.6}$$

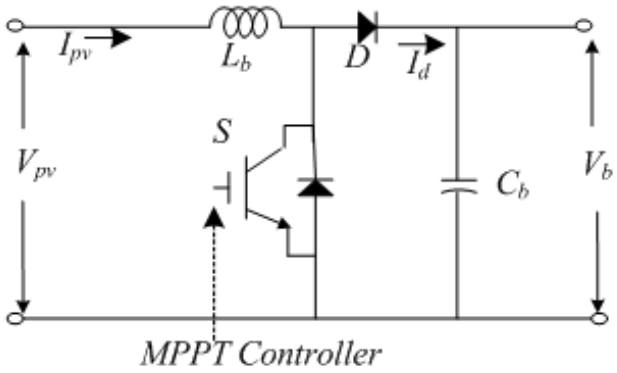

Figure 3.5: DC-DC boost converter

3.2.4 Maximum Power Point Tracking for Solar System

The P-V curve of a PV cell shows non-linear characteristics and there is a unique point at which the cell produces maximum power (for given irradiation and temperature). MPPT algorithm track this maximum power point and ensures that the PV module always operates at MPP by providing proper gating pulses to boost converter. Several MPPT methods that have been studied and researched [15–21]. Amongst the commonly used techniques are Perturbation and Observation(PO) and Incremental Conductance method (IC). The block diagram of the MPPT system for the PV MPPT system is shown in Fig. 3.6.

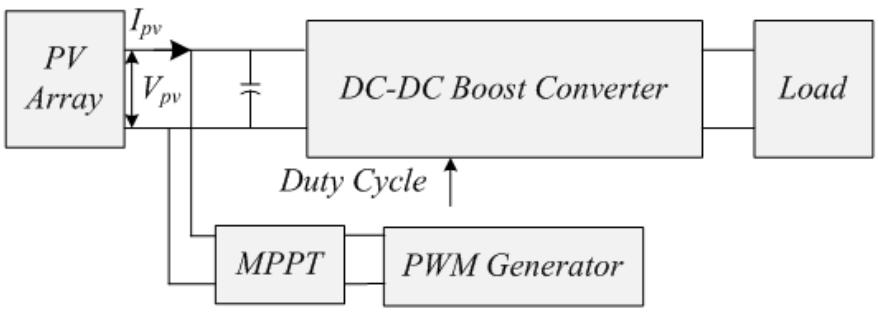

Figure 3.6: Block diagram of MPPT control

3.2.5 Perturbation and Observation Control Technique

Perturbation and observation is the most commonly used MPPT control technique due to its simplicity. The summary of the algorithm for the PO is given in Table 3.1.

Table 3.1: Summary of the PO algorithm

Perturbation	**Change in Power**	**Next Perturbation**
Positive	Positive	Positive
Positive	Negative	Negative
Negative	Positive	Negative
Negative	Negative	Positive

It can be observed from Table 3.1 that incrementing the voltage increases the power when operating on the left of the MPP and vice versa. Therefore, for increment in power, the subsequent perturbation should be kept at the same level to reach the MPP and if there is a decrement in power, the perturbation should be reversed. The process is repeated periodically until MPP is reached. However, the PO has certain limitations such as its performance is not very accurate under fast-changing atmospheric conditions. The IC method overcomes the limitations of the PO.

3.2.6 Incremental Conductance Algorithm

This method is based on incremental conductance of the PV module by comparing incremental conductance with instantaneous conductance. IC method uses voltage

and current sensors to sense the output voltage and current of the PV array. Source conductance is given by equations (3.7) - (3.11) below:

$$G = \frac{I}{V} \tag{3.7}$$

and the source incremental conductance:

$$\Delta G = \frac{dI}{dV} \tag{3.8}$$

In general output voltage from a source is positive. According to this algorithm:

$$if \frac{dP}{dV} > 0, then G > \Delta G \tag{3.9}$$

$$if \frac{dP}{dV} = 0, then G = \Delta G \tag{3.10}$$

$$if \frac{dP}{dV} < 0, then G < \Delta G \tag{3.11}$$

The flow chart of PO and IC algorithms is given in Fig 3.7. The flow chart gives insight steps to realize the PO and IC MPPT algorithms which control the switching action of boost converter to achieve MPP operation.

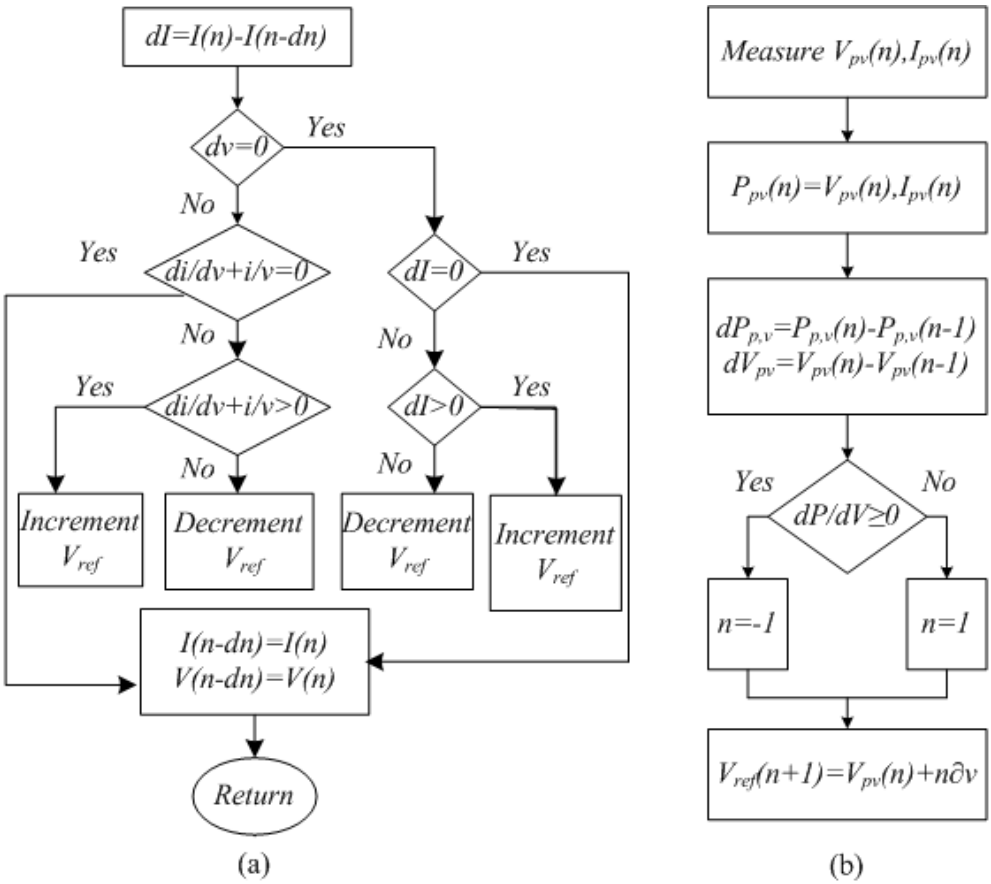

Figure 3.7: Control flow chart for (a) PO algorithm (b) IC algorithm

3.2.7 Results for MPPT algorithms

Fig. 3.8 shows the MPPT result for the PO and IC algorithms under the variation of temperature and irradiation level. It is observed from Fig. 3.8 that both the algorithms reached MPP but the dynamic response of the PV system for two MPPT algorithms are different. PO obtained power response is slower and is easy to implement whereas, the IC MPPT is more adaptable for variable perturbation.

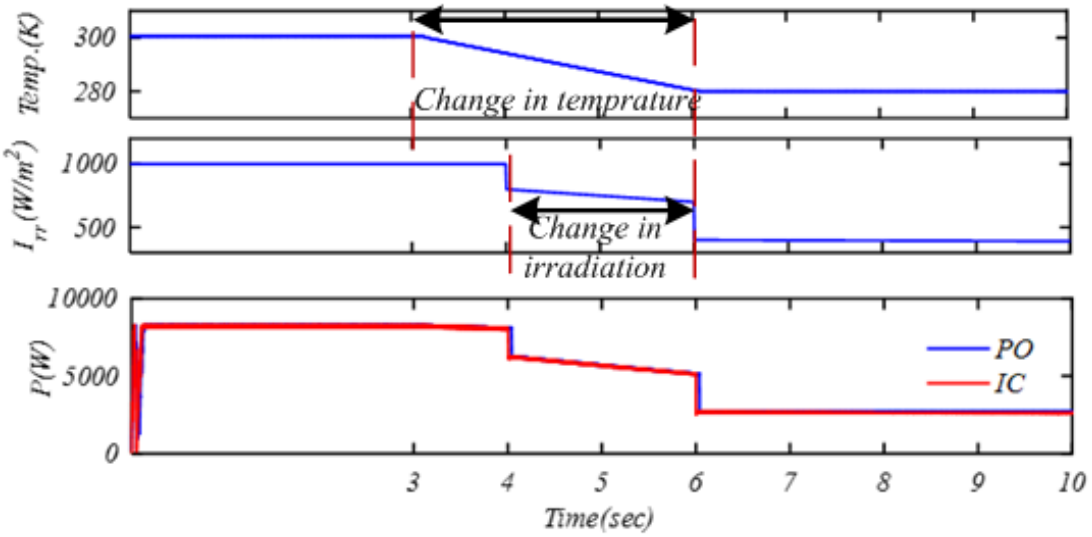

Figure 3.8: MPPT response of PO and IC algorithm

3.3 Wind Power Generation System

Wind energy power generation system (WPGS) is shown in 3.9. Various components of WPGS are described in subsequent sections.

3.3.1 Wind Turbine

The wind turbine is used to convert the kinetic energy of wind into mechanical torque, which can be calculated from available mechanical power at the turbine. The mechanical power extracted by the wind turbine can be expressed mathematically as given by equation (3.12) [24]:

$$P = \frac{1}{2}\rho S v^3 C_\rho(\mu, \alpha) \tag{3.12}$$

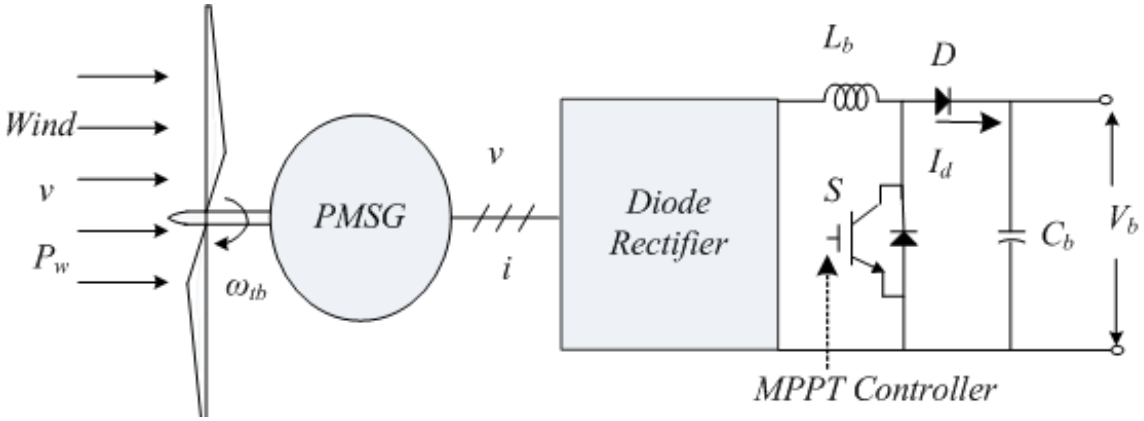

Figure 3.9: Wind power generation system

where v is wind velocity S is swept area of blades and C_ρ is defined as the ratio of total power converted into mechanical energy to the total power received by the turbine and can be mathematically expressed by equation(3.13) [96]:

$$C_\rho(\mu,\alpha) = 0.5176((\frac{116}{\mu+0.8\alpha}) - 0.4\alpha - 5)e^{-\frac{21}{\mu}} + 0.0068\mu \tag{3.13}$$

where P, α, μ and v are mechanical power output of the turbine, blade pitch angle, tip speed ratio and velocity of the wind respectively. C_ρ-μ characteristics are shown in Fig. 3.10 and it can be observed that after a certain point C_ρ starts to decline at the same slope hence there is only one optimized point where power is maximum.

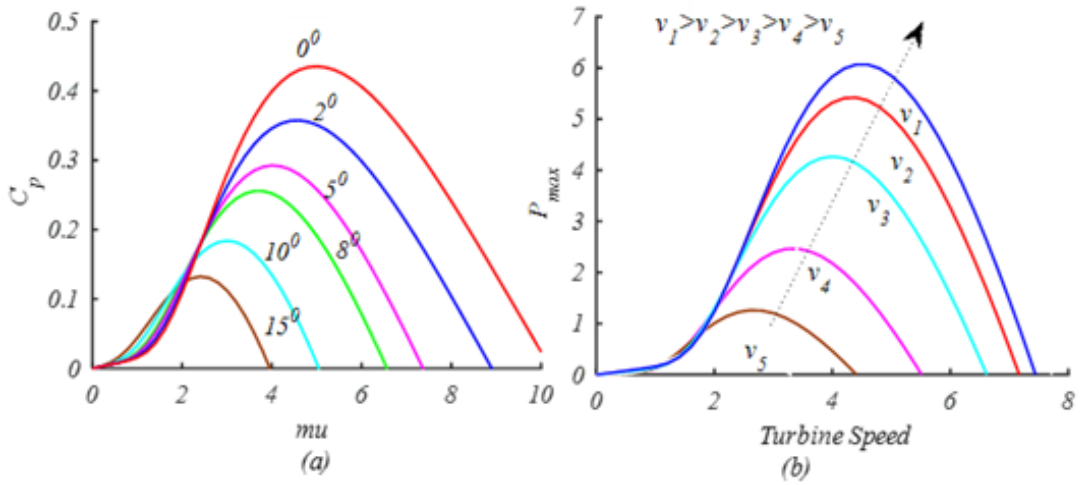

Figure 3.10: Wind turbine characteristics (a)C_ρ-μ curve (b)P-N curve for varying wind speed

3.3.2 Permanent Magnet Synchronous Generator

In the developed microgrid system, wind turbine shaft is coupled to the permanent magnet synchronous generator (PMSG) shaft. In this work, cylindrical rotor type

PMSG is modelled. The excitation field is produced through a permanent magnet, rotor speed and magnetic field speed are equal to the synchronous speed. The magnitude of torque is given by equation (3.14):

$$T_t = \frac{\pi}{2}(\frac{p}{2})^2 \phi_r F_f \sin\delta \tag{3.14}$$

where $\phi_{\,\mathrm{r}}$ is the angle by which MMF produced by flux ($\mathrm{F_f}$) and MMF produced by air gap flux ($\mathrm{F_r}$) and p is permeance per pole. The dynamic equation (3.15) of PMSG operation can be given as:

$$V_t = E_r - I_a(R_a + jX_L) \tag{3.15}$$

where $\mathrm{R_a}$ is machine resistance, $\mathrm{X_L}$ is leakage reactance in series with the resistance between the terminal voltage($\mathrm{V_t}$) and air gap MMF for each phase. PMSG is modelled as two-mass drive train. The differential equations (3.16)-(3.18) which governs the mechanical dynamics of two mass drive train [23] can be given by:

$$2H_{tb}\frac{d\omega_{tb}}{dt} = T_m - T \tag{3.16}$$

$$\frac{1}{\omega_{eb}}\frac{d\theta_t}{dt} = \omega_{tb} - \omega r \tag{3.17}$$

$$2H_p\frac{d\omega_r}{dt} = T - T_g \tag{3.18}$$

where $\mathrm{H_{tb}}$, $\mathrm{H_p}$, θ_{t} and ω_{tb}, ω_{r}, ω_{eb} represents the turbine inertia constant, PMSG inertia constant, shaft twist angle and angular speed of the wind turbine, rotor speed of the PMSG, electrical base speed (rad/s) respectively. The shaft torque (T) can be represented by equation (3.19):

$$T = m_s\theta_t + D_t\frac{d\theta_t}{dt} \tag{3.19}$$

where $\mathrm{m_s}$ is the shaft stiffness and $\mathrm{D_t}$ is the damping coefficient.

3.3.3 AC to DC Three-Phase Diode Rectifier

The generated power is converted into DC power through three-phase diode rectifier, the mathematical equation (3.20) is given as:

$$P = 3V_{ph}I_{ph} = V_{dc}I_{dc} \tag{3.20}$$

where P, V_{ph}, I_{dc}, are generated power, phase voltage, phase current and rectified DC current respectively. DC voltage (V_{dc}) can be given by:

$$V_{dc} = \frac{3}{\pi}\int_{-\frac{\pi}{6}}^{\frac{\pi}{6}} V_{LLmax} cos\theta d\theta = \frac{3}{\pi} V_{LL} \tag{3.21}$$

where V_{LLmax} is peak value of line to line input voltage of rectifier.

3.3.4 MPPT Controller for WPGS

The MPPT system is implemented using the Hill-Climbing control algorithm [96]. The objective of this control mechanism is to evacuate generated power at a point close to maximum power by controlling the duty cycle of the switch. Fig. 3.11 shows the block diagram of the wind MPPT system. The current and speed of

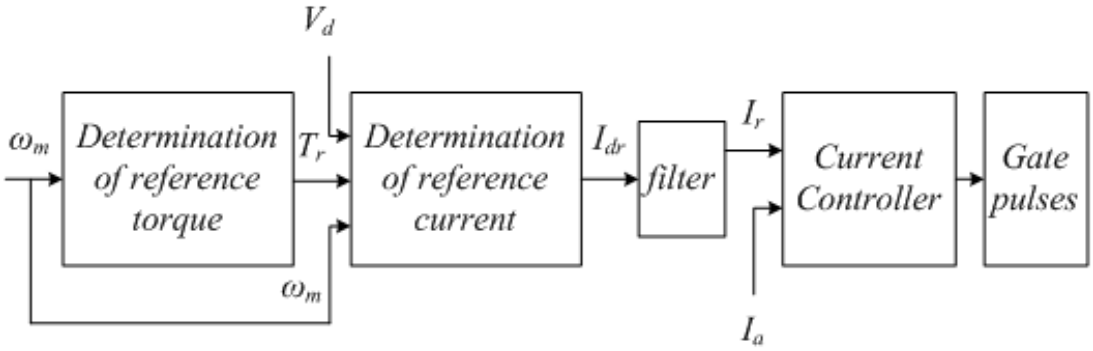

Figure 3.11: Block diagram of MPPT controller

PMSG are taken as inputs for the controller and wind speed and then generated reference torque is measured. This reference torque is used to calculate the reference currents with the help of rectifier output voltage and wind speed. The reference currents are compared with actual generated currents through hysteresis current controller and pulses generated by the controller are used for the control of IGBT switches of the boost converter. If generated speed is less than maximum speed or generated torque (T_g) is greater than turbine torque (T_m), the acceleration takes place. Deceleration occurs when the generator speed is greater than the maximum speed hence T_m and T_g are controlled at MPPT to give maximum power. Reference torque is calculated through the equation (3.22) and is given below:

$$T_r = m_{op}(\omega_{tb})^2 \tag{3.22}$$

Reference is current is given by equation (3.23)

$$I_r = \frac{T_r * \omega_{tb}}{V_b} \tag{3.23}$$

Generator torque estimation of increment or decrement of speed is calculated from the difference of turbine torque T_m and generator torque T_g. Mechanical power is given in equation (3.24)

$$T_m = \frac{P}{\omega_{tb}} \tag{3.24}$$

$$\mu = \frac{\omega_{tb}}{v} \tag{3.25}$$

To satisfy the maximum power condition μ=μ_{op} = X; where X is any constant

$$\frac{\omega_{tb1}}{v_1} = \frac{\omega_{tb2}}{v_2} \tag{3.26}$$

When WPGS is under MPPT Cp=1p.u. and ρ, swept area of blade (S) is constant, the mechanical torque can be written by equation (3.27):

$$T_m \propto \frac{v^3}{\omega_{tb}} \tag{3.27}$$

From the equations (3.26) and (3.27), it can be seen that

$$\frac{T_{m1}}{T_{m2}} = \frac{v_1^2}{v_2^2} \tag{3.28}$$

To test the MPPT operation of WPGS system, wind speed is reduced from 12m/s to 10 m/s at t=1s and further increased to 13m/s at t=2s. The response of the turbine and shaft torque under wind dynamics has been shown in Fig. 3.12 and it is observed in Fig. 3.12 (a) that shaft torque dynamic is slower as compared to turbine torque. This is because of the more realistic two-mass drive train model which is used to realize the PMSG. To verify MPPT operation of the wind energy system, the mechanical torque is plotted for wind speed reduction from 12m/s to 10m/s. It is also found in Fig. 3.12 (b) the ratio of initial torque to final torque is approximately 1.44 ($(12/10)^2$=$(0.72/0.5)^2$) which satisfies the equation (3.28). This ratio proves effectiveness of the designed MPPT controller. Fig. 3.12 (c) shows the generated torque and reference torque. It is noticed that actual generated torque is following reference torque which verifies that the system is working efficiently.

The switching of the boost converter is controlled through MPPT algorithm and designing parameters of the boost converter are explained in section 3.2.3.

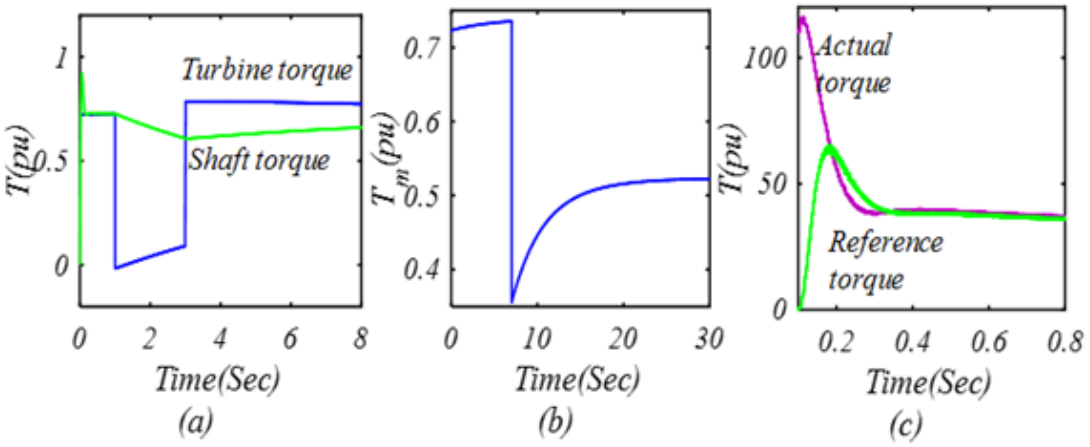

Figure 3.12: Responses of torque for WPGS MPPT system

3.4 Fuel Cell Power Generation System

The main advantage of using FCGS is that it uses non-hydrocarbon fuel to produce clean power. The fuel cell is classified on the basis of type of electrolyte used viz. polymer electrolyte fuel cell, alkaline fuel cell, phosphoric acid fuel cell, molten carbonate fuel cell and solid oxide fuel cell (SOFC). Amongst all the SOFC is considered as the most powerful type of fuel cell due to its higher efficiency, fuel flexibility, lower temperature operation, which is desirable for cost reduction and system durability [32]. Further, solid oxide fuel cells power density is higher in comparison to other fuel cell variants, solid oxide fuel cell systems are recently becoming popular in portable applications within the power range of about 20–250W.

3.4.1 Fuel Cell Modelling

Fig 3.13 depicts the dynamic model of FC. The solid oxide fuel cells (SOFCs) model [32] is simulated with pre-assumptions that the stack is fed with the hydrogen and oxygen, thermal properties of system are steady and there is only ohmic losses occurs in the system. The utilization factor is the ratio of input fuel-flow $q^i_{H_2}$ into the stack and consumed-fuel $q^c_{H_2}$. The utilization factor is considered 0.85 in

development of the model. UF is expressed by equation (3.29):

$$UF = \frac{q^i_{H_2}}{q^c_{H_2}} \tag{3.29}$$

The consumed and input molar-flow of hydrogen is computed with the help of electro-chemical equation (3.30) and equation (3.31) and respectively.

$$q^c_{H_2} = \frac{NI^c_{f_c}}{2F} = 2K_r I^c_{fc} \tag{3.30}$$

$$q^i_{H_2} = \frac{2K_r I^c_{f_c}}{0.85} \tag{3.31}$$

where $\mathrm{K_r}$, I^c_{fc}, N and F are constant (mol/(sA)), feedback-current of fuel cell (A), numbers of series-cell of SOFC's stack and Faraday constant (C/mol). For the computation of the partial pressure, each gas treated separately for the computation and the perfect gas equation has been implemented. Hydrogen gas equation is presented here as an example (3.32):

$$p_{H_2} V_a = \eta_{H_2} RT \tag{3.32}$$

where R, T, $\mathrm{V_a}$, $\mathrm{pH_2}$ and η are universal gas-constant (J/(mol K)), temperature of solid oxide fuel cells stack (K), anode-volume, partial-pressure of the hydrogen (atm) and the number of hydrogen-moles respectively. Differentiating pressure with respect to time is given as:

$$\frac{dp_{H_2}}{dt} = (\frac{RT}{V_a}) q_{H_2} \tag{3.33}$$

where q_{H_2} is time derivative of η_{H_2} Hydrogen molecular flow is contributed by input fuel ($q^i_{H_2}$), output fuel ($q^o_{H_2}$) and consumed fuel ($q^c_{H_2}$), equation (3.33) become as:

$$\frac{dp_{H_2}}{dt} = (\frac{RT}{V_a})(q^i_{H_2} - q^o_{H_2} - q^c_{H_2}) \tag{3.34}$$

It can be assumed that molar flow of hydrogen through the valve is directly proportional to the pressure inside and it can be represented by equation (3.35)

$$\frac{q_{H_2}}{p_{H_2}} = \frac{K_a}{\sqrt{M_{H_2}}} = k_{H_2} \tag{3.35}$$

where K_{H_2}, M_{H_2} and $\mathrm{K_a}$ are hydrogen flow valve molar constant, molecular masses of hydrogen, anode valve constant respectively. Replacing equation (3.30) and

(3.35) in equation (3.34) and taking Laplace both sides, expression is found to be:

$$p_{H_2} = \frac{\frac{1}{K_{H_2}}}{1 + \sigma_{H_2} s}(q^i_{H_2} - 2K_r I^c_{f_c}) \tag{3.36}$$

$$\sigma_{H_2} = \frac{V_a}{K_{H_2}} RT \tag{3.37}$$

The same operation is applied to all reactants and products and on application of Nernst's equation and Ohm's law, the equation of stack voltage is given by equation (3.38):

$$V = N(E_0 + \frac{RT}{2F}[ln\frac{P_{H_2}P^{0.5}_{O_2}}{P_{H_2O}}]) - rI^c_{f_c} \tag{3.38}$$

where E_o is the voltage associated with the reaction free energy (V), R is the same gas constant as previous but is unit (J/(Kmol K)), r denotes ohmic losses of the stack.

The stack voltage output is connected at DC input of the controlled voltage source as shown in Fig. 3.13. The DC-DC boost converter is used to boost the stack voltage from 300V to 750V. Designing parameters of boost converter are explained in Section 3.2.3.

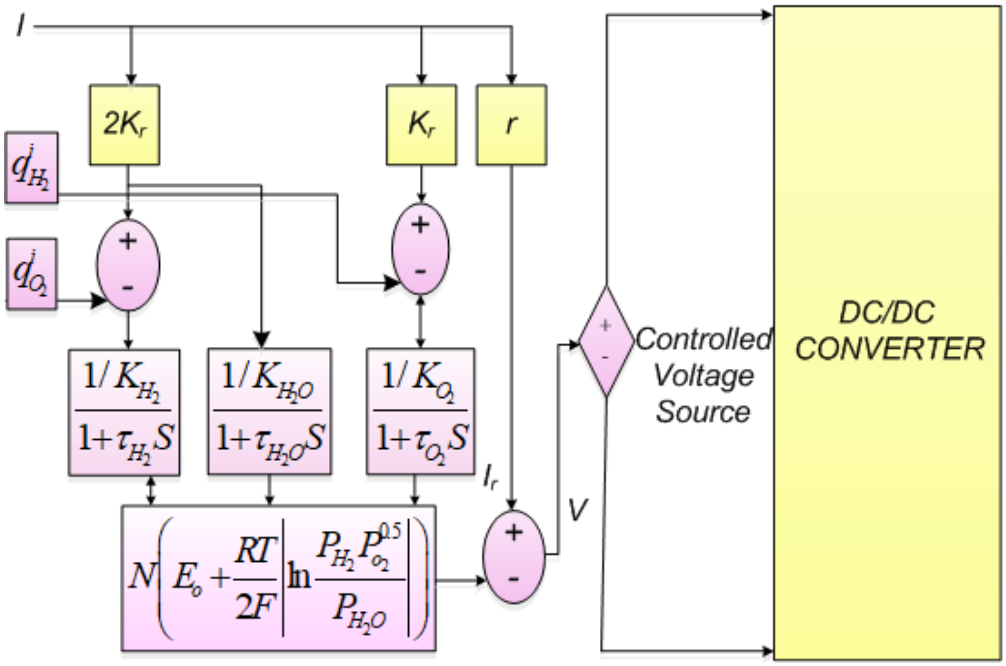

Figure 3.13: Developement of SOFC stack dynamic model under MATLAB/SIMULINK using equation(3.38)

3.5 Design of Grid-Connected Microgrid

The block diagram of the MG system with all components is shown in Fig. 3.14. The voltage source converter (VSC) interlinks different RESs to the grid. The VSC is a power conditioning device that is used to interface the RESs to the grid and AC load. It consists of a DC-link capacitor which is also responsible for the generation of compensating currents. The detailed mathematical analysis and calculations are given in the following subsections.

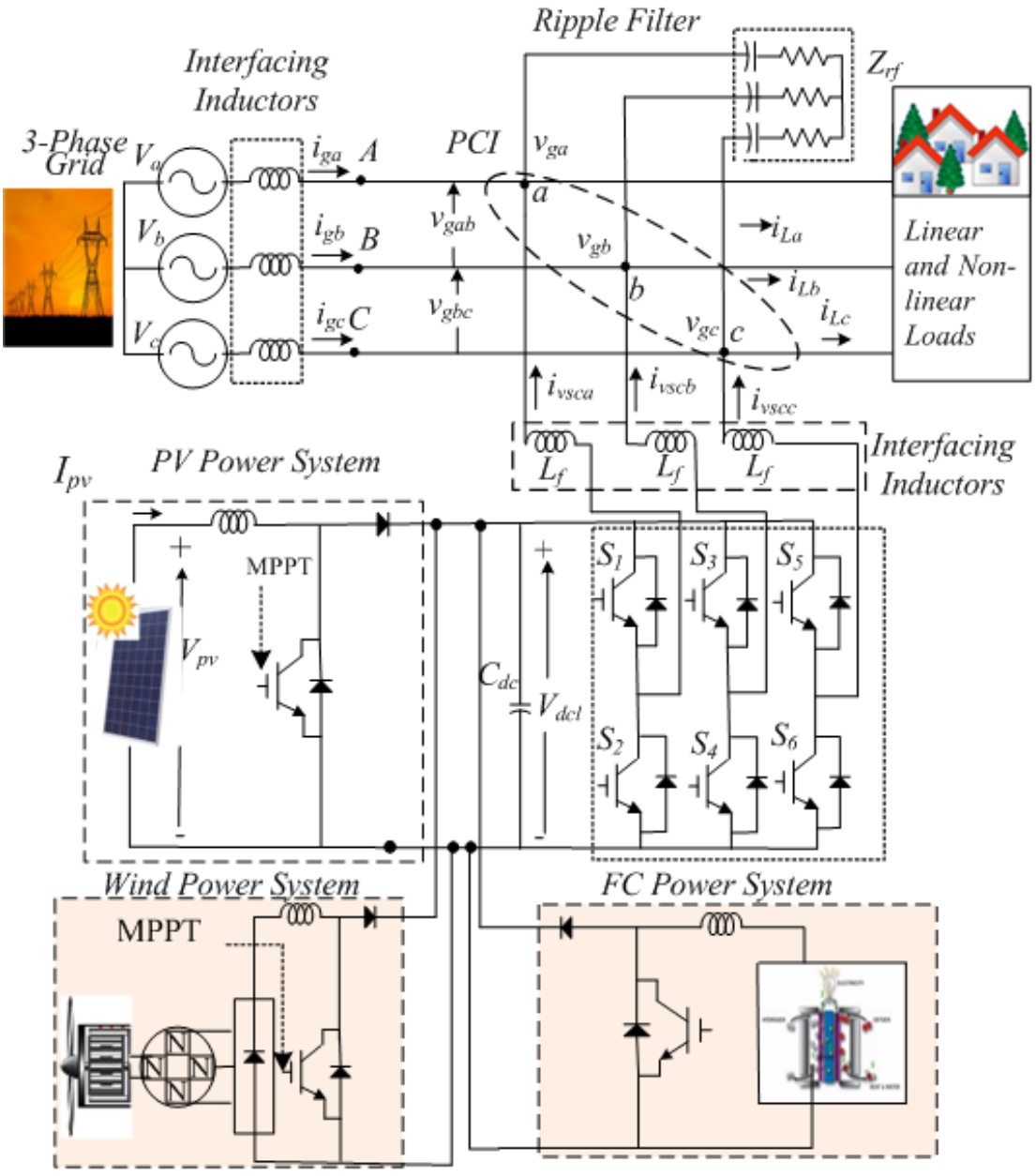

Figure 3.14: Block diagram of microgrid system

3.5.1 DC-Link Voltage Calculation

The value of DC-link voltage is selected for accurate PWM control and its value must be greater than the peak value of supply line to line voltage. In three-phase system it can be calculated by equation (3.39) and given as:

$$V_p = \frac{\sqrt{2}V_{LL}}{\sqrt{3}} \tag{3.39}$$

where V_p is the peak value of AC Phase voltage, V_{LL} line to line RMS AC voltage So the DC-link voltage can be obtained by equation (3.40) and given as:

$$V_{dcl} = \frac{2\sqrt{2}V_{LL}}{\sqrt{3}m} \tag{3.40}$$

where V_{dcl} is DC-link voltage, m is modulation index. The line voltage for the designed system has been taken 415V.

$$V_{dcl} = \frac{2 * \sqrt{2} * 415}{\sqrt{3} * 0.9} \tag{3.41}$$

The calculated DC-link voltage is 760V and the reference is taken as 750V for the developed system.

3.5.2 Calculation for DC-Link Capacitor

The value of the DC-link capacitor should be large enough to handle system dynamics, hence its value depends upon the instantaneous energy available to the VSC during transients. DC-link voltage should be maintained at constant value irrespective of the changes occur in the load and generation. The value of DC-link capacitor based on the principle of energy conservation is given by equation (3.42):

$$C_{dc} = \frac{\frac{P_{dcl}}{V_{dcl}}}{2\omega\triangle V_{dcl}} = \frac{\frac{17500}{750}}{2 * 2 * 3.14 * 50 * .01 * 750} = 4953\mu F \tag{3.42}$$

where P_{dcl} is power at DC-link, V_{dcl} is DC-link voltage of VSC, $\triangle V_{dcl}$ is ripple in DC-link voltage. Considered value of DC-link capacitor is 5000 μ F.

3.5.3 Calculation for Interfacing Inductor

The inductor is interfaced at the output of VSC to filter out ripple of the current. Also, voltage drop across the inductor (filter inductor) should be minimum in order to perform the proper operation of system. Interfacing inductor can be calculated equation (3.43):

$$L_f = \frac{m * V_{dcl}}{6 * h * f_s * i_{rip}} = \frac{0.9 * 750}{6 * 1.1 * 10,000 * 23 * .01} = 54mH \tag{3.43}$$

where L_f is the value of interfacing inductor, f_s is switching frequency, i_{rip} is peak to peak ripple current, m and h are constant and chosen 1 and 1.1 respectively. Considered value of interfacing inductor is 60mH.

3.6 Conventional Algorithms for VSC Control

A brief introduction of two conventional algorithms is presented in this section through basic formulae involved. Using these conventional algorithms, the grid reference currents are generated in the microgrid system. The switching losses are substantial and have to be considered in modelling the system. The computational formula to estimate the losses is given by equation (3.44):

$$i_{loss}(m) = i_{loss}(m-1) + K_p(e_{dc}(m) - e_{dc}(m-1)) + K_i(e_{dc}(m)) \tag{3.44}$$

where $e_{dc}(m)$ is error and difference between the reference voltage of DC-link ($V^*_{dcl}(m)$) and measured DC-link voltage ($V_{dcl}(m)$). $e_{dc}(m)$ can be given by equation (3.45):

$$e_{dc}(m) = (V^*_{dcl}(m) - V_{dcl}(m)) \tag{3.45}$$

K_p and K_i are the proportional and integral gains of the DC-link PI controller. The loss component ($i_{loss}(m)$) corresponding to the active power required by VSC is obtained. This loss component is added to the fundamental active power component of load current (I_{Ld}), which is extracted using control techniques under consideration.

3.6.1 Synchronous Reference Frame Theory (SRFT)

The block diagram of the controller is shown in Fig 3.15. The sensed load current components are transformed into two-phase stationary coordinates [109, 110]. '$a-b-c$' phases can then be transformed into $\alpha-\beta$ coordinates by Clark's transformation using 'sine and cosine' signals generated by a phase-locked loop (PLL) and given by equation (3.46).

$$\begin{bmatrix} i_\alpha \\ i_\beta \end{bmatrix} = \sqrt{\frac{2}{3}} \begin{bmatrix} 1 & -1/2 & -1/2 \\ 0 & \sqrt{3}/2 & -\sqrt{3}/2 \end{bmatrix} \begin{bmatrix} i_{La} \\ i_{Lb} \\ i_{Lc} \end{bmatrix} \tag{3.46}$$

Then using θ as the transformation angle, these currents can be transformed from α-β to d–q frame using equation (3.47) (Park's transformation).

$$\begin{bmatrix} i_{Ld} \\ i_{Lq} \end{bmatrix} = \sqrt{\frac{2}{3}} \begin{bmatrix} cos\theta & sin\theta \\ -sin\theta & cos\theta \end{bmatrix} \begin{bmatrix} i_\alpha \\ i_\beta \end{bmatrix} \tag{3.47}$$

The load currents after Clark's and Park's transformation provides $\mathrm{i_{Ld}}$ and $\mathrm{i_{Lq}}$. The component $\mathrm{i_{Ld}}$ is passed through a low pass filter to give $\mathrm{i_{Ld}}$. DC-link loss factor is calculated using equation (3.44), which is added with i_{Ld} to obtain $\mathrm{I_{Lp}}$.

$$I_{Lp} = i_{loss} + i_{Ld} \tag{3.48}$$

Now Inverse Clark's and Park's transformation are used to obtain three-phase reference source current using equation (3.49) and equation (3.50). Reverse Park's transformation is given as:

$$\begin{bmatrix} i^*_\alpha \\ i^*_\beta \end{bmatrix} = \sqrt{\frac{2}{3}} \begin{bmatrix} cos\theta & -sin\theta \\ sin\theta & cos\theta \end{bmatrix} \begin{bmatrix} I_{Lp} \\ 0 \end{bmatrix} \tag{3.49}$$

Reverse Clark's Transformation

$$\begin{bmatrix} i^*_{ga} \\ i^*_{gb} \\ i^*_{gc} \end{bmatrix} = \sqrt{\frac{2}{3}} \begin{bmatrix} 1 & 0 \\ -1/2 & \sqrt{3}/2 \\ -1/2 & -\sqrt{3}/2 \end{bmatrix} \begin{bmatrix} i^*_{s\alpha} \\ i^*_{s\beta} \end{bmatrix} \tag{3.50}$$

Generated reference currents $\mathrm{i^*_{ga}}$, $\mathrm{i^*_{gb}}$, $\mathrm{i^*_{gc}}$ are compared with instantaneous grid currents ($\mathrm{i_{ga}}$, $\mathrm{i_{gb}}$, $\mathrm{i_{gc}}$) and fed to Hysteresis Current Controller (HCC) to generate

switching signals for VSC.

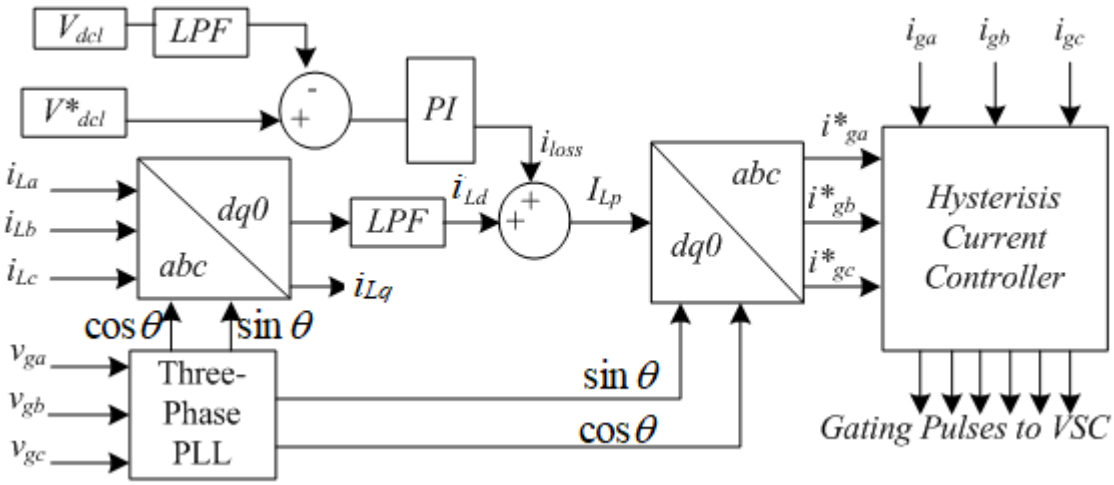

Figure 3.15: Block diagram of SRFT control technique implementation

3.6.2 Power Balance Theory

The realization of Power Balance Theory (PBT) is based on unit template generations. Fundamental active load current components are estimated using power. The PBT control technique is used for compensation and it is dependent upon the appropriate generation of templates. These computed templates are in phase with the grid voltage. To generate reference supply current these templates are multiplied to active components of load currents. The block diagram of PBT control is shown in Fig. 3.16.

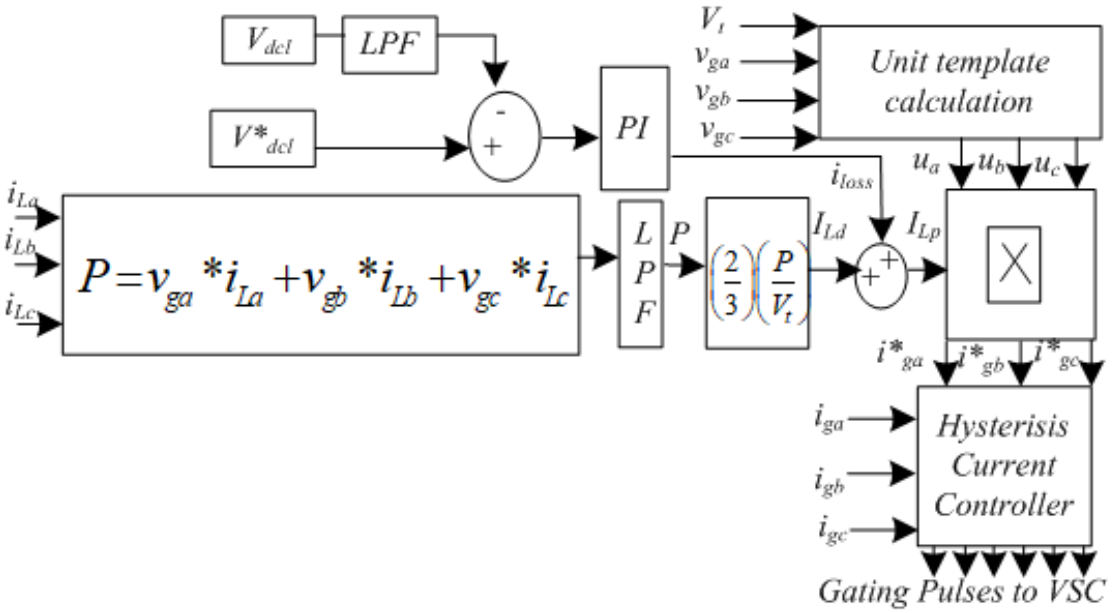

Figure 3.16: Block diagram of PBT control technique

Load and utility interfaced with system at the point of common interconnection (PCI). The magnitude of PCI voltage (V_t) [12] is calculated by equation (3.51):

$$V_t = (\frac{2}{3})^{\frac{1}{2}}(v_{ga}^2 + v_{gb}^2 + v_{gc}^2)^{\frac{1}{2}} \tag{3.51}$$

The unit template can be estimated by equation: (3.52) given below:

$$u_a = \frac{v_{ga}}{V_t}; u_b = \frac{v_{gb}}{V_t}; u_c = \frac{v_{gc}}{V_t} \tag{3.52}$$

where V_{ga}, V_{gb}, V_{gc} are phase voltages. The real time active power of the load current has two components. One component of load current corresponds to the DC value whereas other component is of oscillating nature and computed by equation (3.53):

$$P = v_{ga} * i_{La} + v_{gb} * i_{Lb} + v_{gc} * i_{Lc} \tag{3.53}$$

where i_{La}, i_{Lb}, i_{Lc} are load currents. The active component of load current can be represented by equation (3.54) given below:

$$I_{Ld} = (\frac{2}{3})(\frac{P}{V_t}) \tag{3.54}$$

where P is the average component of real-power of load and it is pass through LPF to estimate its value. Instantaneous value of the fundamental active power component of reference supply current is given by equation (3.55):

$$I_{Lp} = I_{Ld} + i_{loss} \tag{3.55}$$

The active real-power in-phase component of generated reference current signal can be estimated by equation (3.56):

$$i_{ga}^* = I_{LP} * u_a; i_{gb}^* = I_{LP} * u_b; i_{gc}^* = I_{LP} * u_c \tag{3.56}$$

PI controller is implemented for the regulation of DC link voltage. Computed reference currents for the grid and sensed grid currents are passed through hysterisis current controller to generate gate pulses of VSC.

3.7 Results and Analysis for VSC Control using Conventional Techniques

The MATLAB/SIMULINK model of the grid-connected microgrid system is developed. SRFT and PBT conventional control techniques are implemented for VSC control and obtained results of the MG system are analyzed. The performance is analyzed for various parameters such as three-phase grid voltages (v_{ga}, v_{gb}, v_{gc}) three-phase grid current (i_{ga}, i_{gb}, i_{gc}), three-phase nonlinear current (i_{La}, i_{Lb}, i_{Lc}), three-phase PCI voltage(V_{PCI}) and DC-link voltage (V_{dcl}).

3.7.1 System Response using SRFT

Figs. 3.17 and 3.18 show the performance of microgrid under conventional control technique SRFT. Response of the system for a nonlinear balanced and unbalanced load is shown in Fig. 3.17. To observe the response of the system for nonlinear load (diode bridge rectifier 25Ω resistance and 100mH inductance) is integrated into the system. Load unbalancing is introduced at t=0.8s to 0.95s by removing phase 'c' of the load. Hence the phase 'c' load current becomes zero. However, the grid current of phase 'c' is sinusoidal and grid currents are also balanced. It is observed from Fig. 3.17 the system is working proficiently under unbalanced nonlinear and the grid is supplying a balanced three-phase current. Moreover, the PCI voltage remains regulated and DC-link voltage is also maintained at its reference value. Rated power of solar, wind and fuel cell system is 8kW,6.5kW and 3kW respectively. Hence total generated power is 17.5kW at its rated capacity. Load demand is 12.5kW so that the surplus power (5kW) is feeding into the grid. At t= 0.8s the load is further reduced to 5.5kW due to the removal of one phase. Hence power feeding into the grid increased ($P_g = 12kW$) correspondingly. phase 'c' reintegrated into the system at t=0.95s and system perform under balanced nonlinear load again. Results show that the power balance is maintained during the operation. The results exhibit that the VSC is multitasking i.e. it provides reactive power compensation, harmonics suppression, unity power factor operation and maintains power balance.

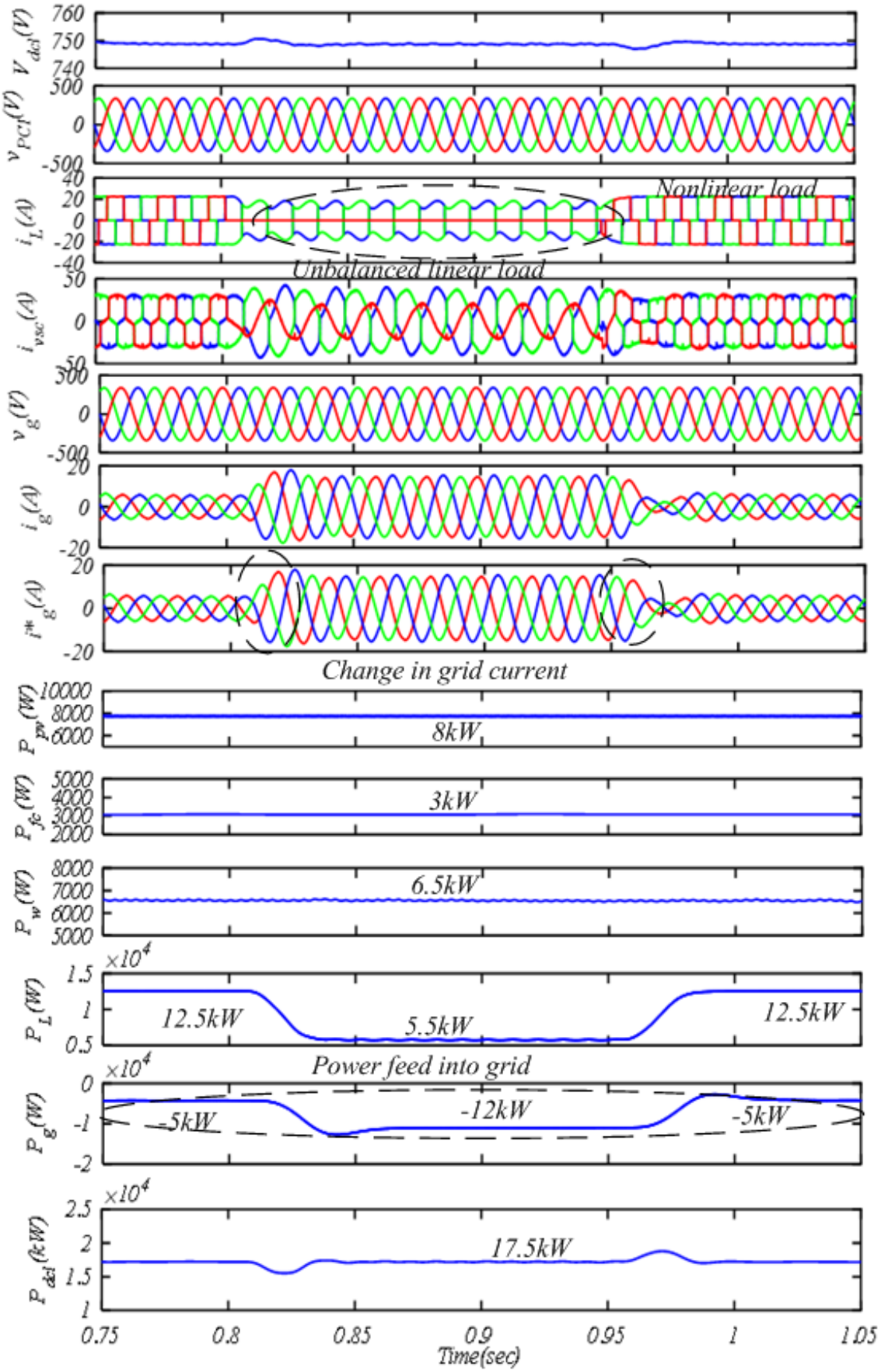

Figure 3.17: MG response using SRFT for balanced and unbalanced nonlinear load

The developed system is capable of working when power generation form the RESs is zero. During no power generation of RESs, system goes to work under DSTATCOM mode. To verify the DSTATCOM operation system is considered working under constant linear load. Initially, system is integrated with 20kW load at unity power factor and works under rated power generation. At t=0.45s the FC generation goes to zero, it is noticed from Fig. 3.18 that power available at the DC-link is reduced to 14.5kW and after 5 cycles it becomes steady. Grid power increased correspondingly to maintain power balance since load demand is constant. Further at t=0.6s, another RES i.e. WPGS power goes to zero due to very low wind speed. It is observed that the power available at the DC-link is reduced to 8kW and after 5 cycles it becomes steady. Grid power increases correspondingly to maintain power balance since load demand is constant. Further, at t=0.75s PV power generation becomes zero due to low irradiation and the grid starts to fulfill all the active power demand of the load. At this point no active power generation is available and the system starts performing in DSTATCOM mode. In this mode, the complete active load demand of 20kW is supplied through the grid and power balance is maintained even when no RESs generated power is available.

It is noticed that the grid currents are balanced and sinusoidal during the entire operation. Grid currents are following the generated reference currents accurately. Further, balanced, sinusoidal and constant amplitude voltage is available at consumer end (at PCI). A unity power factor operation is obtained. DC-link voltage is maintained constant after short transients.

The internal signals of VSC control algorithm are shown in Fig. 3.19. The intermediate signals are taken for nonlinear load operation. THD content of phase 'a', phase 'a' grid current phase 'a' load current (i_{La}) (i_{ga}) and grid voltage (v_{ga}) are shown in Fig. 3.20 respectively. THD is computed under nonlinear load performance. It is noted that THD of grid voltage (v_{ga}) is 1.21%, grid current (i_{ga}) THD is 2.21% which is under 5% even under highly distorted load current with 34.91% THD.

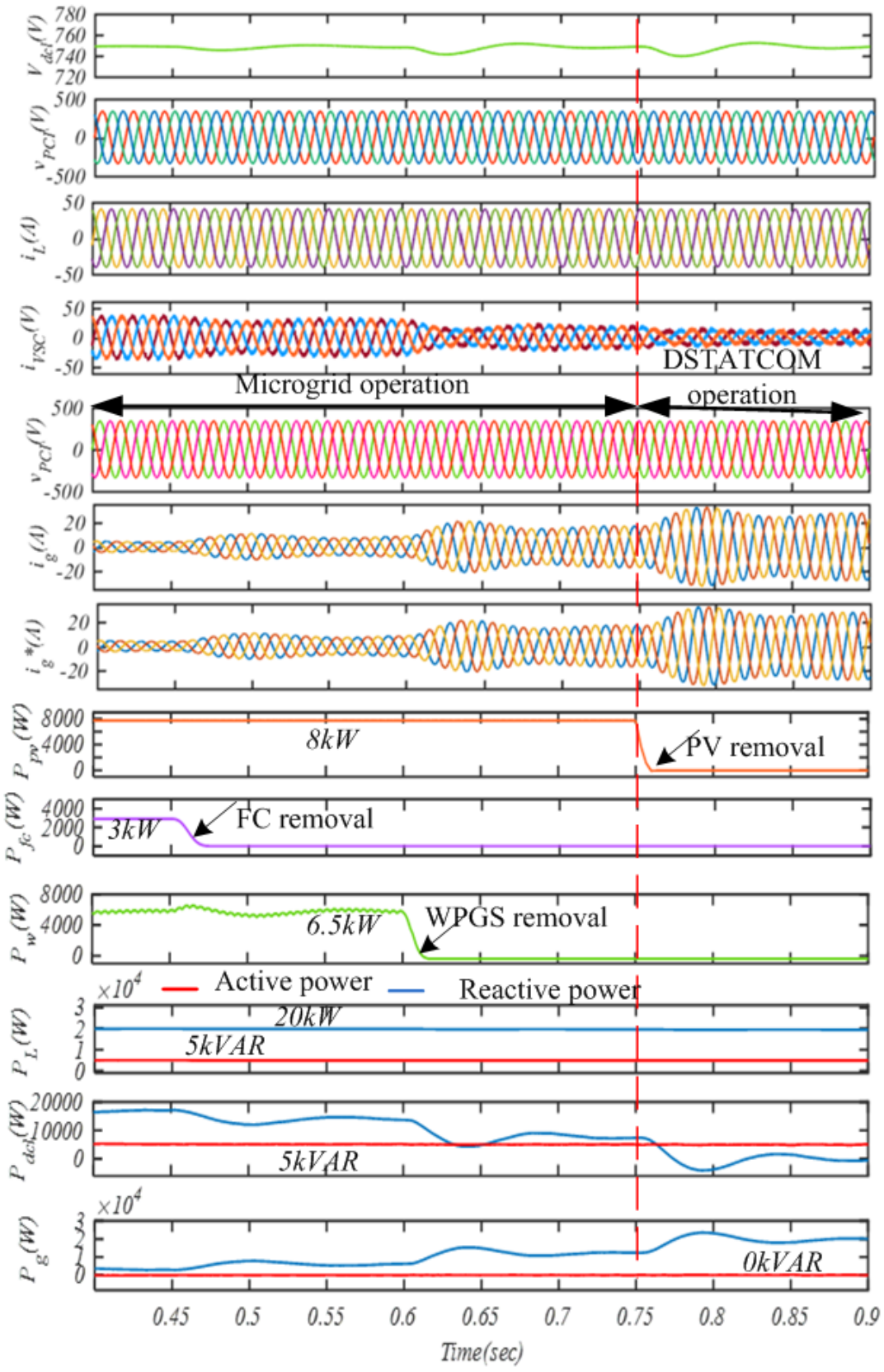

Figure 3.18: MG response under no RESs generation

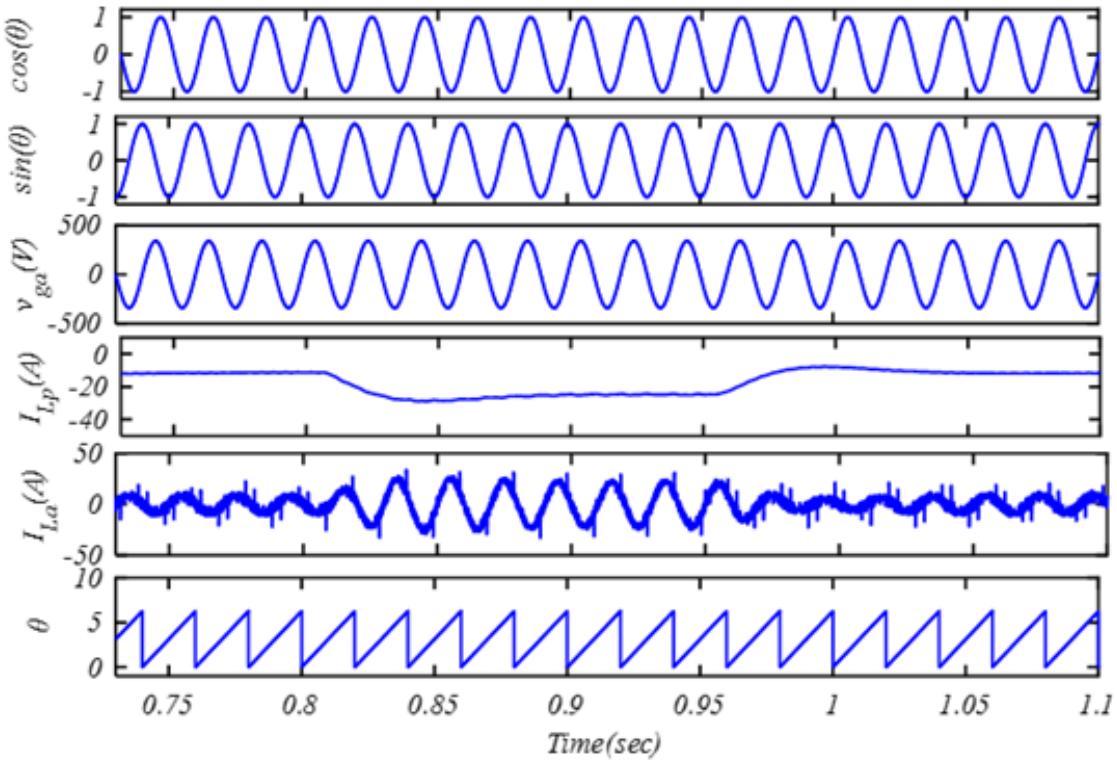

Figure 3.19: Intermediate results using SRFT control technique

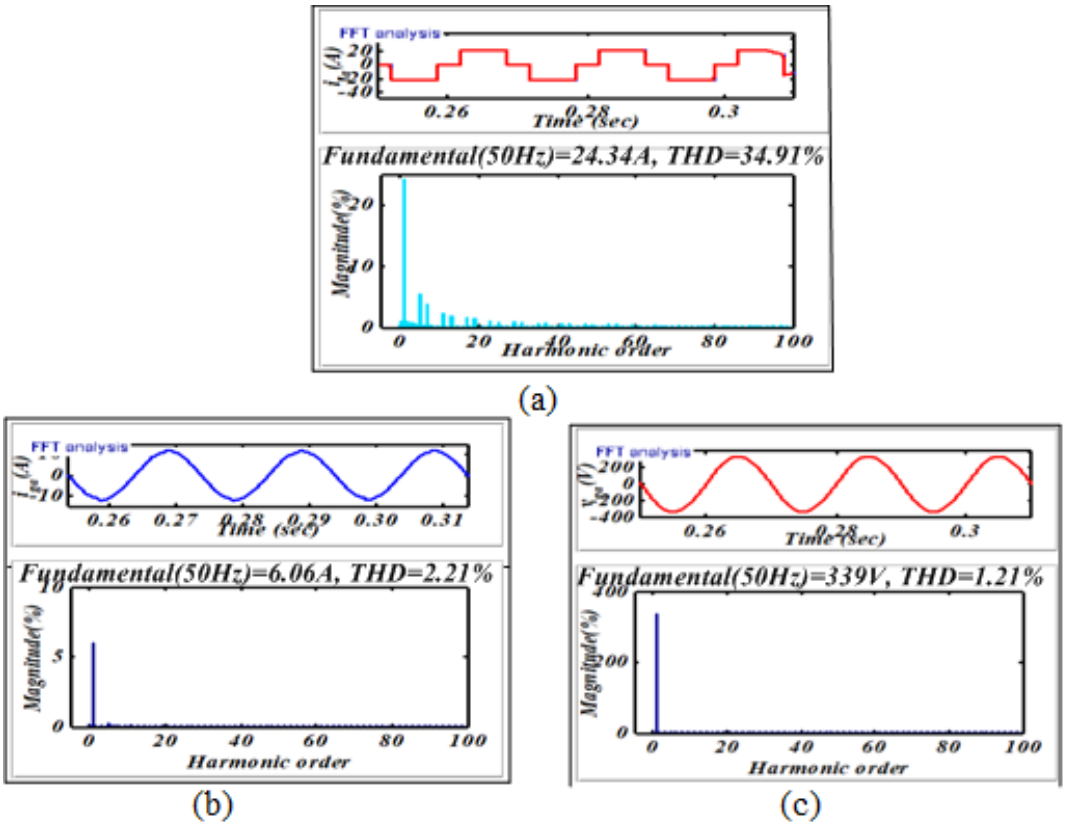

Figure 3.20: Harmonic spectra using SRFT control technique for the nonlinear load (a) waveform of i_{La} and its THD (b) waveform of v_{ga} and its THD (c) waveform of i_{ga} and its THD

3.7.2 System Response using PBT

Figs. 3.21 to 3.22 show the simulation results of microgrid system performance using PBT control technique. To observe system response a nonlinear load (diode bridge rectifier 25Ω resistance and 100mH inductance) is integrated into the system. Load unbalancing is introduced from t=0.8s to 0.95s by removing phase 'c' of the load. Hence the phase 'c' load current becomes zero. Fig. 3.21 shows that the grid currents are sinusoidal and balanced even under highly distorted nonlinear load. DC-link voltage is maintained at constant value 750V and PCI voltage is regulated. Fig. 3.21 shows the power allocation during the transients and exhibits that the power equilibrium is maintained throughout the system performance. It is assumed that rated capacities of PV power (P_{PV}) is 8kW, wind power (P_W) is 6.5kW, fuel cell power is (P_{fc}) is 3kW. Hence total generated power is 17.5kW at its rated capacity. Load demand is 12.5kW so that the surplus power (5kW) is feeding into the grid. At t= 0.8s the load is further reduced to 5.5kW due to the removal of one phase. Hence power feeding into grid is increased to (P_g=12kW). To verify the DSTATCOM operation, the system is considered working under constant linear 20kW upf load. Initially, system is working under rated power generation. At t=0.45s the FC generation goes to zero, it is noticed from Fig. 3.22 that power available at the DC-link is reduced to 14.5kW and after 5 cycles it becomes steady. Grid power increased correspondingly to maintain power balance since load demand is constant. Further, at t=0.6s, another RES i.e. WPGS power goes to zero due to very low wind speed. It is observed that the Power available at the DC-link is reduced to 8kW and after 5 cycles it becomes steady. Grid power increases correspondingly to maintain power balance since load demand is constant. Further, at t=0.75s solar irradiation goes to zero results in no PV power generation and the grid starts to fulfill all the active power demand of the load. At this point, no active power generation is available and the system starts performing in DSTATCOM mode. Complete active load demand of 20kW is supplied by grid and power balance is maintained even under zero RESs generation. Balanced and sinusoidal grid currents, constant DC-link voltage and balanced, sinusoidal and constant amplitude PCI voltage are achieved during the entire operation.

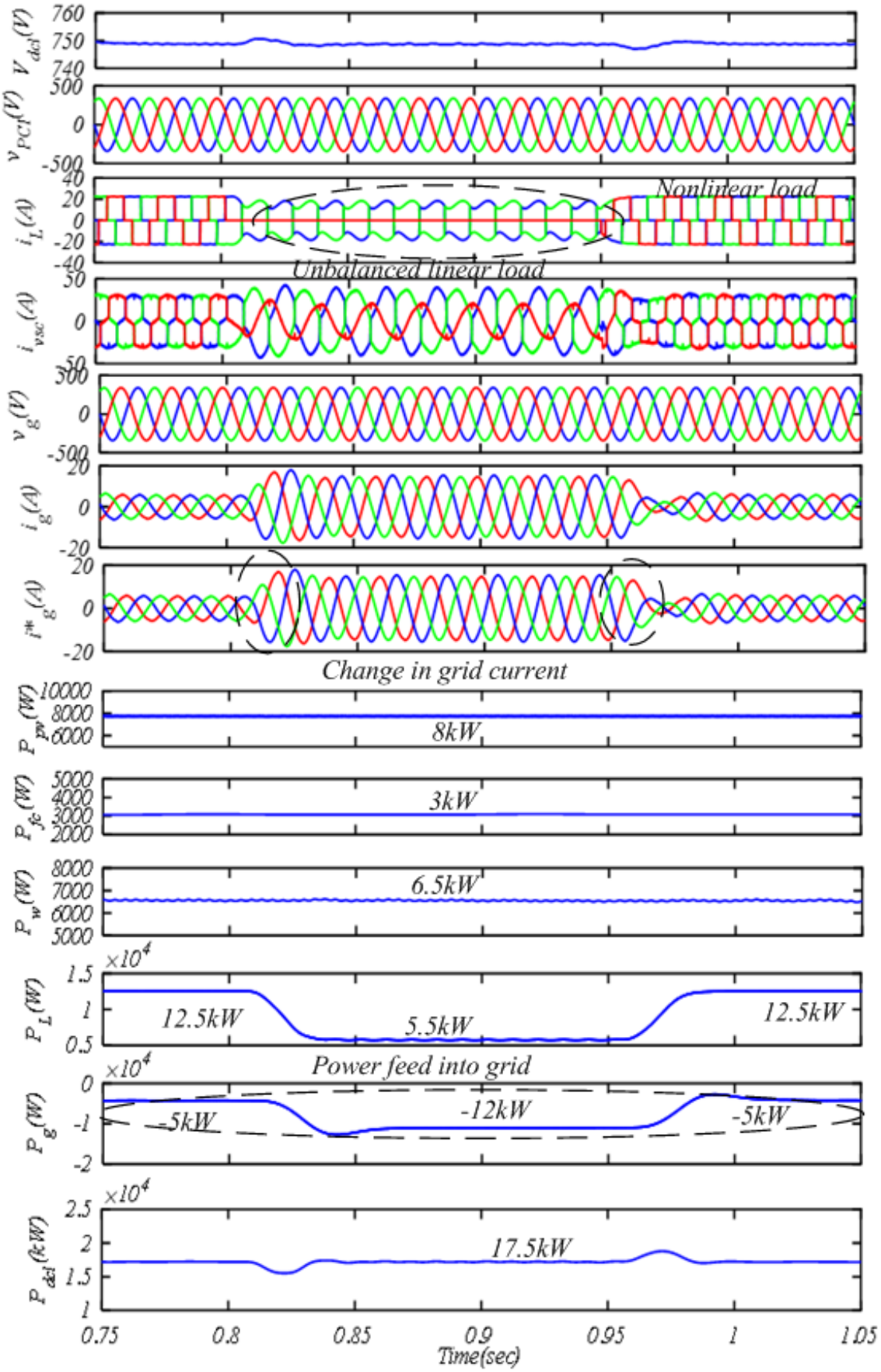

Figure 3.21: MG response using PBT for balanced linear and nonlinear load

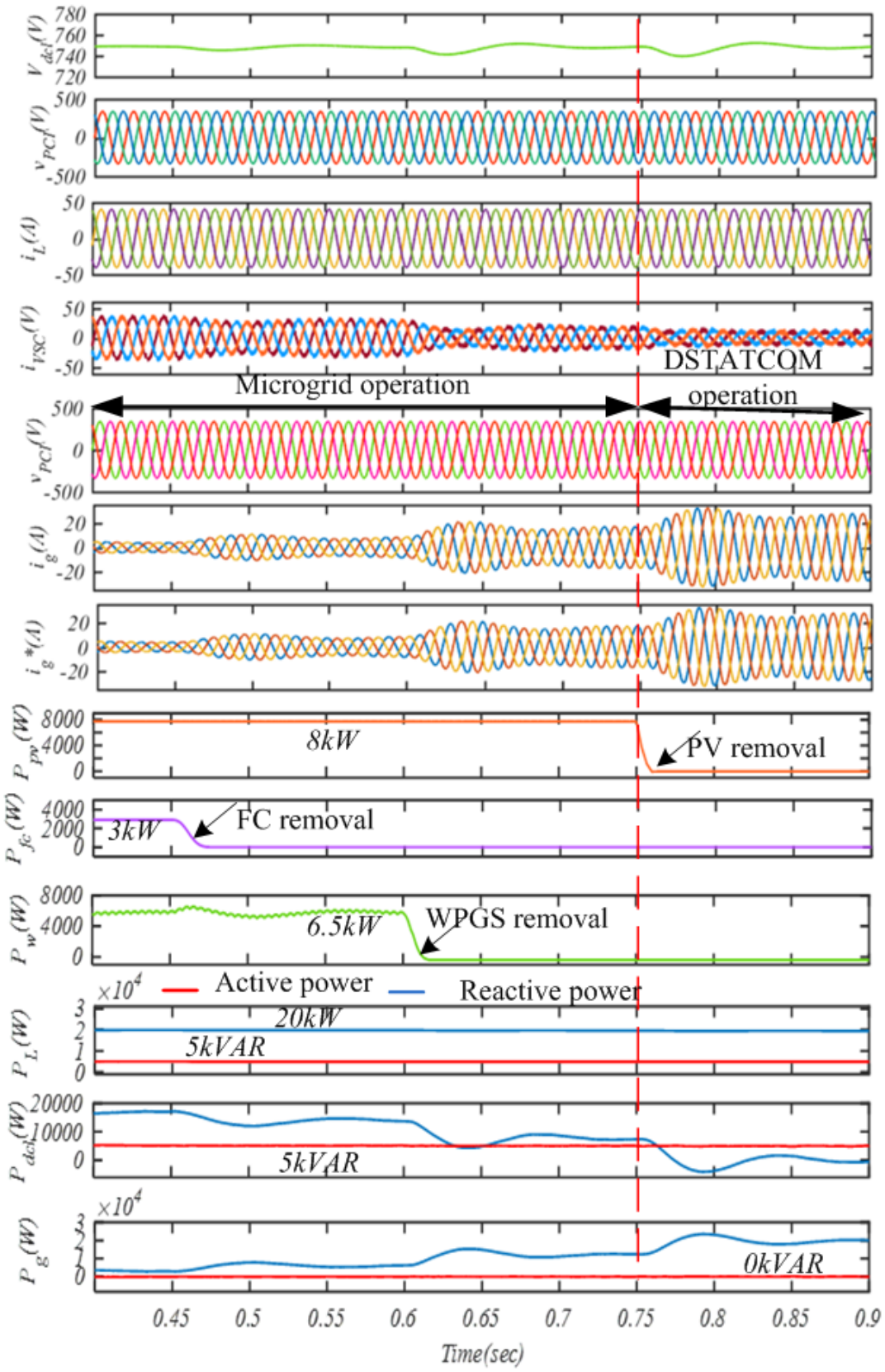

Figure 3.22: MG response under no RESs generation using PBT

Fig. 3.23 shows the internal signals of the VSC control algorithm. Figs. 3.24-3.25

shows the THD content of phase 'a' load current (i_{La}), phase 'a' grid voltage (v_{ga}) and phase 'a' grid current (i_{ga}) respectively. It is noted that THD of v_{ga} is 1.21%, grid current THD is 2.43%, which is under 5% even under highly nonlinear load, load current THD is 34.01%.

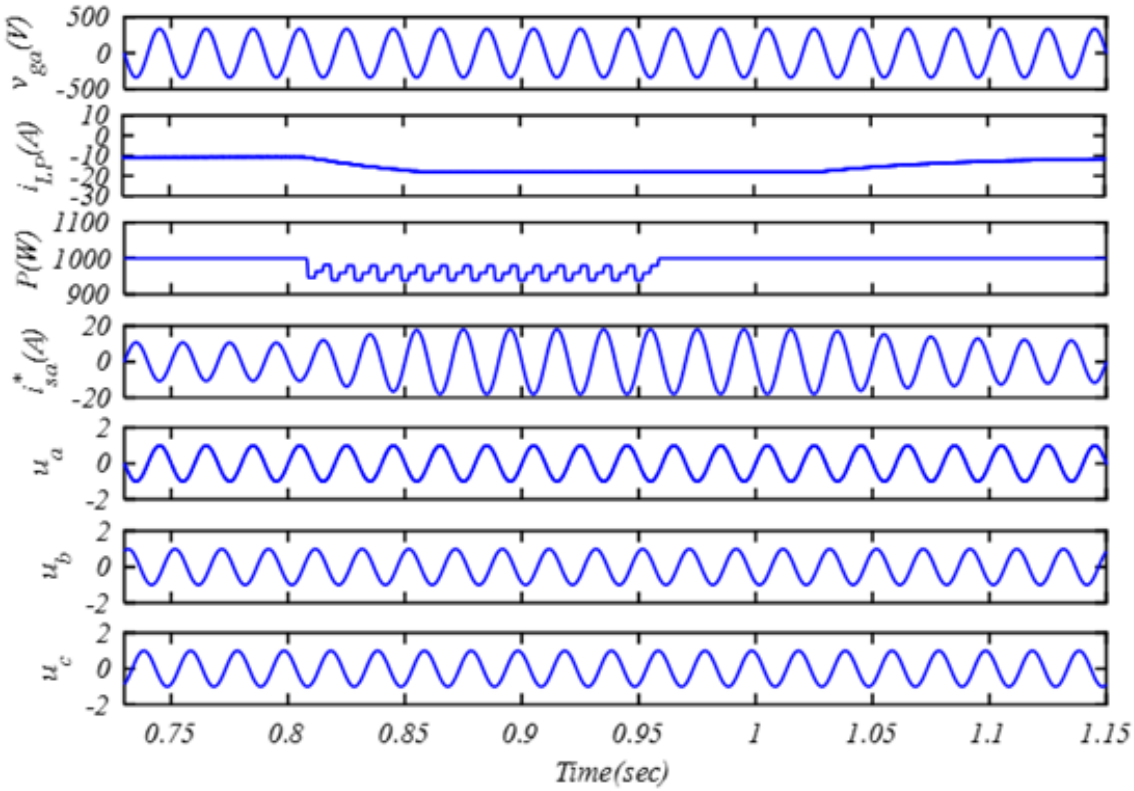

Figure 3.23: Intermediate results using PBT control technique

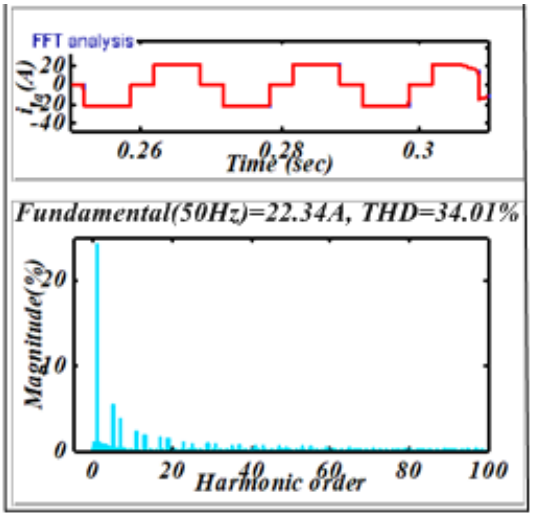

Figure 3.24: Harmonic spectra using PBT control technique for the nonlinear load waveform ($i_{La)}$ and its THD

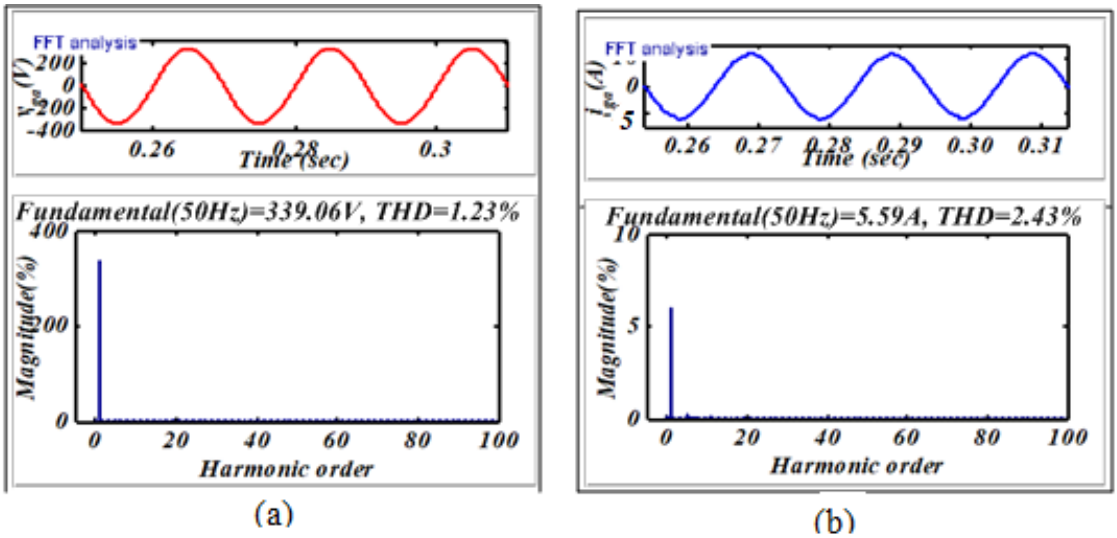

Figure 3.25: Harmonic spectra using PBT control technique for the nonlinear load (a) waveform of v_{ga} and its THD (b) waveform of i_{ga} and its THD

3.8 Comparative Evaluation of Conventional Control-Techniques

Table 3.2 shows the comparative analysis of conventional control techniques in the presence of a nonlinear balanced load. The nonlinear load current has high THD($\approx$ 34%) but the grid current THD is under prescribed limit defined by IEEE-519 standards for both SRF and PBT control. It has been observed that grid current THD is lesser (2.21%) for SRFT control technique, while PBT is less complex as compared to SRFT since it does not require PLL for grid synchronization which can be achieved through unit templates.

Table 3.2: Comparison of PBT and SRFT under non-linear load

Quantity	**SRFT**	**PBT**
THD (%) and Magnitude of Load Current(phase-a)	34.91%, 22.34A	34.01%, 22.34A
THD (%) Magnitude of Grid Current	2.21%, 6.06A	2.43;% 5.59A
THD and Magnitude of Voltage (phase-a)	1.21%; 339V	1.23%; 339.06V

3.9 Conclusions

In this chapter, the selection and design of components of energy sources and grid-connected microgrid are exhibited. The proposed microgrid is investigated for PQ improvement using conventional control techniques of VSC viz. SRFT and PBT. The microgrid is investigated and analyzed successfully for balanced and unbalanced non-linear load conditions. Further, microgrid operation is tested when there is no RESs power is available. During zero RESs power generation, the microgrid is shifted to DSTATCOM mode. The DC bus voltage (V_{dcl}) and PCI voltage (V_{PCI}) are maintained at the desired level for different conditions along with harmonic reduction and load balancing. Also, no reactive power needs to be supplied by the grid. Successful implementation of conventional techniques indicates that the system is suitable for using new control techniques to improve the system performance.

Chapter 4

DC-LINK VOLTAGE REGULATION FOR GRID CONNECTED MICROGRID

4.1 Introduction

In this chapter, DC-link voltage regulation control techniques for a grid-connected hybrid source microgrid system are discussed in detail. Unbalanced nonlinear load is considered for performance analysis. Four intelligent control techniques are developed for DC-link voltage regulation under varying load conditions.

The power system is a large, complicated network comprising of dynamic loads. Microgrid systems consist of the number of generation systems operating to meet the load demand. Due to any sudden change of load or change in generating power, the amount of power flow in the lines is changed. The change in power carried through the line generates oscillations. These oscillations must be damped quickly for reliable and efficient working of the system. Therefore, a controller which can maintain constant voltages during the system transients (occurs due to abrupt change of load demand or any sudden change in generation capacity) is necessary for effective operation and to achieve PQ standards within the prescribed limit. For controlling DC-link voltage, the PI controller is commonly used but it cannot successfully regulate DC-link voltage under different dynamic operating

conditions. Suitable intelligent controllers are designed to replace the conventional PID controller, as they provide a better transient response. These techniques are simulated in MATLAB/SIMULINK environment. A block diagram of the VSC control using the SRFT control technique is shown in Fig. 4.1.

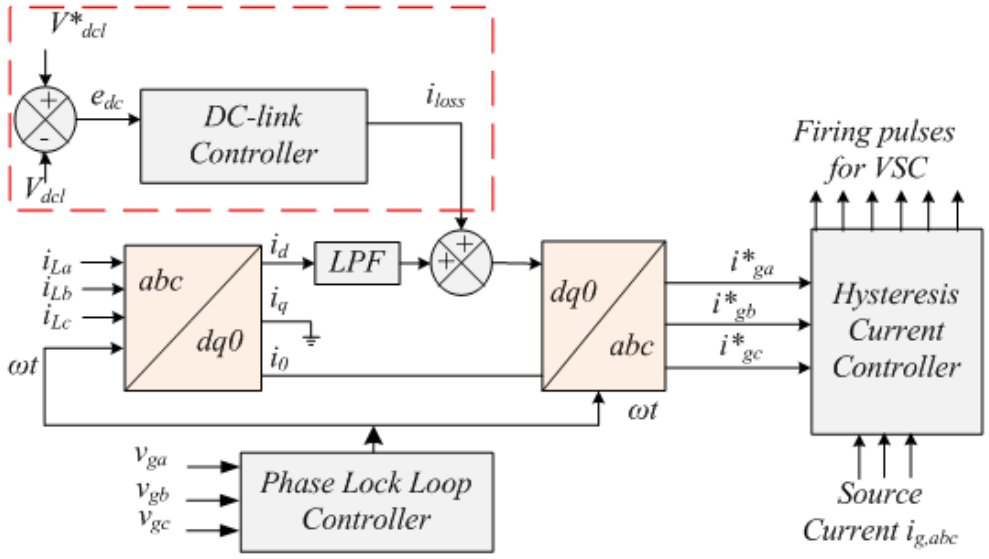

Figure 4.1: Block diagram of SRFT control including DC-link voltage control

4.2 Intelligent Control Algorithms for DC-Link Voltage Regulation

In this section Fuzzy logic controllers (FLC), Hybrid PI-Fuzzy logic controllers (H-FLC), Takagi-Sugeno Fuzzy Logic Controller (TSFLC) and ANFIS based controller are developed and implemented for DC-Link voltage regulation. The details of the developed control techniques are presented in this section.

4.2.1 Fuzzy Logic Controller

For variable operating conditions, complicated and nonlinear processes fuzzy control is a good choice over PID controller. Replacement of PI by FLC requires complete modification in the control. Instead, a simple and effective technique is to supervise the gains of the PI controller using fuzzy logic to improve response of the system is investigated. FLC has many advantages over the conventional PI controller such as FLC does not require an accurate mathematical model and can deal with inexact inputs. Further, these controllers are able to work under non-linearity

and are more robust than the PI controller. For unknown system models, the FLC is found to be very useful. It is based on simple linguistic rules obtained from experience of the system operator. FLCs are efficient with respect to large uncertainties, disturbances and transients in the process behavior [100].

Due to the presence of an integral term, the PI controller ensures zero steady-state error. But ripples are present in DC-link voltage. The scaling of fuzzy controller is designed to provide a required output value irrespective of the ripples, which occurs during the transients. Accuracy of the FLC depends upon the selection of right inputs and outputs and designing of rule base of the FLC is shown in Fig. 4.2. The block diagram of FLC to control the DC-Link voltage of microgrid system is shown in Fig. 4.3.

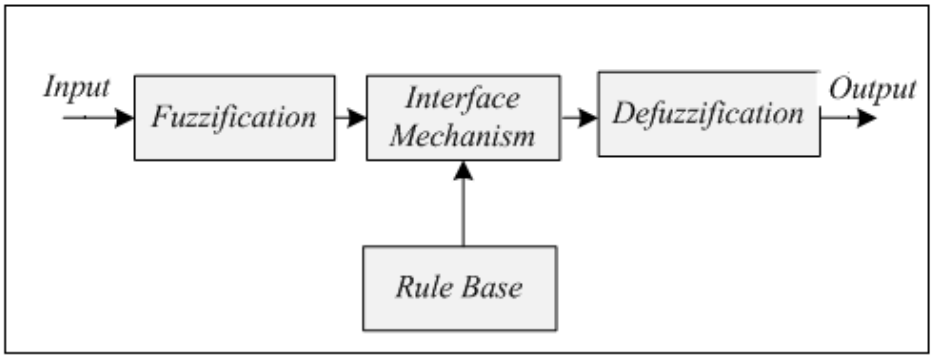

Figure 4.2: Fuzzy Logic control architecture

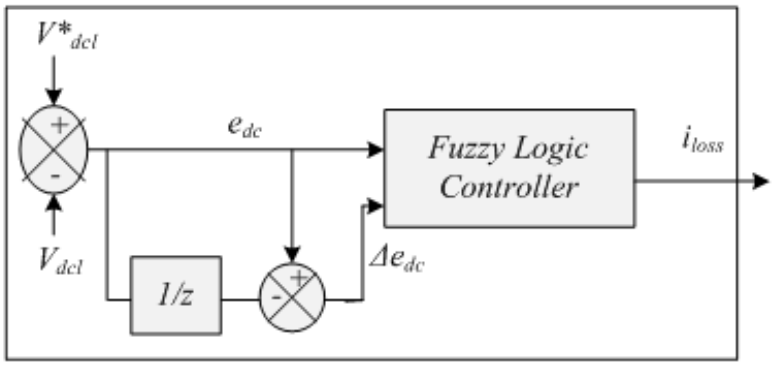

Figure 4.3: Fuzzy Logic-based control scheme for DC-link voltage regulation

4.2.1.1 Fuzzification

The fuzzification interface modifies the inputs to a form in which they can be used by the inference mechanism. It takes in the crisp input signals error/change in error and allocates a membership value to the membership-functions (MFs),

input signals lie within the allocated range. The FLC system has considered two normalized inputs, error (e_{dc}) and change of error ($\triangle e_{dc}$), which are given by equation (4.1) and equation (4.2) respectively.

$$e_{dc}(m) = (V^{*}_{dcl}(m) - V_{dcl}(m)) \tag{4.1}$$

$$\Delta e_{dc}(m) = V_{edc}(m) - V_{edc}(m-1) \tag{4.2}$$

where V_{dcl} and V_{dcl}^{*} are the DC terminal measured voltage across DC-link and reference voltage (750V) respectively. All membership functions for the fuzzy logic controller's input and output are dispersed in the [-1, 1] band and their shapes are symmetric triangles. These symitric-triangular MFs are overlapped and shown in Fig. 4.4.

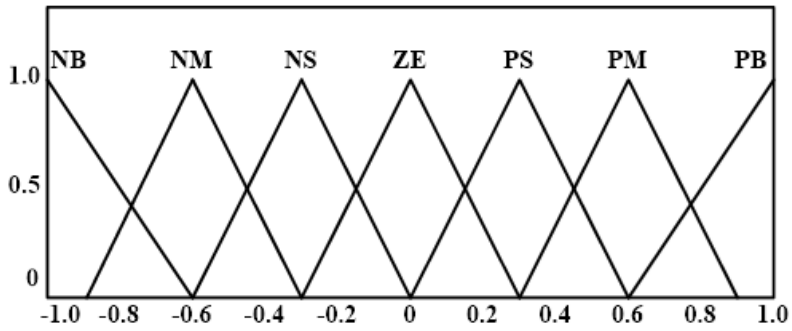

Figure 4.4: Input/output membership functions

4.2.1.2 Inference Mechanism

The two major attributes of the inference mechanism are given as: (a) To determine the appropriate rule applied for the current situation which is based on MFs, e_{dc} and $\triangle e_{dc}$ inputs. (b)After determination of the rule, the certainty of the control action is ascertained. Thus, in the end, there is a set of rules with particular certainty. The control action is then obtained on the database containing these rules.

4.2.1.3 Rule Base

Structuring the rule base is an imperative part of designing the regulator. It is significant how the standard rule base has been designed. Fig.4.5 shows the DC-link voltage waveform during transient without any controller. This waveform is split

into various parts which depend upon the sign of e_{dc} and $\triangle e_{dc}$. The rules of the rule base table are designed based on the parts of the waveform, which is under consideration. The control rules are based on the characteristics of the response, if the V_{dcl} is moving far away from the set-point, a large output current is required to pull it towards the set-point, whereas a small output current is required when V_{dcl} is close to the set point. The MFs are expressed as NB, NM, NS, ZE, PS, PM and PB which denotes for Negative Big, Negative Medium, Negative Small, Zero, Positive Small, Positive Medium, Positive Big respectively. Two dimensional rule base to calculate i_{loss} and the loss components are shown in Table 4.1.

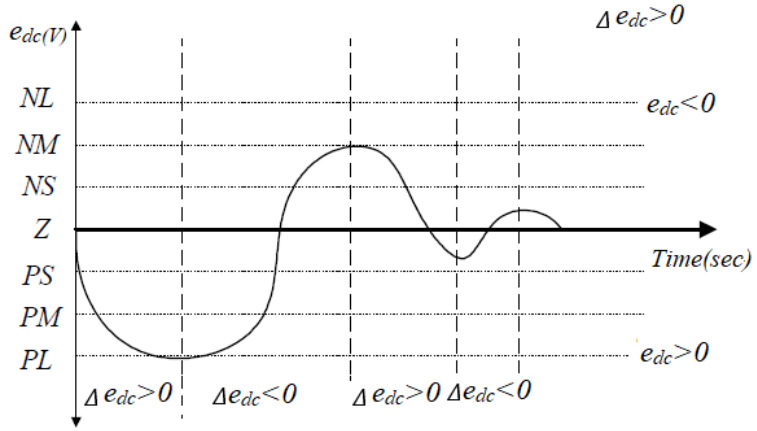

Figure 4.5: Typical DC-link voltage response during transients

Table 4.1: FLCs rule base for computation of i_{loss}

$\mathbf{e_{dc}}$ / $\mathbf{\triangle e_{dc}}$	**NB**	**NM**	**NS**	**ZE**	**PS**	**PM**	**PB**
NB	NB	NB	NM	NM	NS	NS	NS
NM	NM	NM	NS	NS	NS	ZE	ZE
NS	NM	NS	NS	NS	ZE	ZE	ZE
ZE	NS	NS	ZE	ZE	ZE	PS	PS
PS	ZE	ZE	PS	PS	PS	PM	PM
PM	ZE	ZE	PS	PS	PM	PM	PM
PB	PS	PS	PS	PM	PM	PB	PB

4.2.1.4 Defuzzification

The defuzzification combines the effect of obtained rules and their respective updated values to give crisp, numerical output. Obtained output of the fuzzy logic controller is i_{loss}. Output corresponds to differential error ($\triangle$ e_{dc}). The DC bus voltage is given by equation (4.3):

$$i_{loss} = \frac{2}{3} * \frac{\Delta e_d}{V_{sm} * T_x} \tag{4.3}$$

$$\Delta e_d = e_d^* - e_d = \frac{1}{2} * C_{dc} * [(V_{dcl})^2 - (V_{dcl}^*)^2] \tag{4.4}$$

and V_{sm} is the peak voltage magnitude and T_x is given by equation (4.5):

$$T_x = \frac{1}{6} * T_s = \frac{1}{6} * \frac{1}{f_s} \tag{4.5}$$

Thus, the fuzzy control action is transformed into a non-fuzzy control action. The 'center of gravity' method is commonly employed for this purpose. Advantage of this method is that the resultant output is sensitive for all active fuzzy outputs of the inference mechanism. In the process of designing FLCs, once the MFs and rule bases are constructed, the scaling factors are tuned. The scaling factors required for normalization of inputs and de-normalization of output play an important role in controller stability and performance as in a conventional controller, as they are the source of possible instability, oscillations and decayed damping effects. The relationship between the scaling factors K_e, $K_{\triangle e}$ and K_{iloss} and the input output variables of the FLC is given by equation (4.6):

$$e_N = K_e * e; \triangle e_N = K_{\triangle e} * \triangle e; i_{loss} = K_{i_{loss}} * i_{loss} \tag{4.6}$$

The expert knowledge of the system controller gives the idea to select suitable values of scaling factors and also can be found through trial and error.

4.2.2 Hybrid PI-Fuzzy Logic (H-FLC) Controller

Under steady-state conditions, a conventional the PI controller gives better performance as compared to FLC. The advantages of both FLC and PI controller can be obtained by implementing a Hybrid Fuzzy-PI controller in a combination of series/parallel connection. The fuzzy regulator is actuated uniquely during the

transient period and once the estimation of the DC-link voltage settles down, the controller gains are kept steady at the steady-state value. In this configuration, a hybrid model of FLC and PI is developed in which the outputs of FLC and PI controller are added to produce the DC loss component of current (i_{loss}). The schematic block diagram of the H-FLC for the microgrid system is shown in Fig. 4.6. The error (e_{dc}) and change in error ($\triangle$ e_{dc}) are the two normalized inputs used

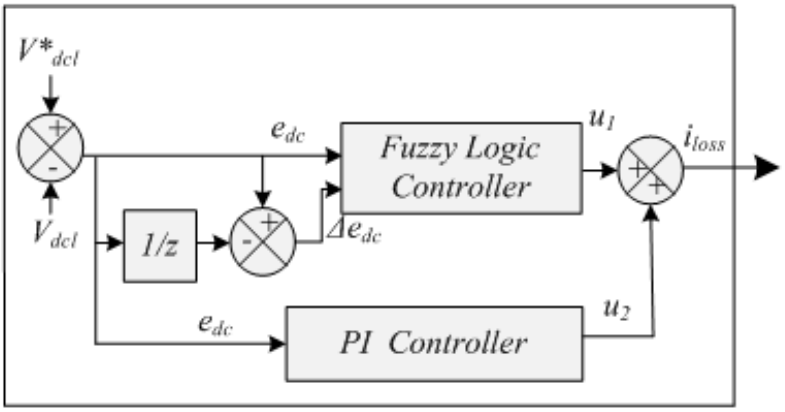

Figure 4.6: Schematic diagram of DC-link regulation using H-FLC controller

to produce FLC output, while the input to PI controller is error to achieve the output. Both the outputs are added to estimate the loss component of currents (i_{loss}) to control the DC-link voltage. Controlling of rule base and the membership function design remain the same as explained in previous section.

4.2.3 Takagi Sugeno-Fuzzy Logic Controller (TSFLC)

The commonly used FLC is based on Mamdani's fuzzy inference method [105]. In this section, the Takagi-Sugeno method of fuzzy inference is presented. Both methods have similar parts i.e. fuzzifying the inputs and application of the fuzzy operator. In the control algorithm, the actual DC side capacitor voltage (V_{dcl}) is sensed and then the same is compared with the set reference (V^*_{dcl}). The error signal (e_{dc}) and change of error signal ($\triangle e_{dc}$) are used as two inputs for the fuzzy logic controller. The schematic block diagram of the TSFLC is given in Fig. 4.7 Let $Y_1(m)$ and $Y_2(m)$ represents the error and change in error. Therefore,

$$Y_1(m) = V^*_{dcl} - V_{dcl} = e_{dc}(m) \tag{4.7}$$

$$Y_2(m) = \int_0^t (V^*_{dcl} - V_{dcl}) = \Delta e_{dc}(m) \tag{4.8}$$

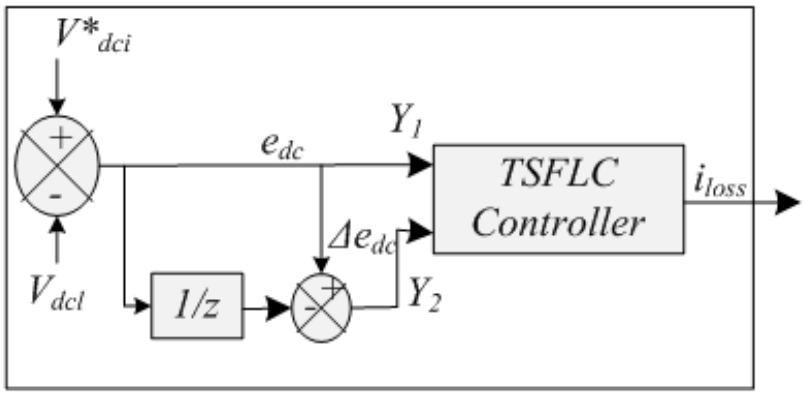

Figure 4.7: Schematic diagram of DC-link regulation using TSFLC scheme

Error is fuzzified using two input fuzzy sets positive (P) and negative (N). Positive set membership function (μ_{p}(Yi) is given by equation (4.9) and negative set membership function (μ_{n}(Yi) is given by equation (4.10).

$$\mu_p(Y_i) = \begin{cases} 0 & Y_i < -\beta_i \\ \frac{Y_i+\beta_i}{2\beta_i} & -\beta_i \leq Y_i \leq \beta_i \;\; For\ i = 1,2 \\ 1 & \beta_i \end{cases} \tag{4.9}$$

$$\mu_N(Y_i) = \begin{cases} 0 & Y_i < \beta_i \\ \frac{Y_i-\beta_i}{2\beta_i} & -\beta_i \leq Y_i \leq \beta_i \;\; For\ i = 1,2 \\ 1 & \beta_i < Y_i \end{cases} \tag{4.10}$$

Here β_1 and β_2 are maxima of the e_{dc} and $\triangle e_{dc}$. The relation of membership functions e_{dc} (m),$\triangle e_{dc}$(m) and β_1, β_2 are given in Fig. 4.8 respectively. TS method uses four rules which is the major advantage over the Mamdani fuzzy interface method. The four rules framed for the system are listed below:

Rule 1: If e_{dc}(m) is "Positive", and‘ $\triangle e_{dc}$(m) is "Positive" then u_1(m)=$B_1 e_{dc}$(m) +$B_2 \triangle e_{dc}$(m).

Rule 2: If e_{dc}(m) is "Positive" and $\triangle$ e_{dc}(m) is “Negative” then u_2(m)=$B_2 u_1$(m).

Rule3: If e_{dc}(m) is "Negative" and $\triangle$ e_{dc}(m) is “Positive” then u_3(m)=$B_3 u_1$(m).

Rule 4: If e_{dc}(m) is "Negative" and $\triangle e_{dc}$(m) is “Negative” then u_4(m)=$B_4 u_1$(m).

The output of TS fuzzy controller can be represented by equation (4.13) [173]:

$$u(m) = \frac{\sum_{t=1}^{4}((\varepsilon_j)^{\gamma} u_j(m))}{\sum_{t=1}^{4}(\varepsilon_j)^{\gamma}} \tag{4.11}$$

Above equation can be simplified for γ =1 as:

$$u(m) = ae_{dc}(m) + b\triangle e_{dc}(m) \tag{4.12}$$

$$a = B_1 M;\ b = B_2 M; M = \frac{\varepsilon_1 + \varepsilon_2 B_2 + \varepsilon_3 B_3 + \varepsilon_4 B_4}{\varepsilon_1 + \varepsilon_2 + \varepsilon_3 + \varepsilon_4} \tag{4.13}$$

here M is control gain and dependent on the operational conditions. The effective value of control gains fluctuates in a wide range during the control procedure. The values of B_2, B_3, B_4, a, b selected in this work are 1.1, 0.35, -0.5, 1.8, -0.08 respectively. The output obtained from the fuzzy controller represents the loss component.

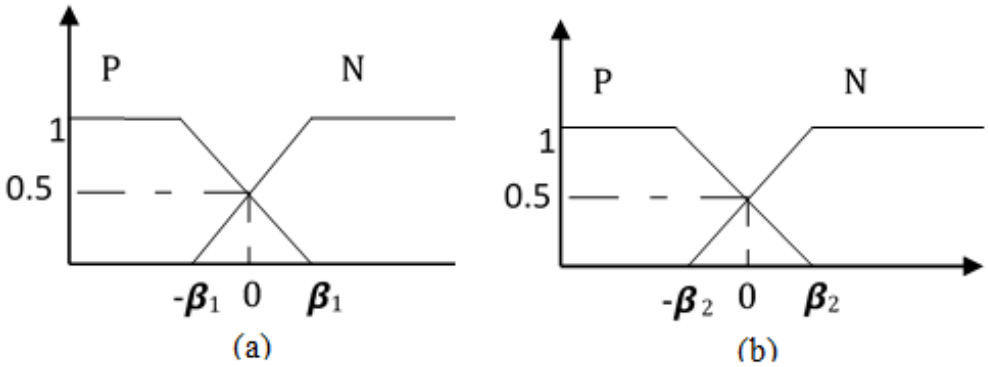

Figure 4.8: Membership function (a) e_{dc}(m) (b) $\triangle e_{dc}$(m)

4.2.4 Adaptive Neuro-Fuzzy Inference System

The adaptive neuro-fuzzy inference system (ANFIS) is a hybrid intelligent controller implemented for DC-link voltage regulation in this work. The simplified block diagram of ANFIS controller-based generation of reference currents signal with SRF theory is shown in Fig. 4.9. Since ANFIS [102] integrates neural networks (learning and parallel data processing abilities) and fuzzy logic (reasoning abilities), it offers the advantage of both in a single model.

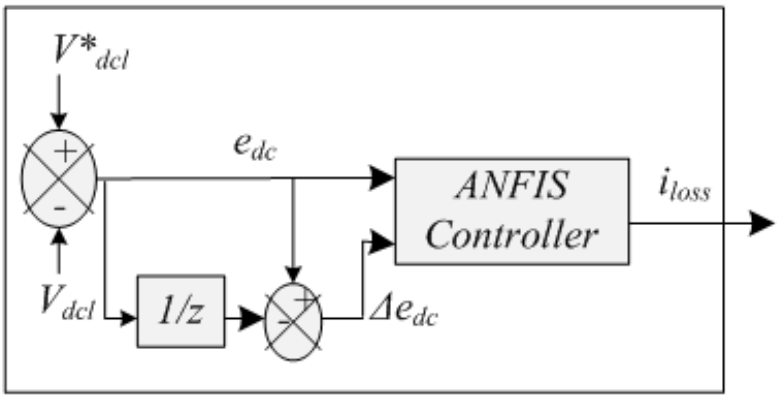

Figure 4.9: Schematic Diagram for DC-link regulation using ANFIS controller

Typical architecture of the five-layer feed-forward network ANFIS is shown in Fig. 4.10 in which circular nodes symbolize the fixed node and square symbolizes variable nod with adaptive abilities. It represents the multi-layered feed-forward network where each layer performs a particular function on the input signal. Designed ANFIS has dual inputs (e_{dc}, $\triangle e_{dc}$), dual membership functions (MFs) and single-output (z). The organization of the ANFIS in the five-layer and function of each layer is specified.

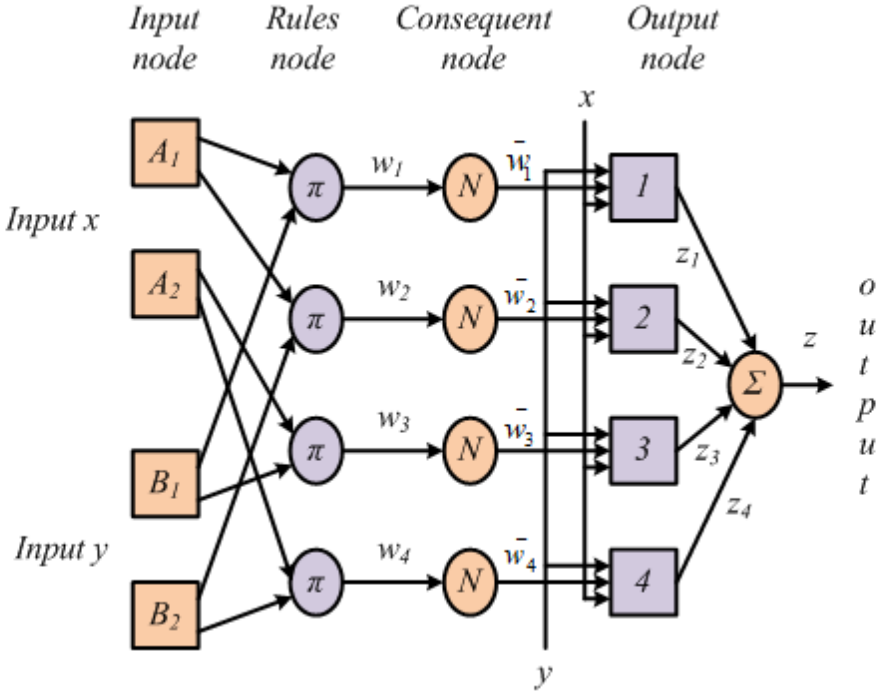

Figure 4.10: Five-layer ANFIS feed-forward network [1]

In the first layer, each node (A_1, A_2, B_3, B_4) comprises of membership function allotted to each input (e_{dc} and $\triangle e_{dc}$), this layer is an adaptive node. The values of parameters of this layer change according to the error signal and generate the proper

value of each membership function. Every node in this layer is characterized by its corresponding output function and store the parameters to express a Bell-shaped membership function that represents the profile of linguistic variables (e_{dc} and$\triangle e_{dc}$). Layer 2 is also known as rule nodes. In this layer, the system recognizes the rules, this is a rule storage level. Each rule is represented by one node. In this layer, the outputs of the first layer have been multiplied with each other to determine the degree of fulfillment of the rule and forwarded it to the next layer.
Layer 3 is the average node layer. This level calculates the regularized firing power of each rule and a unit computes a relative degree of fulfillment for every rule.
Layer 4 computes the consequent of the rule. The junction point of this level is linked to all feed in junction points and with precisely single junction point in the third layer. Each junction in this layer computes the output for the rule.
Finally, layer 5 is the summation layer. This layer performs the computation of overall output is obtained by summing all incoming signals. The de-fuzzification process converts each fuzzy result into crisp output in layer 5, it is commonly known as output nodes. The feed-out junction point estimates the ultimate output from the addition of all feed in signals coming from level 4.

4.2.5 Design of ANFIS for Voltage Regulation

ANFIS controller is designed to maintain a constant DC-link voltage at the input of grid-connected VSC. Neural network optimization has been used to generate a rule base for fuzzy logic control (FLC system). The MATLAB neuro-fuzzy toolbox has been used to control the FLC. To train the neural network, first input-output data pairs have been collected and fed as an array to the toolbox, this data has been used to generate FIS file using grid partitioning method. The generated FIS file has two inputs and one output and has been fed to FLC. The rule base is Sugeno based and five Gaussian Bell MFs have been used for both input and output as shown in Fig. 4.11. Both input and output MFs have the same G_ Bell-shape MFs to conduct system training and this type of function gives higher accuracy.

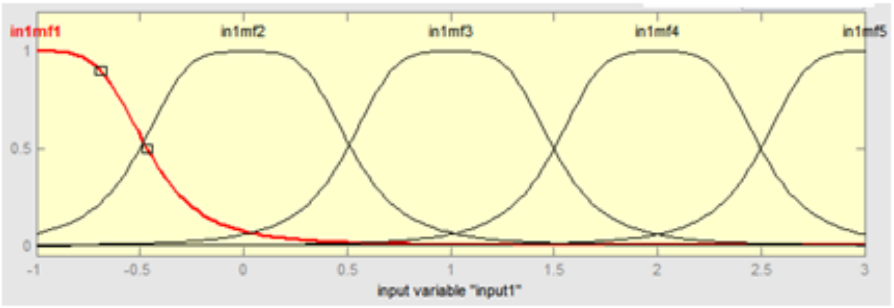

Figure 4.11: Plot of membership functions plot

The trained ANFIS holds five input MFs and 25 rule base. The linguistic variable of error (e_{dc}) signal from input variables of ANFIS is represented by In1mf1, In1mf2, In1mf3, In1mf4 and In1mf5. The linguistic variable of change in error ($\triangle$ e_{dc}) signal from output variables of ANFIS is represented by In2mf1, In2mf2, In2mf3, In2mf4 and In2mf5. The output of Sugeno type ANFIS contains a real number hence the output cannot be represented like the input MFs. The ANFIS output signal is made up of 25 real numbers ranged -3.515 to 0.9328. The rule base is tabulated in Table 4.2. MF parameters must be tuned by the training data. To update the weights of epoch adaptive error back-propagation has been used. Training set (70%) and validation set (30%) are two sets and this includes the testing data set (15%) which is used to avoid over-fitting problems. Now the final error is obtained by the root-mean-square (RMS) comparison between the current and desired outputs.

Table 4.2: Rule Base using ANFIS toolbox

$\mathbf{e_{dc}}$ $\mathbf{\triangle e_{dc}}$	**in1mf1**	**in1mf2**	**in1mf3**	**in1mf4**	**in1mf5**
in2mf1	-1.221	-1.022	-1.028	-0.8012	-0.1528
in2mf2	1.189	0.0297	1.319	-0.02458	0.01552
in2mf3	-3.515	0.641	0.9328	0.03428	0.006819
in2mf4	-0.4305	0.4893	0.06705	0.004406	0.02793
in2mf5	-0.07154	0.4702	0.03378	0.02392	0.4676

Flowchart of ANFIS training in MATLAB is shown in Fig.4.12.

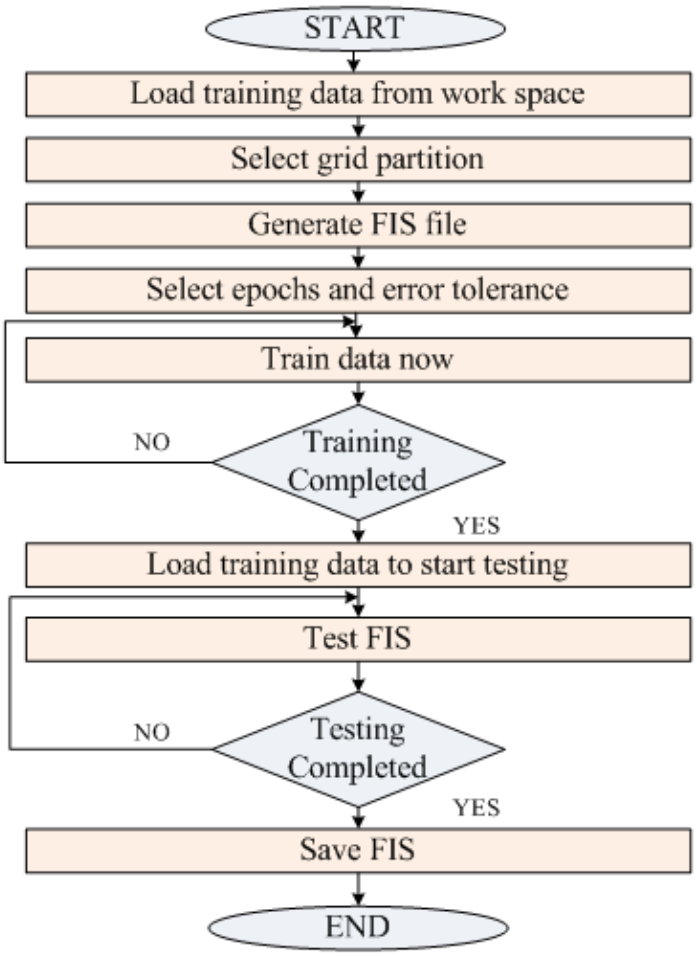

Figure 4.12: Flowchart of ANFIS training in MATLAB

4.3 Results and Analysis for DC-link Voltage Control Techniques

This section presents the result for DC-link voltage variation during transients under MATLAB/SIMULINK environment. The DC-link voltage response for different control schemes is compiled in a single plot and performance under dynamic conditions is shown in Figs. 4.13-4.15. The results are shown for the regulation of DC-link voltage under transients which are introduced by removing and including one phase (phase 'a') of the nonlinear load at t=0.3s and t=0.6s respectively. Results exhibit that the constant DC-link voltage is achieved. Under varying load conditions DC-link voltage is maintained at 750V under all implemented control techniques.

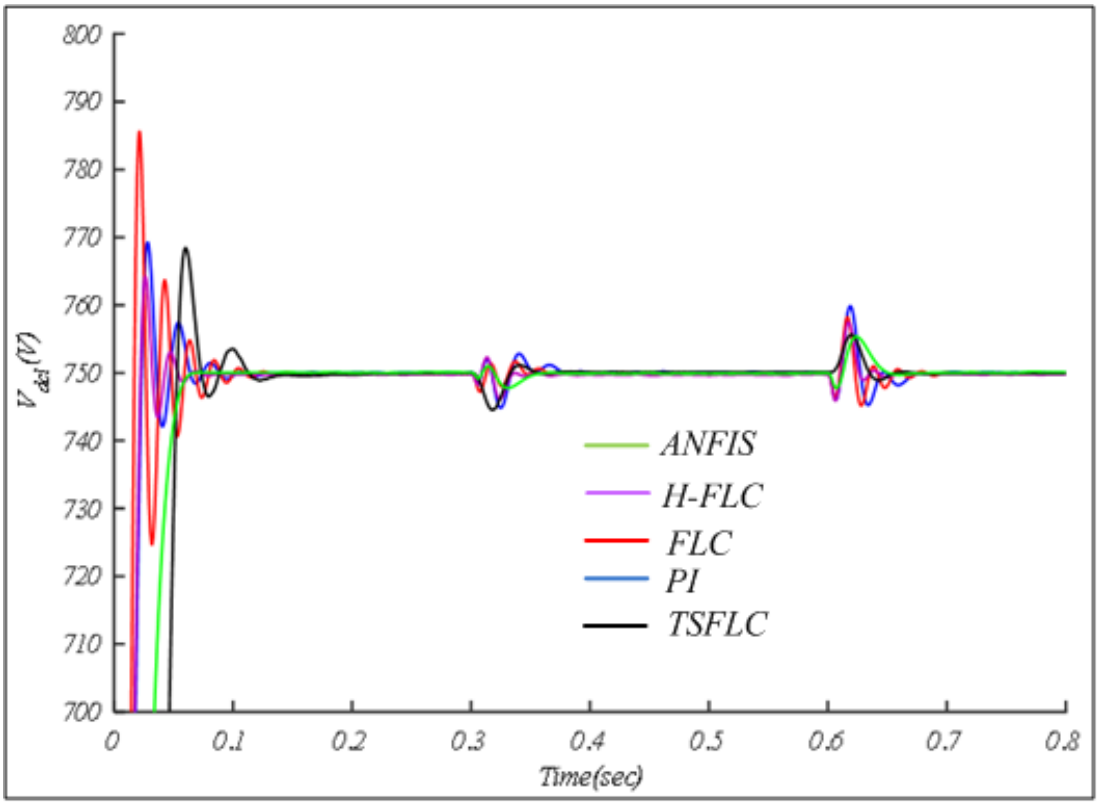

Figure 4.13: DC-link voltage response

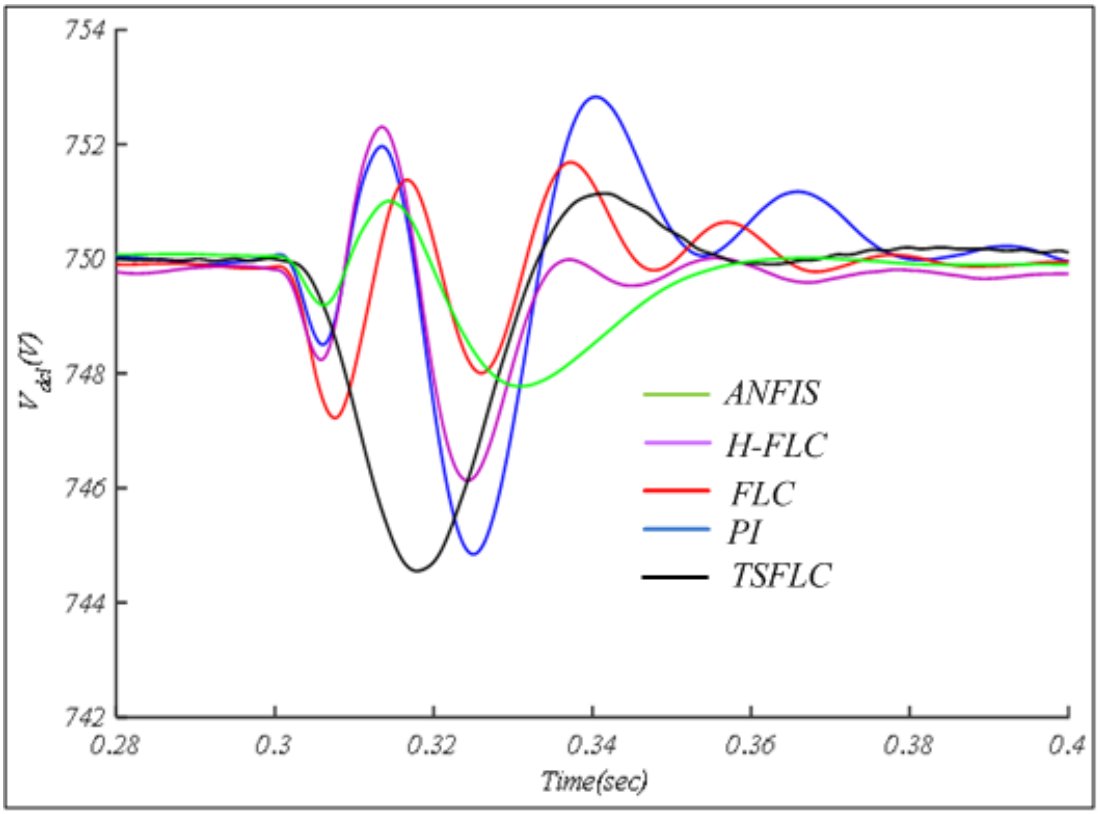

Figure 4.14: DC-link voltage response after removal of phase 'a' for nonlinear load at t=0.3s

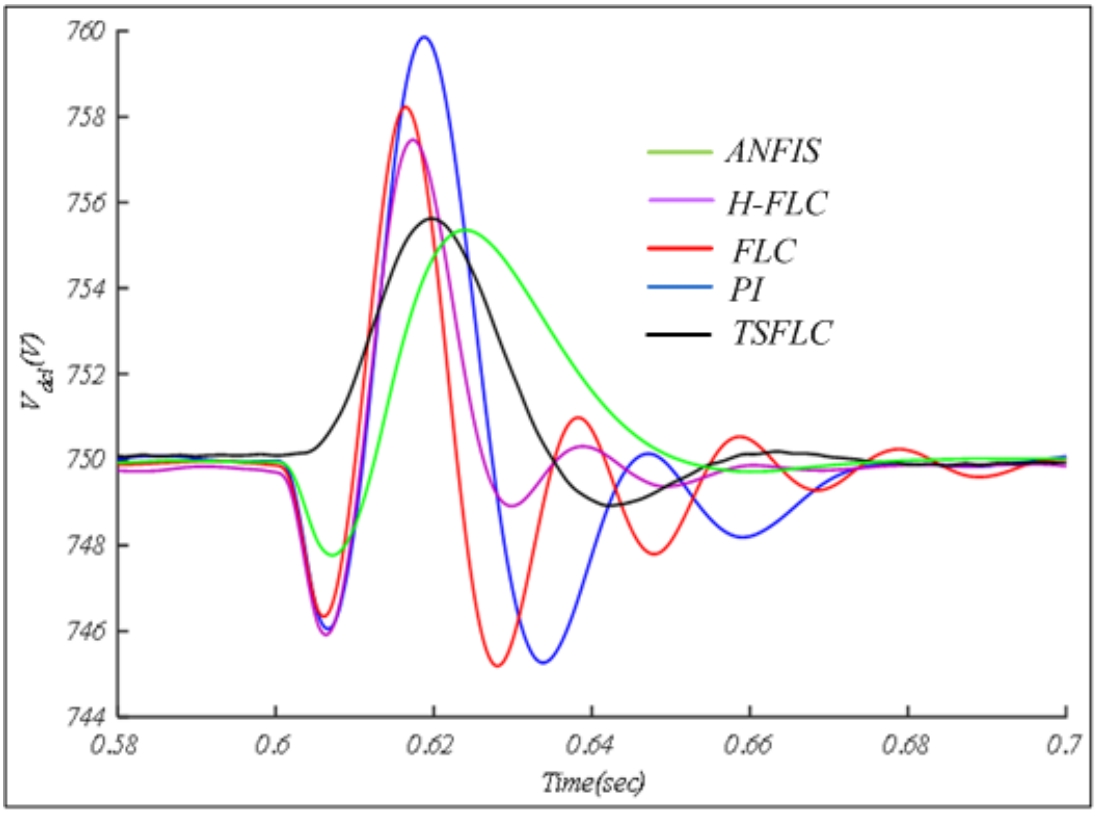

Figure 4.15: DC-link voltage response after inclusion of phase 'a' for nonlinear load at t=0.6s

4.4 Comparative Evaluation of DC-Link Voltage Control Techniques

The comparison of the performance of PI, FLC, ANFIS, TSFLC and H-FLC control techniques have been tabulated in Table 4.3 for various parameters like undershoot, overshoot and settling time. DC-link is effectively regulated under the unbalanced nonlinear load. At t=0.3s one phase of the nonlinear load is removed. For the removal of phase, ANFIS exhibits 2V undershoot while overshoot of 1V is noticed and settling time is found to be 0.06s. For the same transient, the PI controller shows 3V overshoot, undershoot of 5V and time taken to achieve the steady-state is 0.1s. The H-FLC exhibits undershoot of 4V, overshoots of 2.1V and settling time is 0.08s for the same transients. Further, FLC shows overshoot, undershoot and settling time to be 1.8V, 3V and 0.08s respectively. TSFLC observed 1V overshoot, 5V undershoot and 0.08s settling time after removal of phase. When the removed phase is reconnected, the overshoot, undershoot and settling time are

tabulated in Table 4.3 for PI, FLC, H-FLC, TSFLC and ANFIS controller. It has been observed from Table 4.3 that the DC-link voltage settles down fastest with ANFIS control technique. Moreover, ANFIS controller results in lowest overshoot and undershoots during transients.

Table 4.3: Comparison of DC-link control schemes

	PI	**FLC**	**H-FLC**	**TSFLC**	**ANFIS**
Overshoot(V) at t=0.3s	3	1.8	2.1	1	1
Overshoot(V) at t = 0.6s	10	8.2	7.8	5.8	5
Undershoot (V) at t = 0.3s	5	3	4	5	2
Undershoot(V) at t = 0.6s	5	5	5	1	2
Settling Time(sec) at t=0.3s	0.1	0.08	0.08	0.08	0.06
Settling Time(sec) at t=0.6s	1	0.08	0.08	0.08	0.07

4.5 Conclusions

The detailed design and development of intelligent DC-link voltage control techniques viz FLC, H-FLC, TSFLC and ANFIS for the microgrid system have been discussed. Different control schemes have shown promising results for regulation of DC-link voltage to its reference value. A fair comparison is performed on the basis of the obtained results. The performance of the algorithms under dynamic load changes (unbalancing of nonlinear load) has also been investigated. It has been observed that the response of ANFIS control technique is best out of all the techniques in terms of settling time, undershoot and overshoot during transients. DC-link voltage settles down quickly in less than one cycle during the inclusion and removal of one phase under nonlinear load. Conventional PI-controller takes the longest time in settling DC-link voltage to attain steady-state value, but it is less complex in real-time implementation. The performance of H-FLC and TSFLC controllers is approximately the same but the TSFLC is simpler to design as it needs only four rule bases. Finally, it can be concluded that the performance of ANFIS is slightly superior amongst all the DC-link voltage controllers under transient conditions.

Chapter 5

PQ ENHANCEMENT OF MICROGRID

5.1 Introduction

The integration of a microgrid with the utility power network has major concerns of maintaining desired PQ standards. Harmonics in the system, disturbances in DC-link voltage, PCI voltage, poor PF and unbalancing are some of the major power quality problems observed in the distribution system. A large number of nonlinear loads and power electronic devices connected in the power network causes poor quality of the power at the consumer end and inject harmonics into the grid. Fluctuations in DC-link voltage and PCI voltage primarily occurs due to change in load and environmental conditions. Presence of single-phase load results in unbalanced PCI voltage. To distribute the load equally in all three phases under all loading conditions is also a major challenge. Moreover, the connected load in the distribution system is generally resistive-inductive type. High inductive load results in poor power factor (PF) which causes lower active power transfer. These PQ problems must be mitigated to ensure the good performance of microgrid. Persistence of PQ problems over a long period may even damage the equipment. Shunt connected VSC is a feasible solution to accommodate the aforementioned PQ issues. Shunt interfaced VSC can be suitably controlled to provide PQ improvement for all types of load. It is also capable of providing reactive power compensation

locally. The suitable control algorithm of the VSC or power conditioning device may improve PQ problems.

Many advanced control techniques such as hyperbolic tangent least mean square (H-LMS), adaptive neuro-fuzzy inference system least mean square (ANFIS-LMS), zero attracting quaternion (ZAQ-LMS) and modified shrinkage widely linear complex valued least mean square (MSWL-CLMS) is developed in this chapter for the mitigation of PQ problems under transient conditions. The new controls are developed and their implementation in the microgrid system for PQ problem mitigation is discussed in this chapter. These techniques are simulated in MATLAB /SIMULINK environment. The configuration of the microgrid is shown in Fig. 5.1.

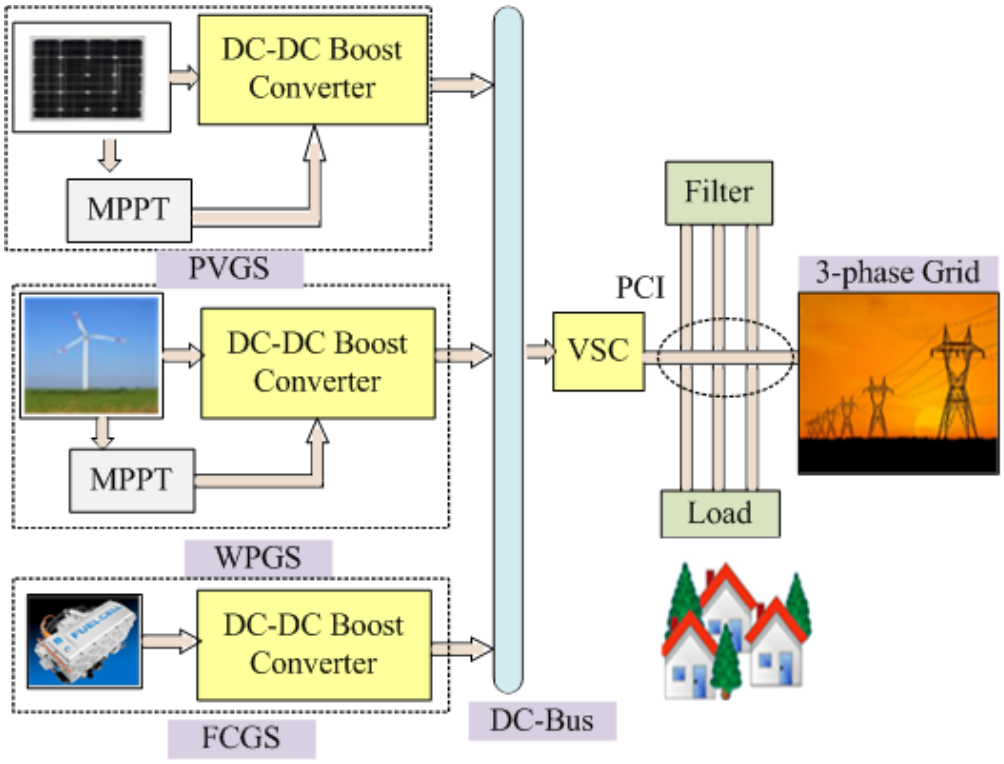

Figure 5.1: Block diagram of hybrid power source microgrid system

5.2 Developed Control Algorithms in Microgrid

In this Section H-LMS, ANFIS-LMS, ZAQ-LMS and MSWL-CLMS based control techniques are developed for the microgrid system. The extraction of fundamental active weight components of the load current(w_{avg}) using H-LMS, ANFIS-LMS, ZAQ-LMS and MSWL-CLMS are presented in the following subsections.

5.2.1 Hyperbolic Least Mean Square Control Algorithm

The H-LMS control technique is used to estimate the fundamental component of load current (weight $W_t(m)$) in order to reduce the error signal. This algorithm is based on an iterative computation of weight $W_t(m)$ to minimize the error between sensed load current and fundamental component of load current extracted through H-LMS. The block diagram of the H-LMS control scheme is shown in Fig. 5.2.

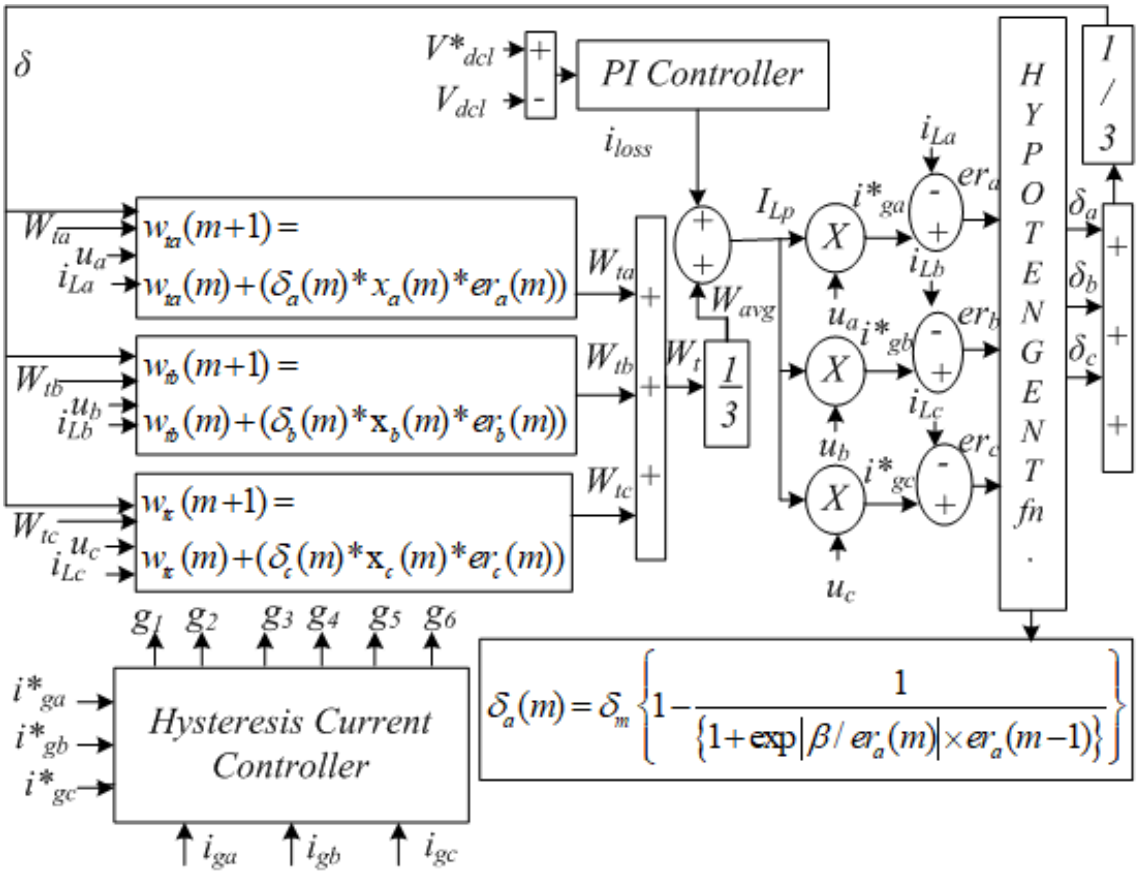

Figure 5.2: Block diagram of H-LMS control technique

The weight updation is represented by equation (5.1):

$$W_t(m+1) = W_t(m) + 0.5\delta[-\nabla(E(er^2(m))] \tag{5.1}$$

where δ is the step size and this is based on the functioning parameters and $er^2(m)$. The mean-square error can be given by equation(5.2):

$$er^2(m) = [i_L(m) - (W_t(m) * u(m))]^2 \tag{5.2}$$

where u(m) is unit voltage template for phase 'a', 'b', 'c' and i_L(m) represents load current for that phase. Formulation of the iteration rate at m^{th} instant for the approximation of active power component for the generation of reference currents is expressed by equation (5.3):

$$W_t(m+1) = W_t(m) + \delta(m) * u(m)[i_L(m) - (W_t(m) * u(m)] \tag{5.3}$$

$$W_t(m+1) = W_t(m) + (\delta(m) * u(m) * er(m)) \tag{5.4}$$

$$er(m) = i_L(m) - W_t(m) * u(m) \tag{5.5}$$

The step size ($\delta(m)$) depends upon the operating parameters. The step size must be updated according to the loading conditions and dynamics of the system. Continuous update of ($\delta(m)$) provides superior performance. In this HLMS control, step size varies on the basis of equation (5.6) can be given as:

$$\delta(m) = u(m)[1 - \frac{\delta_m(m)}{1 + exp(\beta|er(m) * er(m-1)|)}] \tag{5.6}$$

The mean of weight component for the three-phase system can be deduced by equation (5.7):

$$W_{avg}(m) = \frac{1}{3}[W_{ta}(m) + W_{tb}(m) + W_{tc}(m)] \tag{5.7}$$

The mean of the weights provides a load balancing feature in the system. The active power component (W_{avg}) is used to calculate reference currents for VSC is discussed in the next section.

5.2.2 Adaptive Neuro-Fuzzy Inference System Control

Fig. 5.3 shows the block diagram of ANFIS–LMS controller, where ANFIS controller has been used to update the step size. This method updates the step size δ(m), which varies due to variation in load or system dynamics. ANFIS is used to find optimum weights so that the mean square error in the active component of load current can be minimized. The algorithm is based on the iteration of weights (W_t(m)). Continuous update of the weight aims to minimize the error between sensed load current and actual load current.

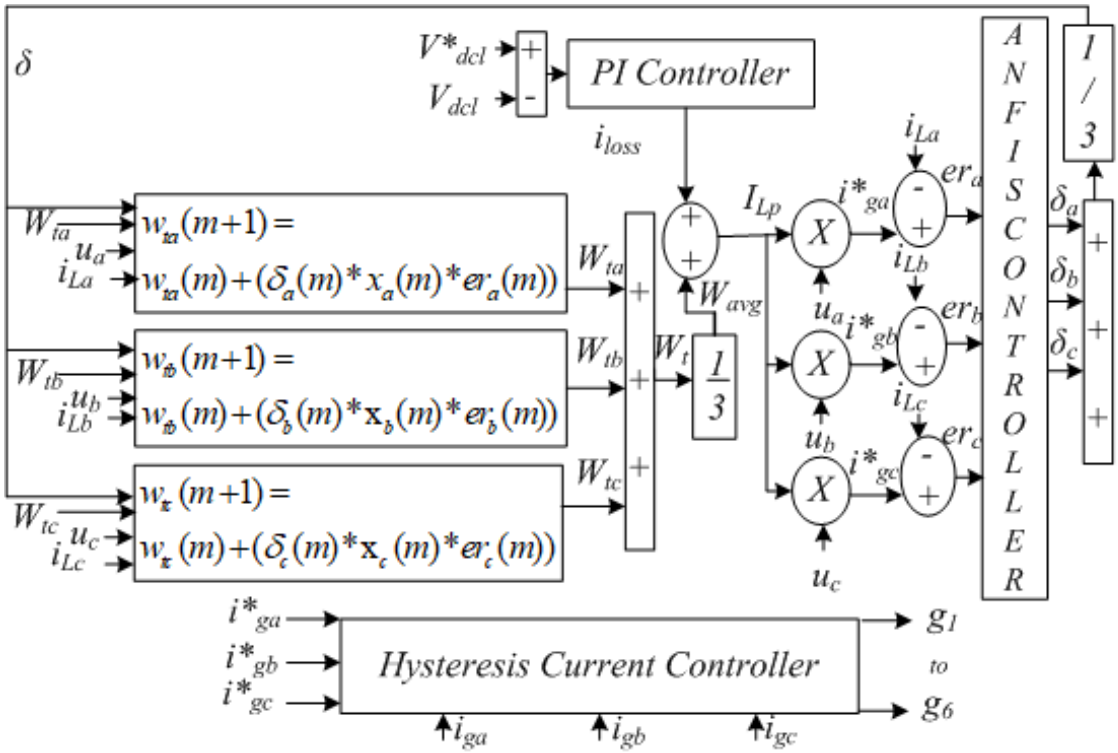

Figure 5.3: Block diagram for ANFIS-LMS control technique

The weight can be represented by equation (5.8):

$$W_t(m+1) = W_t(m) + 0.5\delta[-\nabla(E(er^2(m))] \tag{5.8}$$

where δ is the step size. Convergence and stability are dependent on δ. The δ may be fixed or variable. It has been observed that for fixed δ, algorithm does not attain minimum static error with a fast convergence rate. With the higher value of δ, the fast convergence is obtained with a higher static error. Whereas, with the lower value of δ, slow convergence is obtained with the lower static error. An ANFIS-based variation of step size δ solves this contradiction between the convergence rate and steady-state error. Therefore, to achieve faster convergence with minimum static error, ANFIS-based variation of step size (δ) is used. Computation of weight is the same as in H-LMS control technique, both differ in step size updatation method. The weight updation is given by equation (5.9):

$$W_t(m+1) = W_t(m) + \delta(m) * u(m)[i_L(m) - (W_t(m) * u(m)] \tag{5.9}$$

$$W_t(m+1) = W_t(m) + (\delta(m) * u(m) * er(m)) \tag{5.10}$$

$$er(m) = i_L(m) - W_t(m) * u(m) \tag{5.11}$$

where u(m) is a unit voltage template for phase 'a', 'b' and 'c'. The comprehensive process for error minimization can be established through the independent ANFIS controller [102]. The typical architecture of the Sugeno rule-based five-layer feed-forward ANFIS controller is realized through multi-iteration and hybrid learning. The development and tuning of the ANFIS controller are discussed in Section 4.2.4. A Gaussian Bell (G-Bell) shape MFs are used to train the system. The trained ANFIS has 5 input MFs and 25 rule base. In this control scheme, neural network optimization has been used to generate the rule base for fuzzy logic control system. Error is obtained by subtracting the actual load current from the generated references grid current and this error is minimized by ANFIS controller. The process of minimization of error gives step size which is continuously updated for system transients. This step size further update the weight signal in order to enhance the performance of the LMS based algorithm. The mean value of weights (W_{avg}) and it can be given by equation (5.12):

$$W_{avg}(m) = \frac{1}{3}[W_{ta}(m) + W_{tb}(m) + W_{tc}(m)] \tag{5.12}$$

5.2.3 Zero-Attracting Quaternion LMS Algorithm

The control scheme proposed is based on zero-attracting quaternion LMS (ZAQLMS) and used for system identification. ZAQLMS is used to extract the fundamental components of load current. The block diagram of the ZAQ-LMS control scheme is shown in Fig. 5.4. The active fundamental weight element (W_t) is evaluated as:

$$W_t(m+1) = W_t(m) + \frac{1}{2}(\delta - 4\chi)(er(m)u(m) - \varepsilon_{pn} sign(W_t(m)) \tag{5.13}$$

$$er(m) = i_L(m) - W_t(m)u(m) - k_{dcn}(m) \tag{5.14}$$

$$k_{dcn}(m+1) = k_{dcn}(m) + \zeta er(m) \tag{5.15}$$

where er(m) is the error of the load current active component, ζ is a constant which decides DC-offset capability. The inclusion of the term K_{dcn} introduces the high DC-offset rejection capability in the signal. χ is a constant and controls the zero attractor signal strength and δ is a convergence component, which decides the rate of convergence. u(m) is active elements of the unit templates and the sign is the signum function. The introduction of ε_{pn}sign(W_t) term includes the zero

attraction feature by keeping error near to zero. The average active (W_{avg}) weight given by equation (5.16):

$$W_{avg}(m) = \frac{1}{3}[W_{ta}(m) + W_{tb}(m) + W_{tc}(m)] \tag{5.16}$$

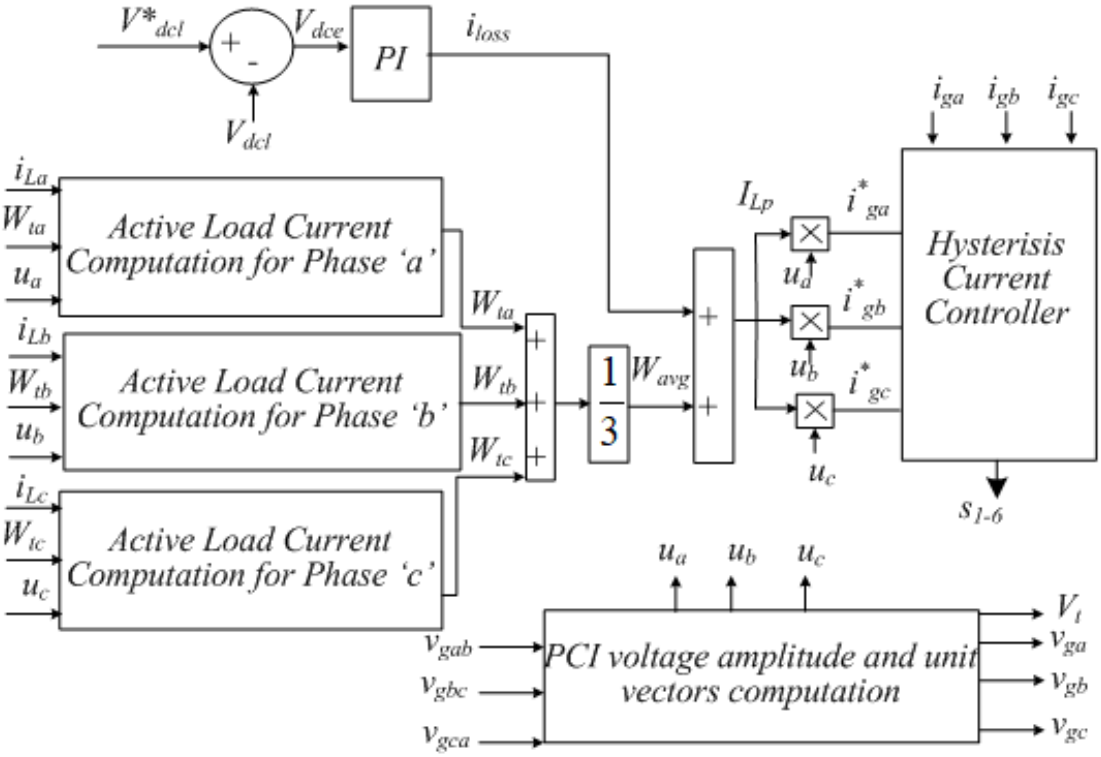

Figure 5.4: Block diagram of ZAQ-LMS control technique

5.2.4 Modified Shrinkage Widely Linear Complex-Valued LMS Technique

The block diagram of the MSWL-CLMS control scheme is shown in Fig. 5.5. Shi et al. [2015] have proposed SWL-CLMS (Shrinkage Widely Linear Complex-Valued Least Mean Squares) algorithm [174]. However, MSWL-CLMS is modified with the inclusion of zero attractors (ZA) term and DC-offset rejection capability. The pioneering attribute of the proposed control technique is its capability of rejecting the DC-offset component from the load current and extraction of the fundamental component, which helps in the quick estimation of the reference source current to generate the switching pulses for VSC.

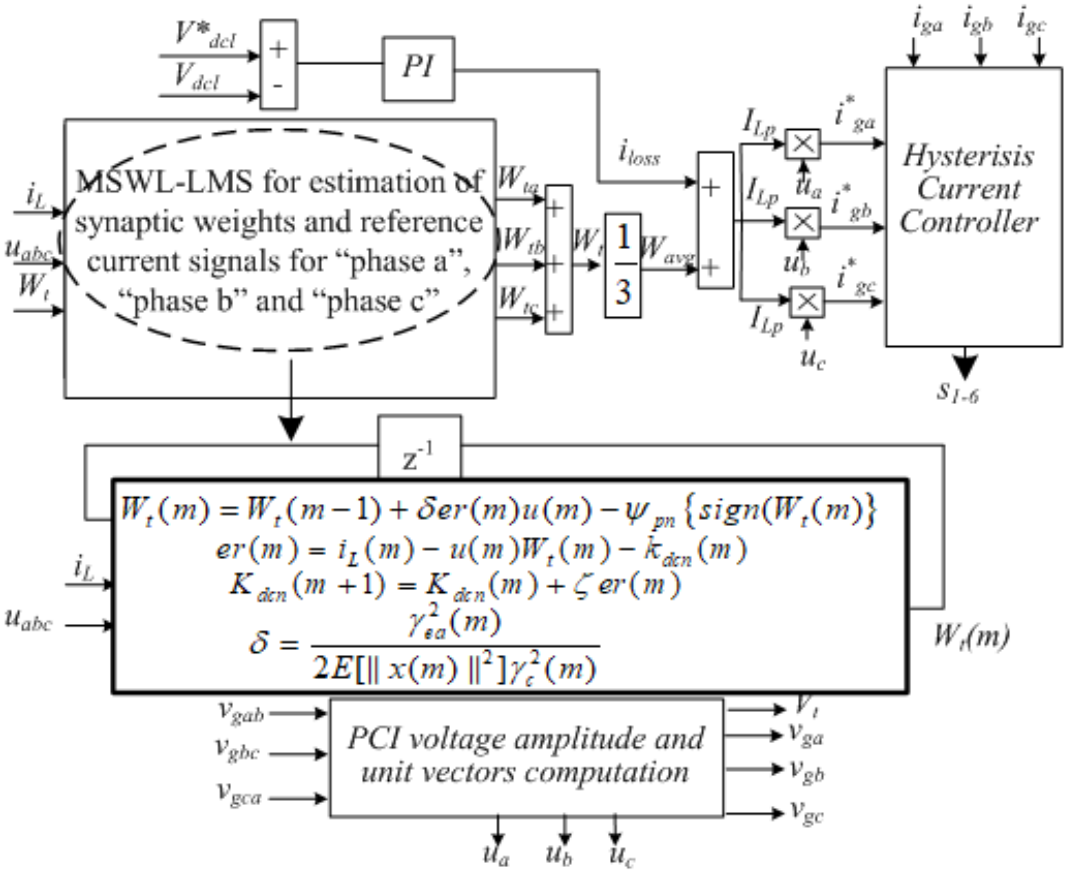

Figure 5.5: Block diagram of MSWL-CLMS control technique

The currents drawn by the nonlinear load consists of DC, fundamental frequency current and current of multiple fundamental frequencies, and can be mathematically formulated by equation (5.17):

$$\hat{y(t)} = \sum_{m=0}^{m=k} \hat{y_m}(t) \tag{5.17}$$

Consider the desired signal $i_L(m)$ at the m^{th} instant.

$$i_L(m) = W_0 u(m) + \psi_{pn} \tag{5.18}$$

where W_0 is system vector of L length, $u(m) = u_1(m), u_2(m), u_3(m), ...u_T(m)$. Here ψ_{pn} accounts for noise with 'zero' average and variance.

$$\psi_{pn}^2 = E[|\psi_(m)|^2] \tag{5.19}$$

$$er(m) = i_L(m) - u(m)W_t(m) - k_{dcn}(m) \tag{5.20}$$

$$k_{dcn}(m+1) = k_{dcn}(m) + \zeta er(m) \tag{5.21}$$

here ζ is a constant which decides DC-offset capability. The inclusion of the term K_{dcn} introduces the high DC-offset rejection capability in the signal. $W_t(m)$ is the estimated weight at the m^{th} instant The objective of the control technique is mean-square error minimization. Here, the weight is updated in order to update the error (er(m)) signal. In the modified SWL-CLMS algorithm, updated weight is given by equation (5.22):

$$W_t(m) = W_t(m-1) + \delta er(m)u(m) - \varepsilon_{pn} sign(W_t(m)) \tag{5.22}$$

δ signifies step size adaptation gain. ε_{pn} is a constant and sign is the signum function. The introduction of $\varepsilon_{pn} sign(W_t)$ term includes the zero attraction feature by keeping near to zero quantity at zero accelerated convergence rate. $\zeta_n(m)$ is the noise-free posteriori estimation error signal and is given as:

$$\varepsilon_n(m) = \varepsilon_{opt}(m) - \varepsilon_f(m) \tag{5.23}$$

$$\varepsilon_f(m) = u(m)W_opt - x_n(m)W_opt(m+1) \tag{5.24}$$

Equation (5.23) and (5.24) is used to calculate the value of variable step size parameter δ and give by equation (5.25):

$$\delta = \frac{\gamma_{ea}^2(m)}{2E[||x(m)||^2]\gamma_e^2(m)} \tag{5.25}$$

The quantity $\gamma_e^2(m)$ and $\gamma_{ea}^2(m)$ are computed by equations (5.26)-(5.28):

$$\gamma_e^2(m) = \mu\gamma_e^2(m-1) + (1-\mu)|er(m)|^2 \tag{5.26}$$

$$\gamma_{ea}^2(m) = \mu\gamma_{ea}^2(m-1) + (1-\mu)|\hat{er}(m)|^2 \tag{5.27}$$

$$\widehat{er}_a(m) = sign[er(m)]max(|er(m)| - t, 0) \tag{5.28}$$

where t is threshold parameter, μ is forgetting factor $0<\mu \leq 1$

$$sign[er(m)] = \frac{er(m)}{|er(m)|} \tag{5.29}$$

γ and t is a threshold with $1 \leq \theta \geq 4$. Using equation (5.22) the average active (W_{avg}) weight given by equation (5.30):

$$W_{avg}(m) = \frac{1}{3}[W_{ta}(m) + W_{tb}(m) + W_{tc}(m)] \tag{5.30}$$

5.2.5 Generation of Reference Currents

The losses in the IGBT are determined using the equation (5.31) and (5.32) as:

$$e_{dc}(m) = V^*_{dcl}(m) - V_{dcl}(m) \tag{5.31}$$

$$i_{loss}(m) = i_{loss}(m-1) + k_p e_{dc}(m) - e_{dc}(m-1) + k_i e_{dc}(m) \tag{5.32}$$

The PI controller output (losses) is added to the average fundamental load current W_{avg} component to get an effective active power component (I_{Lp}) which is given by equation (5.33).

$$I_{Lp} = W_{avg} + i_{loss} \tag{5.33}$$

Unit templates are computed using phase voltages (v_{ga}, v_{gb}, v_{gc}) and amplitude of PCI voltage (V_t), which are computed by equation (5.34):

$$V_t = [\frac{2}{3}(v^2_{ga} + v^2_{gb} + v^2_{gc})]^2 \tag{5.34}$$

$$v_{ga} = \frac{2v_{gab} + v_{gbc}}{3}; v_{gb} = \frac{-v_{gab} + v_{gbc}}{3}; v_{ga} = \frac{-v_{gab} - 2v_{gbc}}{3} \tag{5.35}$$

where v_{gab} and v_{gbc} are the line voltages. Governing equations for unit phase template (u_a, u_b, u_c) are given by equations (5.36):

$$u_a = \frac{v_{ga}}{V_t}; u_b = \frac{v_{gb}}{V_t}; u_c = \frac{v_{gc}}{V_t} \tag{5.36}$$

To estimate the sinusoidal reference source currents i^*_{ga}, i^*_{gb}, i^*_{gc}, unit templates are multiplied with active reference source current(I_{Lp}). Reference currents can be given by equations (5.37):

$$i^*_{ga} = u_a I_{Lp}; i^*_{gb} = u_b I_{Lp}; i^*_{gc} = u_c I_{Lp} \tag{5.37}$$

The obtained sinusoidal reference source currents thus obtained are compared with sensed source currents and error has been passed through the hysteresis current controller, which generates gate pulses for the VSC. Generated reference grid currents are sinusoidal, balanced in phase with grid current and their magnitude is proportional to active power demanded by the load.

5.3 Results and Analysis for PQ Enhancement

The developed control techniques such as H-LMS, ANFIS-LMS, ZAQ-LMS and MSWL-CLMS are simulated in MATLAB/SIMULINK platform. The simulation study on a hybrid source microgrid system is carried out to test the effectiveness of new control techniques for PQ improvement and appropriate power allocation. All four developed algorithms differ in estimation of step size, DC-offset rejection capability and harmonic suppression ability. Therefore, simulation results of the MSWL-LMS algorithm for microgrid under all possible dynamics are discussed in detail. Further, the remaining three developed algorithms viz. H-LMS, ANFIS-LMS and ZAQ-LMS are discussed under nonlinear balanced and unbalanced conditions only. Whereas, intermediate results analysis and harmonic spectra are studied separately for all four algorithms.

The response of the microgrid is analyzed on the basis of various performance parameters such as DC-link voltage(V_{dcl}), sinusoidal PCI voltage (V_{PCI}), non-sinusoidal three-phase lagging PF load current (i_L), three-phase VSC currents (i_{VSC}), sinusoidal and balanced three-phase grid voltage(v_g) and grid currents (i_g).

5.3.1 System Response using MSWL-CLMS Algorithm

A linear load (16kW,5kVAR) with the combination of resistors and inductors for each phase is considered initially for 415V, 50Hz grid-connected microgrid. Fig. 5.6 shows system response under linear load. To analyze the performance of the microgrid for transients, active and reactive load demand is increased to 24kW, 7.5kVAR at t=0.35s. Further, at t=0.5s solar perturbation is introduced in the system (solar irradiation is decreased by 50%). This results in reduction of PV generation by 50%. The grid currents are observed to be perfectly sinusoidal and balanced during all dynamics. DC-link voltage is regulated at the 750V through the PI controller during the transients. Some disturbance is noticeable which is overcome within a cycle and becomes regulated after a very short transient. The rated power generation of PVGS (P_{pv}), FCGS (P_{FC}) and WPGS (P_w) is 8kW, 3kW and 6.5kW respectively. Power required by the load (P_L)is 16kW, 5kVAR which is further, increased to 24kW,7.5kVAR at t=0.35s, grid supply power(P_g) and power

available at DC-link terminal (P_{dcl}) i.e. power generated by RESs altogether. The total rated power generation by the RESs is 17.5KW under steady-state conditions. The VSC controller ensures that the real power demand of the load is fulfilled by the grid only and the surplus power is injected into the grid. Moreover, the deficit power is evacuated from the grid. Whereas, the reactive power requirement of the load is delivered locally through VSC and grid is free from supplying reactive power. Due to the power compensation feature of the presented control schemes, the reactive power supplied by the grid remains unaffected ('0'kW). A constant DC-link voltage is observed and the corresponding power values are shown in Fig. 5.6. The variation in load demand causes a change in grid current and grid power. However, power available at DC-link remains unaffected. The result shows that the power equilibrium is achieved and the system is working effectively under dynamics. The developed control algorithm is working satisfactorily to generate the appropriate reference currents.

Fig. 5.7 shows the system results for the balanced and unbalanced nonlinear load. In this case, to realize the nonlinear load a three-phase diode bridge rectifier is used, DC side of the rectifier has 25Ω resister and 100mH inductance. The load currents are non-sinusoidal, distorted and of higher THD due to nonlinear load. The microgrid system with nonlinear load is subjected to unbalancing with the sudden removal of one phase. The control algorithm generates the reference currents, these reference currents are in phase with the grid voltage this results in PF improved operation. For load unbalancing is achieved by removing one phase of the load from t=0.8s to 0.95s. The grid currents are observed as sinusoidal, balanced and in phase with the grid voltage. Total generation is kept constant at RESs rated values to study the performance under nonlinear load. Total generated power 17.5kW is available and a load of 12.5kW is connected to the system at t=0.7s. One phase of the system is disconnected at t= 0.8s and load requirement is reduced to 5.5kW. Hence, power feed into the grid is increased to 12.5kW. Fig. 5.7 depicts the perfect power balance is achieved for the nonlinear balanced and unbalanced load.

During the transients, it is noticed that PCI voltage is sinusoidal, balanced and constant in amplitude. Grid currents and voltages are sinusoidal and balanced for all transients this ensures the good quality of grid supply.

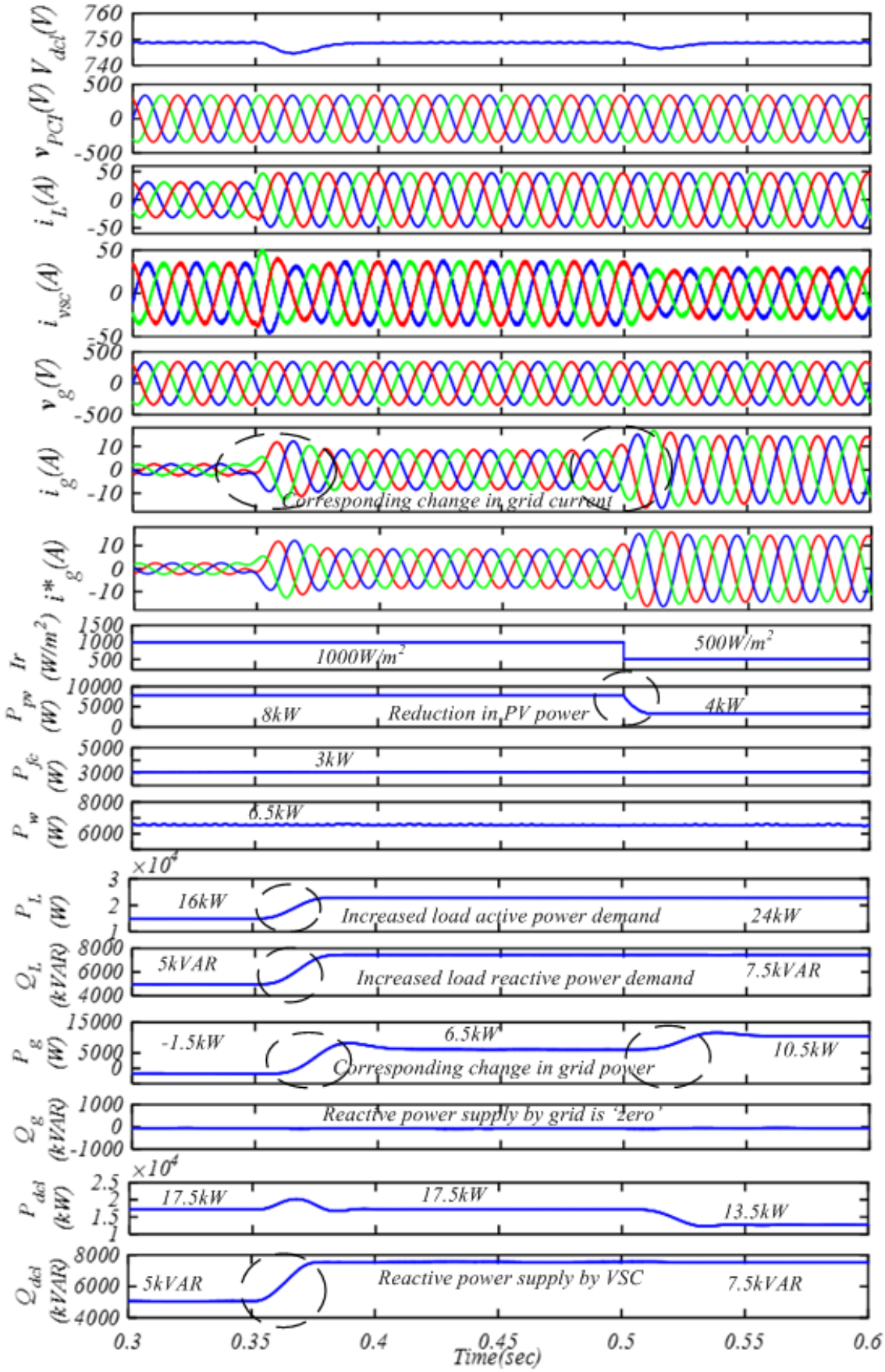

Figure 5.6: Performance under variable load and solar irradiation using MSWL-CLMS technique

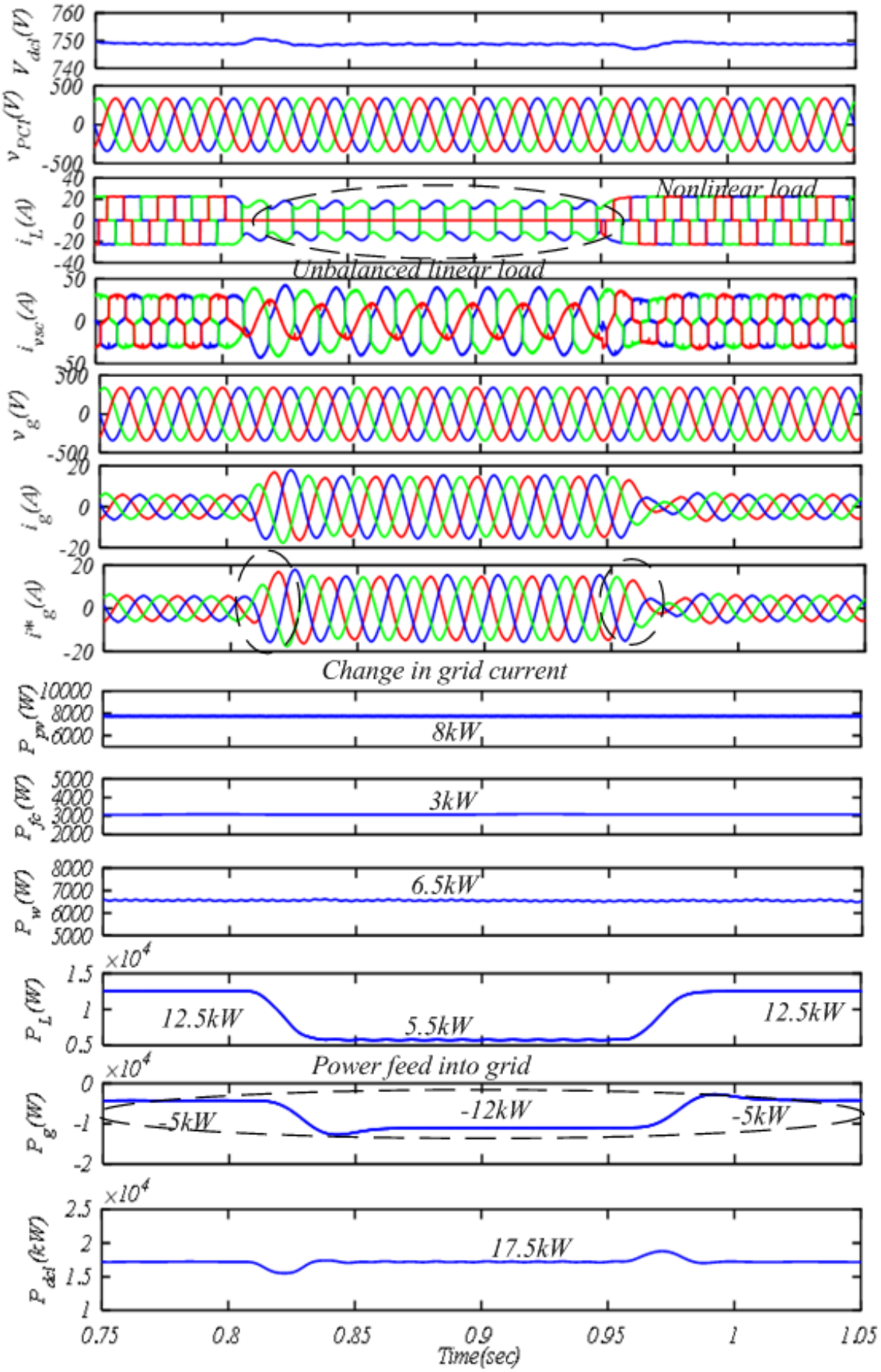

Figure 5.7: Performance under balanced and unbalanced nonlinear load using MSWL-CLMS technique

The performance of the microgrid under the change in wind speed is exhibited in Fig. 5.8. To study the system response for variable wind generation, initially, the load demand is kept constant i.e. 24kW and PVGS and FCGS generated power kept constant. This is increased to 26kW at t=8.5s. Reduction in the wind speed from 12m/s to 5m/s is introduced at t=1s. Reduction in wind speed results in reduction in wind power generation. Therefore, the power drawn from the grid is increased to fulfill the load demand. Further, at t=3s speed of the wind again increased to 12m/s and power generated by WPGS is increased. Hence, power delivered by the grid reduced correspondingly to work the system under power harmony. Marked values of power in Fig. 5.8 confirms the power balance is achieved using the developed control technique.

It is observed from Fig. 5.8 that PCI voltage is constant in magnitude, sinusoidal in shape and balanced in nature. Further, grid voltage and grid currents are found to be sinusoidal and balanced, grid voltage is constant in magnitude. DC-link voltage is regulated at 750V. Any change in generation capacity causes the variation in output power available at the input of VSC which disturbs the DC-link voltage momently. Due to two-mass model of the wind turbine, output power dynamics show delay to overcome this disturbance. Hence, there is no transients are observed in DC-link voltage. Further, at t= 8.5s load demand is increased to 26kW. This creates ‘ a power deficit, to fill this gap grid supplied more power which can be noticed in Fig. 5.8. It is concluded from the results that grid supports the load during the power deficit.

Results show that the measured grid current tracks the reference currents under all the transient conditions and demonstrate the acceptable performance of the microgrid system. Generated reference currents are further used to generate accurate gating pulses for VCS. Further, constant magnitude grid voltage and PCI voltage verify the power quality improvement under highly distorted load current. The MSWL-CLMS control approach is multi-objective and works in achieving coordinated power flow, harmonics mitigation, load balancing and reactive power compensation.

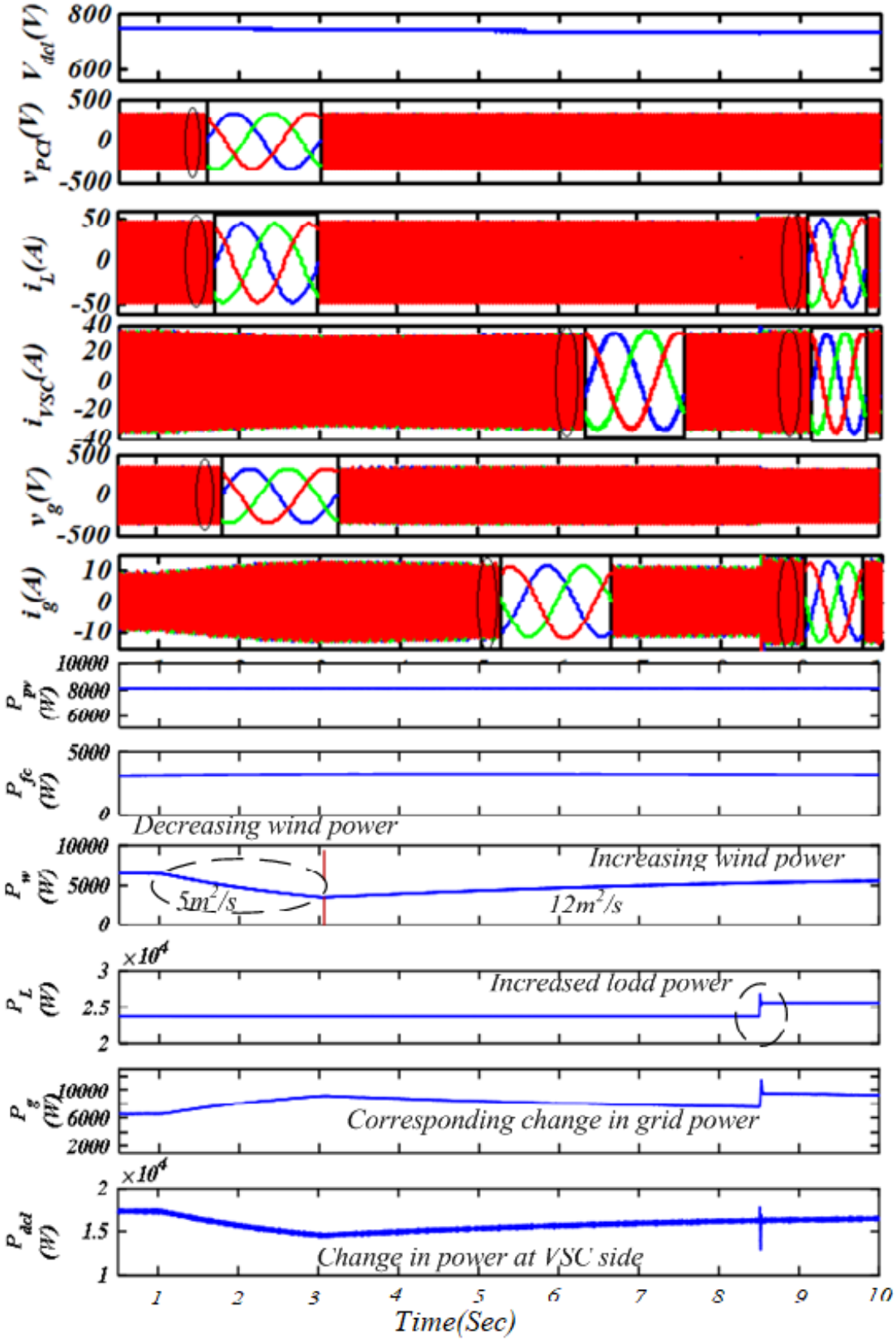

Figure 5.8: Response under varying wind speed using MSWL-CLMS technique

The intermediate signal response of the MSWL-CLMS control algorithm is given in Fig. 5.9. These results have been taken for nonlinear load where unbalancing

is introduced for t=0.8s to t=0.95s. It can be observed that the intermediate error signal oscillates near zero under the nonlinear load. The waveforms and their harmonics spectra of phase 'a' is shown in Fig.5.10 and Fig.5.11 non-sinusoidal load current(i_{La}) with 26.15% THD, grid current(i_{ga}) THD is 1.98% and grid voltage (V_{ga}) has 1.35% THD.

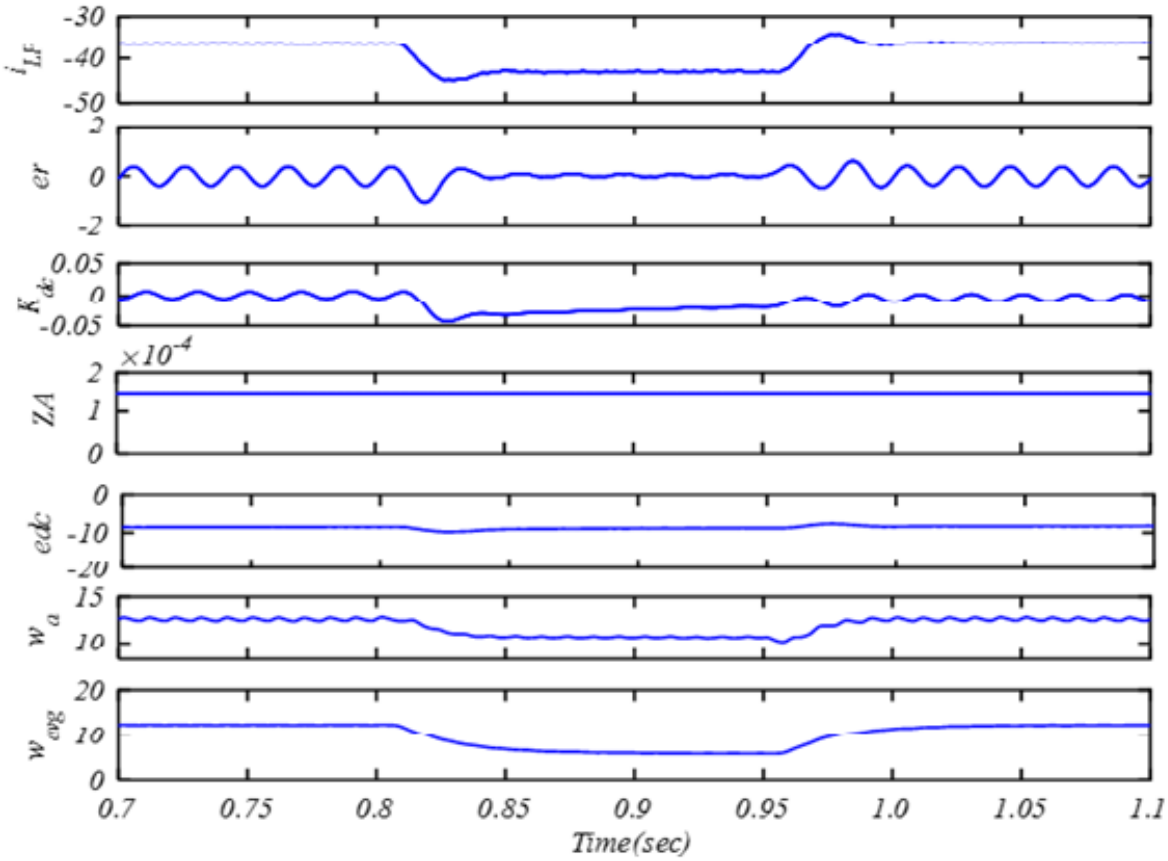

Figure 5.9: Internal signal results using MSWL-CLMS control

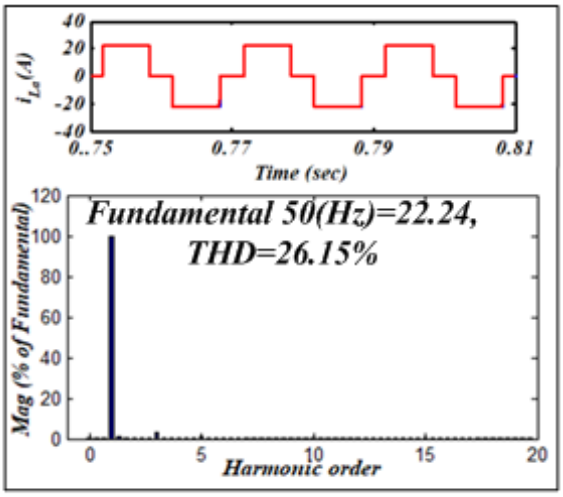

Figure 5.10: Harmonic spectra using MSWL-CLMS control technique for the nonlinear load (i_L) and its THD

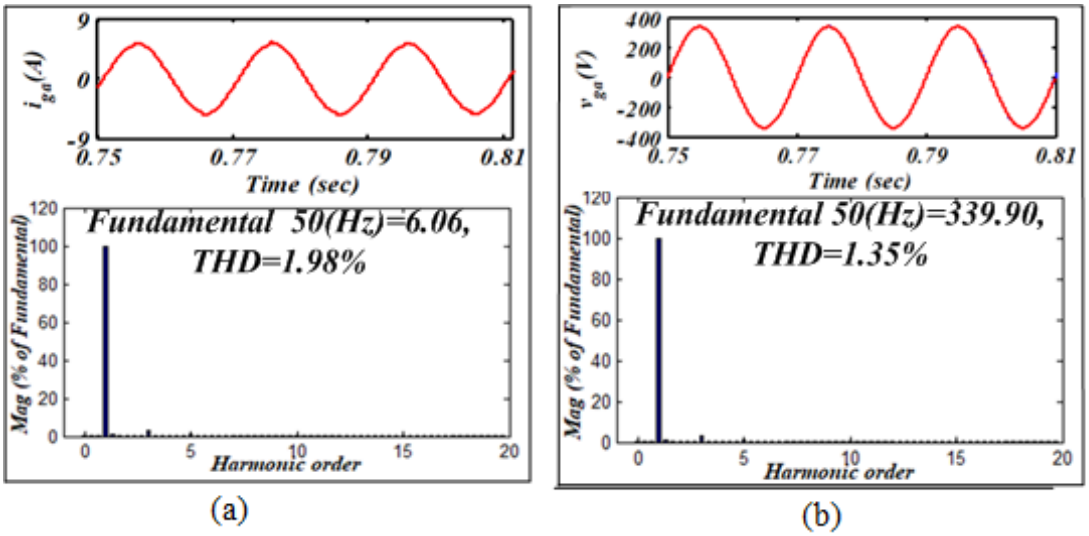

Figure 5.11: Harmonic spectra using MSWL-CLMS control technique for the nonlinear load (a) i_{ga} and its THD (b) v_{ga} and its THD

5.3.2 System Response using ZAQ-LMS Algorithm

Fig. 5.12 shows the system results for the balanced and unbalanced nonlinear load using ZAQ-LMS control algorithm. To realize nonlinear load, a three-phase diode bridge rectifier is integrated into the system (DC side of the rectifier has 25Ω resister and 100 mH inductance). Unbalancing in the nonlinear load is introduced by removing one phase (phase 'a') at t=0.8s and this phase 'a' is reinserted into the system at t=0.95s. Fig. 5.12 shows that the grid currents are perfectly sinusoidal, balanced and in phase with the grid voltage even for highly distorted load currents. DC-link voltage is maintained constant at 750V. The voltage at the consumer end (PCI voltage) is maintained sinusoidal balanced and constant in amplitude. The nonlinear load of 12.5kW is interfaced into the system at t=0.7s and the power generating systems are working at rated values. Hence 17.5kW generated power is available. The surplus power of 5kW is fed back into the grid. Negative notation of power implies that the power is injected into the grid. At t=0.8s one phase of the load is disconnected to introduced the unbalancing. Due to the disconnection of the one phase, load becomes single-phase and therefore, the power requirement is reduced to 5.5kW. Hence power injected into the grid is increased to 12kW. At t=0.95s the phase 'a' of the system is reintegrated and load demand again increases to 12.5kW and power fed back into the grid is reduces to 5kW. The load power distribution among the load and grid verifies the power balance feature of MG.

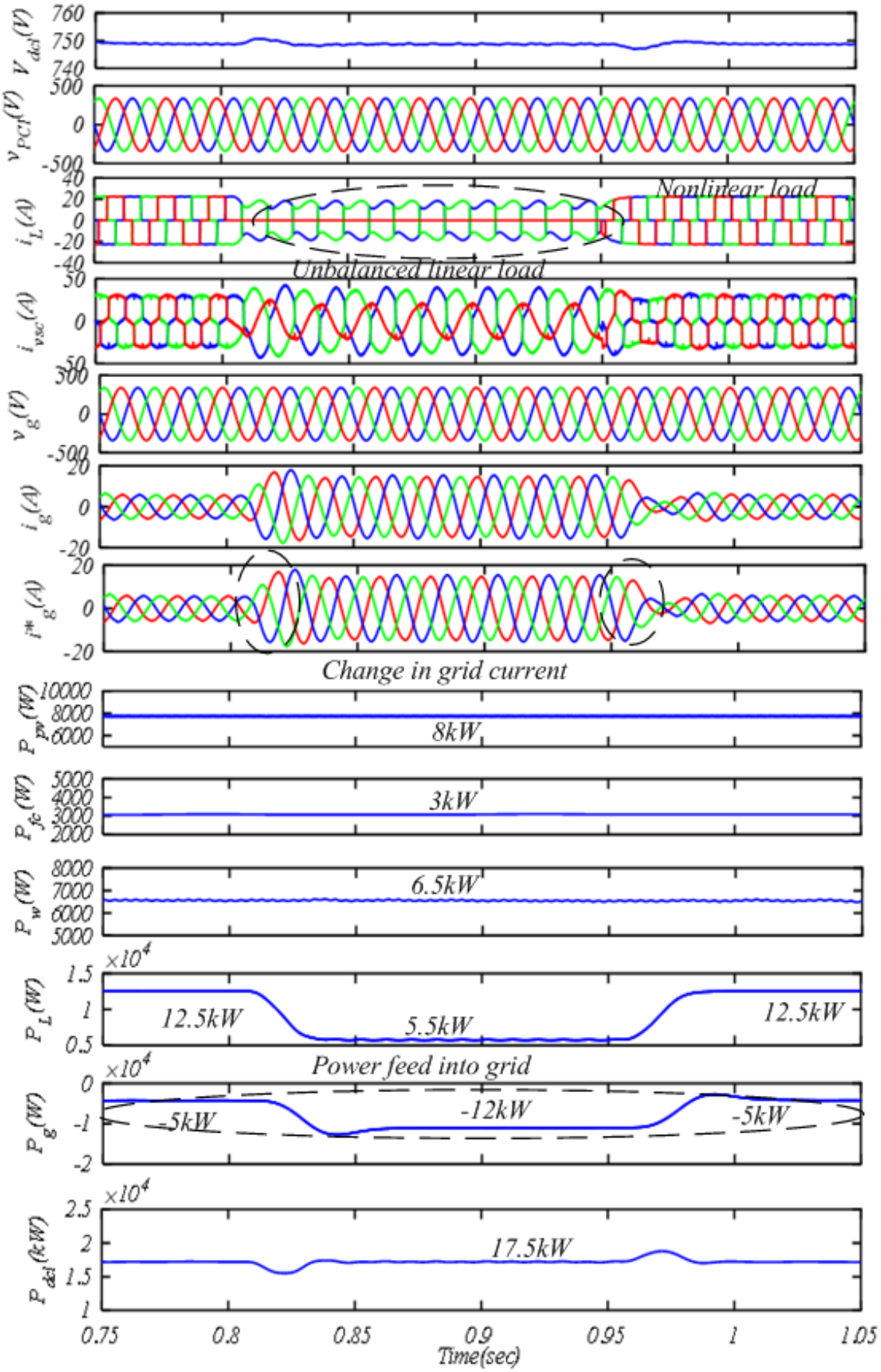

Figure 5.12: Performance under balanced and unbalanced nonlinear load using ZAQ-LMS control technique

The internal signal response of the algorithm is shown in Fig. 5.13. Intermediate results have been taken under nonlinear balanced and unbalanced load, here unbalancing is introduced t=0.8s by removing phase 'a' of the load. The Phase 'a' is reintegrated into the system at t=0.95s. The waveforms and their harmonics spectra of phase 'a' non-sinusoidal load current (i_{La}) with 26.10% THD, sinusoidal grid voltage (V_{ga}) has 1.39% THD and grid current(i_{ga}) THD is 2.23% and is shown in Fig. 5.14 and Fig. 5.15. Results show that the ZAQ-LMS control technique is effective in mitigation of the PQ problem in a hybrid source microgrid.

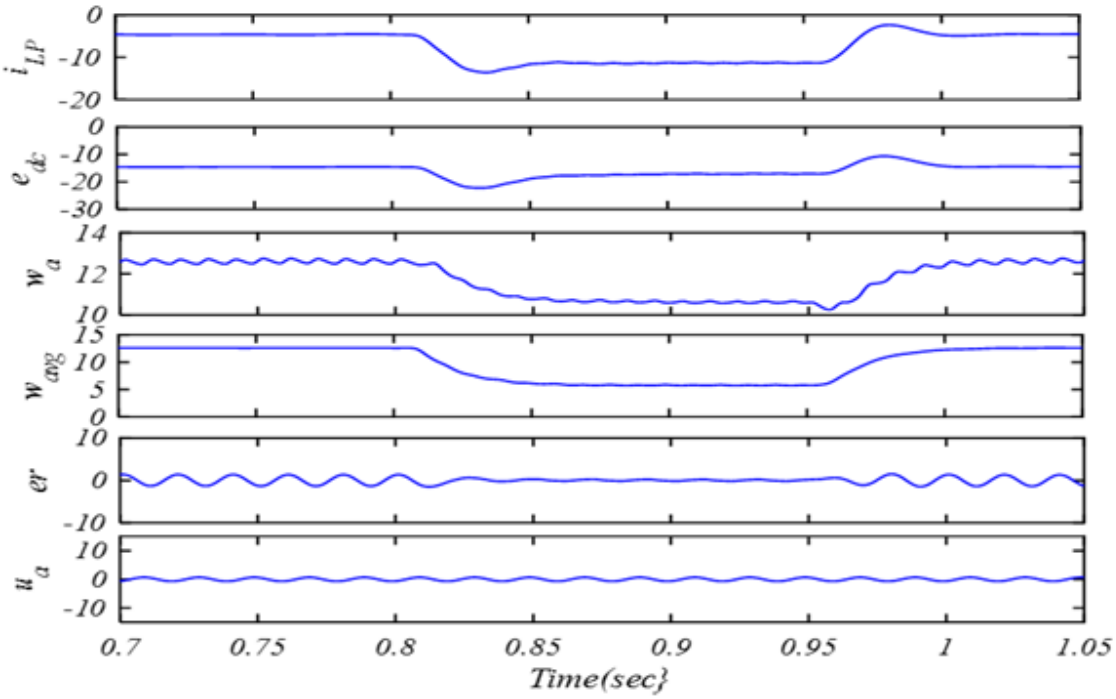

Figure 5.13: Internal signal using ZAQ-LMS control

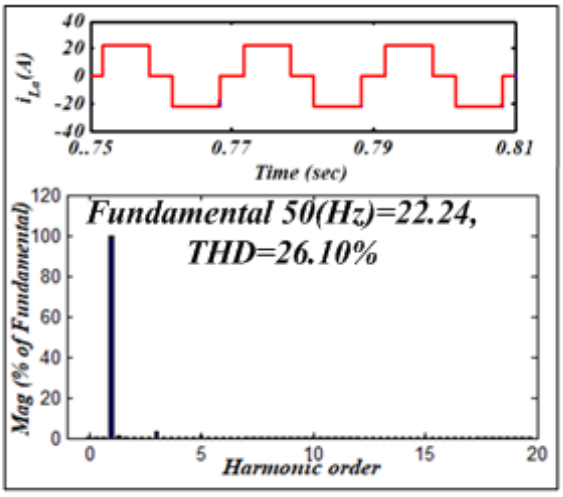

Figure 5.14: Harmonic spectra using ZAQ-LMS control technique for the nonlinear load (i_L) and its THD

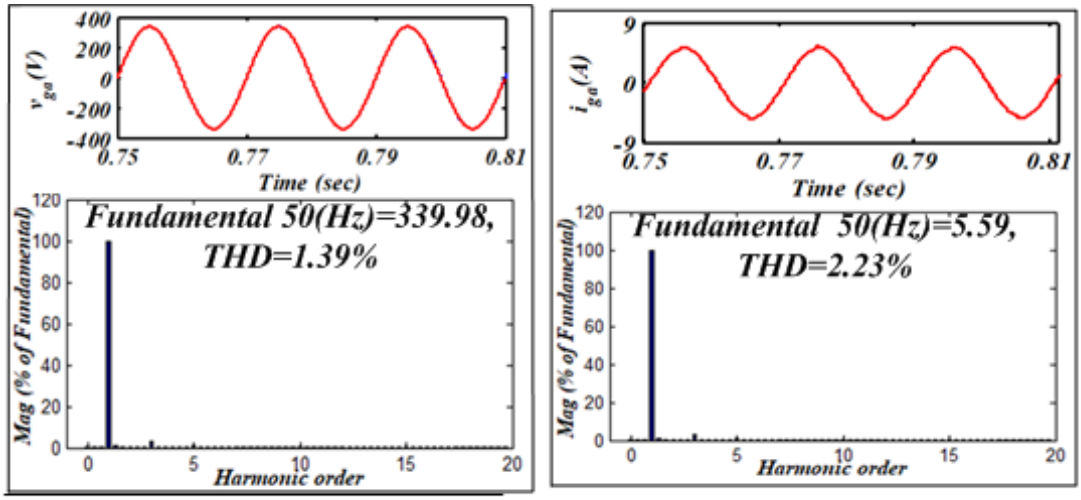

Figure 5.15: Harmonic spectra using ZAQ-LMS control technique for the nonlinear load (a)v_{ga} and its THD (b) i_{ga} and its THD

5.3.3 System Response using ANFIS-LMS Algorithm

Fig. 5.16 depicts the performance of the system under balanced and unbalance nonlinear load. The unbalancing in the microgrid system is introduced with the sudden removal of one phase at t=0.8s and this phase is further reconnected at t=0.95s. Due to the removal of one phase load becomes single-phase and load demand is reduces to 5.5kW which is further increased at t=0.95 to 12.5kW when this phase of the load is reintegrated. Initially, the load demand is 12.5kW and generation is 17.5 kW. Therefore, the surplus power is injected into the grid. Marked values of power in Fig. 5.16confirm the power balance is achieved using the ANFIS-LMS control technique. Fig. 5.16 demonstrates the grid voltage, grid currents, VSC current waveform, VSC voltage waveform, PCI voltage and load current are sinusoidal and balanced under nonlinear load. Further, constant magnitude grid voltage and PCI voltage verify the power quality improvement under highly distorted load current. The fundamental component of these distorted load currents is extracted through the ANFIS-LMS control algorithm for reference current generation. Fig. 5.16 shows that the measured grid current tracks the reference current under the unbalanced condition and demonstrates the acceptable performance of the system. During the transient operation, grid currents are observed sinusoidal, balanced and in phase with the grid voltage. The load currents are non-sinusoidal, distorted and of higher THD.

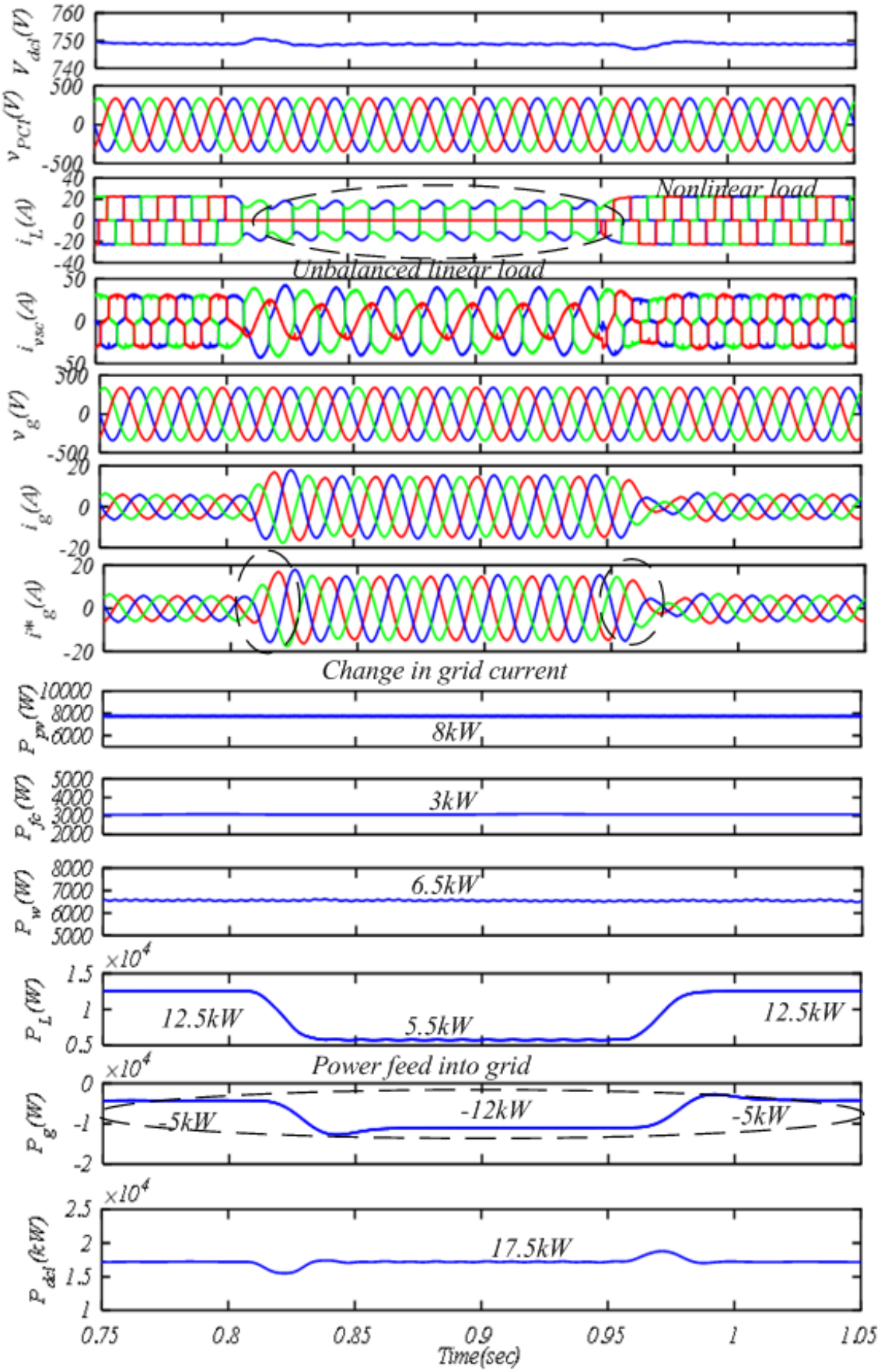

Figure 5.16: Performance under balanced and unbalanced nonlinear load using ANFIS-LMS control algorithm

The intermediate signal response of the ANFIS-LMS control algorithm is given in Fig. 5.17. Intermediate results have been taken under nonlinear balanced and unbalanced load, here unbalancing is introduced t=0.8s by removing phase 'a' of the load. The Phase 'a' is reintegrated into the system at t=0.95s to balance the load. Non linear load current(i_{La}) with 26.18%. THD is shown in Fig. 5.18. The waveforms and their harmonics spectra of phase 'a' sinusoidal grid voltage (V_{ga}) has 1.41% THD, grid current(i_{ga}) THD is 2.13% is shown in Fig. 5.19. The THD of grid current and PCI voltage verifies the power quality improvement capability of the control technique. The control is capable to keep the grid current THD under 5% even under a highly distorted nonlinear load of very high THD. The grid currents and voltages are well within the PQ standards prescribed by IEEE-519. System is working for unity power factor operation, reactive power compensation, load balancing, PQ problem mitigation and power equilibrium.

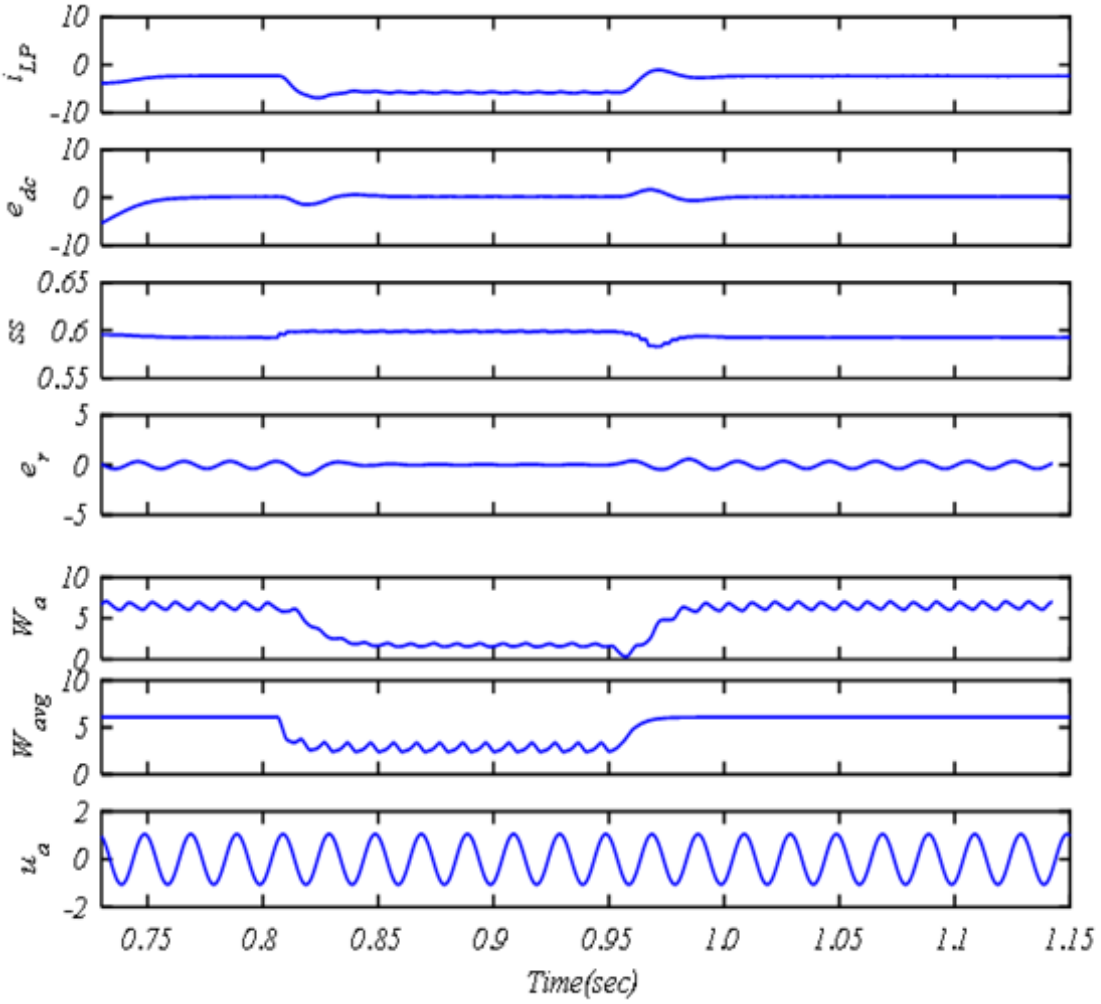

Figure 5.17: Internal signal using ANFIS-LMS control

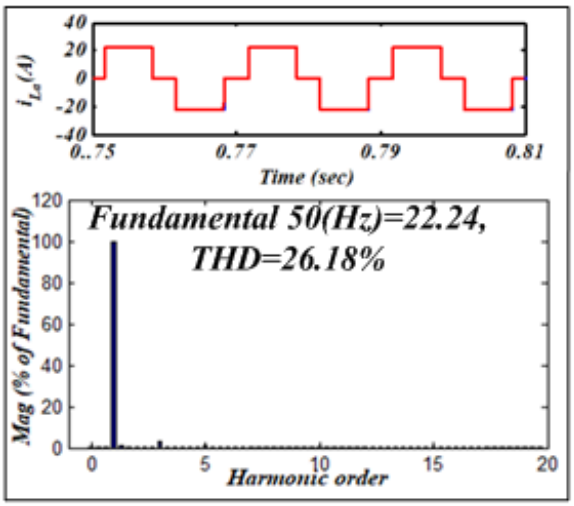

Figure 5.18: Harmonic spectra using ANFIS-LMS control technique under nonlinear load (i_L) and its THD

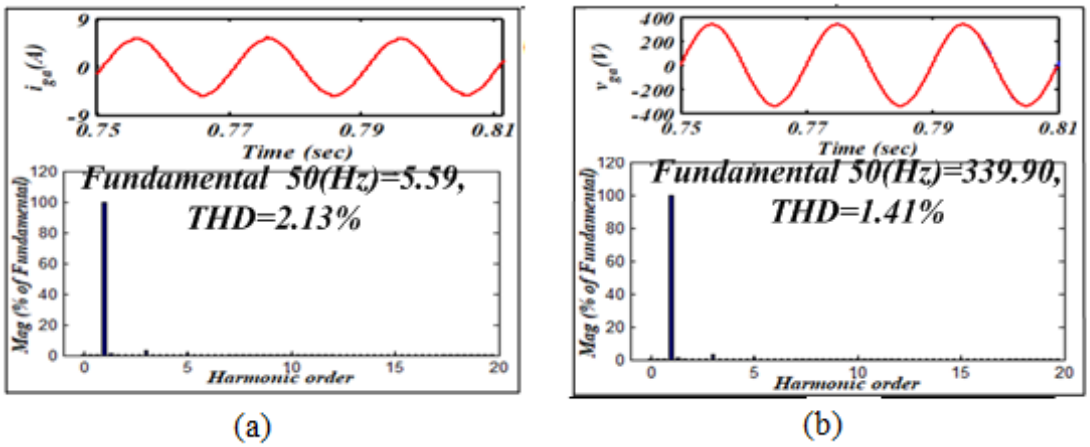

(a) (b)

Figure 5.19: Harmonic spectra using ANFIS-LMS control technique for the nonlinear load (a)i_L and its THD (b) i_{ga} and its THD (c)v_{ga} and its THD

5.3.4 System Response using H-LMS Control

Fig. 5.20 shows response of grid-connected 415V, 50Hz microgrid under nonlinear load using H-LMS control. The grid currents and PCI voltage are perfectly sinusoidal and balanced during all dynamics. DC-link regulated at 750V. The rated power generation of PVGS, WPGS and FCGS is 8kW, 6.5kWand 3kW respectively. Hence total power generated by the RES is 17.5kW. The load demand is only 16kW up to 0.35s so that the surplus power(1.5kW) is injected into the grid, this power is shown by the negative notation of power. The load is increased by to 24kW at 0.35s and deficit power is evacuated from the grid. Results show that the power equilibrium is achieved and the system is working effectively under dynamics.

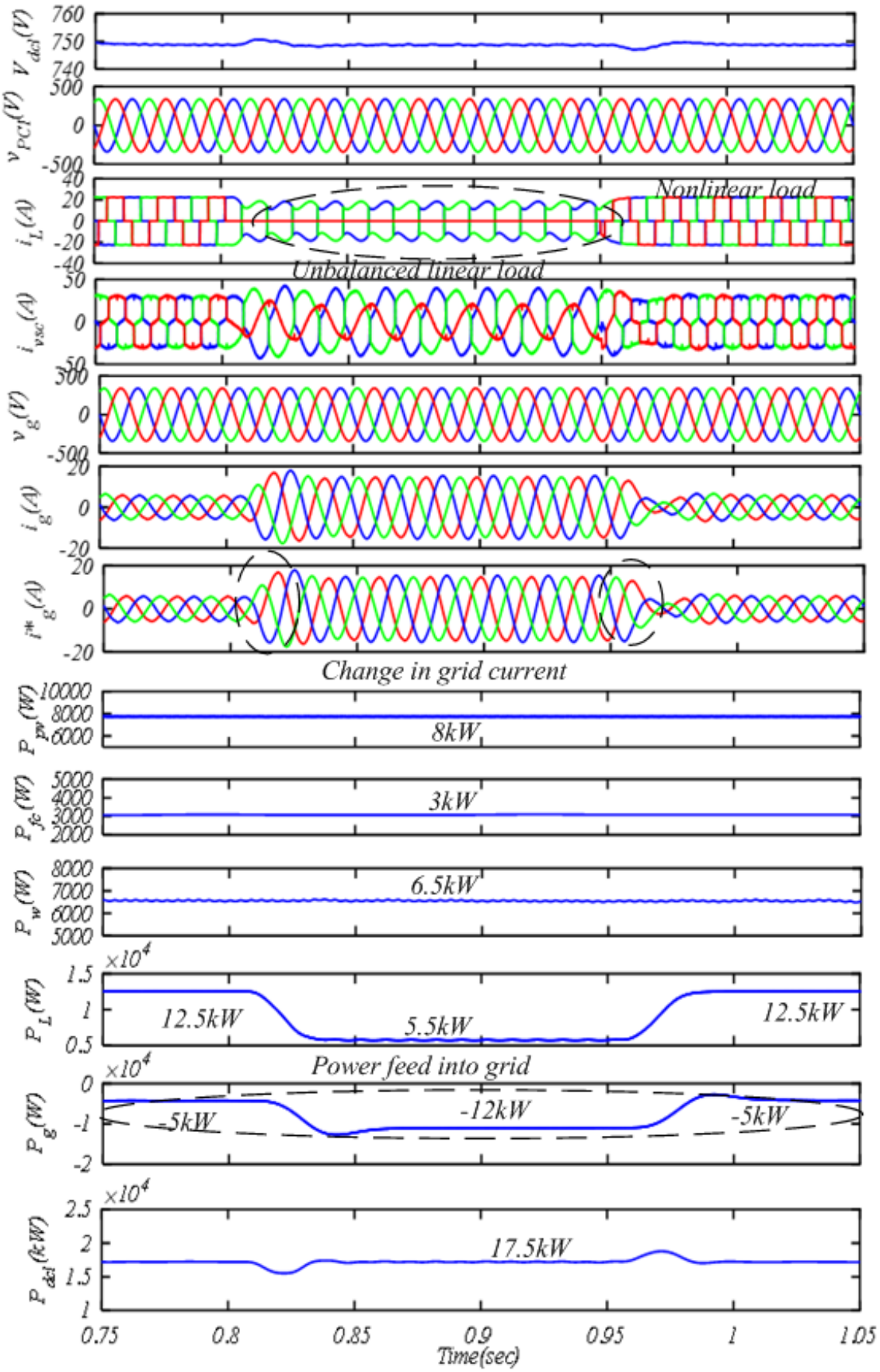

Figure 5.20: Performance using H-LMS under unbalanced nonlinear load

The intermediate signal response is given in Fig. 5.21 for nonlinear load.

Unbalancing is introduced from t=0.8s to t=0.95s. Waveforms and their harmonics spectra of phase 'a' load current(i_{La}), grid current(i_{ga}) and grid voltage (V_{ga}) are shown in Fig. 5.22 and Fig. 5.23 respectively. THD of V_{ga}, i_{ga} and i_{La} are 1.43%, 3.20% and 26.18% respectively. The grid currents and voltages are well within the PQ standards prescribed by IEEE-519.

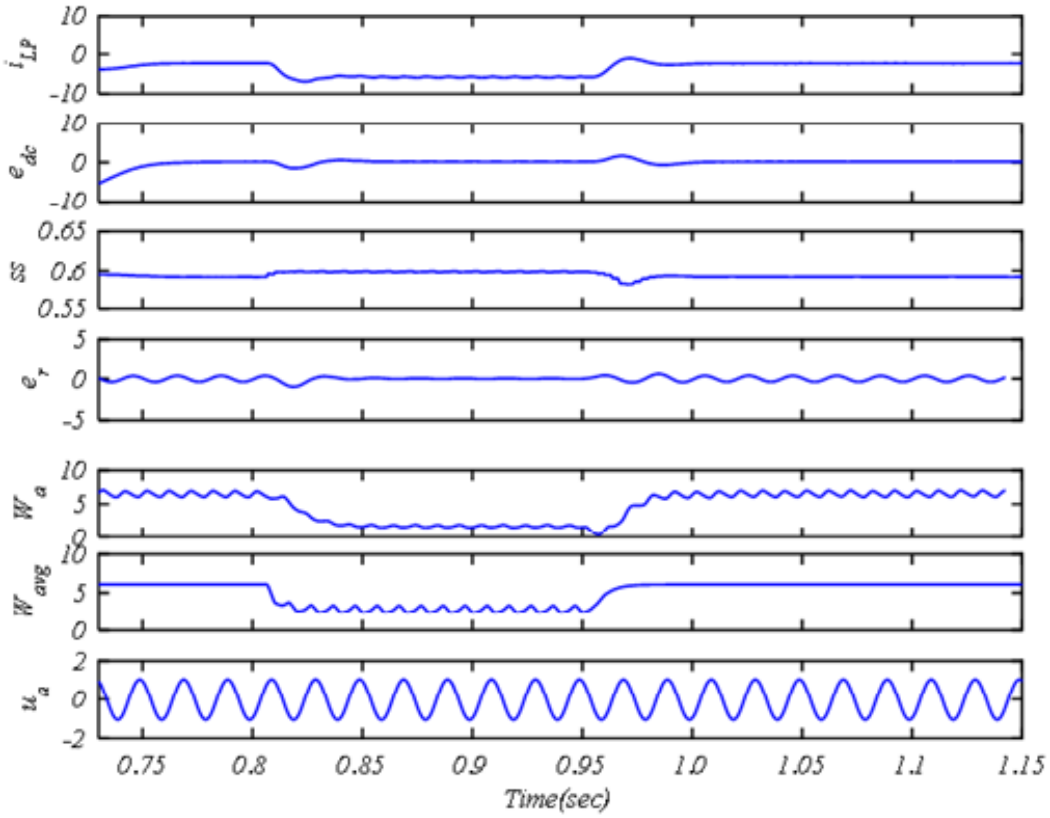

Figure 5.21: Internal signal using H-LMS control

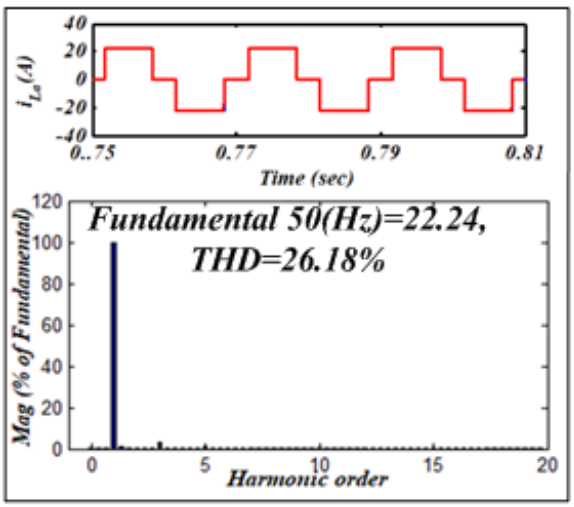

Figure 5.22: Harmonic spectra using H-LMS control (i_L) and its THD

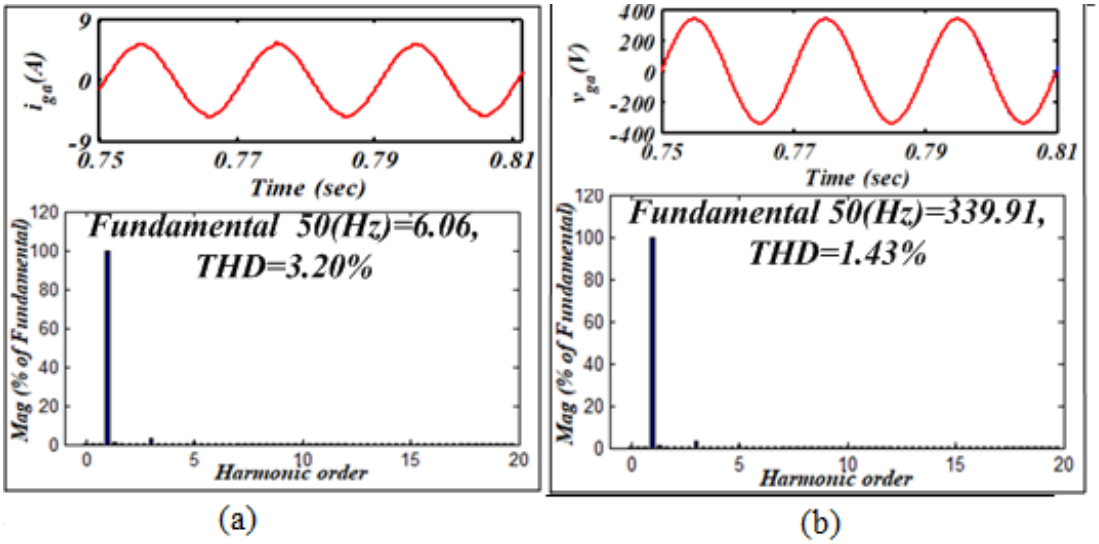

(a) (b)

Figure 5.23: Harmonic spectra using H-LMS control technique for the nonlinear load (a)i_{ga} and its THD (b)v_{ga} and its THD

5.3.5 Comparative Evaluation of Control Techniques

Table 5.1 shows comparative performance based on the THD in supply current, in the presence of nonlinear load. MSWL-CLMS gives the lowest THD level in the grid current. The load current is highly distorted due to the non-linear load with 25% THD. Grid current THD is 3.20%, 2.13%, 2.23% and 1.98% using H-LMS, ANFIS-LMS, ZAQ-LMS and MSWL-CLMS control techniques respectively. The MSWL-CLMS is found to be better in achieving the lowest THD in grid current as compared to H-LMS, ANFIS-LMS and ZAQ-LMS techniques.

Table 5.1: Comparison of H-LMS, ANFIS-LMS, ZAQ-LMS and MSWL-CLMS for Harmonic suppression

Quantity	**H-LMS**	**ANFIS-LMS**	**ZAQ-LMS**	**MSWL-CLMS**
THD and Magnitude of v_{ga}	1.43%; 339.91V	1.41%; 339.90V	1.39%; 339.98	1.35%; 339.90V
THD (%) Magnitude of i_{ga}	3.20%, 6.06A	2.13%, 5.59A	2.23%, 5.59A	1.98% 6.06A
THD (%) and Magnitude of i_{La}	26.18%, 22.24A	26.18%, 22.24A	26.10%, 22.24A	26.15%, 22.24A

Fig. 5.24 shows the comparative evaluation of the VSC control approaches. Four new control algorithms viz. H-LMS, ANFIS-LMS, ZAQ-LMS and MSWL-CLMS have been developed and implemented for PQ problem mitigation in the MG.

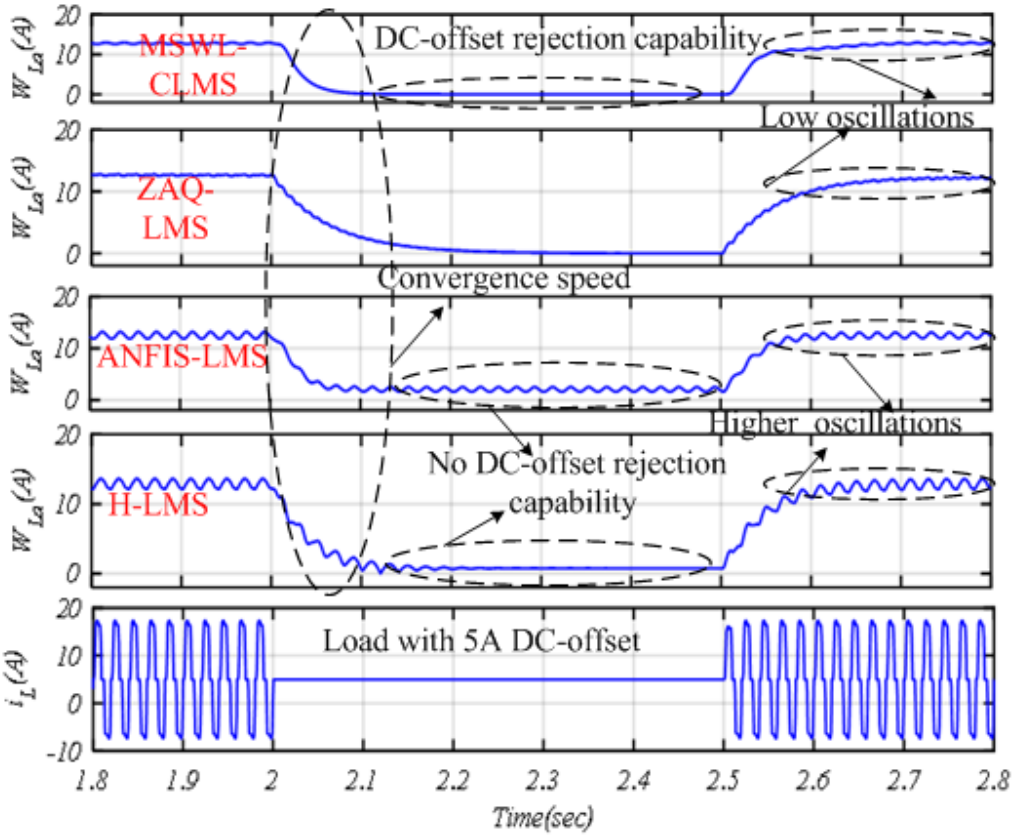

Figure 5.24: Comparison of weight signal

Fig. 5.24 shows that MSWL-CLMS control exhibits superior performance having higher DC-offset rejection competency, faster dynamic response due to low computational complexity and faster convergence speed as compared to the H-LMS, ANFIS-LMS, ZAQ-LMS algorithms. Table 5.2 summarize the performance of developed control techniques on the basis of weight signal extracted.

Table 5.2: Comparison of H-LMS, ANFIS-LMS, ZAQ-LMS and MSWL-CLMS

Quantity	**H-LMS**	**ANFIS-LMS**	**ZAQ-LMS**	**MSWL-CLMS**
DC-Offset rejection capability	no	no	yes	yes
Oscillations	higher	higher	lower	lowest
Settling time	0.1s	0.07s	0.18s	0.05

5.4 Conclusions

The contribution of this chapter is to develop improved control techniques such as H-LMS, ANFIS-LMS, ZAQ-LMS and MSWL-CLMS for grid-connected microgrid for PQ problem mitigation. Results show that the developed control techniques of VSC perform well under dynamics introduced due to load variation and environmental conditions. The developed microgrid system exhibits power equilibrium under all transients. A fair comparison is performed based on the obtained results under identical test conditions. It has been observed that the MSWL-CLMS algorithm is capable of DC-offset rejection and having less computational complexity. Further, it has the lowest steady-state oscillations in the computed weight component. In addition, the grid current THD of 1.35%, which is lowest among the developed techniques i.e. ANFIS LMS, H-LMS, ZAQ-LMS and MSWL-CLMS. The fundamental active power component settles quickly in 0.025s. MSWL-CLMS gives the significant enhancement in convergence speed, improves the steady-state performance and enables the accurate and rapid estimation of fundamental current components for the generation of the reference currents. H-LMS and ANFIS-LMS have shown higher oscillations under steady-state and dynamic conditions. Grid current THD is 1.43% and 1.41% in H-LMS and ANFIS-LMS respectively.

Chapter 6

PQ ENHANCEMENT OF HYBRID MICROGRID

This chapter investigates the performance of hybrid microgrid system for delivering power to DC and AC loads simultaneously. In the presented grid-connected hybrid microgrid, RESs and an Electric Vehicle (EV) load are interfaced at the DC bus. AC load is integrated into the system through a VSC. Further, VSC is integrated with the three-phase grid. EV may support the grid by injecting the power into the grid. EV works under plug and play role, it can be charge through RES generated power and on the other hand, it allows the owner to sell the EV energy to the grid for revenue generation. EV supplies power to the grid only when the owner requires to generate the revenue. The developed hybrid microgrid consists of RESs of PVGS, WPGS, FCGS, AC load, grid and a DC load i.e. EV load. The simulation results obtained from this study have been illustrated for the charging and discharging of EV load. The battery EV load is interfaced at DC-link through a bidirectional buck-boost converter. This enhances battery life and protects it from second harmonics. Further, the presented configuration is tested under the unbalanced grid voltage condition. The key feature of a microgrid is its seamless transition between grid-connected and standalone mode. This needs a robust control strategy for VSC operation and grid synchronization. Grid synchronization allows the practical implementation of such a system in the real-world on a large scale. In this chapter, grid synchronization method is presented and synchronization/de-synchronization operation of the microgrid is

tested.

6.1 Development of Hybrid Microgrid(HMG)

In this section, a hybrid microgrid is developed with an electrical vehicle load (EV), which is interfaced at DC-link as a battery. The system block diagram of the hybrid microgrid is shown in Fig.6.1. In the proposed hybrid microgrid system

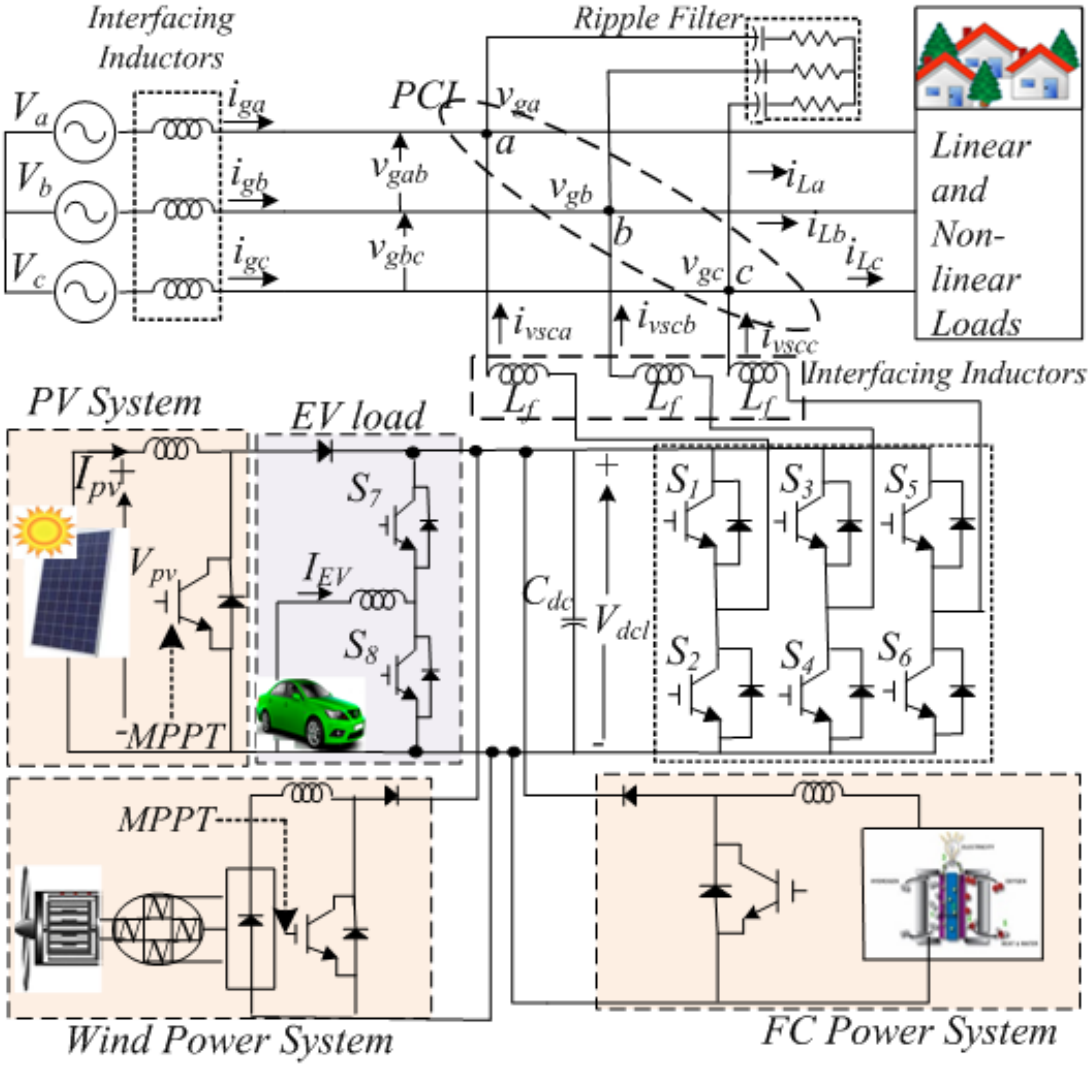

Figure 6.1: Hybrid microgrid for EV load

configuration, the PI controller is used to regulate the DC-link voltage. The EV load is integrated at DC-link through a bidirectional buck-boost converter. During the charging of EV, if RESs generated power is equal to the AC load demand plus EV required power then the grid power becomes zero and during surplus generation, power is injected into the grid. Furthermore, if RES generated power

is less than the total load demand, the deficit power is supported by the grid and power exchange with the grid starts at unity power factor. Hence, during the power deficit condition, grid supports the load and during surplus power time, the power is injected into the grid. The aim of the control technique is to ensure good quality of power supply and grid currents harmonics to be kept below the prescribed limit specified under IEEE-519.

6.1.1 Modelling of EV Load as A Battery Energy System

In the presented study, the EV load is considered as a battery. The electrochemical model of the lead-acid battery can be designed with the help of equations (6.1) to (6.6) [35, 36]. The equivalent circuit diagram of a battery is shown in Fig. 6.2. Open circuit voltage(E_m) of single-cell given in equation (6.24) approximates the internal electro-motive force (emf). The value of emf is considered constant during fully charged conditions and the variation in emf occurs with the change of temperature and state of charge (SOC).

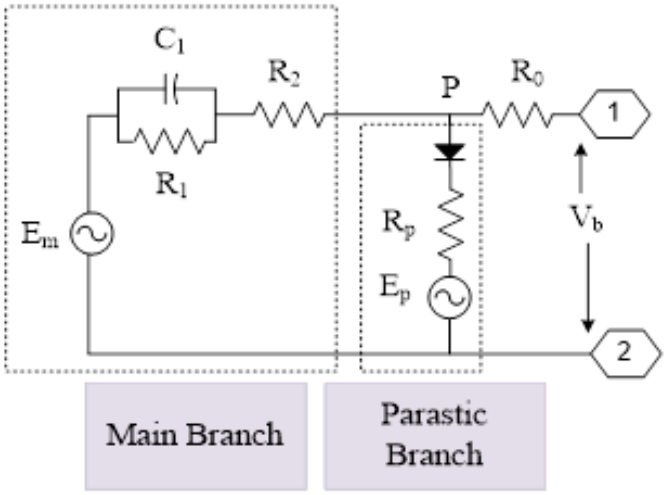

Figure 6.2: Equivalent circuit diagram of battery

$$E_m = E_{m0} - k_E(273 + \theta_e)(1 - SOC) \tag{6.1}$$

E_{m0} is open circuit charge at full voltage, θ_e is electrolyte temperature. During the charging of the battery, parasitic loss current occurs and can be given by equation (6.2):

$$I_p = V_{PN} G_{p0} exp(\frac{V_{pn}}{V_{p_0}(\sigma_p s + 1)} + A_p(1 - \frac{\tau}{\theta_f})) \tag{6.2}$$

where I_p, V_{PN}, G_{p0},σ_p, V_{P0}, A_p and θ_f are current loss in the parasitic branch, voltage at the parasitic branch, a constant in seconds parasitic branch time constant in seconds, constant in volts, another constant and electrolyte freezing temperature in ^{0}C respectively. The charge of the battery is obtained using the integration of the current flowing through the main branch. The extracted charge can be given by equation (6.3):

$$Q_e(t) = Q_{e-init} + \int_0^t -I_m(\sigma)d\sigma \tag{6.3}$$

where Q_e, $Q_{e\%\ init}$, I_m, σ, t are extracted charge (A-s), initial extracted charge(A-s), main branch current (A), integration time variable, simulation time (s). Battery capacity depends on discharge current and electrolyte temperature, whereas to calculate capacity during charging, discharge current is equal to zero in the given equation(6.4).

$$C(I, \theta_e) = \frac{K_c C_o + K_t}{1 + (K_c - 1)(\frac{I}{I^*})^{\delta_c}}; K_t = LUT(\theta_e) \tag{6.4}$$

where K_c, C_0, K_t, θ_e, I, I^*, δ_c are constant, no-load capacity at 0^0C (A-s), temperature-dependent look-up table (LUT), electrolyte temperature in ^{0}C, discharge current (A), nominal battery current (A) and a constant respectively. SOC is given by equation (6.5)

$$SOC = 1 - \frac{Q_e}{C(0, \theta_e)}; DOC = 1 - \frac{Q_e}{C(I_{avg}, \theta_e)} \tag{6.5}$$

where SOC, DOC, C, I_{avg} are the battery state of charge, battery depth of charge, battery's capacity (A-s), mean discharge current in (A) respectively. The thermal model of the battery comprises of thermal resistance and capacitance parameter and given by equation (6.6):

$$\theta_b(t) = \theta_{init} + \int_0^t \frac{P_s - \frac{\theta_b - \theta_a}{R_{\theta_b}}}{C_{\theta_b}} d\sigma \tag{6.6}$$

where θ_b, θ_a, θ_{init}, P_S, R_θ, C_θ, t is battery temperature in ^{0}C, ambient temperature in^{0}C, battery's initial temperature in ^{0}C and assumed to be equal to the surrounding ambient temperature, I^2R power loss of R_0 and R_2(W), thermal resistance in (^{0}C/W), thermal capacitance in (J/^{0}C) and simulation time(s) respectively.

Fig.6.3 shows the waveform of the battery voltage, current and SOC(%) with the variation of power. Initially, battery is charging and the negative notation of power indicates the charging of the battery. Hence, SOC(%) is increasing and battery current is negative. At t=0.5s, battery starts discharging the power to the load and SOC(%) starts increasing and battery current becomes positive.

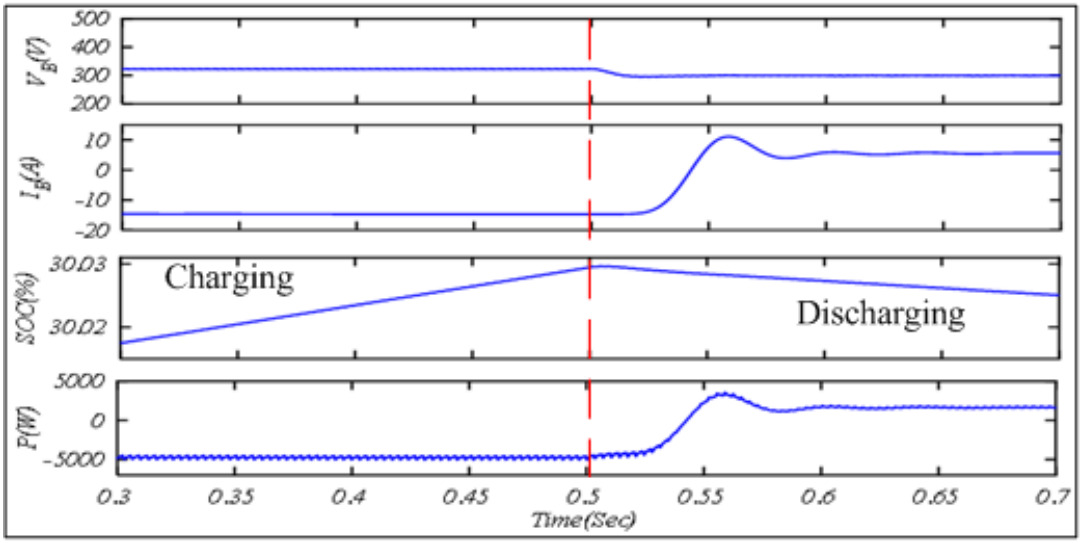

Figure 6.3: Waveform for battery charging and discharging

6.2 Self Tuning Filter Based Control of VSC

Self Tuning Filter (STF) is a class of filters in which the output is fed back to the input and extracts required frequency component from the input signal. STF control technique can be implemented on distorted load current or distorted supply voltage both. To extract the fundamental active load current components and generation of reference currents, STF control technique is implemented which further controls the switching instants of VSC. The STF is tuned for the fundamental frequency (314rad/sec) in this work. Thus, STF extracts the fundamental component from the input signal. Fig. 6.4 shows a complete control block diagram of VSC based on STF for PQ improvement in the HMG. In this work, STF is implemented on the α-β component of load current ($i_{\alpha L}$,$i_{\beta L}$) which are obtained by Clarke transformation. Filtered components ($i_{\alpha Lf}$, $i_{\beta Lf}$) are obtained at the output of the

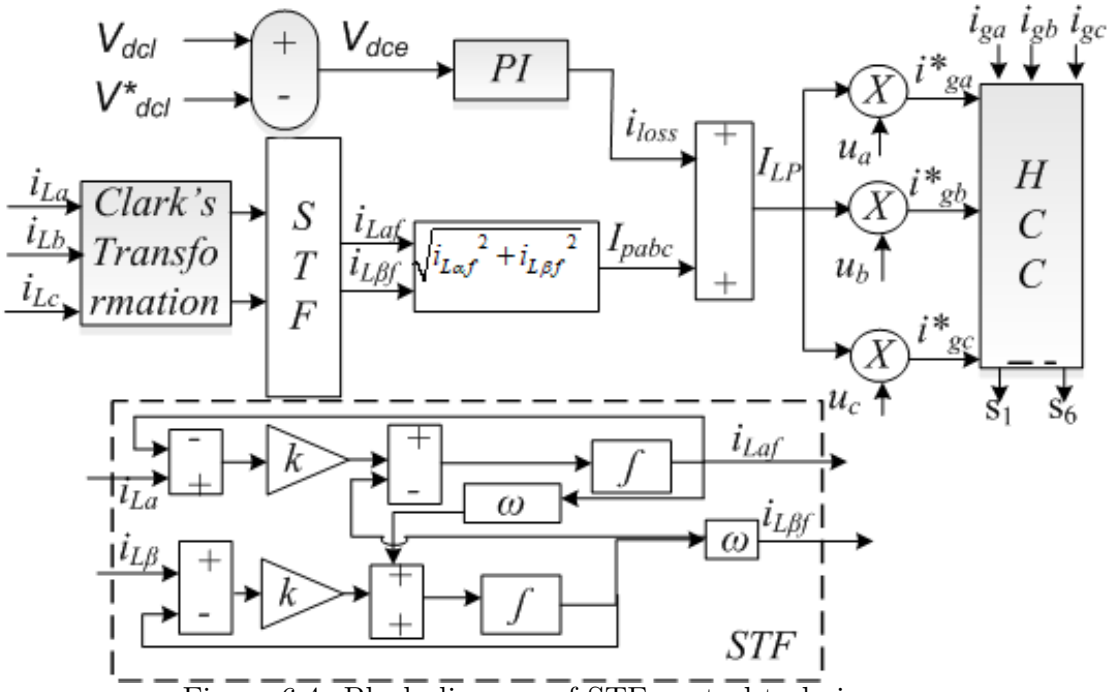

Figure 6.4: Block diagram of STF control technique

STF technique.

$$i_{\alpha Lf} = \frac{K * i_{\alpha L} - K * i_{\alpha Lf}}{s} - \frac{\omega * i_{\beta Lf}}{s} \tag{6.7}$$

$$i_{\beta Lf} = \frac{K * i_{\beta L} - K * i_{\beta Lf}}{s} + \frac{\omega * i_{\alpha Lf}}{s} \tag{6.8}$$

where ω is frequency taken as 314rad/s, K is a constant and taken is 0.5. The block diagram of STF is shown in Fig. 6.4. Three-phase load currents are first transformed into α-β component using Clarke transformation given by equation (6.9):

$$\begin{bmatrix} i_\alpha \\ i_\beta \end{bmatrix} = \frac{2}{3} \begin{bmatrix} 1 & -1/2 & -1/2 \\ 0 & \sqrt{3}/2 & -\sqrt{3}/2 \end{bmatrix} \begin{bmatrix} i_{La} \\ i_{Lb} \\ i_{Lc} \end{bmatrix} \tag{6.9}$$

For the nonlinear loads, the transformed α-β components of the load current are also distorted hence they are processed by STF as per equation (6.7) and (6.8). Obtained filtered load currents α-β components ($i_{\alpha Lf}$, $i_{\beta Lf}$) are used to calculate fundamental active power component (I_p) as given by equation (6.10):

$$I_{pabc} = (i_{\alpha Lf}^2 + i_{\beta Lf}^2)^{\frac{1}{2}} \tag{6.10}$$

The I_{Pabc} is added to the DC-link power loss component (i_{loss}) to obtain the effective active power component (I_{Lp}), which is discussed in the next subsection.

6.2.1 Generation of Reference Currents

As discussed in Section3. , the switching losses in the IGBT switches of VSC can be determined using the equation (6.11) and equation(6.12) as:

$$e_{dc}(m) = V^*_{dcl}(m) - V_{dcl}(m) \tag{6.11}$$

$$i_{loss}(m) = i_{loss}(m-1) + k_p(e_{dc}(m) - e_{dc}(m-1)) + K_i e_{dc}(m) \tag{6.12}$$

Now the PI controller output (switching losses) is added to the average fundamental load current component to get an effective active power component (I_{Lp}) can be given by equation (6.13):.

$$I_{Lp} = I_{pabc} + i_{loss} \tag{6.13}$$

Unit templates are computed using phase voltages (v_{ga}, v_{gb}, v_{gc}) and amplitude of PCI voltage (V_t), which are computed as discussed in chapter 3.

$$V_t = [\frac{2}{3}(v^2_{ga} + v^2_{gb} + v^2_{gc})]^2 \tag{6.14}$$

$$v_{ga} = \frac{2v_{gab} + v_{gbc}}{3}; v_{gb} = \frac{-v_{gab} + v_{gbc}}{3}; v_{ga} = \frac{-v_{gab} - 2v_{gbc}}{3} \tag{6.15}$$

where v_{gab} and v_{gbc} are the line voltages. Governing equations for unit phase template (u_a, u_b, u_c) are given by equation (6.16):

$$u_a = \frac{v_{ga}}{V_t}; u_b = \frac{v_{gb}}{V_t}; u_c = \frac{v_{gc}}{V_t} \tag{6.16}$$

To estimate the sinusoidal reference source currents (i^*_{ga}, i^*_{gb}, i^*_{gc}), unit templates are multiplied with active reference source current(I_{LP}). reference currents are given by equation (6.17)::

$$i^*_{ga} = u_a I_{Lp}; i^*_{gb} = u_b I_{Lp}; i^*_{gc} = u_c I_{Lp} \tag{6.17}$$

Obtained sinusoidal reference source currents are compared with sensed source currents and resultant errors are passed through the hysteresis current controller, which generates the gate pulses for the VSC. Generated reference grid currents are

sinusoidal, balanced, in phase with grid current and their magnitude is proportional to active power demanded by the load.

6.2.2 EV Charging Control in Constant Current/Constant Voltage Mode

The control of EV charging/discharging in constant current/constant voltage (CC/CV) mode is shown in Fig. 6.5. Two proportional-integral (PI) controllers are connected in a cascaded manner which forms two control loops. One loop controls the EV battery voltage and protects the battery from being overcharged. The voltage loop gives the reference currents. Thus, under the charging condition, the battery voltage is lesser as compared to the completely charged voltage value and the battery is charged in the constant current region. During charging of the battery, its voltage reaches the reference value and the charging shifts in the constant voltage region, which results in a decrement of battery charging current. The second loop is the inner current control loop. The error between the reference EV current (I^*_{EV}) and the sensed EV current (I_{EV}) is fed to the PI controller. The signal (I_er) thus obtained is passed through pulse width modulator (PWM) to generate the switching pulses (S_7, S_8) for the bi-directional converter.

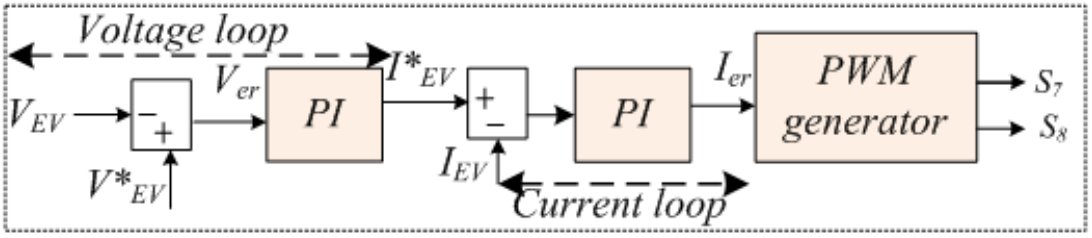

Figure 6.5: Block diagram of EV load control

6.3 Results and Analysis for Hybrid Microgrid

The developed hybrid microgrid system is simulated in MATLAB/Simulink platform. The simulation study on a hybrid microgrid system is carried out to test the effectiveness of control techniques for PQ improvement and appropriate power allocation under EV load. The simulation results for hybrid microgrid for balanced and variable linear load, balanced and unbalanced nonlinear load and variable

environmental conditions are discussed in subsequent sections. Further, the performance of hybrid microgrid is analyzed for charging and discharging of EV.

6.3.1 Response During EV Charging and Linear Load

The performance of the hybrid microgrid is analyzed for the variable linear load, variable solar irradiation and reactive power compensation in this section. EV load is interfaced for charging through the RESs. RES primarily charges the battery and then remaining power is used to maintain power balance between grid load and generation. PV generates 8kW, wind power generation is 6.5kW and fuel cell generation is 3kW under rated conditions. Therefore, the total generated power is 17.5kW under steady-state conditions. Fig. 6.6 presents the plot of parameters such as V_{dcl}, v_{PCI}, i_L, i_{VSC}, v_g and i_g of the hybrid microgrid system. To observe the performance of the MG at variable linear load, at t=0.35s linear load is increased from 16kW, 5kVAR to 24kW, 7.5kVAR. At 16kW AC load, the battery is charged with 0.5kW power and remaining surplus 1kW power injected into the grid. The reactive power requirement is met by VSC locally, hence grid is free form supplying reactive power. At t= 0.35s the load demand is increased to 24kW, 7.5 kVAR, the generated power first goes for battery charging (0.5kW) and thereafter the deficit power of 6kW is supported by the grid. The reactive power requirement is fulfilled through VSC only. Grid is free from supplying reactive power demanded by load. This ensures the reactive power compensation feature of the system. Due to the increased load, the deficit power is supplied by the grid which results in increased grid current. To examine the performance of MG under variable solar power, at t=0.5s the solar irradiation is reduced from 1000W/m^2 to 500W/m^2. This results in reduction in PV power causing the grid power to 10.5kW. The EV charging is still taking place. This verifies that the developed controller is working properly. The controller is designed such that RESs first charge the EV load and the remaining power is distributed among the grid and load. Continuous increment in battery SOC indicates EV charging throughout the operation. The increment in the grid current is noticed because the power supplied by the grid is increased. During all the dynamic changes, the DC-link voltage is maintained constant and PCI voltage is balanced and sinusoidal with constant amplitude.

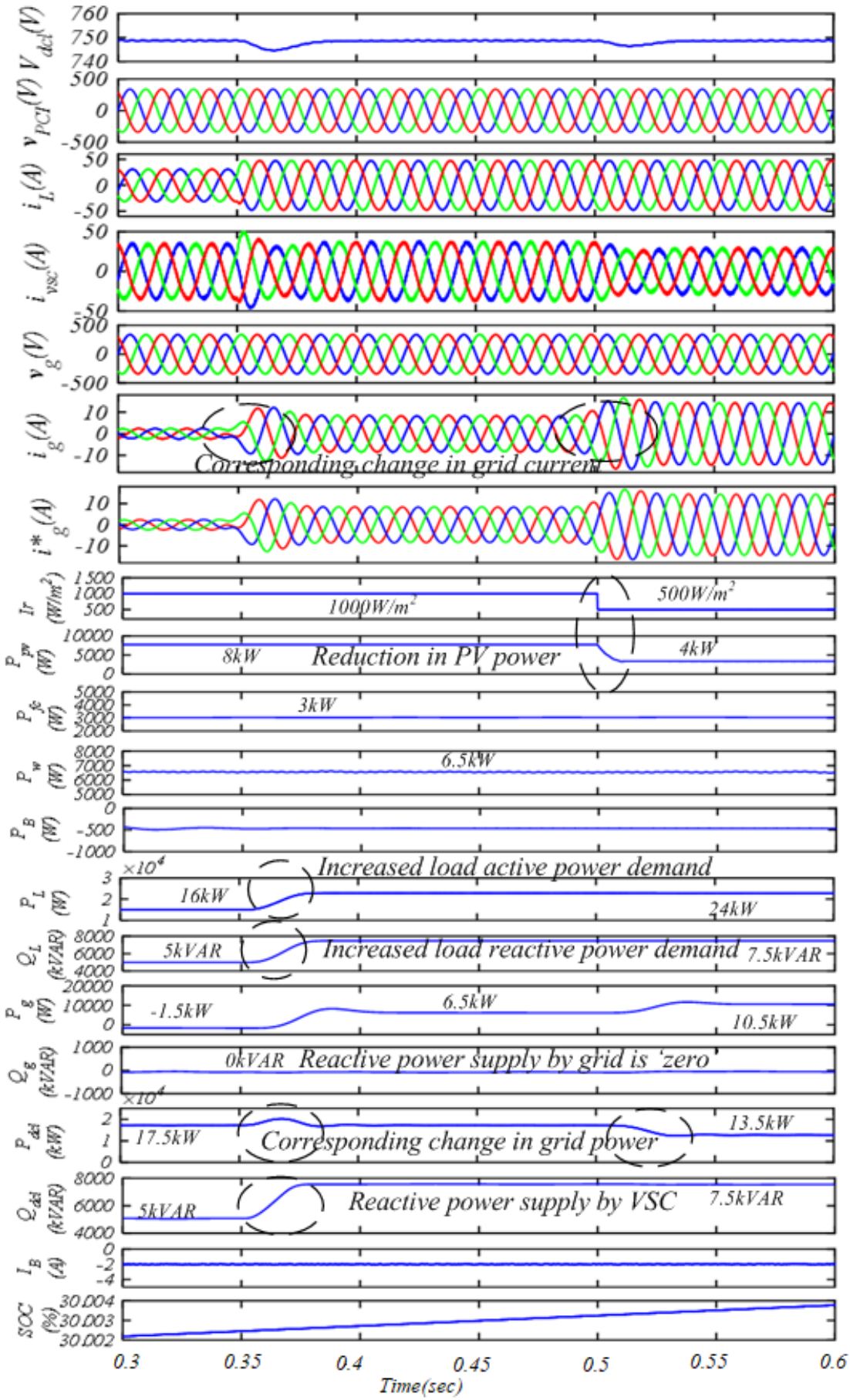

Figure 6.6: performance of HMG at variable linear load and irradiation

6.3.2 Response During EV Charging and Varying Wind Speed

Fig. 6.7 exhibits the performance of the hybrid microgrid for varying wind speed under the balanced linear load. During the operation, it is considered that the EV load is interfaced into the system in neutral condition, hence it will not charge/discharge any power. To study the system response for variable wind generation, initially, the load demand is kept constant at 24kW and HMG is working under the steady-state condition with 12m/s wind speed. The reduction in wind speed is introduced at t=1s and again increased to 12m/s at t=3s. The reduction in wind speed results in reduced wind power generation. At the reduced generation, the power drawn from the grid is increased to supply the deficit power required by the load. However, power supplied by PVGS and FCGS remains constant. At t=8.5s, active power requirement of the load is increased to 26kW. Therefore, the power supplied by the grid is further increased to 9kW. Increased grid power (P_g) can be noticed in Fig. 6.7 during reduced wind speed and the corresponding change in the grid current can also be noticed from Fig. 6.7. A constant DC-link voltage is observed and the corresponding power is shown in Fig. 6.7. Transients in DC-link voltage are negligible due to two mass drive train model, which is more realistic and the response time of this model is slow to capture the change in DC-link voltage. The grid current and PCI voltage are balanced and sinusoidal. The DC-link is controlled at its reference value (750V) throughout the performance by PI regulator. The variation in load demand causes a change in grid current and grid power only. However, power available at DC-link remains unaffected. Furthermore, the charging current and power output of EV load remain unaffected. The SOC of the battery remains unaffected since EV load is interfaced in neutral condition, neither in charging nor in discharging condition. Results show that the power equilibrium is achieved and the system is working effectively under all dynamics. Using the presented topology, a residential microgrid can be developed in which a small wind turbine, fuel cell and a PV array feed the domestic loads, charge the EVs and support the grid with surplus generation along with the power quality improvement.

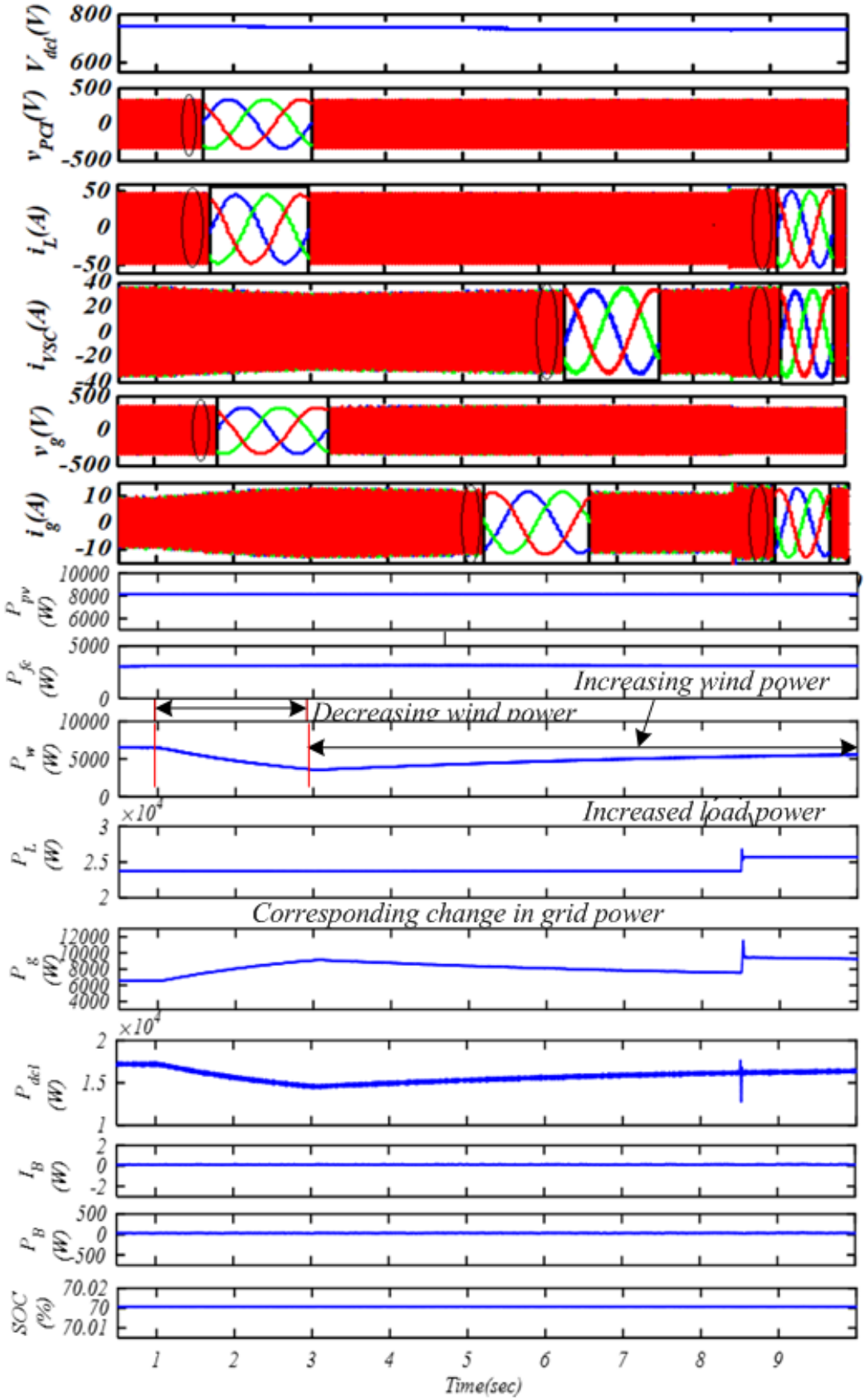

Figure 6.7: Response at varying wind speed

6.3.3 Performance for EV Charging/Discharging at Constant Load and Power Generation

Fig. 6.8 presents the results of the hybrid microgrid system consisting of EV load at DC-link and linear load at the AC bus. Designed microgrid charges the EV together with feeding other loads, feeding power back to the grid and improving the grid's power quality. The result shows the performance of HMG for EV charging/discharging. For a better understanding of hybrid microgrid, its operation is carried out under standard test conditions (constant power generation and constant load). A constant linear load of 12.5kW is considered for the analysis of charging and discharging of the EV load (10Ah, 240V battery). The RESs generation is kept constant and to its rated value of 17.5kW during the analysis. Fig. 6.8 shows the DC-link voltage(V_{dcl}), PCI voltage (v_{PCI}), three-phase load current(i_L), three-phase VSC current (i_{VSC}), three-phase supply voltage(v_g) and three-phase grid currents (i_g) of hybrid microgrid system. The grid currents are sinusoidal and balanced during all the transients. Moreover, the PCI voltages are constant in magnitude and sinusoidal. DC-link voltage is being regulated. These results validate the efficacy of the presented VSC control technique for the linear load. Initially, EV is not connected to the system and EV load is integrated into the system for charging at t=1.3s. The RES power is charging the EV and remaining power is supplied to the load. However, the surplus power of RESs is injected into the grid, therefore at t= 1.3s change in grid power can be noticed and the power injected into the grid is reduced. While at t=1.45s, EV is interfaced for discharging. In this mode of operation, EV is supplying the power to the grid and EV owners may sell the EV power to the grid during peak hour electricity charges when the EV battery is charged, or it can be used to support the household loads (in off-grid mode) in case of the high tariff. This may lead to the source of revenue generation for EV owners. Due to power fed into the grid, grid power is increased and it is noticed from Fig. 6.8. Power equilibrium is achieved for all charging/discharging conditions.

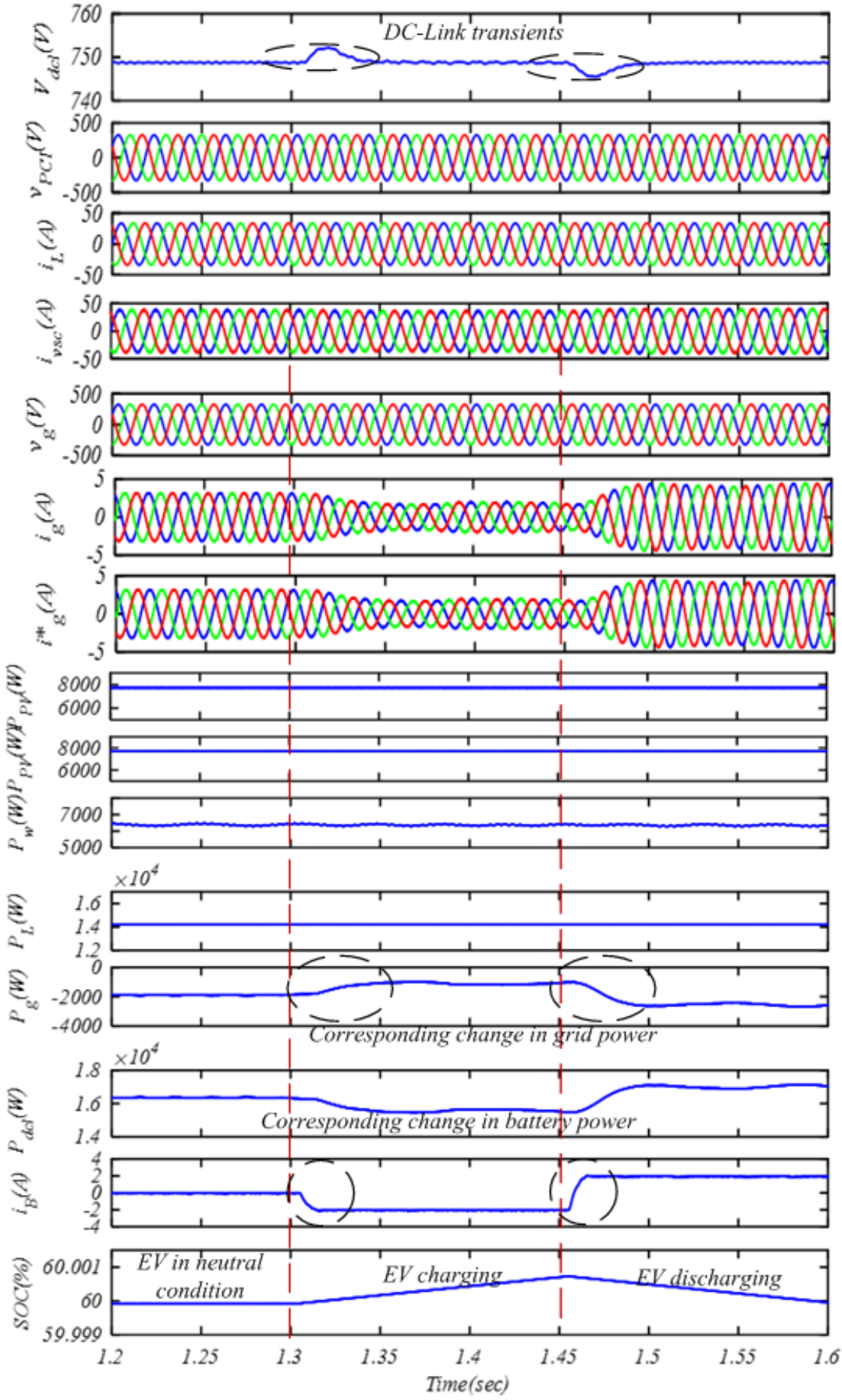

Figure 6.8: Performance of HMG with EV load

6.3.4 Response During EV Discharging and Nonlinear Load

Nonlinear loads create harmonics in the voltages and currents. Hence, the PQ issues occurring during load and generation transients in MG are thoroughly investigated in this section. Fig. 6.9 exhibits the performance of the hybrid microgrid for balanced and unbalanced nonlinear load. During the operation, it is considered that the EV load is interfaced into the system to inject the power into the grid. Therefore, EV load is working under discharging mode. Load unbalancing is introduced by removing the one phase from the load at t=0.8s, further, this phase is reintegrated into the system at t=0.95s. The removal of phase reduced the load demand hence, the grid will draw more power which results in the increment of grid current. With the change in nonlinear load, the corresponding change in grid power and grid current can be noticed in Fig. 6.9. However, the discharging current and power output of EV load remain unaffected during any load change. Increased grid current (i_g) can be noticed in Fig. 6.9 during unbalanced load conditions. Moreover, the balanced sinusoidal grid currents and PCI voltage are obtained even under highly distorted load currents and unbalanced load through extracted signal from the load current and perfectly generated reference for the grid. Grid voltages are also observed as perfectly sinusoidal and balanced with constant amplitude. A DC-link is settled after a small transient and controlled at its reference throughout the operation. Fig. 6.9 shows that the SOC of the battery will be reduced due to the discharging process of the battery. Moreover, the power balance is achieved during the performance. Fig. 6.10 shows the THD spectra of the hybrid microgrid system under nonlinear load. Load current THD is 26.18% and through effective control technique (STF) the grid current THD is reduced to 2.89%. Further grid voltage THD is observed 1.69% this exhibits that the system is perfectly working for PQ improvement. Grid currents and voltages are found to be sinusoidal and balanced. Constant amplitude PCI voltage ensures good quality of power at the consumer end. The developed system is operating to ensure the PQ norms are met satisfactorily.

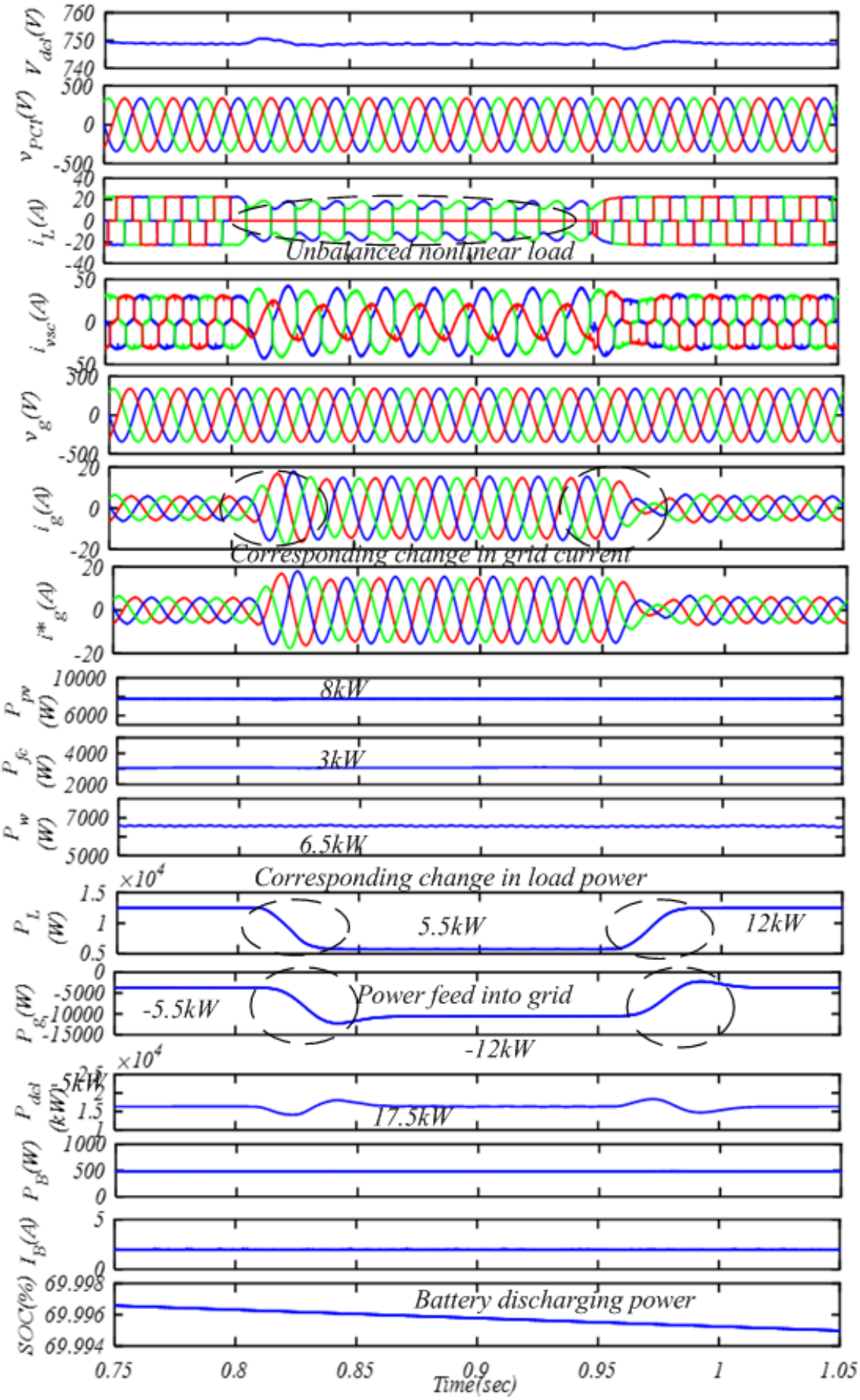

Figure 6.9: HMG performance at unbalanced nonlinear load

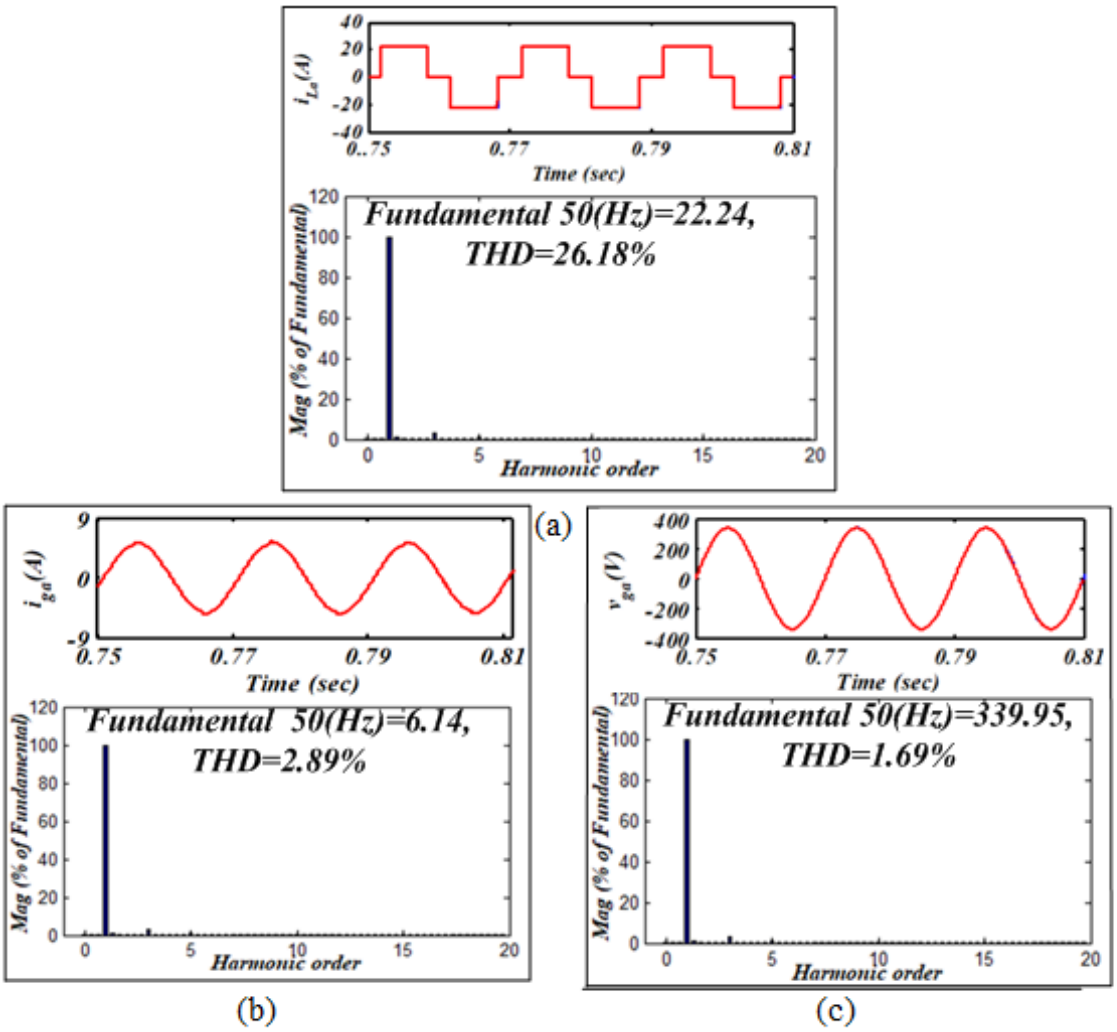

Figure 6.10: Harmonic spectra using STF control technique at the nonlinear load (a)i_L and its THD (b) i_{ga} and its THD (c)v_{ga} and its THD

6.4 Control Under Unbalanced Grid Condition

In the previous section, a detailed analysis of the PQ problem in a grid-connected hybrid microgrid system has been discussed. The assumption in the previous section was that the grid supply is sinusoidal and has low THD. The supply is considered stiff and unaffected by the type of load present. Hence, the generation of unit templates for synchronizing the VSC to the grid can be computed easily. In this section, PQ problems of the unbalanced grid voltage are analyzed. In unbalanced grid voltage conditions, the supply voltage is not perfectly sinusoidal. The waveforms of PCI voltage may be unbalanced and having higher THD than the allowed limit. The generation of templates that are sinusoidal and balanced in

phase is a challenge since the conventional approach of generating unit template does not give an adequate response. The generation of the unit templates under unbalanced grid needs the extraction of the fundamental component of supply voltage to generate sinusoidal reference currents. Here control is divided into two parts viz. the first part extracts the active component of load current to generate reference source current which is estimated by the SOGI control technique. The other part is to extract the fundamental component of grid voltage using a suitable technique. Double Second-Order Generalized Integrator (DSOGI) is used here and simulated to extract the fundamental component of supply voltage to generate sinusoidal unit templates under unbalanced supply voltage conditions. The complete block diagram of VSC control using SOGI is shown in Fig. 6.11.

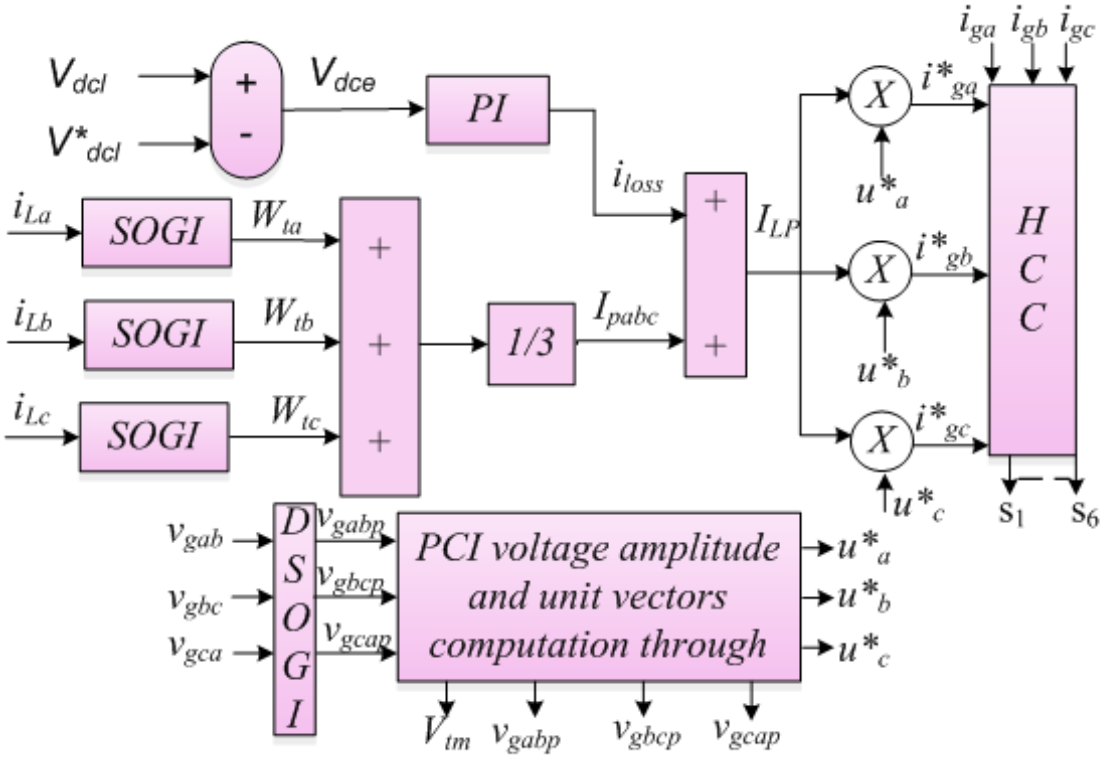

Figure 6.11: Block diagram of VSC control using SOGI

Detailed block diagram of SOGI control is shown in Fig. 6.12 and detailed analysis of DSOGI is discussed in the following subsection.

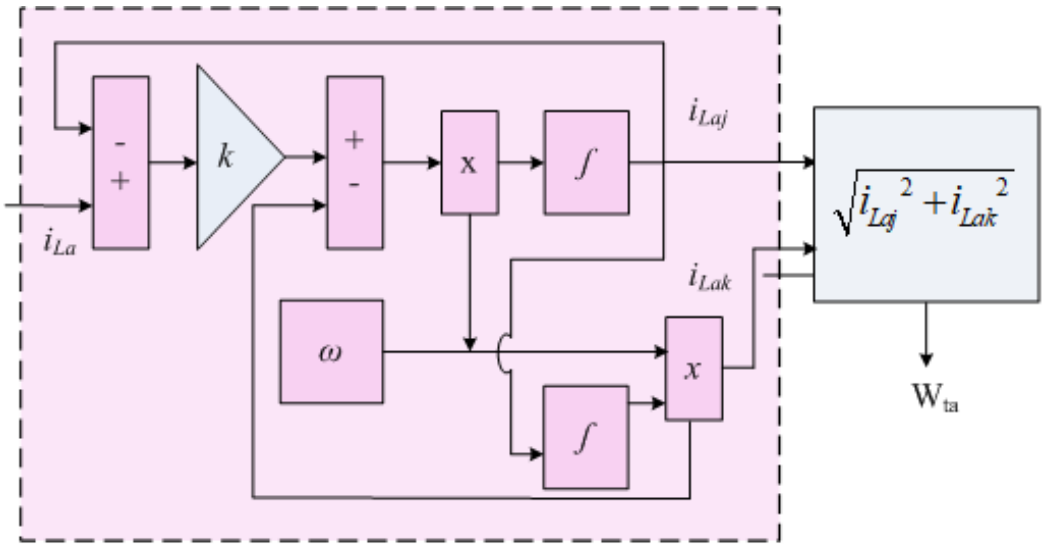

Figure 6.12: Block diagram of SOGI

6.4.1 Double Second Order Generalized Integrator (DSOGI) Based Control

SOGI is a second-order general-purpose transfer function. Under the unbalanced voltage condition, to estimate the harmonic free unit template, the positive sequence voltages are estimated using two SOGI filters as shown in Fig. 6.13.

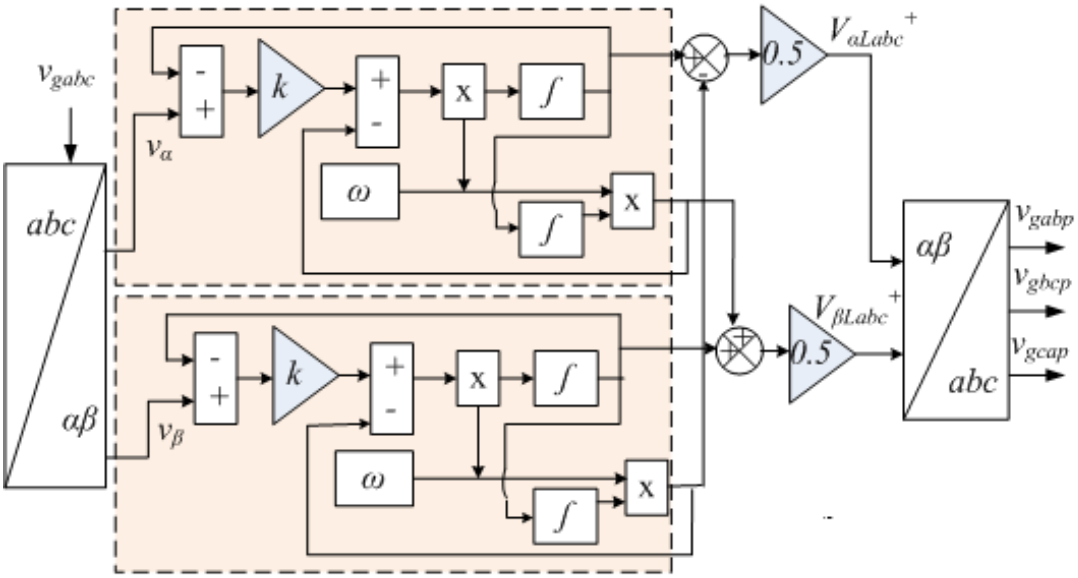

Figure 6.13: Block diagram of DSOGI control

During unbalanced source voltage, SOGI gives positive sequence voltages, which is used to estimate balanced sinusoidal unit templates and further used to

generate sinusoidal reference currents. SOGI is applied to estimate the in-phase and quadrature frequency components of the input signal. The input signal is voltage and its output has two components i.e. in-phase and quadrature components. The in-phase and out phase component of grid voltage can be represented by equation (6.18) and (6.19):

$$\frac{v_{\alpha gabc}}{v_{gabc}} = \frac{\omega s}{s^2 + \omega^2} \tag{6.18}$$

$$\frac{v_{\beta gabc}}{v_{gabc}} = \frac{\omega^2}{s^2 + \omega^2} \tag{6.19}$$

where ω is fundamental frequency and $v_{\alpha\ \mathrm{Labc}}$, $v_{\beta \mathrm{Labc}}$ are in-phase and quadrature output components for the SOGI transfer function. This generalized SOGI function suffers the resonance problem and because of this resonance, the output can increase in an uncontrolled manner. Hence a feedback loop is inserted to mitigate this problem. Transfer function after introducing feedback loop now becomes:

$$\frac{v_{\alpha gabc}}{v_{gabc}} = \frac{K\omega s}{s^2 + k\omega s + \omega^2} \tag{6.20}$$

$$\frac{v_{\beta gabc}}{v_{gabc}} = \frac{K\omega^2}{s^2 + k\omega s + \omega^2} \tag{6.21}$$

where K is constant and s is the Laplace operator. The two outputs of SOGI function are in-phase and quadrature signals. Constant gain k is responsible for the bandwidth of the SOGI function. A small value of k (0-1) leads to narrower bandwidth whereas, the large value leads to slow response. So, the value of k has to be chosen judiciously for obtaining a good rejection band and faster dynamic response. The unit templates are computed using phase voltages (v_{sap}, v_{sbp}, v_{scp}) and amplitude of PCI voltage (V_{tm}), which are computed by equation (6.22):

$$V_t = [\frac{2}{3}(v_{gap}^2 + v_{gbp}^2 + v_{gcp}^2)]^{\frac{1}{2}} \tag{6.22}$$

where v_{gabp} and v_{gbcp} are the positive sequence voltages of v_{gab} and v_{sbc}. Governing equations for unit phase template (u^*_{a}, u^*_{b}, u^*_{c}) are given by equation (6.23):

$$u_a^* = \frac{v_{gap}}{V_t}; u_b^* = \frac{v_{gbp}}{V_t}; u_c^* = \frac{v_{gcp}}{V_t} \tag{6.23}$$

Further, to estimate the sinusoidal reference source currents (i^*_{ga}, i^*_{gb}, i^*_{gc}), unit templates are multiplied with active reference source current component (I_{Lp})

which is estimated using SOGI control approach. Reference currents are given by equation (6.24):

$$i_{ga}^{*} = u_{a}^{*} I_{Lp}; i_{gb}^{*} = u_{b}^{*} I_{Lp}; i_{gc}^{*} = u_{c}^{*} I_{Lp} \tag{6.24}$$

Obtained sinusoidal reference source currents are compared to sensed source currents and errors passed through the hysteresis current controller. Six gating pulses are generated and fed to VSC for proper operation of microgrid system. The supply currents follow the reference currents and hence become sinusoidal and are balanced and sinusoidal.

6.4.2 Results and Analysis for Unbalanced Grid Condition

Fig. 6.14 shows the simulation results with DSOGI control technique for 415V,50Hz, three-phase three-wire microgrid system under the unbalanced grid supply condition. Fig. 6.14 presents supply voltage($\mathrm{v_g}$), filtered positive sequence voltages ($\mathrm{v_{gp}}$), supply currents ($\mathrm{i_g}$), generated reference current (i_g^*), load current ($\mathrm{i_L}$), VSC current ($\mathrm{i_{VSC}}$) and DC-link voltage ($\mathrm{V_{dcl}}$) of the microgrid for balanced and unbalanced nonlinear load. The nonlinear load comprises a diode bridge rectifier with RL load. The supply voltages are observed to be unbalanced initially and at t=0.6 grid supply voltage becomes balanced. The DSOGI control algorithm is implemented to extract the fundamental voltage from the unbalanced grid voltages. The extracted fundamental components (($\mathrm{v_{gp}}$) are distortion-free, balanced and sinusoidal. SOGI control approach for VSC is implemented on the load currents to get the reference currents for the grid. The requisite performance of the controller is observed for nonlinear balanced and unbalanced load conditions. To introduce unbalancing, one phase of the load is removed at t=0.4s and it is reconnected to the system at t=0.5s under unbalanced grid conditions. Removal of one phase of the load leads to reduction in load demand and hence, surplus power is injected into the grid from t=0.4 to t=0.5s. Hence, the magnitude of grid current increases from t=0.4s to t=0.5s. It is observed that the grid currents are purely sinusoidal and balanced for unbalanced grid supply voltage and unbalanced nonlinear load during t=0.4 to t=0.5s. Sinusoidal and balanced fundamental voltages are extracted even under the unbalanced supply voltage. At t=0.6s, the grid supply voltage becomes sinusoidal

and balanced and grid current is reduced to maintain the power balance. The DC-link voltage has been regulated at 750V throughout the operation. The results show that DSOGI control is effective under unbalanced grid supply conditions in PQ problem mitigation.

Figs. 6.15(a)-(b) show phase 'a' load current (i_{ga}) and phase 'a' grid current (i_{La}) waveforms and their THD respectively. The THD of supply current is 1.99% and load current THD is 34.04%. It is observed that SOGI and DSOGI work well for fundamental extraction of current and voltage respectively. Fig. 6.16 shows THD in the filtered supply voltage and it is found to be 1.4%.

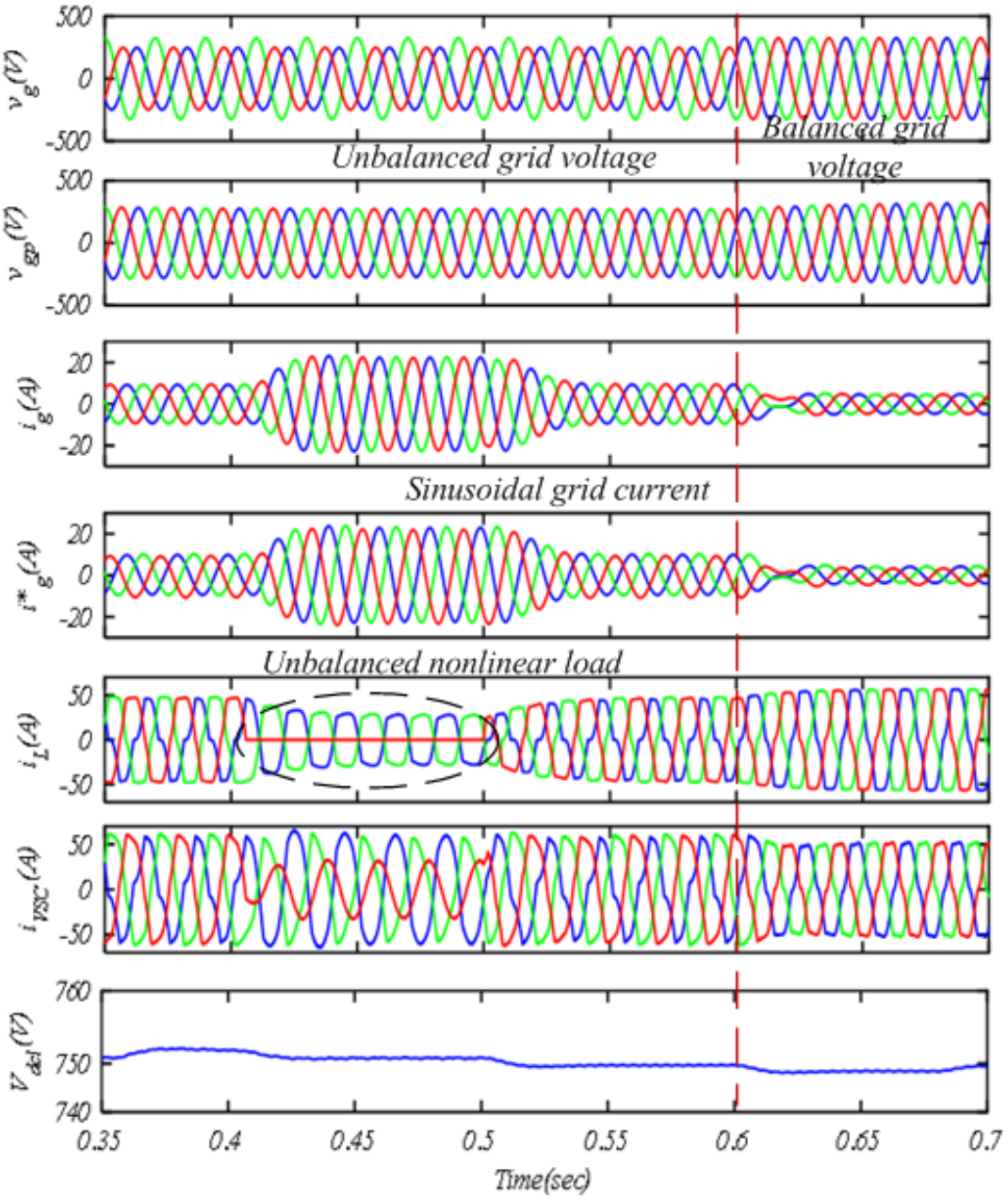

Figure 6.14: System response using DSOGI control for unbalanced grid voltage

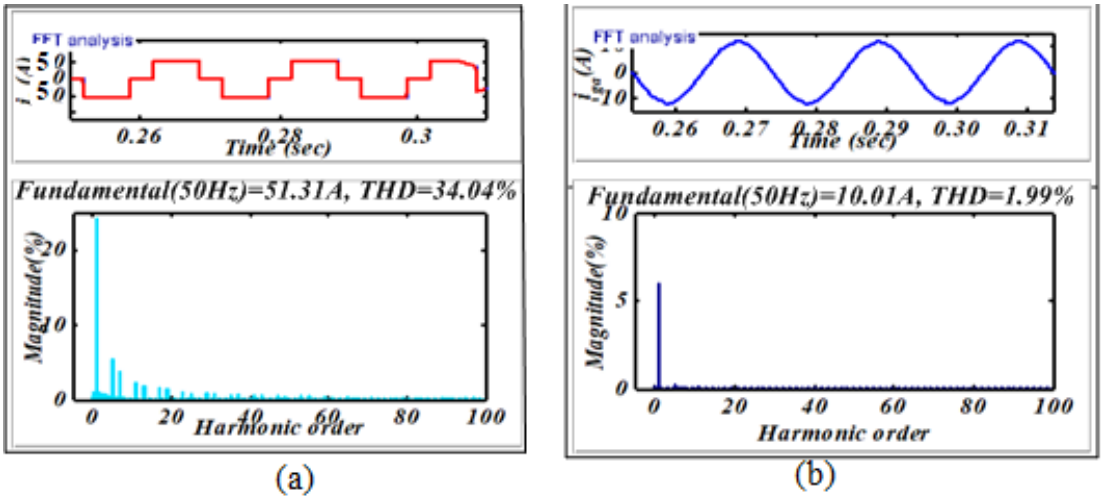

Figure 6.15: Harmonic spectra using SOGI control technique for the nonlinear load (a) i_L and its THD (b) i_{ga} and its THD

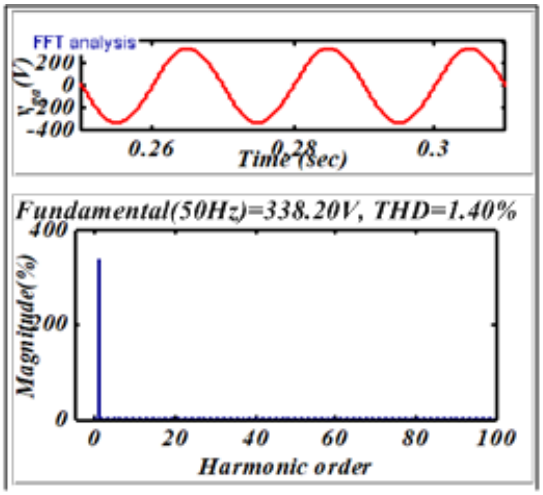

Figure 6.16: Harmonic spectra of v_{gpa} using SOGI control technique and its THD

6.5 Operation Under Grid De-Synchronization and Synchronization

In the previous sections, microgrid operation has been performed in grid-connected mode only. Microgrid is capable to feed the active power with improved power quality of grid currents and load reactive power compensation. One of the prime characteristics of the microgrid is its capability of seamless transition from grid-connected mode to standalone mode to feed critical loads and capability to operate into grid-connected mode after the removal of fault. Under grid fault situation, the developed microgrid is capable of operating in stand-alone mode or

disconnected from the main grid which can be reconnected to the grid after the removal of fault. The resynchronization action is performed through LPN-PLL (Low-Pass Notch Filter Phase Locked Loop) intelligent synchronization control technique. On the basis of operation, the control approach of the microgrid can be divided into three subsections viz. standalone mode, grid interfaced mode, synchronization and interfacing to the grid again.

6.5.1 VSC Control Under Grid-Connected Mode

The STF based VSC control approach is implemented to generate the reference supply current under grid-connected mode. The detailed disruption of STF control technique for grid interfaced system is given in Section 6.2.

6.5.2 VSC Control Under Stand-Alone Mode

In off-grid mode, the VSC is used to generate the three-phase voltage at PCI to supply power to the load. In standalone mode, the objective of the control approach is to realize sinusoidal, balanced and constant magnitude PCI voltages. The VSC control scheme in the standalone mode is shown in Figs. 6.17. VSC generates the rated voltage at PCI through an accurate control approach. The peak value of reference phase voltages is taken as 338.8V at 50Hz frequency. The reference sinusoidal phase voltages are expressed by equation (6.25):

$$V_{ref,a} = V_a sin(\theta_m);\ V_{ref,b} = V_b sin(\theta_m - 120^0);\ V_{ref,c} = V_c sin(\theta_m + 120^0) \quad (6.25)$$

where,$\mathrm{v_{a,b,c}}$ are reference voltage magnitudes, θ_m is the reference phase angle. Thus, achieved reference voltage signals are compared with measured PCI voltage and the obtained error is processed through the PI controller to obtain reference VSC current. The PCI voltages are computed through line voltages and given as:

$$v_{ga} = \frac{2v_{gab} + v_{gbc}}{3}; v_{gb} = \frac{-v_{gab} + v_{gbc}}{3}; v_{ga} = \frac{-v_{gab} - 2v_{gbc}}{3} \quad (6.26)$$

Further, these estimated reference currents are compared with instantaneous PCI currents and thus obtained error signal is passed through a hysteresis controller to generate the switching pulses of VSC.

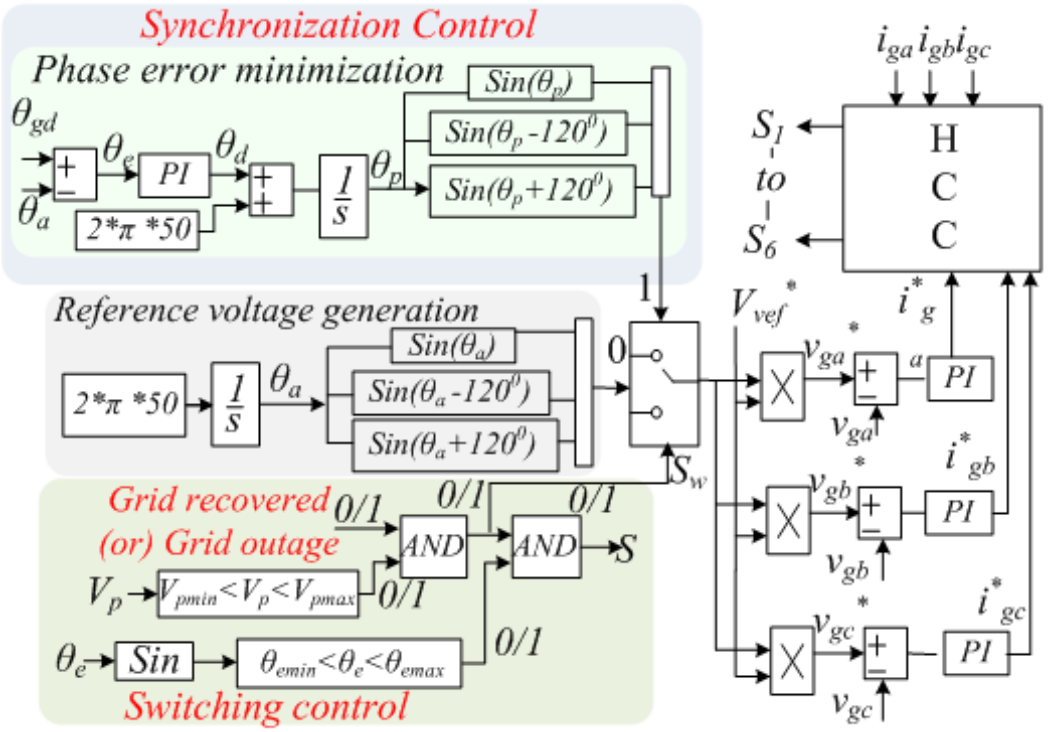

Figure 6.17: Schematic diagram for control in an autonomous mode of MG for VSC and synchronization control

6.5.3 Low-Pass Notch Filter PLL Based Gid-Synchronization Control

A standalone microgrid can be connected to the grid only when the voltage, phase angle and frequency of both grid and standalone MG are synchronized. The synchronization controller is required to estimate the voltage and phase angle of the grid and autonomous MG for the grid restoration. A phase lock loop (PLL) converter is conventionally used for this purpose. In this work, the low-pass notch filter PLL (LPN-PLL) is implemented to realize the restoration of the main grid. The schematic control block diagram is shown in Figs. 6.18. LPN-PLL estimates

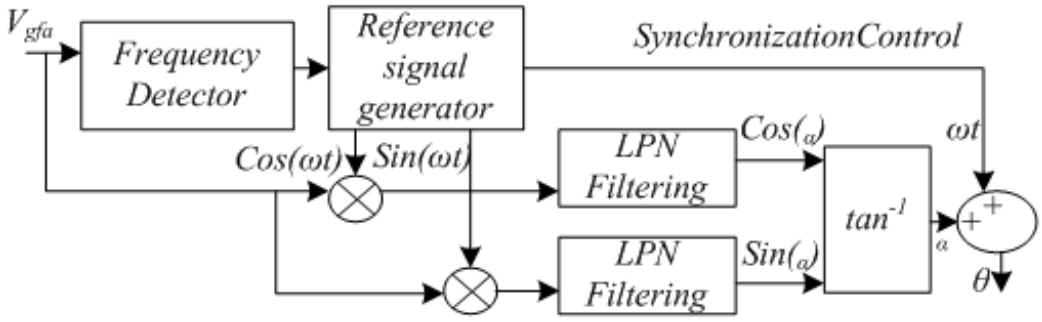

Figure 6.18: Block diagram of LPN-PLL control scheme

the phase angle of the grid and PCI voltage of the standalone system, then a PI controller is used to achieve the synchronization of the grid and PCI voltages. The output of the PI controller is represented by equation (6.27):

$$\theta_d(m) = \triangle\theta_d(m-1) + k_{ps}(\theta_e(m) - \theta_e(m-1)) + k_{is}\theta_e(m) \tag{6.27}$$

where $\theta_{\,\mathrm{d}}$ is a signal obtained from the PI controller and $\theta_{\,\mathrm{e}}$ represents the grid error signal. $\theta_{\,\mathrm{e}}$ is computed by equation (6.28):

$$\theta_e = \theta_{gd} - \triangle\theta_a \tag{6.28}$$

where $\theta_{\,\mathrm{gd}}$ is a voltage angle of the grid and $\theta_{\,\mathrm{a}}$ is the angle of standalone voltage. $\theta_{\,\mathrm{d}}$ and $\theta_{\,\mathrm{a}}$ are used to compute a new phase angle $\theta\,(_{\mathrm{p}})$ and can be expressed as,

$$\theta_p = \theta_a - \triangle\theta_d \tag{6.29}$$

When $\mathrm{V_p}$ magnitude, phase and frequency are within the prescribed limit, the output of AND gate is '1' and the grid restoration takes place. The control logic diagram is shown in Figs. 6.17.

6.5.4 Result and Analysis for Synchronization

Figs. 6.19 shows the performance of HMG under grid-connected, standalone and grid resynchronization mode. The performance is analyzed on the basis of the three-phase supply voltage($\mathrm{v_g}$), three-phase supply currents ($\mathrm{i_g}$), three-phase load current($\mathrm{i_L}$) and three-phase VSC current ($\mathrm{i_{VSC}}$) for balanced and unbalanced nonlinear load. Initially, the system is working under grid-connected mode. The desynchronization takes place during the grid outage. In Fig. 6.19, at t=0.4s, the grid is unavailable. Therefore, the grid currents and voltages become absent. The de-synchronization process appears when the grid outage occurs. At the same instant, the control is changed from the grid-connected to the standalone mode. Therefore, the VSC currents are also changed. It is observed from Figs. 6.19 that during standalone operation the sinusoidal load voltage is obtained. This ensures that the good quality of power is available at the consumer end. At t=0.5s the grid is available and the synchronization process of the hybrid microgrid starts. The grid appears when the grid voltages are available at t=0.5s. The synchronization

process with the grid is accomplished within the few cycles. At t =0.6s, when the magnitude of voltage and angle is within the prescribed limit the synchronization takes place. Therefore, the grid currents (i_{gabc}) have appeared. The grid θ_g and VSC voltages angle θ_s are synchronized. The VSC current is increased as VSC is injecting the surplus power into the grid. The changeover between grid-connected mode to an island mode and further into the grid-integrated mode is realized smoothly using the LPN-PLL synchronization technique.

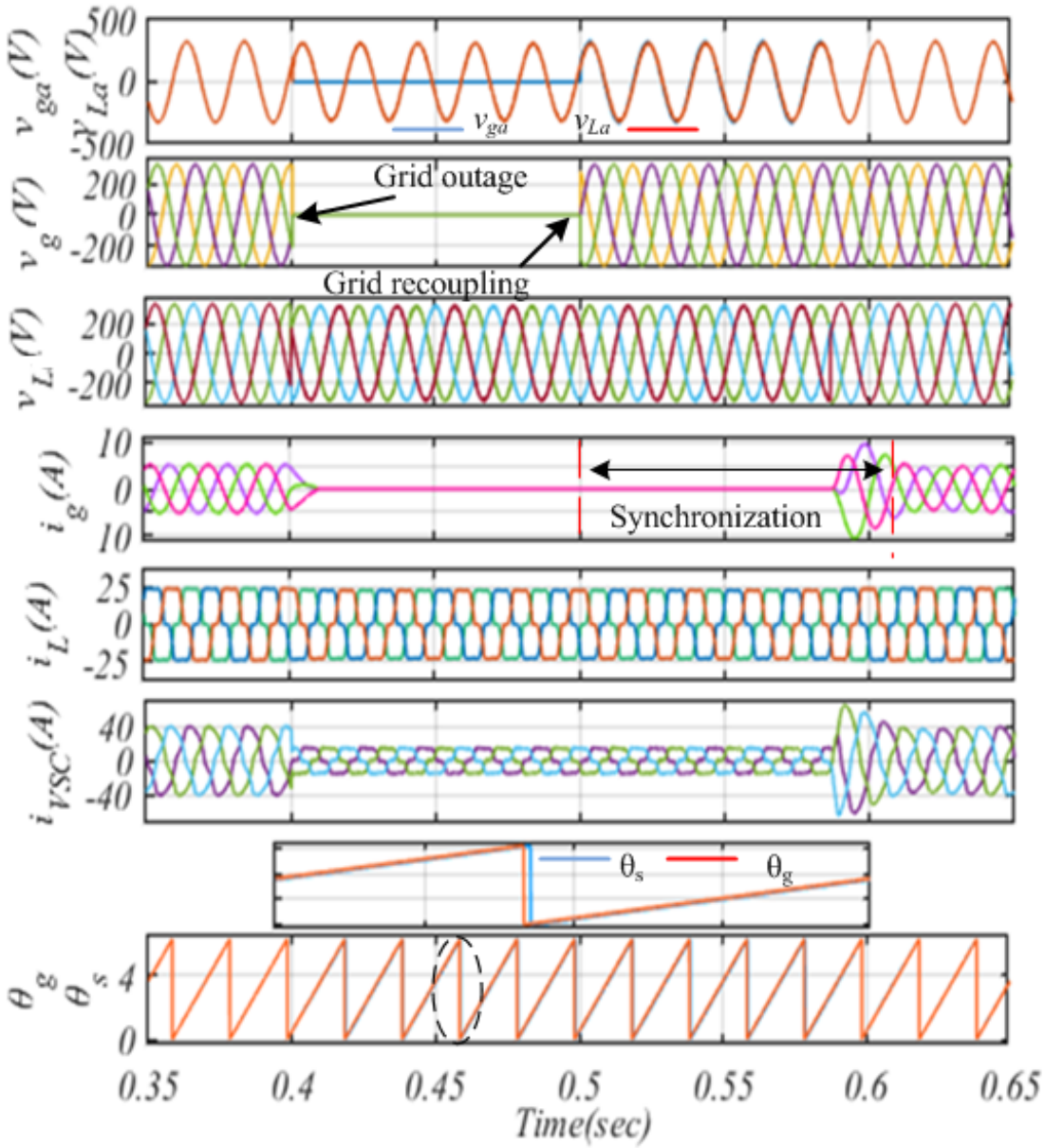

Figure 6.19: System response for grid resynchronization

6.6 Conclusions

A hybrid microgrid is designed in this chapter. Results exhibit that the microgrid and its control system are operating perfectly as designed. PQ problems have been mitigated in the hybrid microgrid under balanced and unbalanced nonlinear load, variable linear load and variable power generation. Results show that the developed configuration is sustainable under dynamic conditions and working under power equilibrium. EV load is interfaced with the DC-link and its charging or discharging does not get affected by the change in load or power generation by the RESs. The developed microgrid is also tested under unbalanced grid voltage conditions using SOGI control technique. Proposed DSOGI control is perfectly extracting the fundamental components of grid voltage to generate the reference voltage. SOGI is implemented to extract the fundamental component of load current to generate the reference signal for VSC switching. Results verify the effective working of both the controls. Furthermore, the presented microgrid has been tested for the seamless transition between grid-connected and standalone mode. The results verify that the synchronization and de-synchronization operation with the grid can be performed seamlessly.

Chapter 7

DEVELOPMENT OF STAND-ALONE MICROGRID

7.1 Introduction

This chapter discusses the design of a standalone hybrid power source microgrid with power controllers and associated controls. The developed microgrid comprises PVGS-WPGS with the backup of FCGS, battery and electrolyzer. The electrolyzer is acting as a dump load. Nonlinear loads are the main sources of poor power quality. In order to alleviate power quality problems and supply good quality voltage to the customer, new and intelligent controllers for the inverter need to be developed. In case of the stand-alone system, control of AC voltage in terms of amplitude and frequency is a critical issue. The inverter controller ensures balanced line voltage at the PCI resulting in good quality supply at the customer end. Moreover, control is developed for integrated power management among different energy sources.

The developed grid-independent microgrid system is shown in Fig. 7.1. It consists of PVGS and WPGS system as a primary energy source and backup power is delivered using FCGS and battery energy system (BES). The electrolyzer is integrated into the system to store the surplus generated power. Each source is connected through its individual DC-DC converter and controlled independently. Power flow is unidirectional due to the presence of the DC-DC converters. All energy sources are

integrated at common DC-link, which is further connected to the PWM inverter and AC load. The topology has the additional advantage of using a single DC-AC inverter which leads to cost-saving.

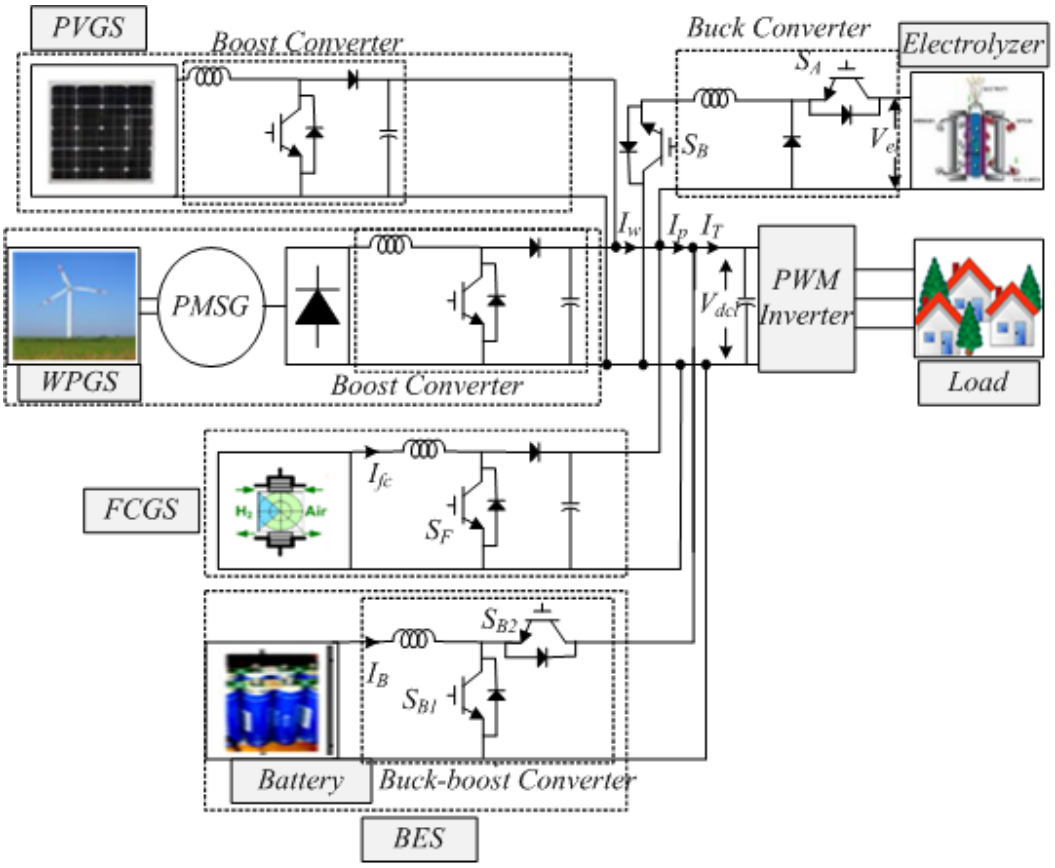

Figure 7.1: Block diagram of stand-alone microgrid

7.2 Modelling of Components

Detailed modelling of PVGS, FCGS, Battery and WPGS is already discussed in Chapter 3. The modelling of BES is explained in Chapter 6. The modelling of electrolyzer is presented in the following subsection.

7.2.1 Modelling of Electrolyzer

An electrolyzer model is developed for the standalone microgrid for rating of 8kW, 30A, 300V. Electrolyzer model is realized using the following equation (7.1) [24]:

$$V = nV_{\text{rev}} + \frac{r_1 + r_2 T}{A} I_{\text{e}} + (s_1 + s_2 T + s_3 T^2).log(1 + (t_1 + \frac{t_2}{T} + \frac{t_3}{T^2}).(\frac{I_{\text{e}}}{A})) \tag{7.1}$$

where n, V_{rev}, T, I_e, S, r_1, r_2, s_1, s_2 and s_3 represent the number of electrolyzer's cell, reversible cell potential (V), temperature (C), current density (A/m), area of the electrode cell m^2, Ohmic resistance parameters and over-voltage coefficients respectively. The developed electrochemical model of the electrolyzer is connected to the buck converter to step down from 750V to 300V.

7.3 Energy Management

The controllers of the system are developed such that PVGS and WPGS are primary energy sources. On the other hand, FCGS and BES are secondary sources and electrolyzer act as a dump load. FCGS, BES and electrolyzer are integrated with the system for power backup. During the sunshine and sufficient wind speed, load is mainly fed by the PVGS and WPGS together. Moreover, when PV and wind power is not available, BES provides deficit power supply to load and starts discharging. During the discharging process, when SOC of the battery falls below 20%, FCGS begins to supply requisite power to the load. FCGS has slow dynamic response hence, controller is developed such that battery will supply power until FC comes into a steady-state. Once FC attains steady-state condition, battery will stop supplying power to the load. During the time of surplus power, first, the battery will be charged until its SOC reaches 80%, then this surplus power is pushed into the electrolyzer. This energy management strategy is achieved through the designed controller. The aforementioned energy power flow coordination among the integrated energy sources is shown in Fig. 7.2. Each converter has its own individual controller. The logic of the controller controls the switching action of the respective converter to perform desired functions.

7.4 Control of Integrated Converters

Complete energy management is achieved through the developed controllers. The developed controllers are capable of maintaining the power quality of the system, regulating the PCI voltage even under highly distorted load current condition and maintains power equilibrium.

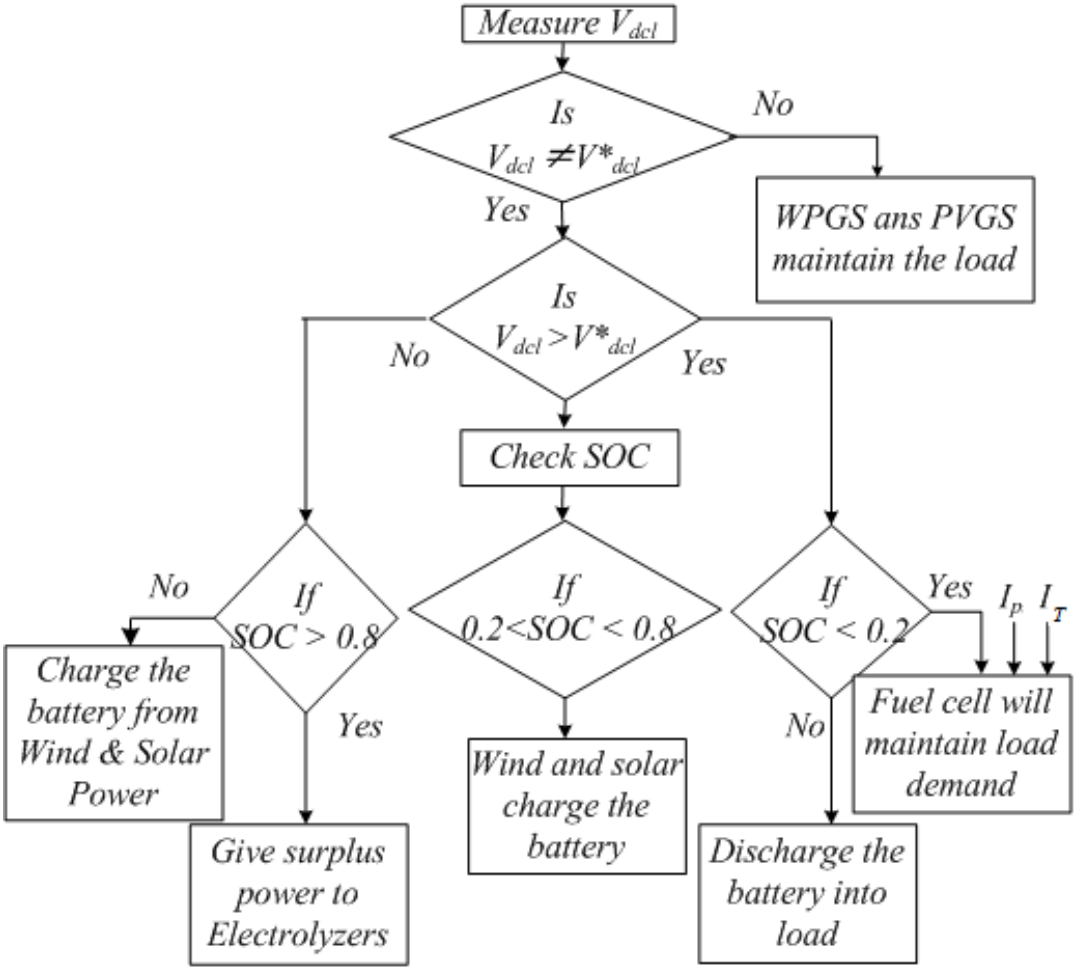

Figure 7.2: Flow diagram of energy management

7.4.1 VSC Controller

The unbalanced load results in unbalanced current in different phases. This further leads to unequal voltage drop in individual phase and results in unbalanced PCI voltage. For a reliable power supply, it is mandatory to have balanced voltage at PCI. Hence to compensate for the unbalancing at PCI, the proposed designed control scheme is shown in Fig. 7.3. Two PI controllers are used in order to achieve balanced PCI voltage. The first PI controller (PI-1) minimizes the error between the reference voltage and the measured PCI voltage. The second PI controller (PI-2) tracks the power difference between generated power (total power available PV power P_{pv}, wind power P_w, fuel cell power P_{FC}) and total load power (battery power P_B, electrolyzer power P_E and load power P_L) in order to find the reference current (I_{ref}). A unit sine wave generator (virtual PLL) is used to generate reference voltage for each phase. With the help of these references,

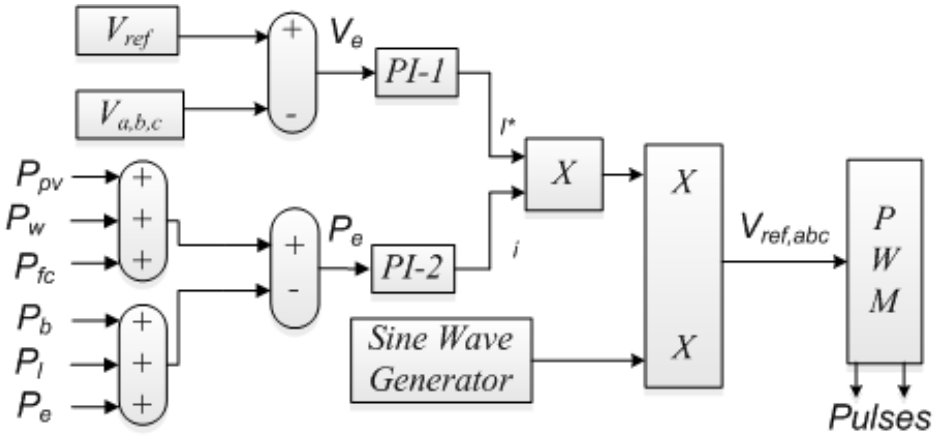

Figure 7.3: Proposed control scheme of inverter

the PWM generator generates the control pulses (gating pulses) for the inverter. The proposed control scheme is able to balance PCI voltage during unbalanced load conditions. The amplitude of PCI voltage is controlled by maintaining the DC-link voltage at its reference value and the sine wave generator maintains the frequency in the proposed system. The reference sinusoidal phase voltages are given by equation(7.2):

$$V_{ref,a} = V_a sin(\theta_m);\ V_{ref,b} = V_b sin(\theta_m - 120^0);\ V_{ref,c} = V_c sin(\theta_m + 120^0) \quad (7.2)$$

7.4.2 DC-DC Boost Converter Controller for FC Power Generation system

FCGS is connected to DC-link through the DC-DC boost converter. The proposed controller for the boost converter is shown in Fig. 7.4. The controller is developed on the basis of measured current (I_P, I_T) to regulate the duty cycle of boost converter which in turn controls the power flow. The battery can not fulfill the load requirement for long duration so the fuel cell is interfaced with the system. In the presented system, the battery is used for a very short duration (during transients only) and this consequently enhances battery life span. FCGS has slow power dynamics and cannot supply power instantaneously for the sudden change of load. Therefore, the control algorithm of the DC-DC converter is designed in such a manner that the battery will supply the power immediately and the output of the battery starts decreasing proportionally with increase in FCGS power. Battery

provides power coordination up to SOC>0.2. Furthermore, when battery SOC<0.2, fuel cell will provide power to the battery as per controller shown in Fig. 7.4.

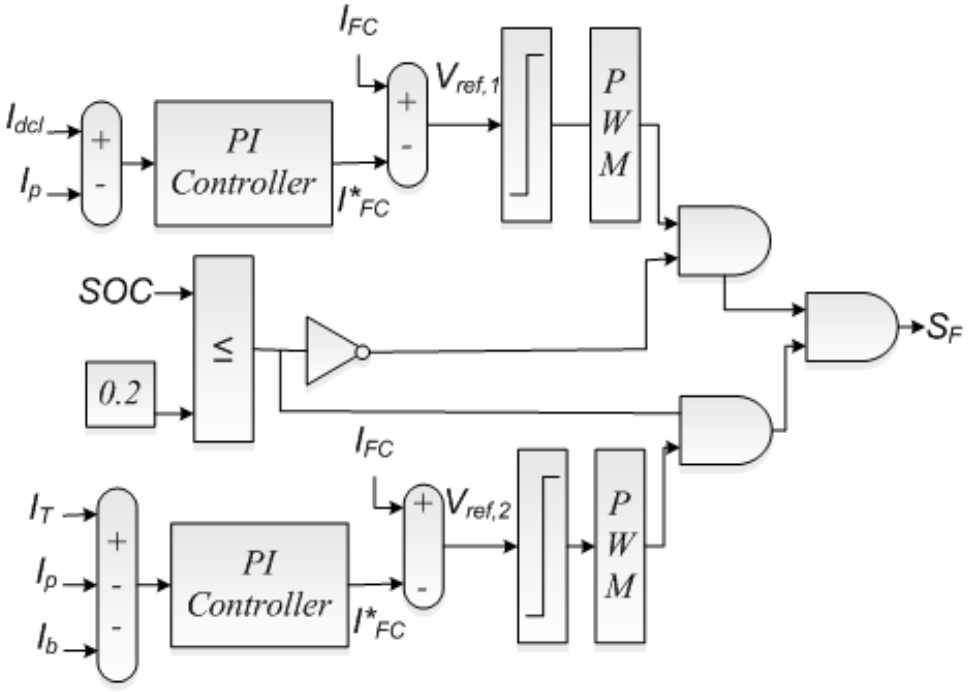

Figure 7.4: Controller for the FC boost converter

7.4.3 DC-Link Control Strategy

Dynamics in load demand and generation create a power mismatch in the system, which leads to fluctuation in DC-link voltage. The disturbances in DC-link voltage cause a change in AC voltage at PCI. This is not acceptable for any reliable system. Hence regulation of DC-link voltage irrespective of any change in the system is mandatory. Therefore, BES, FCGS and electrolyzer are integrated into the system to achieve power equilibrium. A battery is integrated into the system through a buck-boost bidirectional DC-DC converter. The DC-DC converter controls the charging/discharging of the battery in order to maintain constant DC-link voltage. In case of surplus power, battery charges. During the charging process SOC of the battery increases. when its SOC hits the upper level of SOC which is specified as 80% in this work, the surplus power is absorbed by the electrolyzer which is acting as a dump load. The switching control logic of the buck-boost converter integrated to the battery is developed as shown in Fig. 7.5. The control logic is designed to keep charging/discharging current within specified limits (0.2<SOC<0.8).

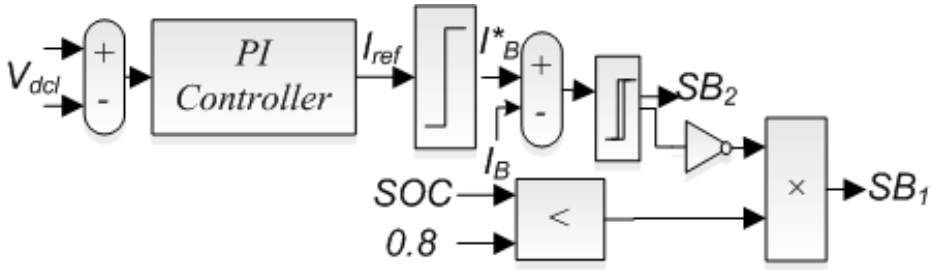

Figure 7.5: Controller for the buck-boost converter of battery

7.4.4 Electrolyzer Buck Converter Controller

The control logic for the switch, which is used to interface electrolyzer in the system is shown in Fig. 7.6. It is controlled by switch S_B. The electrolyzer is integrated into the system through a buck converter to dump additional generated power. Developed logic continuously monitors the SOC status of the battery and if the SOC level crosses its highest set limit of 0.8, the controller will drive to push this surplus power to the electrolyzer.

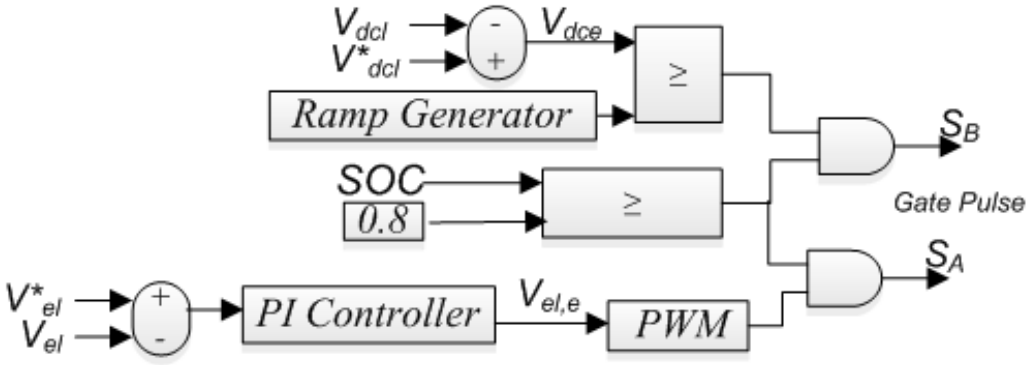

Figure 7.6: Controller for dump load buck converter and switch S_B

7.5 Results and Discussion

The effectiveness of the proposed system is validated using MATLAB/SIMULINK platform under various steady-state and dynamic conditions.

7.5.1 Performance for Fuel Cell and Battery Operation

To study the performance of integrated fuel cell and battery, a constant linear balanced load of 12.5kW at unity power factor is connected to the system. Fig. 7.7 shows that DC-link voltage (V_{dcl}) is maintained at 750V. Since the battery is

connected through a bidirectional DC-DC converter, therefore, battery charges during surplus power condition and discharges in power deficit conditions through controllers action. Though battery operation is electrochemical in nature, it can discharge three times its rating during rapid transients. The controller is designed for charging and discharging limits of battery as 80% and 20% respectively to enhance the battery life cycle. FC is integrated into the system at the DC-link through a boost converter. To study the system operation under fuel cell power generation it is assumed that the battery SOC is near its lowest value initially. FC controller is developed in such a manner that FC supplies the power only when battery SOC falls below its lowest limit (20%). 10kW load demand is fulfilled by PVGS and WPGS altogether and the battery is supplying deficit 2.5 kW power to the load. By doing so, its SOC level drops below 20% at t=1.25s, then FCGS starts to supply the load through controllers action. Fig. 7.7 shows that the FCGS power delivery response is inadequate as compared to increment in load requirement and its dynamics are slow to instantaneous change of load. To overcome this sluggishness, power supply through battery reduces slowly and is maintained until FCGS starts to deliver the required deficit power (i.e.2.5kW). Steady-state of FC power is achieved at t=2.14s and battery stops delivering power supply at t=2.14s. Henceforth, as power output of FCGS system increases, the output power of battery energy systems decreases correspondingly. When power output of FCGS reaches to the steady value, the power delivered by battery becomes zero. However, the battery is able to attain high slope instantaneously and meets load demand. From Fig. 7.7, it can be concluded that the designed system successfully achieve power equilibrium under fuel cell and battery operation by using proposed intelligent controllers. Such intelligent coordination is accomplished through the controllers shown in Fig. 7.4 and Fig. 7.5. Dynamics in SOFC are very slow subsequently its power slope is extremely less, whereas load demand may change instantaneously. However, the battery can meet exceptionally high slant during the dynamics in the system, provided the maximum discharging limit of the battery is within three times of its rating. Fig. 7.7 shows the response of the stable DC-link voltage, load current (i_L) and PCI voltage (V_{PCI}), which is stable and balance during the entire operation. Fig. 7.7 depicts the current response of all integrated energy sources.

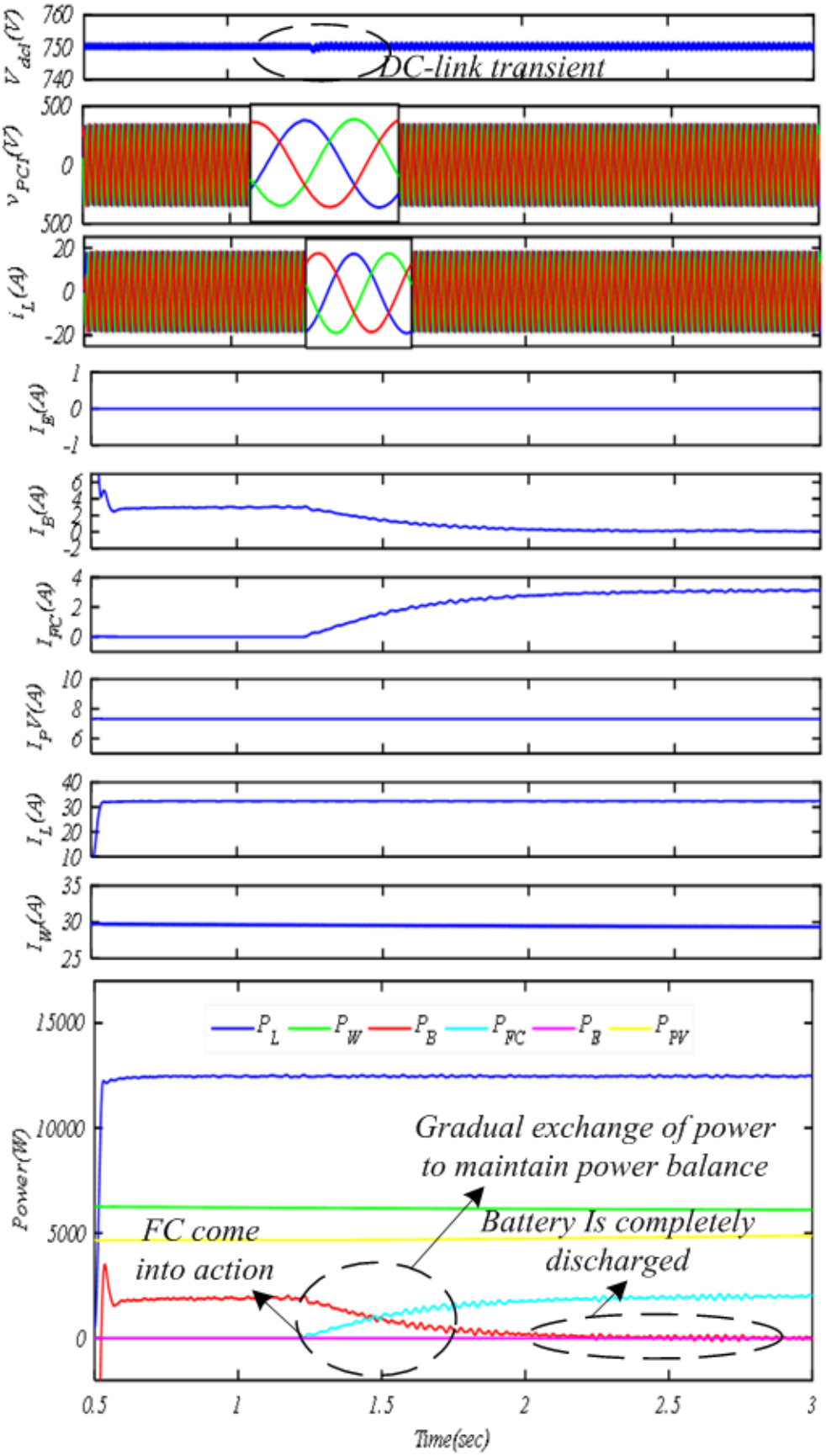

Figure 7.7: System response under FC and battery operation

7.5.2 Performance for Electrolyzer and Battery Operation

Electrolyzer is integrated as a dump load into the system to absorb surplus generated power. The controller is developed with the aim that as soon as the battery is fully charged, the electrolyzer starts to absorb the surplus power. Electrolyzer is integrated into the system through buck converter and the control action of this buck converter is designed as shown in Fig. 7.6. Switching control of the buck converter and battery's bidirectional converter switches control the action. To observe system response under electrolyzer operation, the simulation is initiated with the assumption that the battery is approximately fully charged. Initially, no electrolyzer current is observed in Fig. 7.8. Since battery is not fully charged so that the power goes into the battery for charging purposes. Negative notation of battery current and battery power indicates the charging mode of the battery. At t= 0.69 battery SOC reaches its upper level (80% of SOC) therefore, surplus power is available which has to be dumped to maintain power balance. Through the designed controller's action, the surplus power is injected into the electrolyzer and battery stops charging since SOC of the battery goes up to 80%. Fig. 7.8 shows that at t=0.69s electrolyzer current becomes negative and no battery current is observed after t= 0.69s. Results exhibit the effectiveness of the developed controller. system responses show that effective coordination is achieved between battery and electrolyzer. Fig. 7.8 depicts the response of regulated DC-link voltage, three-phase load current and instantaneous PCI voltage, which is stable and balance for the entire system operation. Solar power generation is 5kW, wind power generation is 6kW and load demand is 4.5kW. Thus, the total generation is 11kW and load demand is 4.5kW. Therefore the surplus generated power 6.5kW is fed to the battery for charging purposes. At t=0.7s battery is fully charged, therefore the controller connects the electrolyzer to the system and surplus 6.5kW power is fed into the electrolyzer. Fig. 7.8 depicts the power equilibrium is achieved among all integrated sources. It also verifies that the PCI voltage is sinusoidal balanced and constant in magnitude. This ensures a good quality of power to the end-user.

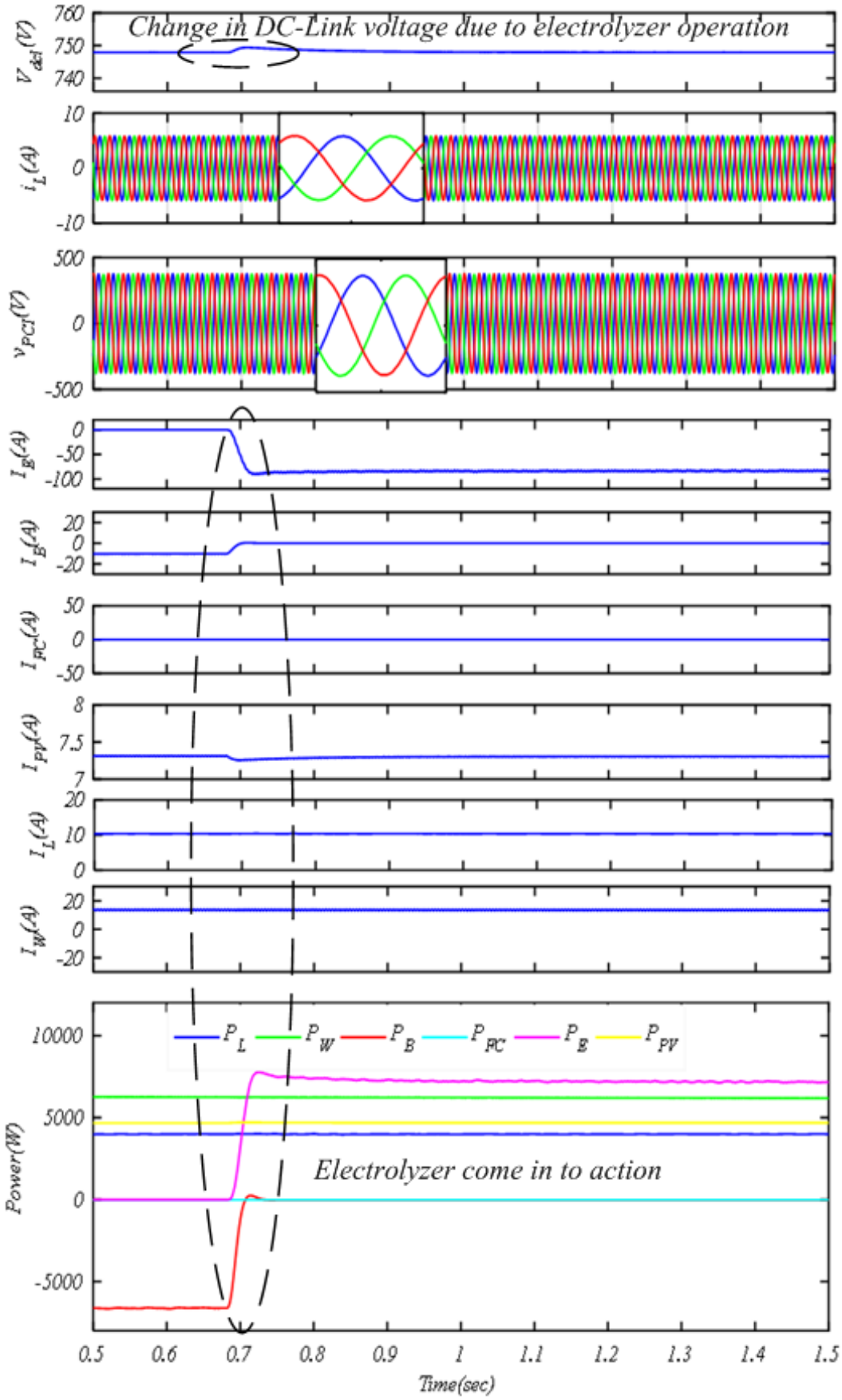

Figure 7.8: System response under electrolyzer and battery operation

7.5.3 Operation under Variable Environmental Conditions and load

To test system adequacy and performance for environmental changes which include solar irradiation perturbation (at t=1s, t=2s) variation in wind speed (at t=3s) and variation in load (at t=4s). Initially, 7.5kW load is connected to the system and the total 11kW generated power (5kW solar power and 6kW wind power) is available. Hence, surplus 3.5kW power is used for battery charging. Solar irradiation is reduced to 600W/m^2 at t=1s and further, it is reduced to 400W/m^2 at t=2s. Decreased solar irradiation resulting in the reduction in PV generated power which further reduction in battery charging to maintain power balance. With the change in solar power generation, the corresponding change in battery current can be noticed in Fig. 7.9. Wind speed is reduced to 10m/s from 12m/s at t=3s. This resulting in the reduced total available generated power which results in reduction in battery charging. Furthermore, at t=4s load demand is reduced to 6kW and battery is charging with more power to maintain power balance. The corresponding response of DC-link voltage (maintained at $750V$), instantaneous PCI voltage and three-phase load current is shown in Fig. 7.9. The PCI voltage is observed as balanced and sinusoidal during the variation in wind speed, load demand and solar irradiation. Fig. 7.9 also shows the current waveform in the interfaced power generators, load and battery. It can be noticed that during the operation battery does not hit the minimum and maximum level of SOC. Hence, fuel cell and electrolyzer do not come into action to supply power. Therefore, electrolyzer and fuel cell current are at 'zero' value. Results under variable environmental and variable load conditions ensure the effective and reliable working of presented microgrid system for transient operation. Hence presented microgrid offers a sustainable solution for rural areas and urban areas for the critical load. It is found that for different types of disturbances the system could function satisfactorily keeping current and voltage quality at the load and within the standards. Power distribution among the integrated sources exhibits that the system is working under power harmony despite of all dynamics and ensure effective working under transients.

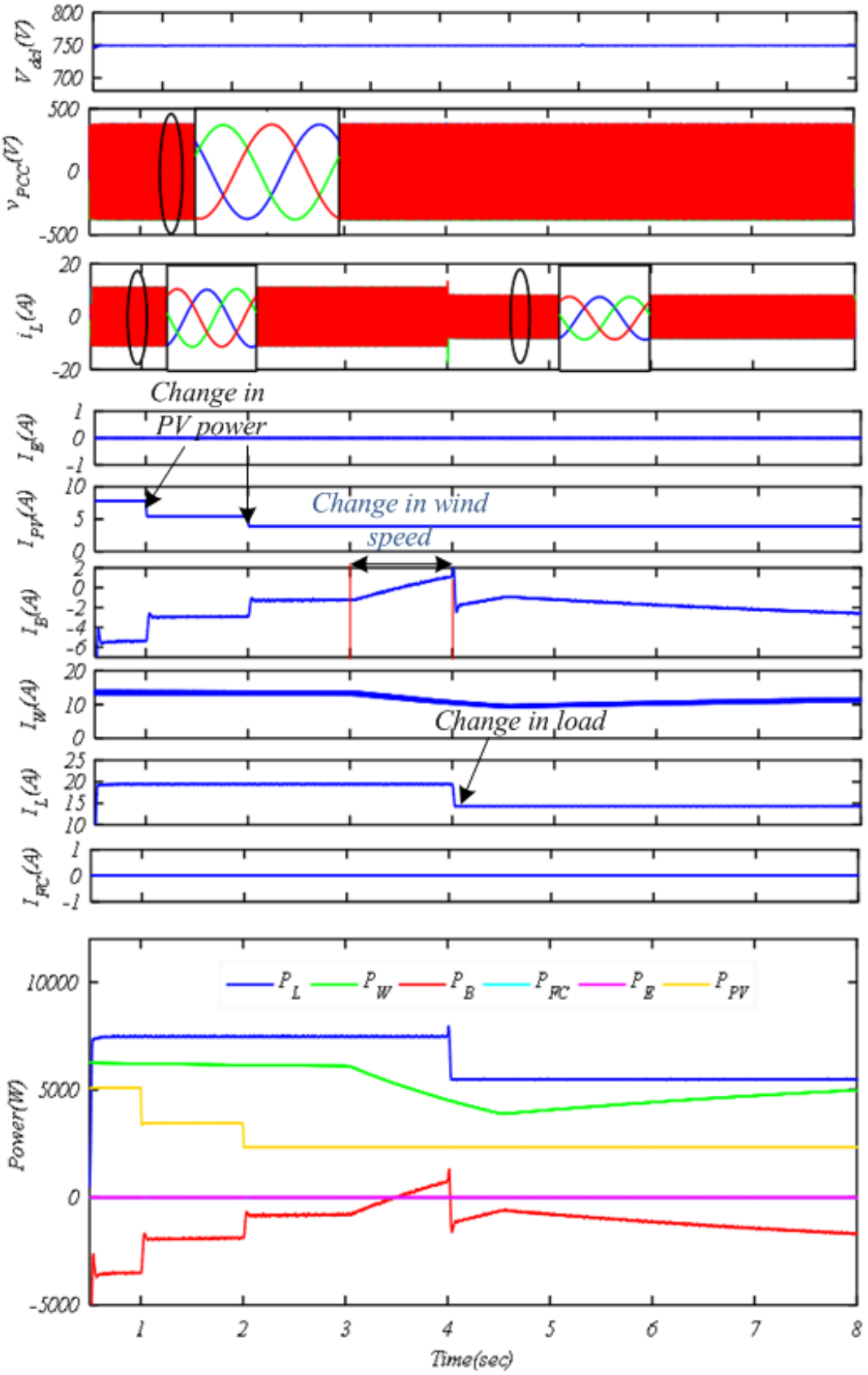

Figure 7.9: System response under variable meteorological conditions

7.5.4 Response Under Nonlinear and Unbalanced Load

In this section, the performance of stand-alone microgrid is examined under different loading conditions such as nonlinear load and unbalanced linear load conditions. To analyze the working under these loads the generation is kept constant and at their rated values. Initially, a nonlinear load, which is realized through diode bridge rectifier 50Ω resistance and 500mH inductance, is integrated into the developed system. The nonlinear load causes harmonics, good quality of power can be supplied to the consumer using proper control technique of the inverter. Under nonlinear load, PCI voltage is found to be balanced and sinusoidal. The total available generation is 11kW, which is generated by WPGS (6kW) and PV (5kW), while load demand is only 5.5kW. Therefore extra generated power (5.5kW) goes to the battery for charging purpose. At t=1s, the system is interconnected to unbalanced linear load. The unbalanced load is realized with different loads in three phases is connected to the MG with the load current of phase 'a'=23A, phase 'b'=9A, phase 'c'=4.8A. Due to the unbalanced load, PCI voltage may become unbalanced. Proposed PWM inverter control mitigates this unbalancing and maintains it within the prescribed limit (below 1%) by generating three different modulation indexes. It can be seen in Fig. 7.10 that the implemented control strategy is able to supply good quality of voltage at the consumer end. Fig. 7.10 shows three-phase PCI voltage, three-phase load current and DC-link voltage which is maintained at $750V$ during all the operation. Fig. 7.10 depicts the current response of all the integrated sources, load and battery. During unbalanced linear load conditions the load demand increased to 8.5kW and generated power 11kW is available. Therefore, surplus 2.5kW goes into battery for charging purpose. Form Fig. 7.10 it is depicted that the response of the battery is fast and it can meet the rapidly increasing load demand. Fig. 7.10 shows power allocation as per load demand and generation to validate the effectiveness of the developed controllers. The result shows that the MG is able to perform adequately for all possible transient conditions without much delay.

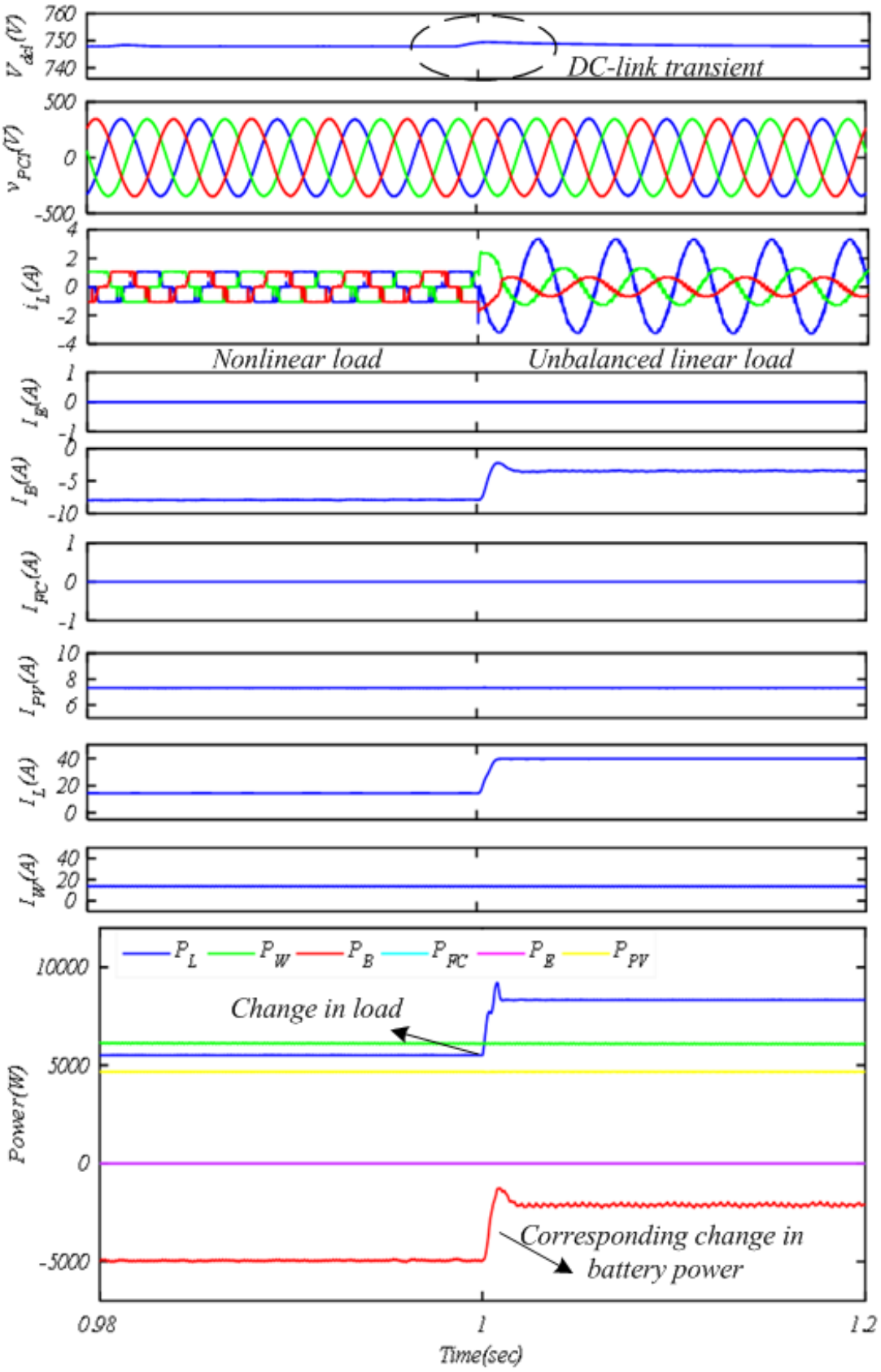

Figure 7.10: System response under nonlinear and unbalanced linear load

7.6 Conclusions

A standalone microgrid consisting of PVGS-WPGS system with FC, battery and electrolyzer has been developed. FC and battery are secondary energy sources and electrolyzer is acting as a dump load. The novel power controllers based on simple logic gates are developed for standalone microgrid systems. Results show that the developed system is effective in energy management. Power-sharing in the system is based on the regulation of DC-link voltage and SOC of the battery. The system responds adequately and timely to fulfill the shortfall in load demands. The battery is connected to offset the slow response of the FCGS system which maintains the power balance until FC comes to steady-state condition. Inverter control is responsible to regulate PCI voltage. Therefore, the developed system and associated control strategy can provide good quality, reliable and sustainable electric power for remote communities.

Chapter 8

MAIN CONCLUSIONS AND FUTURE SCOPE OF WORK

8.1 Introduction

The microgrid concept integrates RESs to the conventional power system to produce clean energy and meet electrical energy demand from sources other than depleting fossil fuel reserves. The main objective of this thesis is the development of a microgrid and study of its performance aspects. A hybrid power source based microgrid for power quality enhancement has been presented in this thesis. The performance of microgrid is analyzed in MATLAB/SIMULINK environment. MG has been tested for various PQ problems such as load unbalancing, harmonic elimination, pf improvement and distortion in voltage, etc. The microgrid system is tested for various transient conditions that occur due to changes in load and environmental conditions. New DC-link voltage control techniques have been developed and tested successfully with the help of the conventional control technique (SRFT) of VSC. New control techniques of VSC control for mitigation of PQ problems have been developed, tested and analyzed. Balanced variable linear loads and balanced/unbalanced nonlinear loads have been used in combinations to analyze the microgrid system with the modern control algorithm. Various control techniques such as ANFIS-LMS, H-LMS, ZAQ-LMS, MSWL-CLMS, etc. have been successfully implemented for control of VSC for PQ mitigation and real power

extraction from RESs. A hybrid microgrid containing EV load at the DC bus is developed and tested for the dynamic conditions with the new self-tuning filter for VSC control. The distortion in supply voltage is introduced and the effective control of the microgrid system is demonstrated. Further, a stand-alone microgrid system has been developed. The hybrid microgrid is tested for various operating conditions. The summary of the main contributions and further scope of work related to the objectives are presented in the following subsections.

8.1.1 Main Conclusions

The work of the thesis has been broadly classified into five parts. In order to analyze the operation of the microgrid system both the modelling and control of the system are important issues. The first part of the thesis deals with the development of grid-connected microgrid with conventional control schemes such as PBT and SRFT. The modelling of RESs and two MPPT techniques PO and hill climbing have been discussed in detail. The modelling of PV, wind and fuel cell have been carried out in this chapter. The control schemes have been tested for load balancing, PF improvement and harmonics reduction under non-linear and linear load conditions. Further, the performance is tested when the RESs power generation goes to zero due to any fault or environmental changes. The destined microgrid operates successfully under the DSTATCOM mode of operation when no RESs power generation available. In case of nonlinear load, grid current THD is considerably improved up to 2.21% and harmonics have been effectively filtered. The microgrid performs under the unity power factor in case of the nonlinear load. Out of two conventional algorithms, the performance of SRFT is better in reducing harmonics from grid current.

In the second part of the thesis, DC-link voltage control algorithm such as ANFIS, H-FLC, FLC and TSFLC have been investigated to achieve faster damping of DC-link voltage. A fair comparison of all four control techniques and PI has been presented in this section. Algorithms are compared in terms of settling time, overshoot and undershoot. ANFIS control technique is found to be giving a better and faster response by .02s (TS-FLC) during transients. The comparison has been done for the starting point and inclusion/removal of one phase of the nonlinear

load.

The next chapter is discussed the grid-connected microgrid system consisting of PV, wind and fuel cell as RES. The system is investigated for PQ problems such as load unbalancing, reactive power compensation and harmonics reduction. The system is also investigated under the variation of solar irradiation and wind speed variation. The four control schemes have been developed viz. H-LMS, ANFIS-LMS, ZAQ-LMS and MSWL-CLMS. The controllers are developed such that the reactive power requirement of the load is met locally by the VSC and the grid is free from supplying reactive power. Various cases of load and generation are considered for transient performance investigation. The algorithms are developed to extract fundamental active power component of load for generating the reference signal for the grid. Further, these reference signals are used to generate the switching pulses for the VSC. All the control algorithms have been able to improve the grid current profile nearly sinusoidal even under highly distorted load conditions. The power balance has been achieved under all the dynamics. From the comparison of algorithms performance, it has been noticed that the MSWL-CLMS control technique is able to offset the DC component and fundamental component extraction is faster furthermore, the lowest THD 1.35% in grid current is noticed.

In the fourth part of the thesis, a hybrid microgrid is developed. An EV load is interfaced at the DC bus. The EV load is in the form of a lead-acid battery, the detailed modelling of the battery has been discussed in this section. EV load can be integrated at the DC bus as per the requirement of charging/discharging. In discharging mode the EV load injects power into the grid and therefore may be used for revenue generation. During the charging process, the power generated from the RESs is supplying the load and charging the EV load. Any change in load or generation by RESs does not affect the charging or discharging of the EV load. All the considered cases verify the hybrid microgrid performance for PQ improvement such as load balancing, harmonics elimination, reactive power compensation, etc. PQ mitigation is achieved through the STF method of VSC control. The grid current THD is obtained 1.45% under the STF control. Further, DSOGI control along with the SOGI control scheme is also implemented and tested under distorted grid conditions. DSOGI algorithm is implemented to extract the fundamental

component from distorted grid supply voltages and SOGI is used for VSC control. It is found that DSOGI effectively extracts the positive sequence voltages under unbalanced grid supply and generates sinusoidal grid current using SOGI for VSC control. The synchronization and de-synchronization of the presented microgrid are tested and verifies its seamless transition between grid-connected mode and stand-alone mode. The synchronization is achieved through new LPN-PLL under 5 cycles.

In the last section, a hybrid source standalone microgrid is considered and an electrolyzer load is integrated into the system as a dump load. For the regulation of DC-link voltage and PCI voltage new and simple controllers have been developed. With the help of these controllers, the energy management function in the hybrid source microgrid is performed. The system is developed such that the PV and WPGS are primary energy sources and FCGS is a backup energy source. Further to accommodate the slow dynamics of the fuel cell a battery is integrated into the circuit. The attery is interfaced as a storage device. A bidirectional DC-DC buck-boost converter is used to interface the battery into the microgrid. To absorb the surplus power during the low load condition an electrolyzer is also interfaced at the DC bus through buck converter. Various considered cases verify the coordinated working of the microgrid under all dynamics. The microgrid has been working effectively and supply the quality voltage to the consumer. The transient conditions due to intermittent in the wind/PV power, load demand, load unbalance and nonlinear load have been considered to verify the performance. The proposed microgrid switches its operation in DSTATCOM mode when there is no RESs power available. Further, it is capable of operating in is-landing mode under grid fault condition and synchronized with the grid after the removal of the fault.

8.1.2 Future Scope of the Work

Future scope of the presented work is listed as follows:

(i) In this thesis, the conventional MPPT control algorithm has been considered to extract maximum power from PV and wind energy systems. New and modern control techniques can also be investigated to improve the efficiency of the system. Further, conventional DC-DC converters are interfaced into

the system, which can be replaced by other converters viz. cuck converter to enhance the performance of the system.

(ii) Two-level VSC is considered to interface the source and grid. Microgrid having the different configuration of the inverter can be used to mitigate the power quality problems. The multilevel inverter-based microgrid can be used for higher power levels.

(iii) In this thesis PV, wind, fuel cell based RESs have been considered. Integration of biomass energy system, microturbines can also be considered for the viability of the proposed microgrid.

(iv) The use of the ultracapacitor in place of the DC-link capacitor is also another dimension of future work.

(v) Research work on protection issues and working under undesirable fault conditions can also be considered.

(vi) Prototype hardware of the presented microgrid can be developed to test its performance under a more realistic environment. An attempt can also be made to develop new controllers.

APPENDIX

Parameter for PV cell: I_{mp} = 2.94 A, V_{mp} = 17.0 V, P_{max} = 50 W, I_{sc} = 3.17 A, V_{oc} = 21.0 V, K_v = 0.123 V/K, K_i = 4.4 mA/K, No. of series module of WS50 = 18, No. of parallel module of WS50 = 10, L (Boost converter) = 1.5 mH, C (Boost converter) = 250 μ F

System Parameters AC line voltage = 415 V, 50 Hz, modulation index = 1, line impedance(Rs) = 0.05 Ω, Ls = 1 mH, L_1L_2 (Filter) = 1.2 mH, C (Filter) = 1000 μ F, DC-link capacitor = 5000 μ F.

Parameter of PMSG: Number of poles = 10, rated speed = 153 rad/s, armature resistance (Rs) = 0.425 Ω, magnetic flux linkage = 0.433 Wb, stator inductance (L_s) = 8.4 mH, rated torque = 40 Nm, rated power = 6.5 kW. Parameter of two mass drive train H_{tb} = 4 s; H_g = 0.1 H $_p$, K_{sh} = 0.3 p.u./el.rad, Dt = 0.7 p.u.s/el.rad.

Fuel cell parameter: Ohmic losses(r) = 32813$\times$ $10^{-8}\Omega$, response time for oxygen flow = 78.3 s, response time for hydrogen flow = 26.1 s, K_{o_2} = 2.52$\times$ 10^{-3} (kmol/atm), K_{H_2O} = 2.81$\times$ 10^{-4}(kmol/atm), K_{H_2}= 8.43$\times$ 10^4(kmol/atm), T= 1273 K, F= 96,487 C/kmol, R= 8314 J/kmolK, ideal standard potential(E^0)= 1.18 V, N= 450, K_r= 0.842$\times$ 10^{-68} kmol/s (A).

Parameters of electrolyzer: r_1=000015Ωm^2, r_2=-6.09$\times$ $10^{-6}m^2$ $^0C^{-1}$, S_1= 2.427 V, S_2=-0.0307 V $^0C^{-1}$, S_3=3.90-6.09$\times$ 10^{-4} V^2 $^0C^{-2}$, t_1=0.214 A^{-1} m^2, t_2=-9.870 A^{-1} m^2 ^0C, t_2=119.1 A^{-1} m^2 $^0C^2$, T=70^{0}C, A=873cm^2, 1.1647 V^{rev}=1.1647 V.

Constants: MSWL-CLMS: ζ=.02, ε_{pn}=0.05, μ=0.003, γ=4 t=2, ZAQ-LMS:ζ=0.02, χ=0.009.

BIOGRAPHY

I, Shikha Gupta, an Assistant Professor in Guru Gobind Indraprastha University have been working for the last 10 years in the Electrical and Electronics Engineering Department of Bhagwan Parshuram Institute of Technology, Rohini, Delhi. I completed my Master's in 2005 from SATI, RGTU, M.P. in Electrical Drives specialization. Before that, I graduated in Electrical Engineering from OIST, RGTU, Bhopal in the year 2003. I have 12 publications in different journals, conferences and proceedings.

PUBLICATIONS

The work conducted in this thesis has resulted in the following major publications:

[1] S. Gupta, R. Garg and A. Singh, "Wind/Fuel Cell Hybrid System based on ANFIS-HLMS Control Algorithm for VSC", Accepted in International Journal of Power and Energy Systems,2020

[2] S. Gupta, R. Garg and A. Singh, "Adaptive Control Algorithm to Interface Fuel Cell and Photo Voltaic Energy Sources" Accepted in International Journal of Power Electronics,2020.

[3] S. Gupta, R. Garg and A. Singh, Shikha Gupta, Rachana Garg and Alka Singh, "ANFIS Based Control of Multi-Objective Grid Connected Inverter and Energy Management in Renewable Energy System", Journal of the Institution of Engineers (India): Series B, 101, 1–14, 2020. (IEIB).Springer

[4] S. Gupta, R. Garg and A. Singh, "Modelling, simulation and control of fuel cell based micro grid", Journal of Green Engineering, 7:129–158, 2017.

[5] S. Gupta, R. Garg and A. Singh, "TSFLC Based DC-Link Voltage Regulation of Grid Connected DC Micro Grid", International Journal of Power Electronics, 9(3):229–249, 2018.

[6] S. Gupta, R. Garg and A. Singh, "Grid integrated PMSG based Wind Energy System: Modelling, control and simulation," 2016 IEEE 1st International

Conference on Power Electronics, Intelligent Control and Energy Systems (ICPEICES), Delhi, 2016, pp. 1-6.

[7] S. Gupta, R. Garg and A. Singh, "TS-fuzzy based controller for grid connected PV system," 2015 Annual IEEE India Conference (INDICON), New Delhi, 2015, pp. 1-6.DOI:10.1109/INDICON.2015.7443280.

[8] R. Garg, A. Singh and S. Gupta, "PV cell models and dynamic simulation of MPPT trackers in MATLAB," 2014 International Conference on Computing for Sustainable Global Development (INDIACom), New Delhi, 2014, pp. 6-12. DOI: 0.1109/IndiaCom.2014.6828003.

References

[1] P. García, C. A. García, L. M. Fernández, F. Llorens, and F. Jurado, "ANFIS-Based Control of a Grid-Connected Hybrid System Integrating Renewable Energies, Hydrogen and Batteries," *IEEE Transactions on Industrial Informatics*, vol. 10, no. 2, pp. 1107–1117, 2013.

[2] L. Meng, X. Zhao, F. Tang, M. Savaghebi, T. Dragicevic, J. C. Vasquez, and J. M. Guerrero, "Distributed Voltage Unbalance Compensation in Islanded Microgrids by Using a Dynamic Consensus Algorithm," *IEEE Transactions on Power Electronics*, vol. 31, no. 1, pp. 827–838, 2015.

[3] M. Savaghebi, A. Jalilian, J. C. Vasquez, and J. M. Guerrero, "Autonomous Voltage Unbalance Compensation in an Islanded Droop-Controlled Microgrid," *IEEE Transactions on Industrial Electronics*, vol. 60, no. 4, pp. 1390–1402, 2012.

[4] Q. Liu, Y. Li, S. Hu, and L. Luo, "Power Quality Improvement using Controllable Inductive Power Filtering Method for Industrial DC Supply System," *Control Engineering Practice*, vol. 83, pp. 1–10, 2019.

[5] Y. P. Kumar and R. Bhimasingu, "Performance Analysis of Green Microgrid Architectures by Comparing Power Quality Indices," in *2014 Eighteenth National Power Systems Conference (NPSC)*, pp. 1–6, IEEE, 2014.

[6] R. H. Lasseter, "Microgrids," in *2002 IEEE Power Engineering Society Winter Meeting. Conference Proceedings (Cat. No. 02CH37309)*, vol. 1, pp. 305–308, IEEE, 2002.

[7] R. H. Lasseter and P. Piagi, "Microgrid: A Conceptual Solution," in *IEEE Power Electronics Specialists Conference*, vol. 6, pp. 4285–4291, Citeseer, 2004.

[8] N. Hatziargyriou, H. Asano, R. Iravani, and C. Marnay, "Microgrids," *IEEE power and energy magazine*, vol. 5, no. 4, pp. 78–94, 2007.

[9] F. Shahnia, R. Majumder, A. Ghosh, G. Ledwich, and F. Zare, "Operation and Control of a Hybrid Microgrid Containing Unbalanced and Nonlinear Loads," *Electric Power Systems Research*, vol. 80, no. 8, pp. 954–965, 2010.

[10] M. Nasir, H. A. Khan, A. Hussain, L. Mateen, and N. A. Zaffar, "Solar PV-Based Scalable DC Microgrid for Rural Electrification in Developing Regions," *IEEE Transactions on Sustainable Energy*, vol. 9, no. 1, pp. 390–399, 2018.

[11] G. Bhuvaneswari and R. Annamalai, "Development of a Solar Cell Model in MATLAB for PV Based Generation System," in *2011 Annual IEEE India Conference*, pp. 1–5, IEEE, 2011.

[12] M. Saied, A. Hanafy, M. El-Gabaly, Y. Safar, M. Jaboori, K. Yamin, and A. Sharaf, "Optimal Design Parameters for a PV Array Coupled to a DC Motor via a DC-DC Transformer," *IEEE Transactions on Energy Conversion*, vol. 6, no. 4, pp. 593–598, 1991.

[13] M. G. Villalva, J. R. Gazoli, and E. Ruppert Filho, "Modeling and Circuit-Based Simulation of Photovoltaic Arrays," in *2009 Brazilian Power Electronics Conference*, pp. 1244–1254, IEEE, 2009.

[14] A. Keyhani, "Modeling of Photovoltaic Microgrids for Bulk Power Grid Studies," in *2011 IEEE Power and Energy Society General Meeting*, pp. 1–6, IEEE, 2011.

[15] E. Koutroulis, K. Kalaitzakis, and N. C. Voulgaris, "Development of a Microcontroller-Based, Photovoltaic Maximum Power Point Tracking Control System," *IEEE Transactions on power electronics*, vol. 16, no. 1, pp. 46–54, 2001.

[16] R. Leyva, C. Alonso, I. Queinnec, A. Cid-Pastor, D. Lagrange, and L. Martinez-Salamero, "MPPT of Photovoltaic Systems using Extremum-Seeking Control," *IEEE Transactions on Aerospace and Electronic Systems*, vol. 42, no. 1, pp. 249–258, 2006.

[17] T. A. Ocran, J. Cao, B. Cao, and X. Sun, "Artificial Neural Network Maximum Power Point Tracker for Solar Electric Vehicle," *Tsinghua science and technology*, vol. 10, no. 2, pp. 204–208, 2005.

[18] T. L. Kottas, Y. S. Boutalis, and A. D. Karlis, "New Maximum Power Point Tracker for PV Arrays using Fuzzy Controller in Close Cooperation with Fuzzy Cognitive Networks," *IEEE Transactions on Energy Conversion*, vol. 21, no. 3, pp. 793–803, 2006.

[19] J. Lee and Y.-S. Kim, "Sensorless Fuzzy-Logic-Bbased Maximum Power Point Tracking Control for a Small-Scale Wind Power Generation Systems with a Switched-Mode Rectifier," *IET Renewable Power Generation*, vol. 10, no. 2, pp. 194–202, 2016.

[20] N. Femia, G. Petrone, G. Spagnuolo, and M. Vitelli, "A Technique for Improving P&O MPPT Performances of Double-Stage Grid-Connected Photovoltaic Systems," *IEEE Transactions on Industrial Electronics*, vol. 56, no. 11, pp. 4473–4482, 2009.

[21] F. Liu, S. Duan, F. Liu, B. Liu, and Y. Kang, "A Variable Step Size INC MPPT Method for PV Systems," *IEEE Transactions on Industrial Electronics*, vol. 55, no. 7, pp. 2622–2628, 2008.

[22] F. Mei and B. Pal, "Modal Analysis of Grid-Connected Doubly Fed Induction Generators," *IEEE Transactions on Energy Conversion*, vol. 22, no. 3, pp. 728–736, 2007.

[23] S. Muyeen, M. H. Ali, R. Takahashi, T. Murata, J. Tamura, Y. Tomaki, A. Sakahara, and E. Sasano, "Transient Stability Analysis of Grid Connected Wind Turbine Generator System Considering Multi-Mass Shaft Modeling," *Electric power components and systems*, vol. 34, no. 10, pp. 1121–1138, 2006.

[24] C. Bhende, S. Mishra, and S. G. Malla, "Permanent Magnet Synchronous Generator-Based Standalone Wind Energy Supply System," *IEEE Transactions on Sustainable Energy*, vol. 2, no. 4, pp. 361–373, 2011.

[25] A. M. El-Sebaii, M. S. Hamad, and A. A. Helal, "A Sensorless MPPT Technique for a Grid-Connected PMSG Wind Turbine System," in *2nd IET Renewable Power Generation Conference (RPG 2013)*, pp. 1–6, 2013.

[26] E. Koutroulis and K. Kalaitzakis, "Design of a Maximum Power Tracking System for Wind-Energy-Aonversion Applications," *IEEE Transactions on Industrial Electronics*, vol. 53, no. 2, pp. 486–494, 2006.

[27] M. Karbakhsh, H. Abutorabi, and A. Khazaee, "An Enhanced MPPT Fuzzy Control of a Wind Turbine Equipped with Permanent Magnet Synchronous Generator," in *2012 2nd International eConference on Computer and Knowledge Engineering (ICCKE)*, pp. 77–82, IEEE, 2012.

[28] D. Kumar and K. Chatterjee, "A Review of Conventional and Advanced MPPT Algorithms for Wind Energy Systems," *Renewable and Sustainable Energy Reviews*, vol. 55, 2016.

[29] M. Shirazi, A. H. Viki, and O. Babayi, "A Comparative Study of MaximumPpower Extraction Strategies in PMSG Wind Turbine System," in *2009 IEEE Electrical Power & Energy Conference (EPEC)*, pp. 1–6, IEEE, 2009.

[30] S. M. R. Kazmi, H. Goto, H.-J. Guo, and O. Ichinokura, "A Novel Algorithm for Fast and Efficient Speed-Sensorless Maximum Power Point Tracking in Wind Energy Conversion Systems," *IEEE Transactions on Industrial Electronics*, vol. 58, no. 1, pp. 29–36, 2010.

[31] J. Padulles, G. Ault, and J. McDonald, "An Integrated SOFC Plant Dynamic Model for Power Systems Simulation," *Journal of Power sources*, vol. 86, no. 1-2, pp. 495–500, 2000.

[32] Y. Zhu and K. Tomsovic, "Development of Models for Analyzing the Load-Following Performance of Microturbines and Fuel Cells," *Electric Power Systems Research*, vol. 62, no. 1, pp. 1–11, 2002.

[33] Ø. Ulleberg, "Modeling of Advanced Akaline Electrolyzers: a System Simulation Approach," *International Journal of Hydrogen Energy*, vol. 28, no. 1, pp. 21–33, 2003.

[34] D. Ipsakis, S. Voutetakis, P. Seferlis, F. Stergiopoulos, and C. Elmasides, "Power Management Strategies for a Stand-Alone Power System using Renewable Energy Sources and Hydrogen Storage," *International journal of hydrogen energy*, vol. 34, no. 16, pp. 7081–7095, 2009.

[35] S. Barsali and M. Ceraolo, "Dynamical Models of Lead-Acid Batteries: Implementation Issues," *IEEE Transactions on Energy Conversion*, vol. 17, no. 1, pp. 16–23, 2002.

[36] H. Song, T. T. Kim, Jeong, B. Kim, B. Shin, B. Lee, and H. Heo, "Verification of Battery System Model for Environmentally Friendly Vehicles using a Battery Hardware-in-the-Loop Simulation," *IET Power Electronics*, vol. 6, no. 2, pp. 417–424, 2013.

[37] C. Wang and P. Li, "Development and Challenges of Distributed Generation, the Micro-Grid and Smart Distribution System," *Automation of electric power systems*, vol. 34, pp. 10–14, 2010.

[38] Y. J. Wang, X. Z. Dong, B. Wang, J. Liu, and A. X. Guo, "Microgrid: A Conceptual Solution," in *12th IET International Conference on Developments in Power System Protection (DPSP 2014)*, pp. 1–6, 2014.

[39] E. Hossain, M. R. Tür, S. Padmanaban, S. Ay, and I. Khan, "Analysis and Mitigation of Power Quality Issues in Distributed Generation Systems using Custom Power Devices," *Ieee Access*, vol. 6, pp. 16816–16833, 2018.

[40] M. F. McGranaghan, D. R. Mueller, and M. J. Samotyj, "Voltage Sags in Industrial Systems," *IEEE Transactions on Industry Applications*, vol. 29, no. 2, pp. 397–403, 1993.

[41] N. Edomah, "Effects of Voltage Sags, Swell and other Disturbances on ElectricalEquipment and their Economic Implications," in *20th International Conference on Electrical Distribution*, pp. 1–4, 2009.

[42] G. Montanari, M. Loggini, A. Cavallini, and L. Pitti, "Flicker and Distortion Compensation in Electrical Plants Supplying Arc-Furnaces," in *Proceedings of 1994 IEEE Industry Applications Society Annual Meeting*, vol. 2, pp. 2249–2255, IEEE, 1994.

[43] C. Chen, Y. Chen, and C. N. Chen, "A High-Resolution Technique for Flicker Measurement in Power Quality Monitoring," in *2013 IEEE 8th Conference on Industrial Electronics and Applications (ICIEA)*, pp. 528–533, 2013.

[44] S. Kewat and B. Singh, "Improved Reweighted Zero-Attracting Quaternion-Valued LMS Algorithm for Islanded Distributed Generation System at IM Load," *IEEE Transactions on Industrial Electronics*, vol. 67, no. 5, pp. 3705–3716, 2020.

[45] P. Wang, N. Jenkins, and M. Bollen, "Experimental Investigation of Voltage Sag Mitigation by an Advanced Static VAR Compensator," *IEEE Transactions on Power Delivery*, vol. 13, no. 4, pp. 1461–1467, 1998.

[46] T. Senjyu, Y. Miyazato, A. Yona, N. Urasaki, and T. Funabashi, "Optimal Distribution Voltage Control and Coordination with Distributed Generation," *IEEE Transactions on Power Delivery*, vol. 23, no. 2, pp. 1236–1242, 2008.

[47] D. Zhao and Y. Guan, "Energy-Based Switching Control for DC-DC Buck Converters with Switching Loads," in *2007 2nd IEEE Conference on Industrial Electronics and Applications*, pp. 938–942, IEEE, 2007.

[48] R. T. Ugale, Y. BalaKrishna, and B. N. Chaudhari, "Effects of Short Power Interruptions and Voltage Sags on the Performance of Line Start Permanent Magnet Synchronous Motor," in *2008 4th IET Conference on Power Electronics, Machines and Drives*, pp. 184–188, 2008.

[49] H. Fujita and H. Akagi, "Voltage-Regulation Performance of a Shunt Active Filter Intended for Installation on a Power Distribution System," *IEEE Transactions on Power Electronics*, vol. 22, no. 3, pp. 1046–1053, 2007.

[50] T.-L. Lee, S.-H. Hu, and Y.-H. Chan, "D-statcom with Positive-Sequence Admittance and Negative-Sequence Conductance to Mitigate Voltage Fluctuations in High-Level Penetration of Distributed-Generation Systems," *IEEE Transactions on Industrial Electronics*, vol. 60, no. 4, pp. 1417–1428, 2011.

[51] C. Hochgraf and R. H. Lasseter, "Statcom Controls for Operation with Unbalanced Voltages," *IEEE Transactions on Power Delivery*, vol. 13, no. 2, pp. 538–544, 1998.

[52] A. K. Basu, S. Chowdhury, S. Chowdhury, and S. Paul, "Microgrids: Energy Management by Strategic Deployment of DERs—A Comprehensive Survey," *Renewable and Sustainable Energy Reviews*, vol. 15, no. 9, pp. 4348–4356, 2011.

[53] C. K. Duffey and R. P. Stratford, "Update of Harmonic Standard IEEE-519: IEEE Recommended Practices and Requirements for Harmonic Control in Electric Power Systems," in *Record of Conference Papers., Industrial Applications Society 35th Annual Petroleum and Chemical Industry Conference,*, pp. 249–255, 1988.

[54] J. Boudrias, "Harmonic Mitigation, Power Factor Correction and Energy Saving with Proper Transformer and Phase Shifting Techniques," in *Canadian Conference on Electrical and Computer Engineering 2004 (IEEE Cat. No. 04CH37513)*, vol. 1, pp. 133–136, IEEE, 2004.

[55] I. F II, "IEEE Recommended Practices and Requirements for Harmonic Control in Electrical Power Systems," *IEEE Standard 519-1992, New York, NY, USA*, pp. 1–112, 1993.

[56] S. Khalid and B. Dwivedi, "Power Quality: An Important Aspect," *International Journal Engineering Science Technology*, vol. 2, no. 11, pp. 6485–6490, 2010.

[57] "IEEE Recommended Practice for Powering and Grounding Electronic Equipment," *IEEE Standard 1100-1999*, pp. 1–408, 1999.

[58] "Electromagnetic Compatibility (EMC)-Part 3-4: Limits-Limitation of Emission of Harmonic Currents in Low-Voltage Power Supply Systems for Equipment With Rated Current Greater Than 16 A," *Standard IEC TS 61000-3-4:1998*, p. 29, 1998.

[59] "IEEE Recommended Practice for Electric Power Distribution for Indus-Trial Plants," *IEEE Standard 141-1993*, pp. 1–768, 1994.

[60] M. El-Habrouk, M. Darwish, and P. Mehta, "A Survey of Active Filters and Reactive Power Compensation Techniques," in *2000 Eighth International Conference on Power Electronics and Variable Speed Drives (IEE Conf. Publ. No. 475)*, pp. 7–12, IET, 2000.

[61] A. Kusko and M. T. Thompson, "Power Quality in Electrical Systems," *IEEE Std 446-1995 [The Orange Book]*, 2007.

[62] G. Blajszczak and P. Antos, "Power Quality Park - Idea and feasibility study," in *Proceedings of the 2010 Electric Power Quality and Supply Reliability Conference*, pp. 17–22, IEEE, 2010.

[63] "IEEE Recommended Practice for Emergency and Standby Power Systems for Industrial and Commercial Applications," *IEEE Std 446-1995 [The Orange Book]*, pp. 1–320, 1996.

[64] "IEEE Recommended Practice for Emergency and Standby Power Systems for Industrial and Commercial Applications," *IEEE Std 446-1995 [The Orange Book]*, pp. 1–320, 1996.

[65] "IEEE Recommended Practice for Evaluating Electric Power System Compatibility with Electronic Process Equipment," *IEEE Std 1346-1998*, pp. 0–1, 1998.

[66] "Flickermeter-Functional and Design Speci-Cations, Standard 61000-4-15," *IEC, Geneva, Switzerland, Edition 2.0*, pp. 2010–2017, 2003.

[67] S. Halpin, "Comparison of IEEE and IEC Harmonic Standards," in *IEEE Power Engineering Society General Meeting, 2005*, pp. 2214–2216, IEEE, 2005.

[68] "IEEE Recommended Practice and Requirements for Harmonic Control in Electric Power Systems," *IEEE Std 519-2014 (Revision of IEEE Std 519-1992)*, pp. 1–29, 2014.

[69] R. Zamora and A. K. Srivastava, "Controls for Microgrids with Storage: Review, Challenges, and Research Needs," *Renewable and Sustainable Energy Reviews*, vol. 14, no. 7, pp. 2009–2018, 2010.

[70] K. Strunz, E. Abbasi, and D. N. Huu, "DC Microgrid for Wind and Solar Power Integration," *IEEE Journal of emerging and selected topics in Power Electronics*, vol. 2, no. 1, pp. 115–126, 2013.

[71] Y. W. Li, D. M. Vilathgamuwa, and P. C. Loh, "Robust Control Scheme for a Microgrid with PFC Capacitor Connected," *IEEE Transactions on Industry Applications*, vol. 43, no. 5, pp. 1172–1182, 2007.

[72] A. Mohd, E. Ortjohann, W. Sinsukthavorn, M. Lingemann, N. Hamsic, and D. Morton, "Supervisory Control and Energy Management of an Inverter-Based Modular Smart Grid," in *2009 IEEE/PES Power Systems Conference and Exposition*, pp. 1–6, IEEE, 2009.

[73] O. Omari, E. Ortjohann, A. Mohd, and D. Morton, "An Online Control Strategy for DC Coupled Hybrid Power Systems," in *2007 IEEE Power Engineering Society General Meeting*, pp. 1–8, IEEE, 2007.

[74] X. Liu, P. Wang, and P. C. Loh, "A Hybrid AC/DC Microgrid and its Coordination Control," *IEEE Transactions on Smart Grid*, vol. 2, no. 2, pp. 278–286, 2011.

[75] D. Sindhu, R. Aswinudhaya, G. Irusapparajan, and V. Sudhagar, "Analysis of the Performance of Hybrid AC/DC Microgrid by using dq Transformation," in *2013 International Conference on Circuits, Power and Computing Technologies (ICCPCT)*, pp. 107–114, IEEE, 2013.

[76] V. K. Kannan and N. Rengarajan, "Photovoltaic Based Distribution Static Compensator for Power Quality Improvement," *International Journal of Electrical Power & Energy Systems*, vol. 42, no. 1, pp. 685–692, 2012.

[77] K. N. Reddy and V. Agarwal, "Utility-Interactive Hybrid Distributed Generation Scheme with Compensation Feature," *IEEE Transactions on Energy Conversion*, vol. 22, no. 3, pp. 666–673, 2007.

[78] A. Eid, "Control of Hybrid Energy Systems Micro-Grid," in *2013 IEEE International Conference on Smart Energy Grid Engineering (SEGE)*, pp. 1–6, IEEE, 2013.

[79] N. A. Ahmed, A. Al-Othman, and M. AlRashidi, "Development of an Efficient Utility Interactive Combined Wind/Photovoltaic/Fuel Cell Power System with MPPT and DC bus Voltage Regulation," *Electric Power Systems Research*, vol. 81, no. 5, pp. 1096–1106, 2011.

[80] M. Akbari, S. Tafreshi, and M. Golkar, "Voltage Control of a Hybrid AC/DC Microgrid in Stand-Alone Operation Mode," in *ISGT2011-India*, pp. 363–367, IEEE, 2011.

[81] P. Dash, M. Mangaraj, and T. Penthia, "Mid-point Capacitor Type VSC Based DSTATCOM with a Supercapacitor for Power Quality Improvement under Unbalanced Loading Condition," in *2016 IEEE Students' Conference on Electrical, Electronics and Computer Science (SCEECS)*, pp. 1–6, IEEE, 2016.

[82] A. Ganguly, D. Misra, and S. Ghosh, "Modeling and Analysis of Solar Photovoltaic-Electrolyzer-Fuel Cell Hybrid Power System Integrated with a Floriculture Greenhouse," *Energy and buildings*, vol. 42, no. 11, pp. 2036–2043, 2010.

[83] O. C. Onar, M. Uzunoglu, and M. S. Alam, "Modeling, Control and Simulation of an Autonomous Wind Turbine/Photovoltaic/Fuel Cell/Ultra-Capacitor Hybrid Power System," *Journal of Power Sources*, vol. 185, no. 2, pp. 1273–1283, 2008.

[84] S. Arezki and M. Boudour, "Improvement of Power Quality for Hybrid PV-FC Power Supply System," in *2014 16th International Power Electronics and Motion Control Conference and Exposition*, pp. 725–730, IEEE, 2014.

[85] F. K. Arabul, A. Y. Arabul, C. F. Kumru, and A. R. Boynuegri, "Providing Energy Management of a Fuel Cell–Battery-Wind Turbine-Solar Panel Hybrid Off Grid Smart Home System," *International Journal of Hydrogen Energy*, vol. 42, no. 43, pp. 26906–26913, 2017.

[86] H. Fathabadi, "Novel Standalone Hybrid Solar/Wind/Fuel Cell Power Generation System for Remote Areas," *Solar Energy*, vol. 146, pp. 30–43, 2017.

[87] F. Thanaa, M. N. Eskander, and M. T. El-Hagry, "Energy Flow and Management of a Hybrid Wind/PV/Fuel Cell Generation System," *Energy conversion and management*, vol. 47, no. 9-10, pp. 1264–1280, 2006.

[88] K. Basaran, N. S. Cetin, and S. Borekci, "Energy Management for On-Grid and Off-Grid Wind/PV and Battery Hybrid Systems," *IET Renewable Power Generation*, vol. 11, no. 5, pp. 642–649, 2017.

[89] A. Eid, "Control of Hybrid Energy Systems Micro-Grid," in *2013 IEEE International Conference on Smart Energy Grid Engineering (SEGE)*, pp. 1–6, IEEE, 2013.

[90] I. Vechiu, O. Curea, and H. Camblong, "Transient Operation of a Four-Leg Inverter for Autonomous Applications With Unbalanced Load," *IEEE Transactions on Power Electronics*, vol. 25, no. 2, pp. 399–407, 2010.

[91] A. Mohd, E. Ortjohann, N. Hamsic, W. Sinsukthavorn, M. Lingemann, A. Schmelter, and D. Morton, "Control Strategy and Space Vector Modulation for Three-Leg Four-Wire Voltage Source Inverters under Unbalanced Load Conditions," *IET Power Electronics*, vol. 3, no. 3, pp. 323–333, 2010.

[92] I. Sheikh, "Hybrid Energy Management System for Microgrid Applications," in *2016 International Conference on Energy Efficient Technologies for Sustainability (ICEETS)*, pp. 361–365, IEEE, 2016.

[93] D. Psakis, S. Voutetakis, P. Seferlis, F. Stergiopoulos, and C. Elmasides, "Power Management Strategies for a Stand-Alone Power System using Renewable EnergySources and Hydrogen Storage," *International Journal of Hydrogen Energy I.*, vol. 34, no. 16, pp. 7081–7095, 2009.

[94] Y. Xu, Q. Guo, H. Sun, and Z. Fei, "Distributed Discrete Robust Secondary Cooperative Control for Islanded Microgrids," *IEEE Transactions on Smart Grid*, 2018.

[95] G. Lou, W. Gu, W. Sheng, X. Song, and F. Gao, "Distributed Model Predictive Secondary Voltage Control of Islanded Microgrids with Feedback Linearization," *IEEE Access*, vol. 6, pp. 50169–50178, 2018.

[96] S. Malla and C. Bhende, "Voltage Control of Stand-Alone Wind and Solar Energy System," *International Journal of Electrical Power and Energy Systems*, vol. 56, pp. 361–373, 2014.

[97] A. Mostafazadeh, T. K. Tasooji, M. Sahin, and O. Usta, "Voltage Control of PV-FC-Battery-Wind Turbine for Stand-Alone Hybrid System Based on Fuzzy Logic Controller," in *Electrical and Electronics Engineering (ELECO), 2017 10th International Conference on*, pp. 170–174, IEEE, 2017.

[98] M. Uzunoglu, O. Onar, and M. Alam, "Modeling, Control and Simulation of a PV/FC/UC Based Hybrid Power Generation System for Stand-Alone Applications," *Renewable energy*, vol. 34, no. 3, pp. 509–520, 2009.

[99] H. Myneni, G. S. Kumar, and D. Sreenivasarao, "Adaptive DC-Link Voltage Regulation for DSTATCOM under Load Variations," in *2016 IEEE Region 10 Conference (TENCON)*, pp. 2909–2913, IEEE, 2016.

[100] H. Suryanarayana and M. K. Mishra, "Fuzzy Logic Based Supervision of DC Link PI Control in a DSTATCOM," in *2008 Annual IEEE India Conference*, vol. 2, pp. 453–458, IEEE, 2008.

[101] M. T. Ahmad, N. Kumar, and B. Singh, "A Discrete Derivative Control Technique for DC Link Voltage in Shunt Compensator," in *2015 Annual IEEE India Conference (INDICON)*, pp. 1–5, IEEE, 2015.

[102] M. Murali, K. Srinivasu, and L. N. Rao, "Enhancement of Power Quality with ANFIS Controlled DSTATCOM in Four Wire Three Phase Distribution System," in *2016 Biennial International Conference on Power and Energy Systems: Towards Sustainable Energy (PESTSE)*, pp. 1–8, IEEE, 2016.

[103] Y. V. Ninghot and V. Dhote, "Particle Swarm Optimization Based DSTATCOM with Reduced DC-Link Voltage for Load Compensation," in *2017 Innovations in Power and Advanced Computing Technologies (i-PACT)*, pp. 1–7, IEEE, 2017.

[104] K. K. Prasad, H. Myneni, and G. S. Kumar, "Power Quality Improvement and PV Power Injection by DSTATCOM with Variable DC Link Voltage Control from RSC-MLC," *IEEE Transactions on Sustainable Energy*, vol. 10, no. 2, pp. 876–885, 2018.

[105] Y. Hao, "Constructing Nonlinear Variable Gain Controllers via the Takagi–Sugeno Fuzzy Control," *IEEE Transactions on Fuzzy System*, vol. 6, no. 2, pp. 226–234, 1998.

[106] N. Farokhnia, S. H. Fathi, R. Khoraminia, and S. H. Hosseinian, "Optimization of PI Coefficients in DSTATCOM Nonlinear Controller for Regulating DC voltage Using Genetic Algorithm," in *2009 4th IEEE Conference on Industrial Electronics and Applications*, pp. 2291–2296, IEEE, 2009.

[107] H. Akagi, Y. Kanazawa, and A. Nabae, "Instantaneous Reactive Power Compensators Comprising Switching Devices Without Energy Storage Components," *IEEE Transactions on Industry Applications*, no. 3, pp. 625–630, 1984.

[108] F. Z. Peng and J.-S. Lai, "Generalized Instantaneous Reactive Power Theory For Three-Phase Power Systems," *IEEE Transactions on Instrumentation and Measurement*, vol. 45, no. 1, pp. 293–297, 1996.

[109] S. Bhattacharya and D. Divan, "Synchronous Frame Based Controller Implementation for a Hybrid Series Active Filter System," in *IAS'95.*

Conference Record of the 1995 IEEE Industry Applications Conference Thirtieth IAS Annual Meeting, vol. 3, pp. 2531–2540, IEEE, 1995.

[110] B. Singh and V. Verma, "Selective Compensation of Power-Quality Problems Through Active Power Filter by Current Decomposition," *IEEE Transactions on Power Delivery*, vol. 23, no. 2, pp. 792–799, 2008.

[111] B. N. Singh, B. Singh, A. Chandra, and K. Al-Haddad, "Design and Digital Implementation of Active Filter with Power Balance Theory," *IEE Proceedings-Electric Power Applications*, vol. 152, no. 5, pp. 1149–1160, 2005.

[112] P. Karuppanan and K. K. Mahapatra, "A Novel Control Strategy Based Shunt APLC for Power Quality Improvements," in *2010 International Conference on Power, Control and Embedded Systems*, pp. 1–6, 2010.

[113] P. Gharde, N. Pande, and P. Debre, "Load Compensation of a Stiff System using ISCT Based D-STATCOM Under Unbalanced and Non-Linear Load Condition," in *2017 International Conference on Innovations in Information, Embedded and Communication Systems (ICIIECS)*, pp. 1–4, IEEE, 2017.

[114] R. Elshatshat, M. Kazerani, and M. Salama, "ADALINE-Based Controller for Active Power-Line Conditioners," in *1999 IEEE Transmission and Distribution Conference (Cat. No. 99CH36333)*, vol. 2, pp. 566–571, IEEE, 1999.

[115] B. Singh and J. Solanki, "Load Compensation for Diesel Generator-Based Isolated Generation System Employing DSTATCOM," *IEEE Transactions on Industry Applications*, vol. 47, no. 1, pp. 238–244, 2010.

[116] M. I. M. Montero, E. R. Cadaval, and F. B. Gonzalez, "Comparison of Control Strategies for Shunt Active Power Filters in Three-Phase Four-Wire Systems," *IEEE Transactions on Power Electronics*, vol. 22, no. 1, pp. 229–236, 2007.

[117] T. Zaveri, B. Bhalja, and N. Zaveri, "Comparison of Control Strategies for DSTATCOM in Three-Phase, Four-Wire Distribution System for Power Quality Improvement under Various Source Voltage and Load Conditions,"

International Journal of Electrical Power & Energy Systems, vol. 43, no. 1, pp. 582–594, 2012.

[118] B. Singh and J. Solanki, "A Comparison of Control Algorithms for DSTATCOM," *IEEE Transactions on Industrial Electronics*, vol. 56, no. 7, pp. 2738–2745, 2009.

[119] Y. He, Y. Zou, F. Liu, and H. Li, "Research on an Improved Adaptive Algorithm Applied to Active Power Filters," in *2005/2006 IEEE/PES Transmission and Distribution Conference and Exhibition*, pp. 672–677, IEEE, 2006.

[120] M. Badoni, A. Singh, and B. Singh, "Comparative Performance of Wiener Filter and Adaptive Least Mean Square-Based Control for Power Quality Improvement," *IEEE Transactions on Industrial Electronics*, vol. 63, no. 5, pp. 3028–3037, 2016.

[121] R. K. Agarwal, I. Hussain, and B. Singh, "LMF-Based Control Algorithm for Single Stage Three-Phase Grid Integrated Solar PV System," *IEEE Transactions on Sustainable Energy*, vol. 7, no. 4, pp. 1379–1387, 2016.

[122] T. Aboulnasr and K. Mayyas, "A Robust Variable Step-Size LMS-type Algorithm: Analysis and Simulations," *IEEE Transactions on Signal Processing*, vol. 45, no. 3, pp. 631–639, 1997.

[123] J. B. Evans, P. Xue, and B. Liu, "Analysis and Implementation of Variable Step Size Adaptive Algorithms," *IEEE Transactions on Signal Processing*, vol. 41, no. 8, pp. 2517–2535, 1993.

[124] J. Li and J. Li, "A Novel Variable Step Size LMS Algorithm Based on Decorrelation," in *2010 3rd International Congress on Image and Signal Processing*, vol. 7, pp. 3291–3294, IEEE, 2010.

[125] G. Pathak, B. Singh, and B. K. Panigrahi, "Control of Wind-Diesel Microgrid using Affine Projection-Like Algorithm," *IEEE Transactions on Industrial Informatics*, vol. 12, no. 2, pp. 524–531, 2016.

[126] J. Yoo, J. Shin, and P. Park, "Variable Step-Size Affine Projection Sign Algorithm," *IEEE Transactions on Circuits and Systems II: Express Briefs*, vol. 61, no. 4, pp. 274–278, 2014.

[127] Y. Yan, J. Zhao, Z. Wang, and Y. Yan, "An Novel Variable Step Size LMS Adaptive Filtering Algorithm Based on Hyperbolic Tangent Function," in *2010 International Conference on Computer Application and System Modeling (ICCASM 2010)*, vol. 14, pp. V14–233, IEEE, 2010.

[128] B. Singh, S. K. Dube, and S. R. Arya, "Hyperbolic Tangent Function-Based Least Mean-Square Control Algorithm for Distribution Static Compensator," *IET Generation, Transmission & Distribution*, vol. 8, no. 12, pp. 2102–2113, 2014.

[129] T. Houya, H. Kamata, and Y. Ishida, "Design and Implementation of an Adaptive Filter Using Neural Networks," in *Proceedings of 1993 International Conference on Neural Networks (IJCNN-93-Nagoya, Japan)*, vol. 1, pp. 979–982, IEEE, 1993.

[130] P. Stubberud and J. Bruce, "An LMS Algorithm for Training Single Layer Globally Recursive Neural Networks," in *1998 IEEE International Joint Conference on Neural Networks Proceedings. IEEE World Congress on Computational Intelligence (Cat. No. 98CH36227)*, vol. 3, pp. 2214–2217, IEEE, 1998.

[131] R. K. Agarwal, I. Hussain, and B. Singh, "Application of LMS-Based NN Structure for Power Quality Enhancement in a Distribution Network under Abnormal Conditions," *IEEE Transactions on Neural Networks and Learning Systems*, vol. 29, no. 5, pp. 1598–1607, 2017.

[132] M. Badoni, A. Singh, and B. Singh, "Adaptive Neurofuzzy Inference System Least-Mean-Square-Based Control Algorithm for DSTATCOM," *IEEE Transactions on Industrial Informatics*, vol. 12, no. 2, pp. 483–492, 2016.

[133] A. Bhattacharya and C. Chakraborty, "A Shunt Active Power Filter with Enhanced Performance using ANN-Based Predictive and Adaptive

Controllers," *IEEE Transactions on Industrial Electronics*, vol. 58, no. 2, pp. 421–428, 2010.

[134] B. Singh and V. Rajagopal, "Neural-Network-Based Integrated Electronic Load Controller for Isolated Asynchronous Generators in Small Hydro Generation," *IEEE Transactions on Industrial Electronics*, vol. 58, no. 9, pp. 4264–4274, 2010.

[135] B. Singh, V. Verma, and J. Solanki, "Neural Network-Based Selective Compensation of Current Quality Problems in Distribution System," *IEEE Transactions on Industrial Electronics*, vol. 54, no. 1, pp. 53–60, 2007.

[136] R. Cardoso, J. Kanieski, H. Pinheiro, and H. A. Grundling, "Reference Generation for Shunt Active Power Filters Based on Optimum Filtering Theory," in *2007 IEEE Industry Applications Annual Meeting*, pp. 1621–1627, IEEE, 2007.

[137] V. George and M. K. Mishra, "Design and Analysis of User-Defined Constant Switching Frequency Current-Control-Based Four-Leg DSTATCOM," *IEEE Transactions on Power Electronics*, vol. 24, no. 9, pp. 2148–2158, 2009.

[138] A. Pigazo, V. Moreno, E. Estébanez, M. Liserre, and A. Dell'Aquila, "Harmonic Compensation in Shunt Active Power Filters by Applying Kalman Filtering for Estimation of the Averaged Load Conductance," in *2010 IEEE International Symposium on Industrial Electronics*, pp. 850–855, IEEE, 2010.

[139] T. Jin and K. M. Smedley, "Operation of One-Cycle Controlled Three-Phase Active Power Filter with Unbalanced Source and Load," *IEEE Transactions on Power Electronics*, vol. 21, no. 5, pp. 1403–1412, 2006.

[140] M. Haddad, S. Rahmani, F. Fnaiech, and K. Al-Haddad, "A Lyapunov-Based Current Control Strategy of ThreePhase Shunt Active Power Filter for Harmonic Elimination, Power-Factor Correction, and Load Unbalance Compensation," in *IECON 2012-38th Annual Conference on IEEE Industrial Electronics Society*, pp. 3340–3345, IEEE, 2012.

[141] S. Rahmani, A. Hamadi, and K. Al-Haddad, "A Lyapunov-Function-Based Control for a Three-Phase Shunt Hybrid Active Filter," *IEEE Transactions on Industrial Electronics*, vol. 59, no. 3, pp. 1418–1429, 2011.

[142] P. C. Loh, Y. Tang, F. Blaabjerg, and P. Wang, "Mixed-Frame and Stationary-Frame Repetitive Control Schemes for Compensating Typical Load and Grid Harmonics," *IET Power Electronics*, vol. 4, no. 2, pp. 218–226, 2011.

[143] B. Singh and S. R. Arya, "Implementation of Single-Phase Enhanced Phase-Locked Loop-Based Control Algorithm for Three-Phase DSTATCOM," *IEEE Transactions on Power Delivery*, vol. 28, no. 3, pp. 1516–1524, 2013.

[144] G. A. Ramos and R. Costa-Castelló, "Power Factor Correction and Harmonic Compensation using Second-Order Odd-Harmonic Repetitive Control," *IET control theory & applications*, vol. 6, no. 11, pp. 1633–1644, 2012.

[145] B. Singh and S. R. Arya, "Adaptive Theory-Based Improved Linear Sinusoidal Tracer Control Algorithm for DSTATCOM," *IEEE Transactions on Power Electronics*, vol. 28, no. 8, pp. 3768–3778, 2012.

[146] B. Singh and S. R. Arya, "Back-Propagation Control Algorithm for Power Quality Improvement using DSTATCOM," *IEEE Transactions on Industrial Electronics*, vol. 61, no. 3, pp. 1204–1212, 2013.

[147] S. R. Arya, B. Singh, A. Chandra, and K. Al-Haddad, "Learning-Based Anti-Hebbian Algorithm for Control of DistributionStatic Compensator," *IEEE Transactions on Industrial Electronics*, vol. 61, no. 11, pp. 6004–6012, 2014.

[148] B. Singh, K. Mathuria, I. Hussain, and S. Kumar, "Implementation of Demodulation-SOGI Control Algorithm for Improving the Power Quality," in *IECON 2017-43rd Annual Conference of the IEEE Industrial Electronics Society*, pp. 2540–2545, IEEE, 2017.

[149] P. Rodriguez, R. Teodorescu, I. Candela, A. V. Timbus, M. Liserre, and F. Blaabjerg, "New Positive-Sequence Voltage Detector for Grid

Synchronization of Power Converters under Faulty Grid Conditions," in *2006 37th IEEE Power Electronics Specialists Conference*, pp. 1–7, IEEE, 2006.

[150] M. T. Ahmad, N. Kumar, and B. Singh, "AVSF-Based Control Algorithm of DSTATCOM for Distribution System," *IET Generation, Transmission & Distribution*, vol. 11, no. 13, pp. 3389–3396, 2017.

[151] N. Beniwal, I. Hussain, and B. Singh, "Second-Order Volterra-Filter-Based Control of a Solar PV-DSTATCOM System to Achieve Lyapunov's Stability," *IEEE Transactions on Industry Applications*, vol. 55, no. 1, pp. 670–679, 2018.

[152] B. Singh and S. R. Arya, "Composite Observer-Based Control Algorithm for Distribution Static Compensator in Four-Wire Supply System," *IET Power electronics*, vol. 6, no. 2, pp. 251–260, 2013.

[153] P. Chittora, A. Singh, and M. Singh, "Harmonic Current Extraction and Compensation in Three Phase Three Wire System using Notch Filter," in *2015 IEEE Recent Advances in Intelligent Computational Systems (RAICS)*, pp. 422–427, IEEE, 2015.

[154] B. Singh, K. Kant, and S. R. Arya, "Notch Filter-Based Fundamental Frequency Component Extraction to Control Distribuion Static Compensator for Mitigating Current-Related Pwer Quality PRoblems," *IET Power Electronics*, vol. 8, no. 9, pp. 1758–1766, 2015.

[155] A. Mus-ab and M. K. Mishra, "Wavelet Transform Based Algorithms for Load Compensation using DSTATCOM," in *2017 IEEE PES Asia-Pacific Power and Energy Engineering Conference (APPEEC)*, pp. 1–6, IEEE, 2017.

[156] H. Awad, H. Nelsen, F. Blaabjerg, and M. J. Newman, "Operation of Static Series Compensator under Distorted Utility Conditions," *IEEE Transactions on Power Systems*, vol. 20, no. 1, pp. 448–457, 2005.

[157] L. Coluccio, A. Eisinberg, G. Fedele, C. Picardi, and D. Sgro, "Modulating Functions Method Plus SOGI Scheme for Signal Tracking," in *2008 IEEE International Symposium on Industrial Electronics*, pp. 854–859, IEEE, 2008.

[158] A. Salamah, S. Finney, and B. Williams, "Three-Phase Phase-Lock Loop for Distorted Utilities," *IET Electric Power Applications*, vol. 1, no. 6, pp. 937–945, 2007.

[159] A. Shayestehfard, S. Mekhilef, and H. Mokhlis, "IZDPWM-Based Feedforward Controller for Grid-Connected Inverters under Unbalanced and Distorted Conditions," *IEEE Transactions on Industrial Electronics*, vol. 64, no. 1, pp. 14–21, 2016.

[160] S. Alepuz, S. Busquets, J. Bordonau, J. Pontt, C. Silva, and J. Rodriguez, "Balanced Grid Currents in Three-Level Voltage-Source Inverters Connected to the Utility under Distorted Condition using Symmetrical Components and Linear Quadratic Regulator," in *2007 European Conference on Power Electronics and Applications*, pp. 1–10, IEEE, 2007.

[161] X. Song, Y. Wang, W. Hu, and Z. Wang, "Three Reference Frame Control Scheme of 4 Wire Grid-Connected Inverter for Micro Grid under Unbalanced Grid Voltage Conditions," in *2009 Twenty-Fourth Annual IEEE Applied Power Electronics Conference and Exposition*, pp. 1301–1305, IEEE, 2009.

[162] S. Biricik, S. Redif, Ö. C. Özerdem, S. K. Khadem, and M. Basu, "Real-Time Control of Shunt Active Power Filter under Distorted Grid Voltage and Unbalanced Load Condition using Self-Tuning Filter," *IET Power Electronics*, vol. 7, no. 7, pp. 1895–1905, 2014.

[163] D. Shin, K.-J. Lee, J.-P. Lee, D.-W. Yoo, and H.-J. Kim, "Implementation of Fault Ride-Through Techniques of Grid-Connected Inverter for Distributed Energy Resources with Adaptive Low-Pass Notch PLL," *IEEE Transactions on Power Electronics*, vol. 30, no. 5, pp. 2859–2871, 2014.

[164] R. Chilipi, N. Al Sayari, K. Al Hosani, and A. R. Beig, "Control Scheme for Grid-Tied Distributed Generation Inverter under Unbalanced and Distorted

Utility Conditions with Power Quality Ancillary Services," *IET Renewable Power Generation*, vol. 10, no. 2, pp. 140–149, 2016.

[165] P. Shah, I. Hussain, and B. Singh, "Fuzzy Logic Based FOGI-FLL Algorithm for Optimal Operation of Single-Stage Three-Phase Grid Interfaced Multifunctional SECS," *IEEE Transactions on Industrial Informatics*, vol. 14, no. 8, pp. 3334–3346, 2017.

[166] D. J. Hogan, F. J. Gonzalez-Espin, J. G. Hayes, G. Lightbody, and R. Foley, "An Adaptive Digital-Control Scheme for Improved Active Power Filtering Under Distorted Grid Conditions," *IEEE Transactions on Industrial Electronics*, vol. 65, no. 2, pp. 988–999, 2018.

[167] I. Ullah and M. Ashraf, "Comparison of Synchronization Techniques Under Distorted Grid Conditions," *IEEE Access*, vol. 7, pp. 101345–101354, 2019.

[168] A. Luna, J. Rocabert, J. I. Candela, J. R. Hermoso, R. Teodorescu, F. Blaabjerg, and P. Rodríguez, "Grid Voltage Synchronization for Distributed Generation Systems Under Grid Fault Conditions," *IEEE Transactions on Industry Applications*, vol. 51, no. 4, pp. 3414–3425, 2015.

[169] B. Sun, N. Dai, U. Chio, M. Wong, C. Wong, S. Sin, U. Seng-Pan, and R. P. Martins, "FPGA-Based Decoupled Double Synchronous Reference Frame PLL for Active Power Filters," in *2011 6th IEEE Conference on Industrial Electronics and Applications*, pp. 2145–2150, IEEE, 2011.

[170] P. Rodríguez, R. Teodorescu, I. Candela, A. V. Timbus, M. Liserre, and F. Blaabjerg, "New Positive-Sequence Voltage Detector for Grid Synchronization of Power Converters under Faulty Grid Conditions," in *2006 37th IEEE Power Electronics Specialists Conference*, pp. 1–7, IEEE, 2006.

[171] K. Lee, J. Lee, D. Shin, D. Yoo, and H. Kim, "A Novel Grid Synchronization PLL Method Based on Adaptive Low-Pass Notch Filter for Grid-Connected PCS," *IEEE Transactions on Industrial Electronics*, vol. 61, no. 1, pp. 292–301, 2014.

[172] S. Singh, S. Kewat, B. Singh, B. K. Panigrahi, and M. K. Kushwaha, "Seamless Control of Solar PV Grid Interfaced System With Islanding Operation," *IEEE Power and Energy Technology Systems Journal*, vol. 6, no. 3, pp. 162–171, 2019.

[173] B. C. N., M. S., and J. S. K., "TS-fuzzy-Controlled Active Power Filter for Load Compensation," *IEEE Transactions on Power Delivery*, vol. 21, no. 3, pp. 1459–1465, 2006.

[174] Y. Shi, H. C. So, L. Huang, and C. Qian, "Shrinkage Linear and Widely Linear Complex-Valued Least Mean Squares Algorithms for Adaptive Beamforming," *IEEE Transactions on Signal Process*, vol. 63, no. 1, pp. 119–131, 2015.